Quantifying the Spatial and Temporal Response of UTH and OLR to Deep Convection over Tropical Africa

James Ingram
Space and Atmospheric Physics Group
Department of Physics
Imperial College of Science, Technology and Medicine

A thesis submitted for the degree of
Doctor of Philosophy, University of London

I hereby declare that the work submitted in this thesis
is my own and all else is appropriately referenced.

Abstract

Upper Tropospheric Humidity (UTH) has a strong control on clear-sky Outgoing Longwave Radiation (OLR). Moisture from the boundary layer is transported to the drier upper troposphere by convective ascent in the tropics and realised in the form of deep convective clouds. The spatial and temporal response of UTH and the corresponding OLR are cause for debate. This study uses geostationary satellite imagery from the Spinning Enhanced Visible and InfraRed Imager (SEVIRI) to estimate UTH using water vapour channel radiances. Deep convection over Tropical Africa is detected using the difference between 6.2 μm and 7.3 μm brightness temperatures. The sensitivity of TOA brightness temperatures to cloud properties including cloud top height and optical depth are modelled using the Santa Barbara Disort Atmospheric Radiative Transfer model with thresholds developed using colocated matchups with CloudSat and CALIPSO cloud classifications. The most appropriate thresholds are determined using probability statistics and receiver operating characteristic curves. Deep convective clouds are tracked over their lifetime in June and December 2010 using a cloud tracking algorithm, based on an area overlap method. A general robust pattern in the UTH response emerges. A stronger response of UTH is found in the spatial domain than that over the temporal domain. UTH decreases with distance from the cloud edge, whilst a small increase is seen over the cloud lifetime. This was found to be controlled by cloud size and cloud lifetime, with larger and longer lived clouds causing a stronger perturbation in UTH. The UTH response was found to be stronger in June than in December. A strong negative correlation is found between UTH and OLR perturbations, with OLR measured using the Geostationary Earth Radiation Budget (GERB) instrument. This pattern is stronger in December than June.

Acknowledgments

Firstly I would like to thank the friends I have made over the last 4 years at Imperial for their constant support and help, as well as some fantastic holidays and lots of cups of tea. Thanks also goes to my friends outside of Imperial. I would also like to say a big thank you to my colleagues in SPAT, including Rich for his continued and valued support with all things technical and Nathan for his help with IDL. But my biggest and most heartfelt thanks goes to my supervisor Helen. Without her continued support and forgiving nature when I constantly nodded my head at things I didn't understand, and her rigorous and relentless reading of my repetitive introduction and other chapters, this thesis would have suffered massively. Thanks Helen.

Contents

List of Figures

List of Tables

Chapter I

Introduction

1 Overview

Deep convection, the thermally induced upward motion of mass from the lower to upper troposphere, is a prominent source and a major control on the spatial and temporal distribution of the most potent greenhouse gas - water vapour - in the upper troposphere. The Upper Tropospheric Humidity (UTH) and its spatial and temporal distribution is a strong control on clear sky Outgoing Longwave Radiation (OLR) (Emanuel, 2005).

Moist air from the boundary layer is transported to the drier upper troposphere by convective ascent in the tropics. The water vapour transported upwards is realised in the form of deep convective clouds. It is suggested that as deep convective clouds mature and dissipate, evaporating cloud hydrometeors have a moistening effect on the upper troposphere (Sun and Lindzen, 1993; Zelinka and Hartmann, 2009). Although small in terms of the total column amount, the presence of water vapour in the upper troposphere has a strong direct impact on the absorption and emission of longwave radiation (Gettelmann *et al.*, 2006). OLR emitted to space is highly sensitive to small changes in the UTH, therefore an understanding of the spatial and temporal response of UTH and OLR to deep convection is of key importance.

Although many studies have sought to quantify the response of UTH and OLR to tropical deep convection, there is still large disagreement regarding the spatial and temporal response of both (e.g. Soden, 2000; Zelinka and Hartmann, 2009). This chapter gives a brief discussion on convection and parcel theory with regards to deep convection, followed by an introduction to the spatial and temporal scales of deep convective systems. This is followed by a discussion of the spatial and temporal responses of UTH to deep convection and the atmospheric state, framed in relation to the life cycle of the cloud. Disagreements in the literature concerning the specifics of these responses as the cloud matures and dissipates are highlighted. Lastly, a discussion is given on the OLR response to deep convection and UTH. An outline of the aims of this thesis is then provided at the end of the chapter based on these discussions.

1.1 Deep Convection - a Theoretical Basis

Idealized conditions in which deep convection occurs include large-scale areas of conditionally unstable lapse rates, areas with horizontally uniform high moisture content, and areas of low level convergence. For cloud development, moist convection - in which there is a phase change of the water - needs to occur, rather than dry convection (Henken *et al.,* 2009). A balance between the environmental thermodynamics, cloud radiative forcing and the Convective Available Potential Energy (CAPE) is preferential for the development of deep convective clouds (Jensen and Del Genio, 2003). CAPE is defined as the buoyancy of a parcel vertically integrated between the level of free convection and the level of neutral buoyancy (see figure 1.1). The rising air parcels that result from the warming of a surface are known as thermals and can have a horizontal extent

extending from 0.1 to 10 km (Henken *et al.,* 2009).

Thermodynamically, deep convective events occur when air parcels are able to rise past the Level of Free Convection (LFC) up to the Level of Neutral Buoyancy (LNB), and where conditional instability exists in the troposphere (Fu *et al.*, 1990; Wallace and Hobbs, 2006) (figure 1.1). The LFC is defined as the altitude in the atmosphere where the atmospheric temperature decreases faster than that of the moist adiabat of a saturated parcel of air at the same height (Chandrasekar, 2010). The LNB is defined as the height at which an air parcel is at the same temperature as its environment.

Conversion of CAPE to parcel kinetic energy results in the vertical motion of an air parcel, due to the creation of an unstable layer of air whenever radiative heating of a surface occurs (Rogers and Yau, 1989; Sherwood *et al.*, 2004). If heat sinks and sources are ignored, the air parcel will rise along the dry adiabatic lapse rate - cooling at about 10 K per 1000 m. With this vertical motion, the thermodynamic state of the air parcel changes to preserve mechanical equilibrium - the parcel begins to expand (Salby, 1996).

As the parcel moves vertically through the atmosphere and expands adiabatically, it will reach the Lifting Condensation Level (LCL) (if the parcel has been mechanically lifted) or the Convective Condensation Level (CCL) (if the parcel has been lifted through surface heating) (Bohren and Albrecht, 1998). This is the point at which the saturation mixing ratio equals the actual mixing ratio of the parcel defining the cloud base (Trier, 2003) (figure 1.1). This is because the parcel will conserve its water vapour mixing ratio and as a result of vertical displacement, it will become saturated (Trier, 2003).

As the parcel continues to ascend above the CCL or LCL, it follows the moist adiabatic lapse rate if the parcel is saturated and condensing moisture out creating a net release of latent heat. If no cloud condensation nuclei (CCN) are present, the air parcel will become supersaturated and continue along the dry adiabatic lapse rate. If CCN are present, water vapour begins to condense onto these particles and cloud droplets can begin to form (heterogeneous cloud formation). This production of cloud droplets creates a release of latent heat, which adds positive buoyancy, promoting continued ascent due to this latent heat release preventing the parcel from cooling as quickly as it would at the dry adiabatic lapse rate (Salby, 1996). Deep convection is thus associated with a large net release of latent heat from phase changes within deep convective clouds. The strong vertical growth of deep convective cloud found in the early mature stage of the clouds lifecycle also induces a strong compensating atmospheric subsidence in the region surrounding the parcel. The parcel will continue to rise through the LFC and this process occurs until the updraft can no longer support vertical motion and the cloud droplets are precipitated out (Salby, 1996). This point at which vertical motion can no longer occur is the equilibrium level, or the LNB, where the temperature of the parcel is the same as that of the surrounding ambient environment.

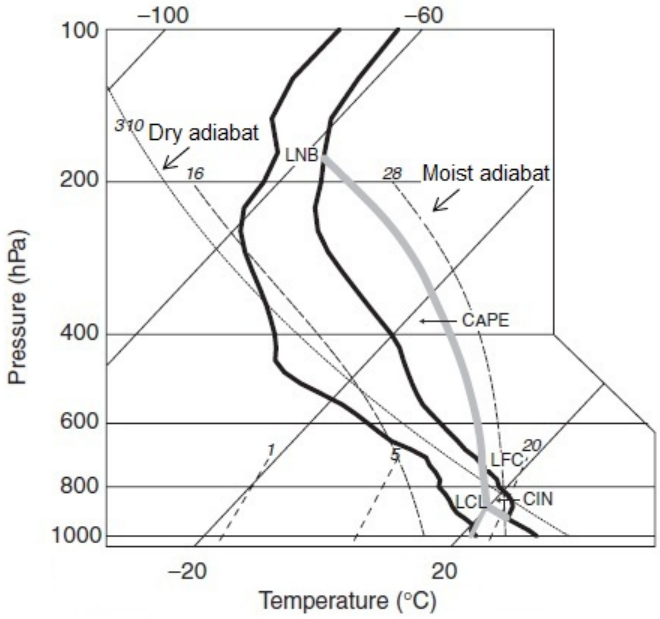

Figure 1.1: Skew T-log P diagrams for a conditionally unstable atmospheric profile for a tropical environment. Solid black lines represent environmental temperature (right) and dew point (left). The grey line represents a theoretical temperature of a parcel moving vertically through the atmosphere. Below the LCL the air parcel ascends along the dry adiabat. It then follows the moist adiabat above the LCL. Areas of positive CAPE occur where an excess of parcel temperature occurs, represented by the space between the LFC and LNB. Taken from: Trier (2003).

The strength of convection is a function of the CAPE and is determined by the vertical temperature profile of the troposphere (figure 1.1), with areas possessing large CAPE above the neutral state allowing the development of deep convective clouds with cloud top heights of 14 – 16 km (Sun and Lindzen, 1993; Jensen and Del Genio, 2003; Chaboureau *et al.*, 2004; Sherwood *et al.*, 2004). Although CAPE provides a useful measure of how strong the vertical movement of a parcel may be, it is only an approximation and does not confirm whether convection will actually occur. For convection to actually occur it must overcome the barrier beneath the LFC. This area is known as the area of Convective Inhibition (CIN) and represents the amount of work that needs to be done on the air parcel for it to reach the LFC, and subsequently rise to the LNB (Trier, 2003).

1.2 Deep Convective clouds - Spatial and Temporal Properties

1.2.1 Spatial

Deep convective clouds are typically found in the tropics - a region conventionally defined as being between 23.5° North and South of the equator and bounded by the tropics of Cancer and Capricorn (for a more detailed discussion of the tropics see chapter 3). Deep convective events range in size from single clouds with diameters of 1-10 km to Mesoscale Convective Systems (MCS) that cover several 1000 km, with some systems seen greater than 90,000 km^2(Roca *et al.,* 2002). However, the convective cloud fraction represents a small percentage of zonally average cloud cover in the tropics (Gettelmann *et al.*, 2002; Laing *et al.*, 2008; Russo *et*

al., 2011). MCSs typically occur when several smaller deep convective towers merge to create extensive cloud formations (Hall and Vonder Haar, 1999). Deep convection is largely organised into these large scale MCSs in regions of low level convergence and over certain orographic features (Wallace and Hobbs, 2006; Zelinka and Hartmann, 2009). In the vertical, deep convective clouds extend from a base height of roughly 1 km, although some have been found with a base height of 4 km (Henken *et al.,* 2009). This is largely dependent on the height of the boundary layer but some deep convective cloud can develop from alto or stratocumulus clouds. Mature deep convective clouds generally reach a height of between 8 and 12 km, though some have been found to vary between 5 km in the early stage of their lifecycle, and up to 18 km in some regions of the world (Krauss *et al.,* 2007). Mature deep convective clouds possess a characteristic anvil shape, due to the stratosphere acting as a lid. Due to the temperature inversion in the stratosphere, the vertically moving convection is hindered and forced to spread horizontally, creating an anvil shape. If a parcel has enough vertical momentum, it may penetrate the stratosphere. This is known as overshooting convection and creates the higher deep convective cloud tops observed.

1.2.2 Temporal

The general life cycle of tropical deep convection follows a developing/growth stage, followed by maturity then a dissipating stage as the cloud decays and cirrus begins to form (Futyan and Del Genio, 2007; Inoue *et al.*, 2009) (figure 1.2). The smaller single celled clouds have been found to have very short lifetimes typically lasting between 3 and 24 hours, compared to the large scale MCS's, which can persist for longer than 24 hours. Based on the timing of cloud life cycles, peak cloud development over continental regions such as tropical Africa, as found by both Yang and Slingo (2001) and Laing *et al.*, (2008) is expected to be seen in the late afternoon (figure 1.2, b), with this dissipating into the early hours of the next morning (figure 1.2, c), when this idealised cycle of convection begins again. In general, the life cycle of deep convection shows a longer dissipation period than development period, with a maximum in cloud cover typically found 9 hours after the growth stage, and the minimum in cloud cover found 15 hours after maximum cloud cover over both Africa (Duvel, 1989) and the Pacific (Udelhofen and Hartmann, 1995). Over tropical Africa, Schröder *et al.,* (2009) find a distinct mean temporal evolution over a clouds lifecycle. Using the Spinning Enhanced Visible and Infrared Imager (SEVIRI; Schmetz *et al.*, 2002) onboard Meteosat 8 Schröder *et al.,* (2009) compared deep convective events in June and December 2006. They found strong vertical growth in the early formative stages of the clouds lifecycle, with the intensity of convection continuous as the cloud enters the mature stage of its lifecycle at around 1530 Local Sidereal Time (LST). The maximum in cold cloud cover fraction was found at around 1730 LST, defined as the end of the mature stage. The following stage - the dissipating stage - is defined by Schröder *et al.,* (2009) as that with the greatest number of split clouds (those that have broken off the main cloud system) and is found to be at 1930 LST, continuing for several hours after. This diurnal cycle in the clouds life is found to be two hours earlier than the corresponding stage during December. A distinct diurnal cycle in cloud cover is also found, which complements the lifecycle stage found over tropical Africa. When compared to the southern hemisphere, Kumar *et al.,* (2014) find the tropical regions of Australia to have a peak in the frequency convection that is earlier than that found in Africa, with a peak found at 1500 LST. This difference may be an artifact of the detection method used, with Kumar *et al.,* (2014) detecting convection using radar reflectivity to detect cloud tops, whilst Yang and Slingo (2001), Laing *et al.*, (2008) and Schröder *et al.,* (2009) use brightness temperature thresholds. The

use of temperature thresholds is suggested to be more arbitrary, whilst the radar reflectivity used by Kumar *et al.,* (2014) was validated with CloudSat cloud classification data.

When comparing land based and oceanic deep convection, a difference in the life cycle and diurnal cycle is found (Futyan and Del Genio, 2007). Diurnal radiative heating over land allows for the development of deep convection during the late afternoon to evening. The development of cloud is suppressed in the early hours due to longwave cooling at night, whereas oceanic convection shows a very weak maximum around the early hours of the morning (Duvel, 1989; Hall and Vonder Haar, 1999; Gettelmann *et al.*, 2002; Futyan and Del Genio, 2007; Laing *et al.,* 2008; Laing *et al.*, 2011). Convective systems over land are found to peak earlier in their life cycle when compared to oceanic systems. Land based systems show a stronger diurnal cycle than over ocean, with the oceanic cloud diurnal cycle showing more noise and a smaller amplitude, relating to the difference between radiative heating of the land and ocean surfaces and lower troposphere, the higher heat capacity of water and the constant warm boundary layer over oceans providing suitable conditions for convective growth (Duvel, 1989; Futyan and Del Genio, 2006). Continental convective systems are also found to provide greater numbers of cloud condensation nuclei to the upper troposphere than maritime convection (Wright *et al.,* 2009). This creates longer lasting clouds due to the smaller cloud particles being less likely to precipitate out.

The main cloud types associated with the three life cycle stages of deep convective complexes over tropical Africa are cumulus, deep cumulonimbus and anvil clouds (figure 1.2, a to c respectively), which will possess different properties (Inoue *et al.,* 2009). The cloud type is also affected by the three modes of convection found in the tropics - shallow convection in the inversion layer with cloud top heights of 1-2 km, cumulus congestus that reaches the zero degree isotherm at ~500 hPa (~6 km), and deep convection (Bechtold, 2009; Kumar *et al.,* 2014). These three cloud types have different impacts on the water and energy budgets of the tropical troposphere. Though this study focuses on deep convection, it has been found that cumulus congetsus with cloud top heights of 3-7 km may precondition the atmosphere for the development of deep convection through moistening (Kumar *et al.,* 2014). If sufficient moistening occurs, cumulus congestus are more likely to develop into deep convection. This moistening is largely a response to the large scale processes that are key to convective initiation, including high levels of moisture convergence (Holloway and Neelin, 2009).

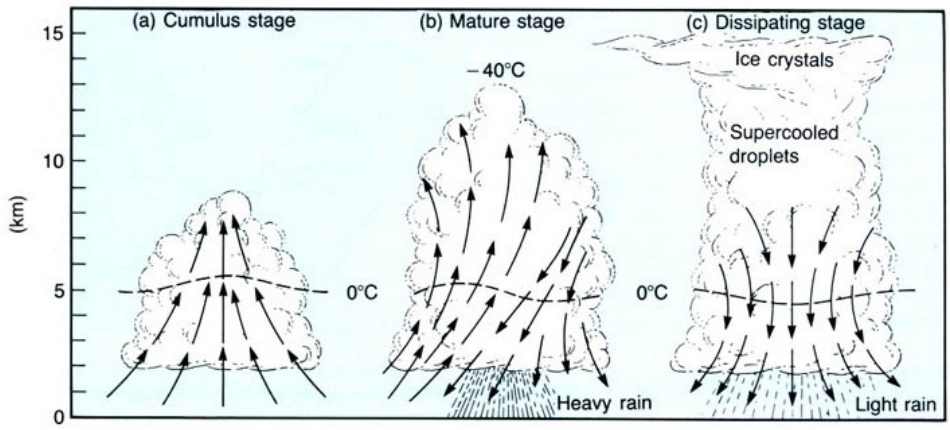

Figure 1.2: Life cycle stages of a single deep convective cloud system. The cloud experiences three stages in its life cycle (a to c) - the growth, mature and dissipating stages. From: University of Rochester (2007).

1.3 Deep Convection and UTH

Although the theoretical understanding of convection, the life cycle stages and diurnal cycles of deep convective cloud are well documented, our understanding of the spatial distribution of UTH in response to deep convection, and its variation over time, remains uncertain. This is an important issue due to the control of UTH on radiative heating, with the net radiation budget being highly sensitive to any changes in upper tropospheric moisture (Sun and Lindzen, 1993; Udelhofen and Hartmann, 1995; Chung *et al.*, 2007; Savtchenko, 2009). UTH can be defined as the vertically averaged relative humidity between 200 and 550 hPa (Soden and Bretherton, 1993). Water vapour is the most important greenhouse gas due to its strong absorption and re-emission of longwave radiation over a large range of the infrared (IR) spectrum, from vibration and rotational bands around 6-8 µm to pure rotational bands in the far infrared ($>$ 15 µm) (Ludlam, 1980; Soden *et al.*, 2005; Andrews, 2010). Understanding the distribution of UTH and magnitude of moistening by deep convection is key to understanding the effect of UTH on infrared absorption and the sensitivity of climate (Soden and Fu, 1995; Wright *et al.*, 2009).

Generally, it is agreed that overall deep convection increases UTH. Using rawinsonde data and observations from the International Satellite Cloud Climatology Project (ISCCP), Wang and Curry (1998) find all deep convective events act to increase UTH, with the magnitude of the moistening being dependent on cloud fraction (the amount of deep convective cloud covering the study region). Similar findings were reported by several studies, including Zelinka and Hartmann (2009) who, using the Atmospheric Infrared Sounder (AIRS), the Tropical Rainfall Measuring Mission satellite (TRMM) and the Aqua satellite, find deep convective events over the maritime region of the Pacific warm pool create a UTH of around 60% in the upper troposphere, with anomalies reaching +10% at the point of peak UTH, from an ambient Relative Humidity (RH) of 50%.

Although there is general agreement that the overall mean UTH is increased by deep convection, and the availability of satellite observations to further quantify this response has grown, the precise response of UTH in relation to convection in the spatial and temporal domains is not well understood and disagreement and uncertainty still exists. The current understandings regarding the UTH response are given in relation to the

spatial and temporal domains and the disagreements surrounding these are discussed in this section.

1.3.1 UTH spatial response to deep convection

The spatial response of UTH to deep convection is an area of uncertainty, with both large and small scale responses seen. Convection is found to be the main source of UTH in the upper troposphere due to the vertical mixing of moisture from the boundary layer to the troposphere, with an almost linear relationship between cold cloud fraction and UTH, but a dehydrating effect is also found due to large scale advection away from the convective core (Soden and Fu 1995; Sassi *et al.,* 2001). Roca *et al.,* (2002) find the relationship between upper level cloud cover and UTH to also possess a strong linear relationship, suggesting there to be a moistening of the upper troposphere by deep convection over the large scale domain.

Although deep convective cloud is believed to moisten the atmosphere in the region surrounding it, a large scale view of the domain in which convection occurs will include areas of precipitation, subsidence and drying (Sherwood *et al.*, 2010). On the scale of zonal mean circulation in the tropics, deep convection acts as a source of water vapour in uprising air, and creates a deficit in moisture in subsiding air. Dehydration of the air begins with the outflow and detrainment of the cloud, giving us the atmospheric motions known as the Hadley cell (meridional) and Walker circulation (zonal) (Sherwood, 1996), discussed further in chapter 3. This suggests a local moistening effect in the upper troposphere around the convective system, with subsidence on the mean circulation scale creating a drying effect (Sun and Lindzen, 1993; Soden and Fu, 1995; Udelhofen and Hartmann, 1995; Gettelmann *et al.,* 2002; Dessler and Minschwaner, 2007).

When considering the large scale spatial response of UTH to deep convection, one has to consider the large scale influences such as the Intertropical Convergence Zone (ITCZ) and the Hadley cell. The position of the ITCZ - the area constituting the ascending branch of the Hadley cell (see chapter 3) (Waliser and Gautier, 1993) - will change depending on season, with the areas of high convective activity following the ITCZ. This is generally located just below the equator in January and near 15°N in July (Riehl, 1979). The long term annual mean of UTH shows maxima in the tropics in the areas associated with the ascending branches of the Hadley cell over tropical Africa and minima in the subtropics associated with the descending regions (Bates and Jackson, 2001). Soden and Fu (1995) also find these areas of frequent deep convection to have a mean UTH of 60% compared to that of 30% in regions of infrequent deep convection, with this not found to be dependent on the spatial scale of the analysis domain. Similarly, Rind *et al.,* (1991) used Stratospheric Aerosol and Gas Experiment (SAGE) II measurements to analyse the moisture transport by deep convection in the Hadley-Walker circulation, finding an increase in upper tropospheric moisture in the ascending regions compared to descending regions of the Hadley cell. This was further confirmed by Chung *et al.,* (2004) and Sohn and Schmetz (2004) who find a negative, albeit weak, correlation between convective cloud fraction and the UTH in dry regions such as the subtropics, suggesting a stronger drying effect from downdrafts when cloud fraction in areas of uplift is greater. Chung *et al.,* (2004) find a negative correlation of -0.16, whilst Sohn and Schmetz (2004) find a negative correlation of -0.33 suggesting this relationship is not strong.

Furthermore, Udelhofen and Hartmann (1995) found a similar spatial response of UTH to deep convection using geostationary satellite observations, and also found that subsidence acts to dry the upper troposphere with increasing distance from the cloud. This study of the water vapour radiances measured by the Geostationary Operational Environmental Satellite (GOES-7) quantified the UTH response, finding UTH to

decrease to 11-15% at a distance of 500 km away the cloud edge, from 44-74% near the cloud edge. Similarly, Wright *et al.,* (2009) found moistening to occur up to 300 km from the deep convective source, with a decrease in UTH found beyond this point. These studies compared the ascending and descending regions of the Hadley cell and confirmed the relationship between areas of ascent and moistening by deep convection, but failed to explicitly address and examine the relationship between the vertical ascent and upper tropospheric moistening. Therefore, there is general agreement that in the large scale, deep convection acts to increase the UTH.

Deep convection also acts on localised, small scales (Betts, 1990; Soden and Fu, 1995; Soden, 2000; Chung *et al.*, 2004). Near the tropopause the horizontal distribution of UTH is found to be largely a response to the distribution of cloud cover over its life cycle (Sassi *et al.*, 2001). For example, the extent of the moistening may be controlled by convective anvil extent, due to the amount of ice increasing with an increase in anvil size (Soden, 2004). Sherwood (1999) found that the magnitude of moistening by deep convection and associated cirrus clouds to be greater than that expected from evaporating hydrometeors alone - evaporation of ice particles as a moistening mechanism is likely constrained by the ambient RH, with ice only moistening the upper troposphere when RH is below saturation point (Wright *et al.,* 2009).

Drying by downdrafts around the deep convective cloud was found by Sun and Lindzen (1993) in the dissipating stage of the cloud life cycle, suggesting a life cycle dependence on the spatial response of moistening. When the air surrounding the cloud is supersaturated the deep convection will act to dry the upper troposphere due to the descending air parcels outside of the convective core, but conversely, low RH in the ambient air will lead to a moistening effect by deep convection (Sassi *et al.*, 2001; Wright *et al.*, 2009). This suggests the effect of convection on UTH can be to both moisten and dry the upper troposphere, depending on the point within the clouds lifecycle and the ambient atmospheric conditions (Lindzen, 1990; Sherwood *et al.*, 2010). It is therefore evident that the disagreements in the spatial response of UTH to deep convection largely come from the small, localised scales closer to the cloud edge, rather than the larger scale responses with regards to the ITCZ and other large scale influences.

1.3.2 UTH temporal response to deep convection

Although there is some disagreement in the spatial response of UTH to deep convection, the greatest area of disagreement is with regards to the temporal response. Although it is generally agreed that there is a point of maximum moistening after a convective event, there is still some disagreement on when this is seen. Some confusion surrounding the temporal response is due to the definition of the point of maximum or most intense convection, this being the point from which most studies base the temporal analysis on. For example, Zelinka and Hartmann (2009) analyse the response of UTH, OLR and a number of other atmospheric variables in relation to their definition of peak convection - this being the point of maximum precipitation intensity - compared to Wright *et al.*, (2009), who define the temporal response as that from when the convective cloud begins to dissipate. These points - the maximum intensity in precipitation and the point at which dissipation occurs - occur at different stages in the cloud lifecycle (the mature stage and dissipating stage respectively). Furthermore, Soden (2004) defined the response in relation to peak convective cloud fraction and used a Lagrangian analysis on GOES-7 observations, finding a 12 hour lag in peak clear sky UTH, this peak UTH appearing in the dissipating stage.

As well as there being disagreement in the definition of peak convection, it is also evident that observation

based studies are divided on when the peak in UTH occurs. It is agreed that a pattern is found in the diurnal cycle of cloud of deep convection and the corresponding UTH response. It is also generally agreed that there is a lag in the response of UTH following that of cloud cover, but it is the length of this lag and when this occurs that is somewhat uncertain. The timescales associated with the UTH response vary from the peak UTH being found to coincide with peak precipitation (when deep convection is at its most intense) to a response still being seen 36 to 48 hours after the main event.

The shortest temporal scales with regards to the UTH response were found by Soden (2000) who shows a peak in UTH two hours after peak cloud cover, but appearing roughly in phase with deep convection over land. Comer *et al.*, (2006) show a similar pattern to Soden (2000) using the same method of cloud masking with the water vapour band brightness temperatures. Though Comer *et al.,* (2006) show an agreement with Soden (2000), this is only seen when the UTH response is averaged over the large scale domain. On a pixel by pixel basis the UTH response and the cloud cover are found to be in phase, which is expected due to the convection transporting water vapour from the lower to upper troposphere as described above. Interestingly, Comer *et al.*, (2006) also find a maximum in UTH preceding the peak convection by 2 hours if the convection is orographically forced, due to the effect of the land surface forcing uplift in water vapour.

A longer lag time is found by Udelhofen and Hartmann (1995). Using the GOES-7 6.7 µm channel dataset, they show an 8 hour lag between deep convection and peak UTH. This peak in UTH is also characterised as being 4 hours before the minimum in cloud cover is seen. Conversely, a minimum in UTH is also found where deep convective cloud cover is at its peak. This suggests there may be a relationship between deep convective cloud cover fraction and the UTH, similar to the linear relationship found by Sassi *et al.,* (2001). Therefore, a different response is seen depending on the definition of peak convection.

Similarly, studies have indicated that peak moistening of the upper troposphere by deep convection occurs within 6 to 9 hours of the convective event, with the enhancement of UTH being a continuous process during the lifetime of the cloud, noticeable up to 12 hours after the peak convection. For example, Johnston *et al.*, (2014) find the greatest enhancement of UTH to occur at 6 hours after peak convection for both land and oceanic convection, whilst Zelinka and Hartmann (2009) find peak UTH over the Pacific warm pool region to occur within the first 9 hours of peak convection, within the dissipating stage of the lifetime of the cloud. Interestingly, Zelinka and Hartmann (2009) found maximum water vapour concentrations at the point of peak precipitation, 9 hours before peak UTH. This pattern can be seen in figure 1.3, whereby the spatio-temporal water vapour and UTH response is shown with corresponding anomalies. It can be seen that a maximum UTH perturbation of 9% (when the corresponding UTH is ~61%) is seen at 9 hours. This variation of UTH was greatest meriodionally rather than zonally around cloud tops and was found to spread from the cloud top for up to 15 hours, continuing after dissipation of the anvil outflow. They also found a pattern between the diurnal cycles of UTH and that of cloud cover, with a lag in the diurnal cycle of UTH following that of deep convective cloud cover. This agrees with the lifetimes of detrained cirrus in the tropics found by Wright *et al.,* (2009).

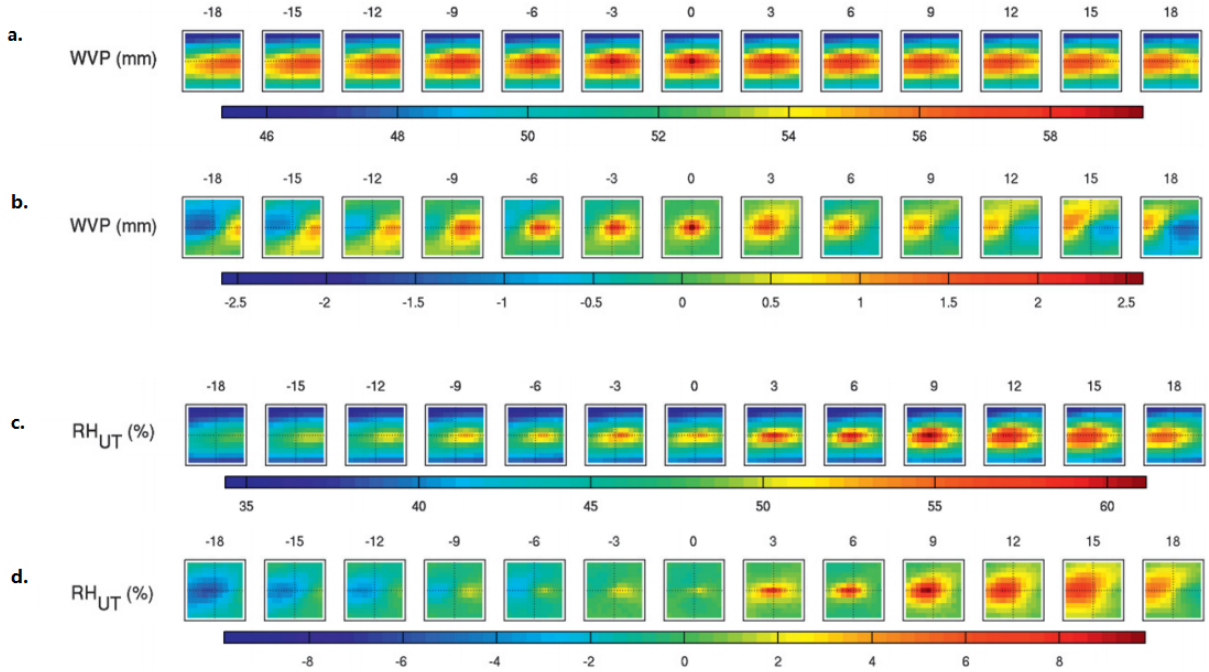

Figure 1.3: The spatio-temporal response of composited mean water vapour (mm) (**a**) and upper tropospheric relative humidity (%) (**c**) over the pacific warm pool. The variables are shown in a plan view, with each box being 11°x11°. The deep convective cloud is at the centre of each box, with the point of detection being time 0, shown 18 hours before and after the cloud is detected. The anomalies for each composited mean variable are also shown, where **b** and **d** are the anomalies of water vapour and UTH respectively. From Zelinka and Hartmann (2009).©American Meteorological Society. Used with permission.

The longest lag in the response of UTH to deep convection was found by Wright *et al.*, (2009). With regards to the temporal response of UTH to deep convection, they find the maximum convective moistening to have occurred within 12 hours of the detrainment of cirrus, whilst still being seen 36 – 48 hours after detrainment when using Tropical Rainfall Measuring Mission precipitation radar data.

It is therefore clear that considerable disagreement in the temporal response of UTH to deep convection exists. It is also found that further disagreement occurs with regards to the cause of the lag. Evidence of a lag in the UTH response is in agreement with the explanation given by Soden (2000), Comer *et al.,* (2006) and Wright *et al.,* (2009), who suggest their findings to agree with the lifetimes of detrained cirrus in the tropics, which may have a moistening effect through evaporation of ice. However, Udelhofen and Hartmann (1995) suggest a simple relationship between evaporation of cloud and ice particles does not completely explain this observed lag in the increase in UTH. They suggest the lag in UTH response is a response to subsidence around the cloud edge in the growth stage of convection, whereby the strong updrafts are compensated for by subsiding air around the cloud edge. This was found to reduce the humidity around the cloud edge in the mature stages of the cloud's lifecycle, making the anomalous perturbation seem greater. It is therefore evident that not only is there disagreement in the temporal response, but also the cause of this response. Interestingly, after a peak in UTH in the dissipating stage of cloud life cycle, Sun and Lindzen (1993) found drying by downdrafts, suggesting a life cycle dependence on the amplitude of moistening, as the convective

towers in dissipating stages of the cloud life cycles consist mainly of downdrafts.

This lifecycle dependence can also be seen in relation to the effect of the clouds lifecycle on the UTH response. The strong vertical growth of deep convective cloud found in the early mature stage induces a strong compensating atmospheric subsidence in the region surrounding the cloud, having a strong effect on decreasing the UTH around the cloud edge. As a cloud grows vertically and reaches the mature stage of the cloud life cycle, maximum column-integrated water vapour concentrations are found (Zelinka and Hartmann, 2009).

As the deep convective cloud ages and reaches the dissipating stage of its life cycle, the cloud top begins to form a detrained anvil (figure 1.4). This detraining deep convection is the main source of high level cirrus cloud and cumuliform precipitation in the tropics, with roughly 50% of cirrus in the tropics related to a deep convective event. The evaporation of cloud hydrometeors from convective cloud top detrainment is found to be the main source of water vapour in the tropical upper troposphere (Fu *et al.*, 1990; Chou and Neelin, 1999; Futyan and Del Genio, 2006; Zelinka and Hartmann, 2009; Johnston *et al.*, 2013). The detrained cirrus clouds associated with deep convection are generally found above an altitude of 6 km and cover between 21-33% of the Earth (Wylie *et al.*, 2005; Wallace and Hobbs, 2006; Krebs *et al.*, 2007; Chae *et al.*, 2011). As mentioned previously, it is also thought that the extent of the moistening is controlled by convective anvil extent and the stage of the life cycle of the cloud, due to the amount of ice increasing with an increase in anvil size (Soden, 2004). The physical mechanisms responsible for anvil and detrained cirrus cloud development in the dissipating stage of the cloud's life cycle and the evaporation of detrained cirrus hydrometeors are given as an explanation for the UTH response when a peak in clear sky UTH is preceded by a peak in detrained cirrus cloud (Sherwood, 1999; Chung *et al.*, 2004; Soden, 2004; Tian *et al.*, 2004). Radiative heating from evaporating anvils causes a moistening of the upper troposphere through diabatic ascent, as well as the moistening from the deep convection itself (Sherwood, 1999; Zelinka and Hartmann, 2009). This results from the radiative effect of the cloud - cirrus clouds may have an overall positive cloud radiative forcing (Sherwood, 1999; Corti and Peter, 2009) - which causes a 'pumping' effect, whereby water vapour is pumped from the surrounding ambient environment into the cloudy profile (Sherwood, 1999).

Overall, it is clear that there is considerable disagreement with regards to the temporal response of UTH to deep convection, with some suggestions of a 2 hour lag, and further suggestions of a 12 hour lag in UTH. There is also some debate as to whether a moistening is always seen, with some studies suggesting a drying in the later stages of the cloud lifecycle (e.g Sun and Lindzen, 1993; Udelhofen and Hartmann, 1995). Further disagreement is also seen in the cause of this moistening, with some suggestions that evaporation of cirrus ice particles enhance humidity, with others suggesting that this alone is not the cause.

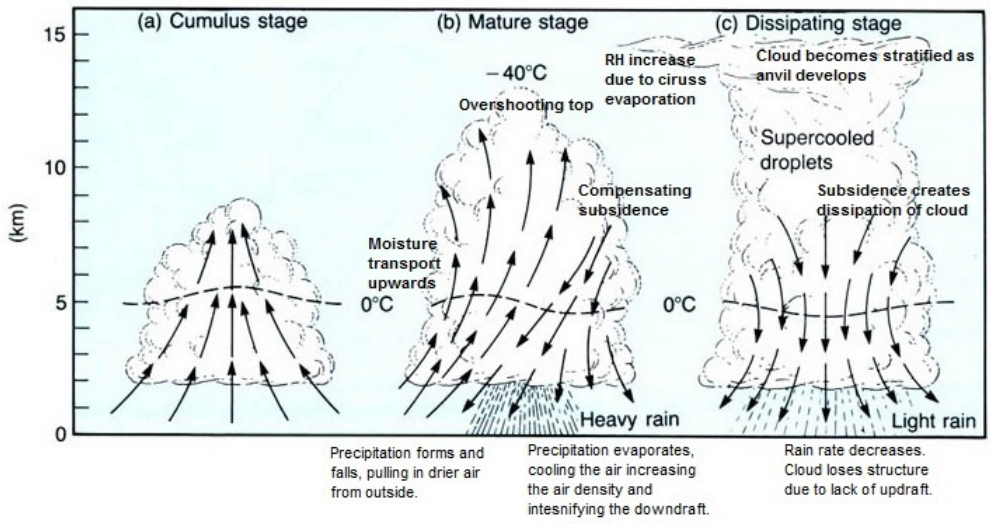

Figure 1.4: UTH in response to the life cycle stages of a single deep convective cloud system, with different UTH responses at each life cycle stage (a to c). Adapted from: University of Rochester (2007).

1.3.3 Ambient Atmospheric Conditions and Preconditioning

The influence of deep convection on the spatial response of UTH is largely a factor of the ambient atmospheric conditions, which controls the evaporation of detrained cirrus particles - viewed as the primary source of UTH - and the propagation of this enhanced UTH downstream of the convective cloud (Soden and Fu, 1995; Tian *et al.*, 2004). This traditional view of the spatial response of UTH enhancement in response to detraining anvils and ambient atmospheric conditions is supported by several studies. Wright *et al.*, (2009) showed that the control of relative humidity with respect to ice on cirrus evaporation depends on the atmospheric conditions around the convective core and up to several thousand kilometers away, and the magnitude of an increase in UTH having the greatest effect on regions with a low ambient RH

The control of atmospheric conditions on the magnitude of moistening can be seen from the temperature of the atmosphere around the detrained cloud top height, with high water vapour concentrations found in western tropical Africa due to higher upper tropospheric temperatures (Wright *et al.*, 2009; Russo *et al.*, 2011). Wright *et al.,* (2009) find that moistening occurs in regions where the ambient UTH is below saturation, with drying occurring in regions where the ambient UTH is above saturation.

Satellite observations show this enhanced UTH to follow patterns of anvil cloud formation, relating to the temporal lag in UTH enhancement. Larger anomalies in UTH are seen in regions of lower rainfall rate and less deep convection, due to the lower ambient RH in such regions compared to the higher RH found in regions of high rainfall. This enhanced UTH also occurs lower in the troposphere due to the reduced intensity of the convection in these regions (Wright *et al.,* 2009; Zelinka and Hartmann, 2009).

The response of UTH to convection is also largely controlled by preconditioning of the atmosphere before the deep convection is initiated. In areas of less convection, for example, the winter hemisphere, it is expected that a single convective event will have a greater perturbation on the ambient UTH than adding a single

event to an area where convection is regular and UTH is already quite high. Udelhofen and Hartmann (1995) find a 0.75% increase in UTH with a 1% increase in cloud cover using a least-squares fit analysis, with the magnitude of an increase in cloud cover having the greatest effect on regions with a low ambient RH.

1.4 Deep Convection and the Radiation Budget

Clear sky OLR is highly sensitive to the perturbations in UTH caused by deep convection. The absorptivity of water vapour is proportional to the logarithm of its concentration (Soden *et al.*, 2005). Water vapour absorption in the infrared comprises the bulk of the Earth's greenhouse effect, whilst OLR emitted by water vapour acts as a fundamental cooling mechanism (Allan *et al.*, 1999). Absorption over a large region of the longwave spectrum and the concentration of water vapour in the atmosphere lead to this being a potent greenhouse gas. Therefore understanding the UTH spatial and temporal response to deep convection is critical to determining the OLR response.

Over the longwave spectrum (>4 μm), water vapour influences the widest range of wavelengths. Some studies have attempted to analyse the water vapour effect and its contributions to absorption over different parts of the spectrum. Positive perturbations of UTH at various altitudes have been found to profoundly reduce OLR when UTH is increased, with these perturbations prescribed to specific spectral regions (Chahine, 1992; Clough *et al.*, 1992; Sinha and Allan, 1994). The response of spectral OLR to a change in the amount of water vapour in the atmosphere is largely dependent on the height in the upper troposphere at which the UTH perturbation occurs (e.g. Shine and Sinha, 1991; Brindley and Harries, 1998). The greatest response to a change in water vapour amounts is in the water vapour vibration-rotation (6-8 μm) and pure rotational (>12 μm) bands (Soden and Bretherton, 1993; Brindley and Harries, 1998).

There is a non-linear relationship between UTH and clear sky OLR as demonstrated by Soden and Bretherton (1993). The non-linear response of OLR to UTH exhibits an exponential relationship, with a higher sensitivity of OLR seen at lower UTH values. This results from an increase in humidity causing a saturation of water vapour absorption bands, lowering the sensitivity as bands become more saturated (Allan *et al.*, 1999). This relationship shows clear-sky OLR is most sensitive to changes in UTH at around 250 hPa, with a slight increase or decrease in UTH having a large impact on the total OLR (Udelhofen and Hartmann, 1995; Sinha and Harries, 1997; Allan *et al.*, 1999; Russo *et al.*, 2011).

A common method of quantifying the clear sky OLR response to deep convection is through the use of the clear sky greenhouse parameter (*G,* defined as the difference between surface emission and OLR) developed by Raval and Ramanathan (1989). This was employed by Soden and Fu (1995) in order to determine the response of OLR to deep convection by analysing the departure from the linear relationship between humidity and temperature expected from thermodynamic processes alone (the Clausius-Clapeyron relationship). They found an enhanced greenhouse trapping (less OLR emitted) with an increase in UTH, with areas of subsidence and drier air showing higher OLR emission. Soden and Fu (1995) find UTH explains greater than 80% of the regional variability in greenhouse trapping of OLR. An increase in UTH of 10% in ITCZ regions creates a simultaneous decrease in OLR of -3.3 W m^{-2}, compared to -5.4 W m^{-2} in a region of subsidence. This represents a relatively large decrease in OLR when compared to a longwave radiative forcing of ~4 W m^{-2} for a doubling of global CO_2 (Houghton, 2002).

Areas of vertical descent in the tropics are characterised by UTH of around 30% and ascending regions are characterised with UTH above 60% over central Africa, with the tropics showing strong negative correlations

between UTH and OLR (Allan *et al.*, 1999). In relation to the point of peak convection, Zelinka and Hartmann (2009) find minimum clear sky OLR to precede the UTH by 6 hours, occurring when anvil thickness is at its greatest, and at altitudes where the highest levels of moistening are found. Their study analysed atmospheric conditions in response to deep convection in comparison to an established and constant background state of RH, which will not be constant in reality, so the OLR seen may not be entirely realistic. The point of maximum convection is also taken as the point of maximum rainfall rate, rather than the spatial centre of the convective system, which may give a distorted spatial response of UTH and OLR to deep convection. They also ignored the potential of cross contamination of time bins - they took each maximum point of rainfall rate as a new system, even if it was still the same system (Zelinka, 2013, personal communication) - which may unintentionally smooth the results.

Johnston *et al.*, (2013) used an improved version of the method used by Zelinka and Hartmann (2009) to analyse spatial and temporal distributions in UTH and OLR, and found OLR to be greatly perturbed for longer than 30 hours after the peak convective event. Modelling studies by Johnston *et al.*, (2013) show UTH in the local scale is elevated by 45% from a background state of 40%, peaking for up to 6 hours after the event. OLR shows a similar pattern, with lowest values following the pattern of maximum UTH with a negative correlation between the two (Johnston *et al.*, 2013). Using the Advanced Microwave Sounding Unit - B (AMSU-B) and Microwave Humidity Sounder (MHS) onboard NOAA-16 and 17, Johnston *et al.*, (2013) find observations show a OLR minimum at 18 hours after convection, which is earlier than peak UTH, and OLR tends back towards its relaxed state after about 48 hours.

Although uncertainty exists in the understanding of the UTH spatio-temporal distribution, overall the mean response to deep convection is an increase in water vapour in the upper troposphere. When considering the spatial pattern of UTH and the corresponding OLR, clouds should increase moisture in the region surrounding the cloud which would have a significant effect on the radiative balance (Sherwood, 1999). It follows that the spatial pattern of OLR therefore also follows a similar temporal pattern to UTH. Similarly to the seasonal pattern in UTH and deep convective frequency found by Soden and Fu (1995), a corresponding pattern in OLR was found following the ITCZ shift, further confirming the spatio-temporal variability in OLR.

1.5 Modelling of UTH and Inherent Limitations

As discussed above, several studies have used models to determine the spatial and temporal response of UTH and OLR to deep convection. Though the development of climate models over time has resulted in more realistic representations of climate phenomena such as deep convection, as can be seen from Johnston *et al.*, (2013), there are still some inherent limitations in the representation of UTH and its response to deep convection. In climate and Earth system models, representation of processes such as deep convection and other clouds remains a challenge (Flato *et al.,* 2013). It is believed with high confidence that the spread in the sensitivity in earth system models largely relates to cloud feedbacks. It was found by Flato *et al.,* (2013) that cloud simulations shows regional biases in the cloud radiative effect of up to several ten of watts per square metre.

Errors in models also come from the parameterisation of phenomena such as deep convection which cannot be represented explicitly in Earth system models. Parameterisation is conducted through the development of conceptual models of the processes of interest in isolation. This uses observations and current understanding

of the processes controlling the phenomenon being modelled. In the case of deep convection, the strongest control is the solar cycle, with the peak in the diurnal cycle occurring around midday. When compared with observational studies of deep convection, its is evident that peaks in the deep convective frequency are found later in the day (Schroder *et al.,* 2013). It was found by Stein *et al.,* (2015) that the parameterisation of deep convection leads to an underestimation of anvil outflow, whilst peaking too far south in the tropics. Day time observations also showed a lack of deep convection in relation to observations.

Such issues with modelling deep convection creates issues in the modelled representation of UTH. To improve the accuracy of humidity simulations, incorporation of observations at a higher temporal and spatial frequency would likely reduce the errors in parameterisations. This is limited by the sparsity of ground based observations, such weather balloons and radiosondes, though satellite observations at a high temporal and spatial resolution are increasing the coverage of observations. Though incorporation of measurements would improve parameterisations, recent findings suggests that the sign of the water vapour feedback differs depending on the type of instrument used to make the measurements. Boehmer (2012) finds that long-term measurements of specific humidity in the upper troposphere show a negative trend when measured by weather balloon, and a positive trend when measured by satellite, though Boehmer (2012) suggests the satellite measurements to be more accurate. Such discrepancies add further uncertainties to the parameterisation of deep convection and the UTH response. Therefore incorporation of satellite measurements would improve the modelling of the UTH response, whilst increasing the understanding and representation at a higher spatial and temporal resolution than weather balloons.

1.6 This Study

Recent advances in satellite capabilities have allowed us to gain an unprecedented insight into the relationship between clouds and their surrounding environment. In order to gain a better understanding of the UTH and OLR response to deep convection over tropical Africa, this study will employ radiance measurements sensitive to water vapour from the Spinning Enhanced Visible and Infra Red Imager (SEVIRI) and OLR measurements from the Geostationary Earth Radiation Budget (GERB) instruments on the Meteosat Second Generation (MSG) satellite (see chapter 2). This study aims to analyse seasonal patterns in the spatial and temporal response of UTH and OLR to deep convection using a compositing method similar to that of Zelinka and Hartmann (2009) and Johnston *et al.,* (2013). This method will employ data collected every 15 minutes with a 3x3 km spatial resolution re-gridded to a 9x9 km resolution, allowing the calculation of robust statistics at a temporal resolution much higher than previous studies. The area of interest, over tropical Africa (0°-15°N, 10°-40° E), will allow for any patterns to emerge within the pronounced diurnal cycle seen over land, and will allow for any spatial patterns over Africa to also be temporally resolved. This region is chosen to answer several key questions relating to the spatial and temporal UTH and OLR response:

1. What are the temporal and spatial scales of the humidity response associated with deep convection in the upper troposphere over Tropical Africa?

2. Is there a clear signature of moisture propagation in the horizontal around the cloud, given the atmospheric dynamics discussed above?

3. What are the associated impacts on OLR and the implications for the net outgoing radiative energy balance?

As discussed above, many studies have been conducted to quantify the global response of UTH and OLR to deep convection over Africa and also the Pacific warm pool – an area of anomalously high convective events and low OLR. This study will allow for a comparison between regions, for example, with that of Zelinka and Hartmann (2009) and provide an understanding as to whether similar mechanisms hold true over tropical Africa. Seasonal differences between a wet and dry season are expected to show differences in the frequency and intensity of convection when the ITCZ passes over the region of interest, similar to that of Soden and Fu (1995). In order to analyse responses of clear sky UTH and OLR to deep convection, cloud detection thresholds and masking techniques need to be developed. The datasets and instrumentation used in the development of these thresholds and the limitations of these are discussed in chapter 2. A discussion on the climate and cloud climatology of this region is given in chapter 3. In order to determine the UTH and OLR response to deep convection a cloud detection proxy and masking method is developed using the SEVIRI water vapour band and window band radiances similar to methods used by Lensky and Rosenfeld (2008). The radiative transfer modeling and the sensitivity tests involved are discussed in chapter 4. Once clouds have been detected, in order to analyse the response over the clouds life cycle, they need to be tracked. A cloud tracking algorithm based on Machado *et al.*, (1998) and Ashpole and Washington (2013) is developed and discussed in chapter 5. The relationship between UTH and water vapour band radiances developed by Soden and Bretherton (1993) and its application to SEVIRI brightness temperatures is shown in chapter 6. This is then applied to water vapour band radiances, alongside the application of the detection and tracking methods, to determine the spatial and temporal response of UTH and OLR to deep convection. An analysis and discussion on the results will also be given in chapter 6, with a concluding summary given in chapter 7.

Chapter II

Radiative Transfer Theory, Instrumentation, Datasets and Modelling Tools

In this chapter, a discussion on the basic radiative transfer theory is given in section 2, including an explanation of weighting functions and their relevance to atmospheric sounding. The discussion is focused on the longwave region of the electromagnetic spectrum, defined as being between 4 µm and 100 µm (Petty, 2006). The instrumentation used throughout the remainder of the thesis is then introduced in section 2.2, followed by a description of the datasets and modelling tools used in this study.

2 Overview

Maintaining radiative equilibrium of the Earth at the top of the atmosphere (TOA) requires the components of the Earth's radiation budget to be in balance. This radiative balance between the Sun and Earth involves two distinct wavelength bands - shortwave, principally originating from the sun, and longwave, principally originating from the Earth (figure 2.1). Very little overlap is seen between the two blackbody emission curves around 3 µm.

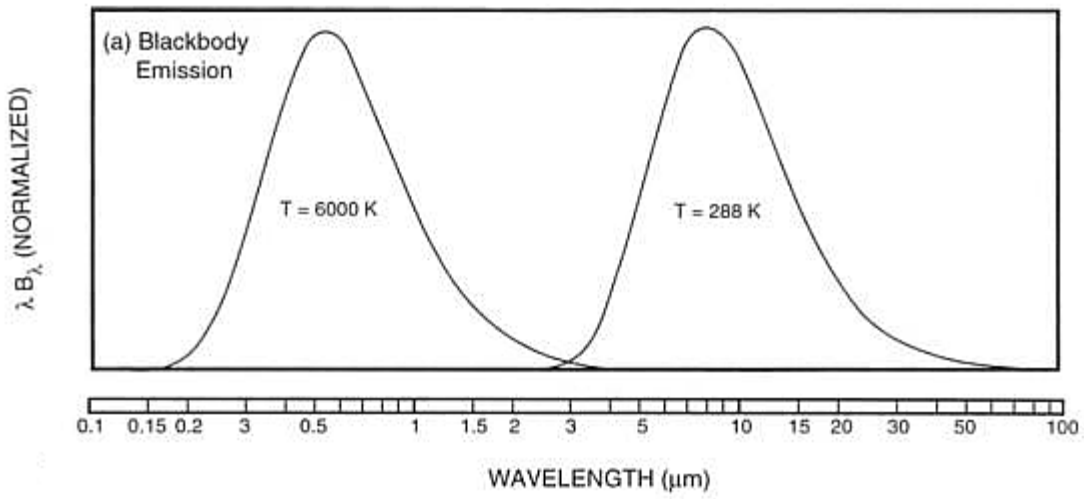

Figure 2.1: Normalised blackbody emission spectra of the Sun (left) and Earth (right) as functions of wavelength (λ) at temperatures corresponding to each emitting body (6000 K and 288 K respectively). From Salby (1996).

The Earth's atmosphere is a strong absorber of longwave radiation. Longwave radiation emitted by the Earth's surface is absorbed and re-emitted as it passes on its journey through the atmosphere to space. These processes of absorption and remission continue until the longwave radiation reaches the TOA, where, apart from in the window regions between 3 µm to 4 µm and 8 µm to 12 µm, it has almost totally been absorbed

by various gases in the troposphere (figure 2.2). Due to the lower troposphere being almost opaque and the upper troposphere being largely transparent to longwave radiation, the upper troposphere and its constituent gases are intrinsically important to the cooling of the Earth to space (Harries *et al.,* 2008).

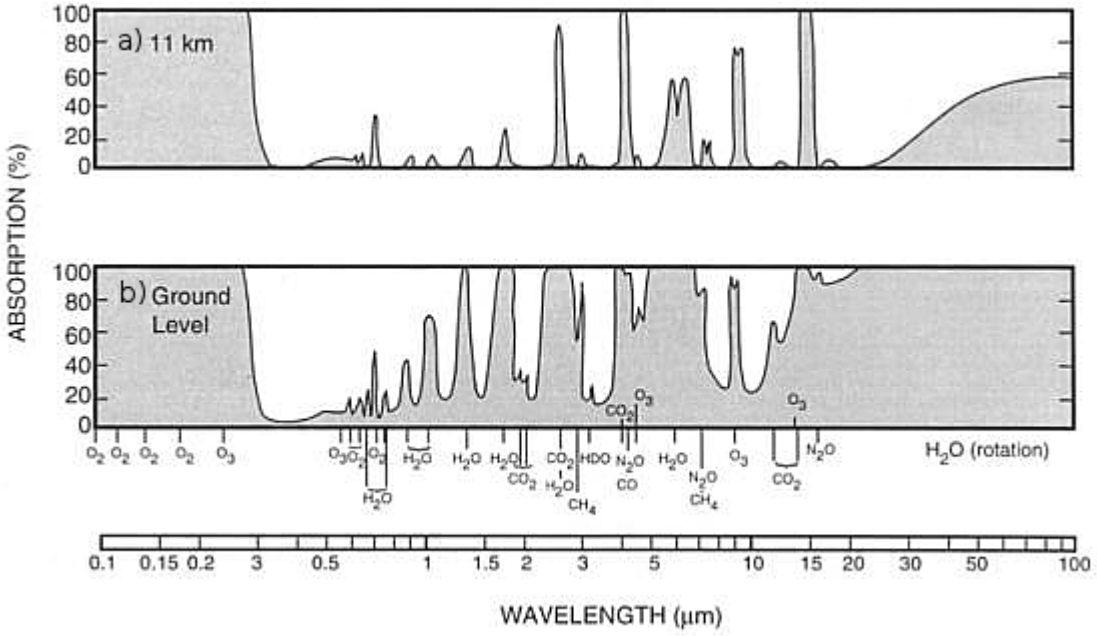

Figure 2.2: **a:** Absorption of radiation as a function of wavelength between the TOA and 11 km, along a vertical path. **b:** Same as in the top image, but from the TOA to the surface. Absorbing constituents are shown at their respective wavelengths. From: Salby (1996)

When a molecule absorbs or emits radiation it may rise to a higher energy level (absorption) or drop to a lower energy level (emission), both processes being associated with discrete changes in the molecular energy levels. The absorption of energy is typically manifested as narrow absorption lines over a line spectrum (Wallace and Hobbs, 2006; Harries *et al.,* 2008). The featureless regions between lines show where the gas is transparent to the particular frequency of radiation. In the infrared, changes in molecular state are associated with vibrational and rotational transitions.

In the atmospheric window region between 8 and 12 μm, in the absence of cloud, the atmosphere is almost transparent to longwave radiation, with most of the longwave emitted by the surface in this region reaching the TOA. From figure 2.2, it is clear that minimal absorption occurs apart from a strong absorption band is present at 9.6 μm, corresponding to absorption by O_3. The little absorption in this region, and the strong absorption over the rest of the spectrum is largely due to water vapour (Houghton, 2002). Water vapour is the most significant overall absorber of longwave radiation, with strong absorption bands centered at around 2.7 μm, 6.3 μm and in the far infrared (figures 2.2 and 2.3). Aside from water vapour, various other gases are strong absorbers in the longwave region, including CO_2 , with bands centered at 4.3 μm and 15 μm, and other gases including CH_4, N_2O and O_3.

Absorption lines experience line broadening, creating characteristic absorption wings. Line broadening occurs due to either natural broadening (relating to Heisenberg's Uncertainty Principle), Doppler broadening

(whereby a line is Doppler shifted due to the motion of a molecule) and pressure or collision broadening (associated with the collisions between molecules) (Petty, 2006). Below 20 km in the atmosphere, pressure broadening is the dominant effect (Wallace and Hobbs, 2006). The broadening of lines can act to close the gaps between closely neighbouring absorption lines, causing the atmosphere to become almost opaque over a continuous range.

Absorption can also occur over a continuum. Unlike line absorption which occurs at discrete wavelengths, continuum absorption occurs over a wider range of wavelengths. Early research noted a discrepancy between the absorption predicted by gaseous line absorption only, and that measured (Roach and Goody, 1958). It has been suggested that there are two possible types of interaction between molecules for the continuum absorption. One suggestion is that due to pressure broadening of the lines, the associated wings of the absorption lines begin to close the transparent gaps between the lines, creating a superposition of the wings of nearby line clusters, effectively creating an absorption continuum (Clough *et al.*, 1989; Wallace and Hobbs, 2006). Taking the H_2O molecule as an example due to it possessing an absorption continuum, a second possible explanation of continuum absorption is the water dimer effect (Scribano and Leforestier, 2007). Due to the attractive force associated with the positive and negative end of molecules of H_2O, a collision between two molecules creates a broadening of absorption line widths through the creation of H_2O clusters (Bignell, 1970). The strength of the continuum increases with wavelength through the far infrared spectrum, but is weaker in the Near-InfraRed (NIR) and IR regions.

2.1 Radiative Transfer

To understand the path taken by a beam of radiation through the atmosphere, an understanding of the basic radiative transfer equations is necessary. The radiative transfer equations given are in the absence of scattering due to the negligible amount of scattering in the longwave in a clear sky.

2.1.1 Emission

To maintain radiative equilibrium the Earth must re-emit longwave radiation at the same rate shortwave radiation is absorbed. For a perfect blackbody emitter this emission can be characterised by the Stefan-Boltzmann law:

$$j^* = \sigma T^4 \tag{2.1}$$

where $j*$ is the isotropic energy flux, or irradiance, emitted by a blackbody at temperature T and where σ is the Stefan-Boltzmann constant. Irradiance is defined as the flux of radiant energy per unit area. The emission of radiation when the emitter is in thermal equilibrium follows Planck's law - the theory of blackbody radiation. Blackbody radiation is an idealisation, whereby the radiation emitted by the emitter in thermal equilibrium is determined by the temperature of the emitter and is the maximum possible at all wavelengths for an object (Petty, 2006). The Planck function, describing the relationship between the spectral radiance, B_λ, emitted and the absolute temperature, T, of the emitter is given as:

$$B_\lambda(T) = \frac{2hc^2}{\lambda^5(e^{\frac{hc}{k_B \lambda T}} - 1)} \tag{2.2}$$

where h is Planck's constant and c is the speed of light and where radiance is defined as the flux of radiation emitted per unit solid angle in a given direction by a unit area. This situation is unlikely to occur in reality due to to most substances not being perfect blackbodies. The emissivity of a substance is defined as the ratio of the irradiance actually emitted to the irradiance emitted by the same substance if it were a blackbody at the same temperature. The longwave radiation emitted by the Earth's surface may be represented as a blackbody curve (shown as dashed lines on figure 2.3 for several temperatures) - the spectral radiance emitted per unit volume and per unit frequency interval against frequency. The solid black line on figure 2.3 represents the spectrally resolved emission spectrum for a clear sky with a surface temperature corresponding to approximately 300 K. At TOA, the longwave emitted in the window region range resembles this blackbody curve with some minimal absorption, whilst all other wavelengths in the longwave region correspond to a colder temperature due to absorption and re-emission by atmospheric gases at a colder temperature (higher in the atmosphere).

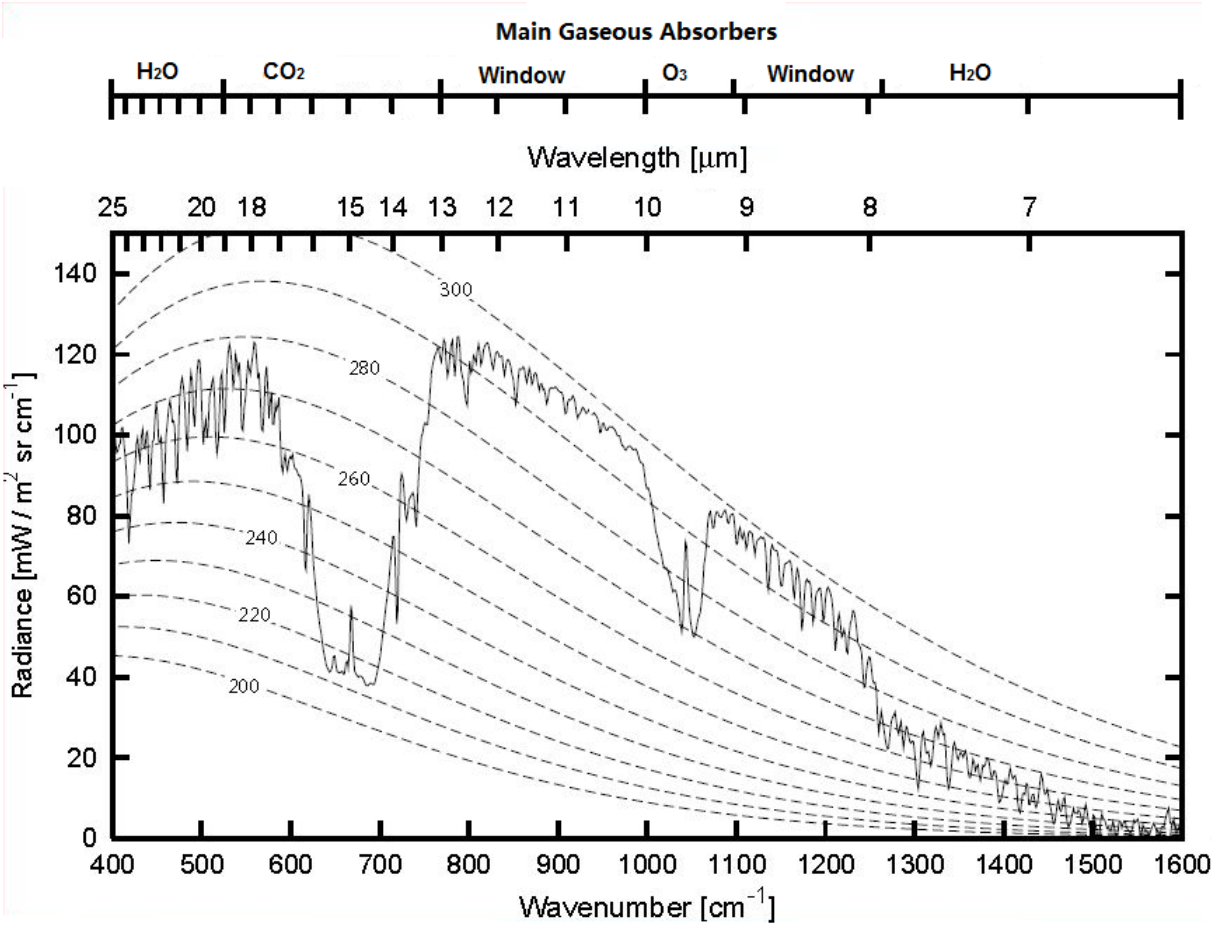

Figure 2.3: The spectrally resolved thermal infrared emission spectrum for a clear sky with a surface temperature corresponding to approximately 300 K. Observed by the Nimbus-4 satellite. Dashed lines are blackbody temperature curves in Kelvin. Main absorbers are shown with respect to their region in the spectrum. Adapted from: Petty (2006)

A slab of atmosphere will emit radiation to maintain thermal equilibrium. In local thermodynamic equilibrium, Kirchoff's law holds when:

$$\varepsilon_\lambda = a_\lambda \tag{2.3}$$

Here ε and a are the emissivity and absorptivity at a given wavelength, λ, respectively. The Earth's atmosphere is in local thermodynamic equilibrium at altitudes below approximately 60 km where the frequency of collisions between molecules is greater than the frequency with which they absorb and emit radiation at a specific wavelength (Wallace and Hobbs, 2006).

2.1.2 Absorption

With regards to absorptivity - defined as the ratio of the irradiance actually absorbed to the irradiance absorbed by the same object if it were a blackbody at the same temperature - radiation traversing the Earth's atmosphere will encounter and be absorbed by radiatively active gases along the path s from the surface to the TOA. The Beer-Lambert law (equation 2.4) states that, with a constant atmospheric state, the absorption that occurs to a beam of radiation of intensity I (units W m^{-2} sr^{-1} per wavelength) when traversing a slab of atmosphere of thickness ds is proportional to the mass of the absorber in the cross sectional unit of atmosphere, where ρ is the density of the absorbing medium (Houghton, 2002; Wallace and Hobbs, 2006):

$$\frac{dI_\lambda}{I_\lambda} = -\rho k_{a\lambda} ds \tag{2.4}$$

here $k_{a\lambda}$ is the mass absorption coefficient, a measure of how strongly a beam of radiation is absorbed at a given wavelength, with units m^2 kg^{-1}. Integrating Equation 2.4 along the path length of the radiation gives:

$$I_\lambda(s) = I_\lambda(0) \exp(-\int_0^s \rho k_{a\lambda} ds') \tag{2.5}$$

where $I_\lambda(s)$ is the amount of radiation originating from (0) that is transmitted over the path s. The intensity of the radiation passing through a medium decreases exponentially with optical path length, τ_λ. This is a measure of optical transparency and is given by:

$$\tau_\lambda(s) = \int_0^s \rho k_{a\lambda} ds' \tag{2.6}$$

The transmissivity, t_λ, is the fraction of incident radiation that remains once a beam has traversed the absorbing medium, and can be expressed as:

$$t_\lambda(z, \mu) = e^{\frac{-\tau_\lambda(z)}{\mu}} \tag{2.7}$$

where z is the layer height and μ is the cosine of the viewing zenith angle (VZA), i.e. $\mu = 1$ for the zenith view, (VZA = 0°), μ = -1 for the nadir view, (VZA = 180°) . Here $\tau_\lambda(z)$ represents the vertical optical path, known as optical depth.

2.1.3 Radiative Transfer Equation

The radiative transfer equation describes the interaction of radiation with the medium through which it passes. Collecting the equations of absorption and emission described above gives the radiative transfer equation in a general form. In the absence of scattering, for a certain wavelength, λ, this is:

$$\frac{dI_\lambda}{\rho k_{a\lambda} ds} = -I_\lambda + B_\lambda(T) \tag{2.8}$$

and is known as the Schwarzchild's equation. The thermal radiation at TOA in the absence of scattering at a certain frequency, I_λ, viewed at a certain zenith angle, consists of a contribution transmitted from the surface and a contribution from the overlying emitting layer and can be expressed as :

$$I_\lambda(\mu) = I_{\lambda,Surf} t(0, \infty; \mu) + \int_0^\infty B_\lambda[T(z)] \{W(z, \mu)\} \, dz \tag{2.9}$$

The intensity of radiation emitted from each atmospheric layer and received at TOA is controlled by the weighting function, W. A weighting function provides information on the regions of the atmosphere which contribute the greatest amount to the measured top of atmosphere radiances at a given wavelength or over a given spectral channel (Tjemkes, 2012). The weighting functions are dependent on the atmospheric state, including the temperature and humidity profile and the gas concentrations within the atmospheric column, being the vertical gradient of transmittance:

$$W(z, \mu) = \frac{\partial t_\lambda(z, \mu)}{\partial z} \tag{2.10}$$

The weighting functions for the SEVIRI instrument used later in this study and described below are shown in figure 2.4.

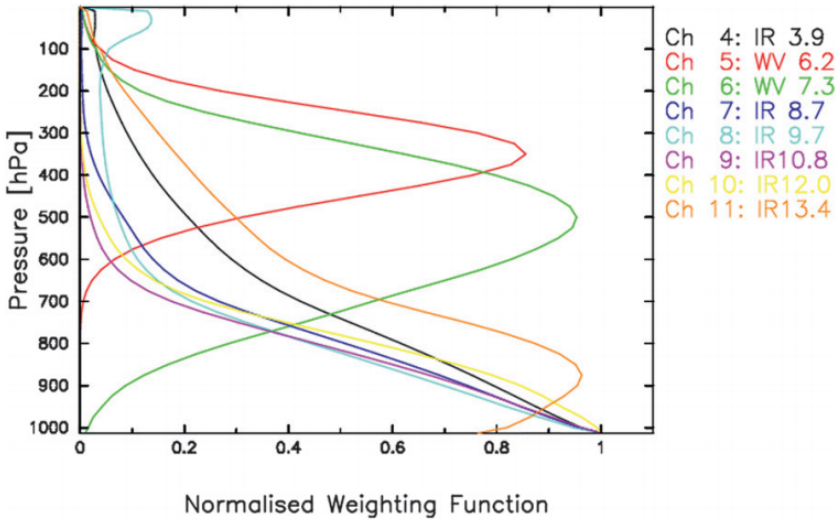

Figure 2.4: Mean weighting functions as a function of pressure for the infrared channels of the Spinning Enhanced Visible and InfraRed Imager (SEVIRI). Taken from Mecikalski *et al.,* (2010)

2.2 Instrumentation

In this section a discussion on the instrumentation used in this study is given.

2.2.1 SEVIRI

Observations of many atmospheric variables including clouds have been made from space using the visible and infrared radiances measured by satellites since the 1960s (Henken *et al.,* 2009). The advances in satellite technology and their capabilities led to the first generation of European meteorological satellites in 1977 with the launch of Meteosat-1. This was followed by 6 more satellites numbered 1-7. Since then, this has been followed by the launch of the second generation of European geostationary meteorological satellites. Launched in 2002 and operational since 2004, the Meteosat Second Generation (MSG) series of satellites were introduced, with these carrying the Spinning Enhanced Visible and Infrared Imager (SEVIRI) as their primary payload. The launch of MSG increased the temporal resolution from 30 minutes with Metoesat-1 to 7, to 15 minutes with MSG, whilst increasing the spatial resolution from 5 to 3 km at the sub satellite point. Meteosat-1 was centered over 0° latitude, 3.5° W longitude (Schmetz *et al.,* 2002), whilst MSG2 is situated at 0°, 0°. Geostationary satellites such as MSG have the same revolution time as the Earth, providing frequent imagery of the same geographical point on Earth. Full disk images up to 80° latitude are taken every 15 minutes by SEVIRI, providing continuous observation of the full Earth disk at a high temporal resolution - useful for tracking atmospheric phenomena such as deep convection. The imaging and spectral properties of SEVIRI are discussed below.

2.2.2 Instrument Properties - Spectral

SEVIRI measures the top of atmosphere radiances in 12 channels, covering the visible wavelengths to the thermal infrared region of the spectrum, between 0.6 µm and 13.4 µm, with one high resolution visible channel (Table 1). SEVIRI has a spatial resolution of 3 km^2 at nadir for the 11 narrow band channels, and 1.67 km^2 for the high resolution visible channel.

Channel	**Spectral region**	**Resolution (km^2)**	**Spectral band (µm)**
High Resolution	Broadband VIS	1.67	0.4-1.1
0.6	VIS	3	0.56-0.71
0.8	VIS	3	0.74-0.88
1.6	NIR	3	1.5-1.78
3.9	IR	3	3.48-4.36
6.2	WV	3	5.35-7.15
7.3	WV	3	6.85-7.85
8.7	TIR	3	8.3-9.1
9.7	O_3	3	9.38-9.94
10.8	TIR	3	9.8-11.8
12.0	TIR	3	11-13
13.4	CO_2	3	12.4-14.4

Table 2.1: Characteristics of the spectral channels of SEVIRI. Source: Schmetz *et al.,* (2002)

Two of the channels (not including the high resolution visible channel) cover the narrow visible part of the spectrum, between 0.56 and 0.88 µm. One channel centered at 1.6 µm covers the near infrared - the area

of the electromagnetic spectrum between the visible and infrared wavelengths. The other 8 wavelength bands are centered in the mid infrared. As apparent from figure 2.3, the infrared channels centered on 3.9, 8.7, 10.8 and 12.0 µm are window channels. Some small effect of the water vapour continuum described previously is seen in the 3.9, 8.7, 10.8 and 12.0 µm channels. The thermal infrared region between 5.35 to 7.85 µm is covered by two wavelength bands known as the water vapour channels. These are centered on 6.2µm and 7.3µm. Within this region there are absorption lines relating to absorbing gases such as N_2O and CH_4 for example, but the dominant absorption lines are related to water vapour (Santurette and Georgiev, 2005).

In order to use SEVIRI data as a method for tracking atmospheric phenomena such as deep convection, observed radiances B_{vc} are converted to brightness temperatures, with the addition of some correction coefficients a and b in equation 2.11:

$$BT = \left(\frac{c_2 v_c}{\ln(1 + c_1 v_c^3 / B_{vc})} - b \right) / a \tag{2.11}$$

where BT is the brightness temperature, B_{vc} is the observed spectral radiances (mW m^{-2} sr^{-1} (cm^{-1} $)^{-1}$), $c1 = 2hc^2$, $c2 = hc/k_B$, and v_c is the central wavenumber of the spectral channel in cm^{-1}. The a and b correction coefficients applied to the Planck function provide an empirical adaption of the Planck function inversion specifically to represent band-integrated values for SEVIRI channels. The a and b coefficients are calculated using a non-linear regression analysis from a pre-calculated look up table relating brightness temperatures to radiances (Tjemkes, 2012).

2.2.3 Instrument Properties - Imaging

SEVIRI uses a spin and scan mirror rotation set up, whereby the spin stabilized satellite, combined with the East-West scan of the instrument and the stepping of the scanning mirror from North to South with each spin gives 1250 scan positions, completed every 12 minutes. This gives a final image in each of wavelength channel of 3712 x 3712 pixels for each 15 minute period. An example of the disk seen by SEVIRI in each wavelength band measured by the instrument is shown in figure 2.5. The high resolution visible channel covers half the disk in the East to West direction. The infrared channels are subject to an onboard calibration (Wright, 2006).

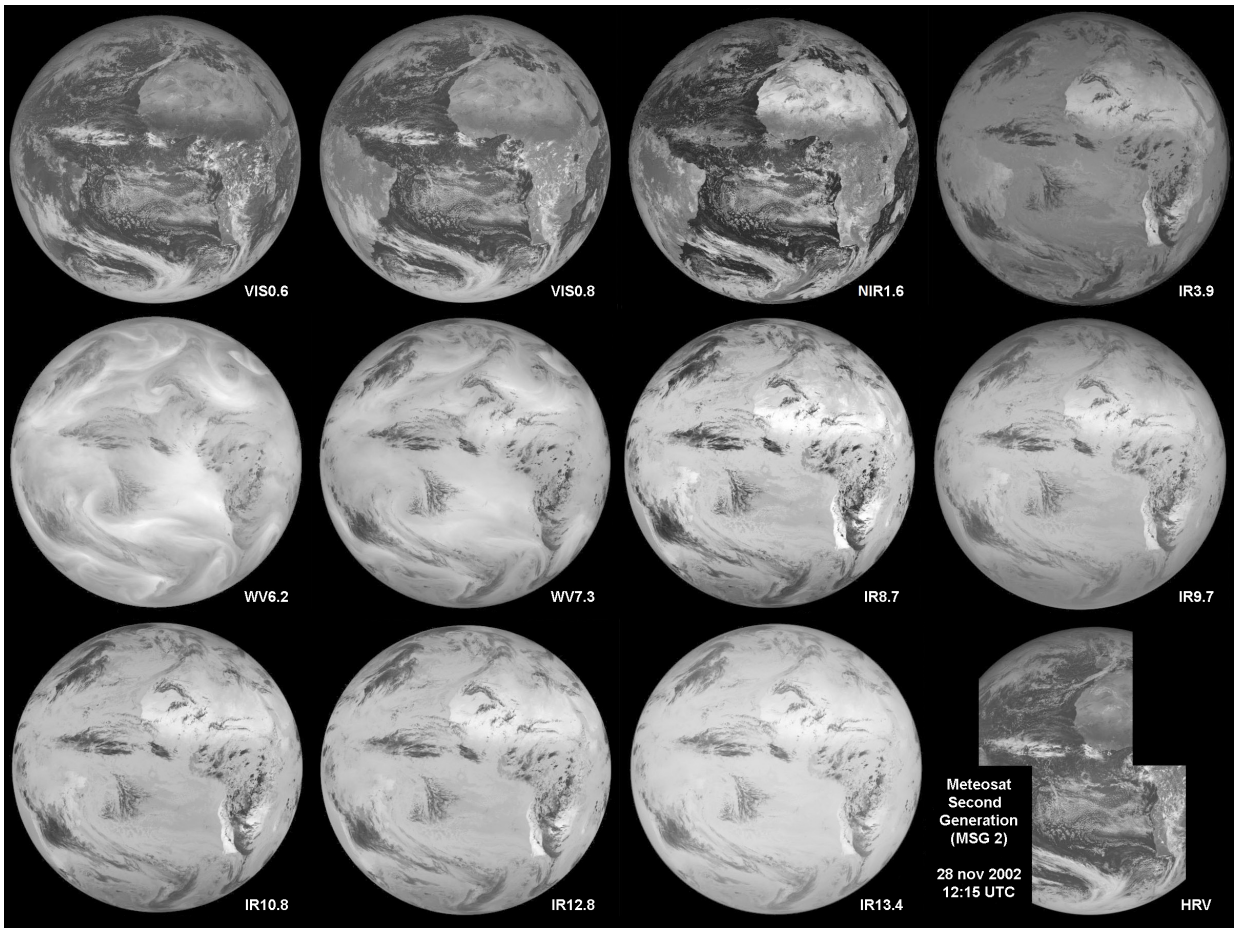

Figure 2.5: All 12 wavelength bands measured by SEVIRI on MSG. The images show the whole disk in each band, taken on 28th November 2002. The high resolution channel only images half of the Earth's disk. Source: University of Paris (2008).

2.2.4 Calibration

The infrared SEVIRI channels are calibrated using an onboard blackbody as its warm source and deep space as a cold source (Schmetz *et al.,* 2002). The calibration procedure for the warm source involves moving the blackbody into the optical path of the instrument, whilst the calibration involving the cold source involves viewing through the entire optical path. The relationship between the SEVIRI digital counts and observed radiances is assumed to be linear:

$$C(L) = GB(\lambda) + C_0 \tag{2.12}$$

where $C(L)$ is the digital count output measured by SEVIRI, $R(\lambda, T)$ is the radiance value, T is the blackbody temperature of a scene, λ is the wavelength, G is the gain (inverse of the calibration coefficient) and C_0 is the offset. The gains and offsets correct for any non linearites and are calculated before launch in the ground calibration stage when converting at sensor counts to radiances. The accuracy of the calibration is expected to be within 1 K for all thermal IR channels (Pili, 2000).

The spectral response functions of the four SEVIRI wavelength channels used in this study are shown in figure 2.6. These response functions show that response of an instrument to radiation at specific wavelengths is not perfect, and are crucial to instrument calibration (EUMETSAT, 2014). The spectral responses are shown in relation to brightness temperatures calculated from a clear sky spectrum of the same spectral region modeled over the study region.

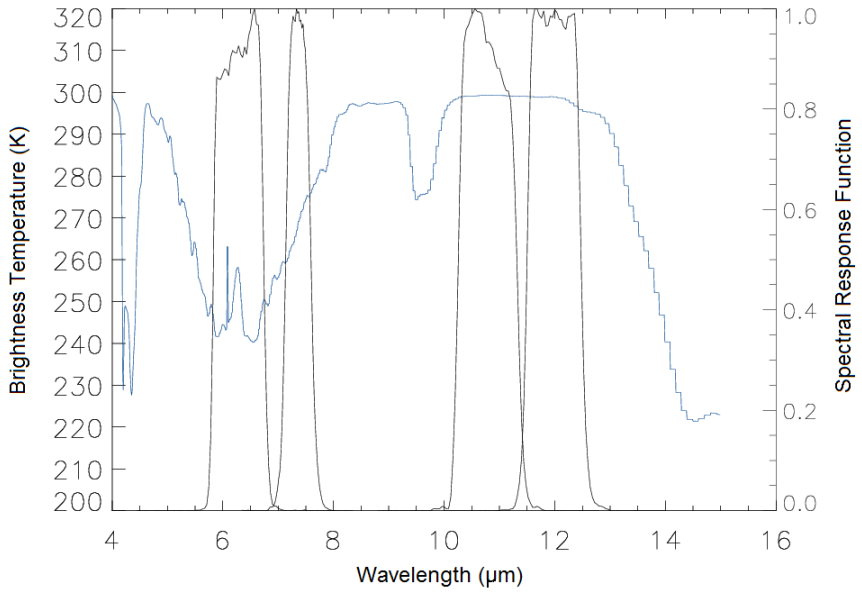

Figure 2.6: TOA brightness temperatures (K) calculated from a clear sky spectrum between 4 and 15 µm for the study region (blue) modeled using SBDART (described in section 2.4.2). These are shown in relation to the spectral response functions for the 6.2, 7.3, 10.8 and 12 µm wavelength channels of SEVIRI (black). These are the 4 channels that will be used in this study.

2.2.5 Geostationary Earth Radiation Budget (GERB) instrument

In addition to SEVIRI, the MSG series carries the Geostationary Earth Radiation Budget (GERB) instrument as its secondary payload. GERB is a broadband scanning radiometer, using a black wide-band detector measuring total radiation nominally between 0.32 µm - 100 µm (Sandford *et al.,* 2003). Using a quartz filter, the detector array also measures the solar component reflected by Earth - between 0.32 µm and 4 µm. The longwave component (4 µm - 100 µm) is found by subtraction. GERB's nominal radiometric absolute accuracy is to within $< 1\%$ (2.4 Wm^{-2} $ster^{-1}$) in the shortwave component and $< 0.5\%$ (0.4 Wm^{-2} $ster^{-1}$) in the longwave, with longwave flux errors expected to be within 10 Wm^{-2}(Russell, 2011; Sandford *et al.,* 2003). GERB has a temporal resolution of 15 minutes, with a spatial scale of 44.6 km^2 in the north-south direction and 39.3 km^2 in the east-west direction at nadir. This gives a full Earth scan in 256 x 282 pixels (Harries *et al.,* 2005). GERB is calibrated using an onboard warm blackbody at 300 K and a cold space view.

Similar to the SEVIRI calibration, GERB calibration is conducted on the ground before flight to characterise the calibration errors. The gain is determined every 5 minutes in orbit (Russell, 2011). Before flight, the ground calibration is conducted using a blackbody with a temperature of 300 K, whilst a blackbody at

liquid nitrogen temperatures is used to represent the deep space view. All of the calibration coefficients are kept constant apart from the gain.

GERB gives further insight into climate processes affecting the Earth's radiation budget at a high temporal scale when compared to low Earth orbit (LEO) measurements such as those available from CERES (Wielicki *et al.,* 1996; Brindley *et al.,* 2015), as well as complementing the simultaneous measurements by SEVIRI. The high temporal resolution, but low spatial resolution allows for a combination with measurements from LEO satellites such as CALIPSO and CloudSat to provide a more detailed understanding of atmospheric phenomena. LEO instruments have a higher spatial resolution and can provide a measurement of the energetics of atmospheric phenomena such as deep convection. Due to their low temporal resolution they may overpass a certain point irregularly, this allows a mean picture of the diurnal cycle to be built up in comparison to that which can be provided by geostationary instruments. The combination of measurements from SEVIRI and GERB should also lead to a better understanding of the physical processes related to deep convection and the response of OLR to this phenomenon.

2.2.6 CloudSat

The CloudSat satellite is part of the A-train constellation of satellites launched by NASA in 2006 to provide information and help to quantify the effect of clouds on the climate, with the close formation of a number of instruments providing near colocated observations (Sassen and Wang, 2008). The A-train is a constellation of satellites that fly in a near circular, sun-synchronous polar orbit with an altitude of 705 km. Polar orbiting satellites fly at a low altitude, providing a high spatial resolution but are limited by their low temporal resolution - producing 14-15 orbits per day. The low temporal resolution of these instruments does not allow for horizontal tracking of environmental variables such as clouds and humidity, but do provide a greater range of senors capable of penetrating cloud layers and providing information that is not available from geostationary satellites (Johnston *et al.,* 2013). CloudSat has a vertical resolution of 240m, an along track resolution of 1.7 km and a cross track resolution of 1.4 km. CloudSat passes over the equator twice daily at ~1.31 pm/am local time, with a groundtrack repeat every 16 days. It uses a 94 GHz cloud profiling radar to provide a vertical representation of the cloud cover based on backscatter as a function of distance from the instrument (NASA, 2012).

An algorithm known as the CloudSat 2B-CLDCLASS product was produced by Sassen and Wang (2008) to detect clouds and classify them based on reflectivity measured by the cloud profiling radar, as well as the cloud base height, top height and the rainfall amount. From this radar reflectivity it is possible to derive several microphysical parameters, such as rainfall rate and ice water content. Using these and other factors clouds can be classified into one of eight classes. The 2B-CLDCLASS descriptions of the cloud classes considered in this study are shown in table 2.2.

Cloud Type	*Cloud Features*	*Characteristics*
Deep Convective Clouds	Base height above ground level (km)	0-3
	Rain	intense shower of rain or hail
	Horizontal Dimension (km)	10
	Vertical Dimension	Thick
	Liquid Water Path	>0
Altostratus	Base above ground level (km)	2-7
	Rain	none
	Horizontal Dimension (km)	10^3, homogeneous
	Vertical Dimension	moderate
	Liquid Water Path	0, dominated by ice
High Cloud	Base above ground level (km)	>7
	Rain	no
	Horizontal Dimension (km)	10^3
	Vertical Dimension	moderate
	Liquid Water Path	0
Altocumulus	Base above ground level (km)	2-7
	Rain	virga possible
	Horizontal Dimension (km)	10^3, inhomogeneous
	Vertical Dimension	shallow or moderate
	Liquid Water Path	> 0
Stratus	Base above ground level (km)	>7
	Rain	no
	Horizontal Dimension (km)	10^3, homogeneous
	Vertical Dimension	shallow
	Liquid Water Path	>0
Stratocumulus	Base above ground level (km)	> 0-2
	Rain	drizzle or snow possible
	Horizontal Dimension (km)	10^3, inhomogeneous
	Vertical Dimension	shallow
	Liquid Water Path	>0
Cumulus	Base above ground level (km)	0-3
	Rain	drizzle or snow possible
	Horizontal Dimension (km)	1, isolated
	Vertical Dimension	shallow or moderate
	Liquid Water Path	>0
Nimbostratus	Base above ground level (km)	0-4
	Rain	prolonged or snow
	Horizontal Dimension (km)	10^3
	Vertical Dimension	thick
	Liquid Water Path	>0

Table 2.2: Characteristic cloud features for the major cloud types used in this study as classified by the 2B-CLDCLASS algorithm developed by Sassen and Wang (2008).

CloudSat possesses some limitations in its ability to detect certain cloud types. The 2B-CLDCLASS product classifies clouds based on a cloud mask detection algorithm. This is limited in its accuracy by the fact that CloudSat cannot easily detect optically thin cirrus (Sassen *et al.*, 2008). CloudSat cloud classification

data does include cirrus in a group of clouds named high clouds, which also includes cirrostratus. To correctly identify high, thin clouds such as cirrus, CALIPSO - another instrument in the A-train constellation and discussed below - is used, which uses a Lidar to detect such clouds.

Examples of advances permitted by CloudSat have been contributions towards understanding cloud radiative forcing by aerosols (Henderson *et al.*, 2012; Chen *et al.,* 2014), whilst also furthering our understanding of cloud systems such as tropical cyclones (Tourville *et al.,* 2015). The main contribution from CloudSat has been to allow for the development of a climatology of the vertical structure of clouds over the globe.

2.2.7 CALIPSO

The Cloud-Aerosol Lidar and Infrared Pathfinder Satellite Observations (CALIPSO) is also part of the A-train constellation carrying the Cloud–Aerosol Lidar with Orthogonal Polarization (CALIOP) instrument, and combines an active Lidar (light detection and ranging) instrument with visible imagers to measure the intensity of the backscattered laser. CALIOP sends pulses at wavelengths of 1.064 µm and 0.532 µm and has a vertical (horizontal) resolution of 60m (1 km). The Lidar onboard CALIPSO is able to penetrate cloud layers and detect thin clouds with optical depths down to $\leq$0.01, but becomes completely attenuated in optically thick cloud (Comstock *et al.,* 2002; Virts and Wallace, 2014). This gives an underestimation of cloud top and base height measurements of thick clouds and optical depths (Comstock *et al.,* 2002).

A combination of the CloudSat cloud classification product (described above) with Lidar data from CALIPSO is used for the detection of cirrus cloud due to the difference in the size of the cloud particles being detected. This is called the 2B-CLDCALSS-LIDAR product and provides a more accurate definition of cirrus clouds than just the use of CloudSat alone (Sassen *et al.,* 2008). This is because radar, such as that used by CloudSat, are better at detecting larger particles, whereas Lidar, with shorter wavelengths are more suited to detecting smaller particles. Radar has difficulty detecting reflectivity below 30 dBz (optically thin clouds) (Comstock *et al.,* 2002). Lidar is able to detect the small particle sizes of cirrus clouds at high altitudes, which can be completely undetected by radar such as CloudSat in the tropical upper troposphere (Sassen *et al.,* 2008). This difference in detection ability is the result of the difference in scattering properties at microwave (Radar) and visible (Lidar) wavelengths. In the radar regime, cirrus clouds act as Rayleigh scatterers because the cloud particles are typically much smaller than the radar wavelength. Using Lidar, the particle acts as a Mie scatterer, with backscattering generally proportional to the diameter squared, meaning more of the Lidar's pulse is backscattered to the instrument in this wavelength range.

2.3 Datasets

In this section a brief discussion on the datasets used in this study is given.

2.3.1 The European Centre for Medium Range Weather Forecasting (ECMWF) Re-Analysis (ERA) Dataset

In order to develop an accurate representation of the recent climate, a data assimilation method providing a reanalysis of historical observations is used to give estimates of a range of atmospheric variables including temperature, pressure, wind speed and precipitation.

A reanalysis gives a numerical description of recent climate produced by combining models with observations. This is produced by assimilating historical observational datasets, using a consistent analysis scheme and model which ingests all the input data every 6-12 hours. In ERA-Interim this ranges between 7 and 9 million observations ingested at all analysis time periods. Re-analyses such as ERA-Interim contain estimates of parameters such as temperature, pressure, rainfall and wind. A reanalysis aims to create the most accurate picture of historical climate as possible, based on a consistent underlying forecast model, nudged by assimilated observations. Though re-analyses provide a consistent global dataset spanning several decades, observational constraints can limit the output due to the lack of observations in some regions of Earth. This includes observations of upper tropospheric humidity and regions such as the tropics in Africa. The lack of observation of UTH due to the limited distribution of weather balloons and radiosondes to collect such data will lead to simulations of such variables being a function of more readily available variables such as temperature. Further, input data of UTH may also come from satellites, using estimations such as that of Soden and Bretherton (1996) to quantify UTH. This in turn will possess errors which may further propagate through to the estimations. Analyses differ from observations in the consistency of the spatial and temporal domains.

The ECMWF used such a method to develop the ERA-interim reanalysis dataset, covering the period from 1979-present (Dee *et al.,* 2011). The first dataset produced by ECMWF using this data assimilation method was the ERA-15 dataset, covering 1979-1993. This was followed by ERA-40, spanning from 1957-2002.

ERA-interim is based on the Integrated Forecast System (IFS) from the EMCWF and has a 12 hour analysis window (Kunz *et al.,* 2014). The available dataset has a temporal resolution of 6 hours, with variables given at 0, 6, 12 and 18 UTC. The spatial resolution of the dataset is ~80 x 80 km (~0.7° x 0.7°) over 37 vertical levels from the surface to 0.1 hPa, with most levels being 25 hPa thick. The reanalysis contains surface and atmospheric variables. The vertical North-South spacing is near uniform, with 128 points from equator to pole at the Greenwich meridian (Dee *et al.,* 2011).

Six hourly global fields of Gaussian gridded pressure level data from the ERA-interim re-analysis dataset are used in this study. Temperature, relative humidity, ozone density (g m^{-3}) and water vapour density (g m^{-3}) at the surface and at vertical pressure-levels are used as input into the several modeling tools used in this study, as discussed below and in chapters 4 and 6.

Early runs of ERA-interim showed that several limitations that were identified in ERA-40, including too intense a water cycle over the ocean, had been eliminated but some still existed. Several adjustments have been made to the integrated forecast system that affect the humidity variables modeled by ERA-interim. This included an ice supersaturation parameterisation by Tompkins *et al.,* (2007). Before the implementation of the new scheme supersaturation immediately converted to ice crystals, whereas relative humidity with respect to ice has actually been observed to exceed 100% and possibly reaching 150% before ice nucleation occurs. This treatment of ice nucleation in ERA-Interim created a dry bias in the upper troposphere. Using the new ice parameterisation scheme, Tompkins *et al.,* (2007) find a difference in the zonal mean RH between this scheme and a control scheme to be 18% in the upper troposphere in the tropics.

In addition, errors in the vapour estimates also existed in ERA-40. Although Flentje *et al.,* (2007) found the distribution of the water vapour to be reasonably accurate, they saw large local differences in water vapour gradients and an overestimation of convective transport of water vapour to the upper troposphere. Kunz *et al.,* (2014) analysed the performance of ERA-Interim with regards to its ability to represent water

vapour through using water vapour measurements derived from the Fast In situ Stratospheric Hygrometer (FISH) dataset. They find a severe underestimation (defined as 10 times lower than observations) of the high water vapour mixing ratios (>300 ppmv) is found in the upper troposphere. They also find an overestimation (within 10% of measured values) in the low water vapour mixing ratios (<10 ppmv) in the lower stratosphere in ERA-interim occurred 13% of the time, with the other 87% showing a good agreement. This has implications for the calculation of specific humidity in this region of the atmosphere and may introduce a cold bias at the tropopause.

Errors that still existed in ERA-Interim after improvements to ERA-40 were found by Dee and Uppala (2009) to be a result of combining numerous different datasets and changes in the observing systems, with many coming from the combination of satellite datasets. The accuracy in the assimilation and in the original measurements, being affected by systematic bias and error, impacts the accuracy of the forecasts and output reanalysis variables. The bias in the measurement from each satellite used in the assimilation varies with location, time, channel and atmospheric state, creating a large scope for error in the input to the ERA-interim reanalysis assimilation (Dee and Uppala, 2009). To overcome this limitation, ERA-interim reanalysis employs an automated bias correction system which tracks bias estimates for each new stream of satellite data introduced to the system.

Using ERA-Interim in this study has both benefits and limitations. ERA-Interim provides a gridded set of data-points that is spatially and temporally consistent at 37 pressure levels through the atmosphere, provided at a 6 hourly temporal resolution. This allows for variables such as UTH to be analysed over a spatially and temporally consistent time period. When comparing UTH measurements with that from reanalyses, ERA-Interim UTH is provided at a much higher spatial resolution than observations.

A common method of observing atmospheric properties such as humidity and temperature is through the use of radiosondes and weather balloons. Though this provides a direct measurement of these variables unlike ERA-Interim reanalysis, radiosondes have a much sparser spatial and temporal resolution, especially over the study region. Use of radiosondes is weighted much more strongly towards the northern hemisphere land regions, though this is very limited over the study region. The use of ERA-Interim therefore provides a consistent set of humidity estimations that is not provided directly through measurements. When using direct measurements of UTH from radiosondes, large errors can be expected. When using measurements of variables such as humidity, measurements become less reliable. Hurst *et al.,* (2011) show radiosonde humidity errors of up to 7.1% between 4 and 1070 hPa, with tending towards larger errors at higher altitudes. Such errors propagate through to variables such as cloud fraction. In regions such as the study region where direct measurements are sparse, including those at high altitudes, variables such as cloud fraction are estimated indirectly from variables such as humidity and temperature. Inaccuracies in the UTH estimations will therefore limit the accuracy of cloud fraction at high altitudes.

Further, measurements of atmospheric variables using radiosondes are generally conducted for short term analyses, which lack the long term stability and measurement traceability of longer term studies using instruments such as satellites. Longer term studies with radiosondes are also questionable due to the poorly documented instrument changes (Hurst *et al.,* 2011).

The information regarding the data used in this study is summarised in the table below:

Dataset	Version	Dates	Resolution	Variables
SEVIRI	V1	June, Dec 2010	3 km x 3 km	6.2 µm, 7.3 µm, 10.8 µm, 12.0 µm
GERB-HR	V003	June, Dec 2010	9 km x 9 km	Broadband OLR
ERA-Interim	2006 release	June, Dec 2010	0.7° x 0.7°,	Pressure, Height, Temperature,
	IFS (Cy31r2)		~83km, 37 levels	Relative humidity, Column water
				vapour, Ozone density
CDIAC	V2010	June, Dec 2010		CO_2
CloudSat	R03	June, Dec 2010		2B-CLDCLASS
CALIPSO	R03	June, Dec2010		2B-CLDCLASS-LIDAR

Table 2.3: Description of all datasets used in this study, including dates, versions and resolutions.

2.4 Modelling Tools

In this section a brief discussion on the modelling tools used in this study is given.

2.4.1 MODTRAN

The MODerate resolution atmospheric TRANsmission 4 (MODTRAN4) model is a narrowband atmospheric radiative transfer code developed to model the propagation of electromagnetic radiation between 0.2 to 100 µm, with a spectral resolution of 1 cm^{-1}. MODTRAN provides a spectral resolution radiative transfer model, with a radiance accuracy of 2-5% in transmittance (Berk *et al.,* 1998). MODTRAN is used in this study to model clear sky TOA radiances between 4 µm and 15 µm using input from ERA-Interim. The modelled TOA radiances and the RH profiles are used in the regression analysis described in chapter 6 to calculate UTH from the 6.2 µm wavelength band radiances, with the particular goal of simulating the dependence of SEVIRI channel brightness temperatures on UTH. MODTRAN requires the input of the vertical temperature profile, the vertical specific humidity profile, the ozone concentration (ppm), and CO_2 (taken here as a constant 397.8 ppm in the vertical (CDIAC, 2014)) as a vertical atmospheric profile. Output TOA radiances from the model are converted to brightness temperatures with their respective SEVIRI filter functions applied.

2.4.2 Santa Barbara DISORT Atmospheric Radiative Transfer (SBDART) Model.

In chapter 4 a method of cloud detection is derived for the detection of deep convection and cirrus cloud. This is based on SEVIRI radiances and follows a study by Lensky and Rosenfeld (2008) using brightness temperature difference thresholds. In order to test the sensitivity of the thresholds to a range of cloud properties and to test whether they are physically sensible, simple model tests have been conducted using the SBDART code (Ricchiazzi *et al.,* 1998).

Specifically, SBDART is used to test the sensitivity of modelled radiances at the TOA between 4 µm and 15 µm to the addition of a cloud layer with different properties. TOA radiances are converted to brightness temperatures with their respective SEVIRI filter functions applied. The SBDART model allows for the input of user defined vertical atmospheric profiles, which again have been taken from ERA-interim reanalysis profiles.

The SBDART model is based on a range of physical models developed by the scientific community to provide a numerically stable algorithm to solve radiative transfer in vertically inhomogeneous atmospheres over a range of zenith angles and heights (Ricchiazzi *et al.,* 1998). SBDART uses the radiative transfer

equation that is integrated with DISORT (DIScreet Ordinate Radiative Transfer) (Stamnes *et al.*, 2000) using LOWTRAN 7 for gas absorption (Kneizys *et al.,* 1988). This is based on low resolution band models developed for the LOWTRAN transmission code, derived from line-by-line calculations which are degraded to a 20 cm^{-1} resolution and provide clear sky atmospheric transmission from 0 to 50,000 cm^{-1}. The model includes the radiative effects of all active molecular species in the atmosphere.

To model cloud, the code requires the cloud top and bottom height, the optical depth, the phase (liquid or ice) and the effective radius to be input by the user. For the sensitivity studies carried out in this thesis, the cloud base and top height and optical depth are assumed to be distributed linearly across the cloud layer. Cloud modelling in SBDART requires the cloud extinction efficiency (equation 2.13), single scattering albedo (equation 2.14) and an asymmetry factor (equation 2.15) that are computed using Mie scattering for spherical droplets with a gamma distribution and the cloud effective radius. The effective radius can be set between 2 μm to 128 μm. The extinction efficiency, a dimensionless parameter, is solved for a particle of radius a, where $\sigma_{e\lambda}$is the extinction cross section:

$$Q_e = \frac{\sigma_{e\lambda}}{\pi a^2} \tag{2.13}$$

Defined in terms of the scattering cross section, $\sigma_{s\lambda}$- the fraction of radiation removed by scattering - the single scattering albedo, ω_λ, is given as:

$$\omega_\lambda = \frac{\sigma_{s\lambda}}{\sigma_{e\lambda}} \tag{2.14}$$

where $\sigma_{e\lambda}$ is the sum of $\sigma_{s\lambda}$ and the absorption cross section, $\sigma_{a\lambda}$. The asymmetry factor, g, represents the strength of the forward scattering in terms of the phase function $P(\cos\Theta)$, where Θ is the three dimensional scattering angle. g is given as:

$$g = \frac{1}{2}\int_{-1}^{1} P(\cos\Theta)\cos\Theta d(\cos\Theta) \tag{2.15}$$

When g=1, all radiation is forward scattered, when g = 0, scattering is isotropic, and when g= -1 all radiation is backscattered. A representative g for a water cloud is 0.85 due to the stronger forward scattering in Mie scattering (Salby, 1996). As noted earlier, the cirrus cloud radiative transfer in the model includes the scattering parameters for spherical ice grains of a fixed size distribution. The assumption of spherical ice crystals is an approximation and adds uncertainty to the cirrus cloud modelling.

2.5 Summary

Having briefly described the datasets, modelling tools and related theory, a climatology of the study region is now given in chapter 3 using ERA-Interim data. This is followed by the development and testing of a detection method for deep convection in chapter 4 using the datasets and instrumentation described above, with the limitations of these considered in the analysis of the results.

Chapter III

Climatology of Tropical Africa

3 Overview

The climate and meteorology of the tropics - a region conventionally defined as being between 23.5° North and South of the equator and bounded by the tropics of Cancer and Capricorn - is largely influenced by intra-annual events such as the meridional movement of the Intertropical Convergence Zone (ITCZ) and associated cloud and precipitation regimes (Laing *et al.,* 2008).

The region of interest for this study is between 10° to 40°E, 0°N to 15°N (figure 3.1, black box). The region covers continental tropical Africa in the northern hemisphere and it contains the region in which the ITCZ propagates in Boreal summer. This region of the tropics experiences the most intense storms, but has the lowest annual precipitation of all equatorial regions (Zisper *et al.,* 2006; Laing *et al.,* 2011). Studying a similar region of tropical equatorial Africa, Tian *et al.*, (2004), Allan *et al.*, (2007), Laing *et al.,* (2008) Schröder *et al.*, (2009) and Chung *et al.*, (2013) show deep convection to be a regular occurrence during the Boreal summer. During Boreal winter months, convection moves southwards following the intertropical convergence zone, as is very evident from the seasonal propagation of deep convection over tropical Africa found by Schröder *et al.*, (2009). The selected region of study thus allows for an analysis of the effect of the ITCZ's movement on convective frequency, and the associated impacts of this on the response of UTH and OLR, in both winter and summer months in the Northern hemisphere. After a discussion on the large scale influences on deep convection over tropical Africa, ERA-Interim estimates of selected variables from June and December over the region of interest (figure 3.1, bottom) are examined and discussed. A particular goal is the characterisation of the convective frequency, cloud top height and cloud thickness as well as the clear sky vertical mean relative humidity profiles at different times of day.

The study location was chosen to enable analysis of purely land based convection. This region cover the tropical region of the northern hemisphere in Africa. Deep convection over this region is found to be the most intense on Earth, therefore this allowing for a quantification of the response of UTH to such phenomena. Though this region is relatively small in comparison to the tropics as a whole, this area covered only land, which allows for a comparison with other tropical land regions. One issue with the size of this region may be that it limits drawing a generalisation of a tropic wide UTH response. A larger study area may allow for a stronger generalisation to be drawn though it would likely also not allow for specific seasonal comparisons as this region does.

Generalisations may also be limited in this study by the use of only two months. Though this allowed for a comparison between a winter and summer period over land to determine whether there was an influence of season on the UTH response, the two months analysed are not the northern and southern most extremes of the ITCZ. The chosen months allowed for a comparison of results with a similar study by Schroder et al (2013). Analysis of the SEVIRI data was also found that some data was missing in January 2010, leading to December being analysed.

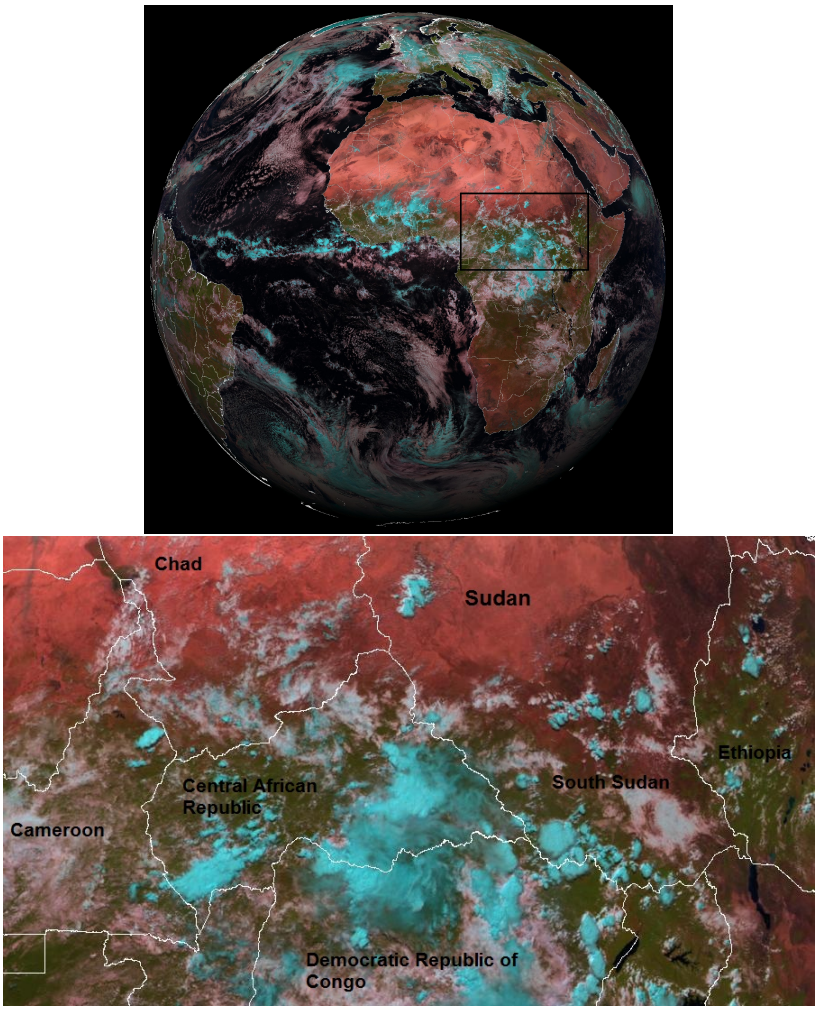

Figure 3.1: **Top**: Whole disk image from SEVIRI, 1st June 2010 at 1200, created using an RGB colour scheme of a combination of 1.6 μm (R), 0.8 μm (G) and 0.6 μm (B) bands of SEVIRI. The study area is shown in the black box. The ITCZ can be seen as a band of cloud around the equator (the high and deep cloud is blue in this image). Deep convective and cirrus clouds appear blue in this imagery due to strong absorption by ice in the 1.6 μm (no red reflectance). RGB composites are based on the approach of Lensky and Rosenfeld (2008). **Bottom**: Zoomed in images of the study area (10° to 40°E, 0°N to 15°N).

3.1 Large-Scale Influences

3.1.1 The Hadley Circulation and the Intertropical Convergence Zone

The largest influence on the climate of tropical Africa is the Hadley circulation and the associated ITCZ. The absorption of solar energy by the landmass and oceans in the tropics, the transfer of this energy to the atmosphere and the relatively small latitudinal variation in the IR emitted to space, results in a meridional temperature gradient between the tropics and the poles (Bechtold, 2009). The need to redistribute this energy results in the Hadley cell - a circulation of air characterised by the ascending branch of warm air over the equatorial zone causing the development of deep convective clouds, a descending branch over the subtropics and a return flow in the boundary layer from the subtropics to the tropics (McIlveen, 1998; Bechtold, 2009).

The ITCZ is classically defined as the convergence of the return flows from the Northern and Southern hemispheres - known as trade winds - at the equatorial trough, centered on average around 6°N (McIlveen, 1998; Houghton, 2007; Nicholson, 2009; Schneider *et al.,* 2014). The slightly northward mean position of the ITCZ is attributed to the cross-equatorial transport of energy northwards by the Atlantic Ocean, but on seasonal scales the movement of the ITCZ is generally towards the warmer hemisphere (Bischoff and Schneider, 2014; Schneider *et al.,* 2014).

It is an area characterised by low pressure, in turn causing a rising motion and the subsequent transport of warm moist air away from the equator and is therefore also known as the equatorial low pressure zone (Waliser and Gautier, 1993; Nicholson, 2009). This vertical motion is associated with increased deep convective activity through the processes introduced in chapter 1. This provides the idea of a straightforward north-south moving band of cloud over tropical Africa that follows the sun, travelling northwards during Boreal summer and southwards during Boreal winter. This simplistic description of the ITCZ is most likely to be seen over oceanic regions, where we see a better defined trade wind convergence zone, which creates a more subtle movement of the ITCZ in these regions, with the ITCZ forming on the equatorward boundary of these trade winds (Holton *et al.*, 1971). This classical view of the Hadley cell and the ITCZ is shown in figure 3.2.

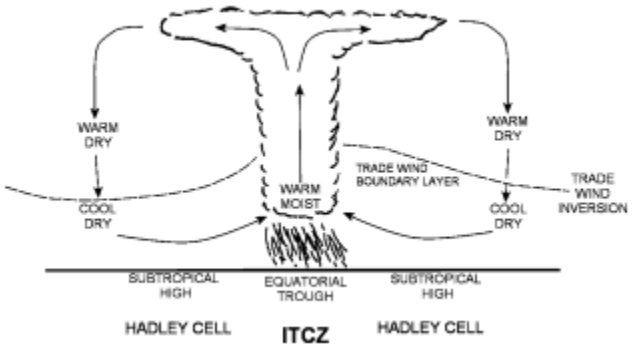

Figure 3.2: The classic view of the ITCZ and the Hadley circulation. The deep convective clouds above the equatorial trough are a product of and denote the ascending branch of the Hadley cell. Warm, dry air denotes the descending branches over the subtropics. Taken from Nicholson (2009).

Large land masses inhibit the development of the ITCZ at continental longitudes. Over continental regions, such as tropical Africa, trade winds are not a feature as these are driven by subtropical high pressure regions over oceans, forming over the subtropical north and south Atlantic and south Indian oceans. When air from these regions reaches land it is generally moisture and cloud laden, developing into mesoscale convective systems (squall lines) giving the ITCZ the appearance of a loci of cloud clusters associated with wave disturbances (Holton *et al.,* 1971; Barry and Chorley, 2003; Nicholson, 2009). This can be seen in figure 3.1, where a band of cloud is seen straddling the equator.

The ITCZ does not move uniformly across tropical Africa. It is characterised by a succession of phases and pauses and is shifted northward and centered around 20°N during the northern hemisphere summer months and ranging between 10°N and 10°S during Boreal winter months (figure 3.3a) (Nicholson, 2009; Janicot *et al.,* 2011). This variability in the position of the ITCZ over land is largely due to the differing heat capacities of land and ocean. Due to this we see a more pronounced movement of the ITCZ over land following the

larger changes in land surface temperatures through a change in the season. Also, the better defined trade wind convergence zone over the oceans allows for the development of a stronger ITCZ.

Longitudinally, the ITCZ is associated with monsoon wind systems and is characterised by cloud development and intense precipitation (Barry and Chorley, 2003) as seen in figure 3.3b. These systems in turn are driven by an uneven heating of the Earth's surface and outflows from decaying storm systems, causing a high degree of variability in the distribution and movement of the ITCZ (Barry and Chorley, 2003). The meridional movement of the ITCZ creates two distinct rainy seasons in regions north and south of the equator. Over the study region, the first African rainy season is seen along the Western coast near Guinea between April and June. The northward shift in the ITCZ brings the associated summer monsoon, its later southward retreat creating another rainy season over the region of equatorial Africa north of the equator, followed by a suppression of convection. The ITCZ and associated monsoon is strongly linked to the time of peak heating and arrival of equatorial pressure troughs, bringing changes to instability, low level convergence and moisture in this region, all of which follow the Sun's migration between hemispheres. The classic definition of the ITCZ shows that the cloud thickness increases with a movement towards the equator (figure 3.3b), with deep convection occurring where this band moves equatorward and uplift is most intense (Nicholson, 2009).

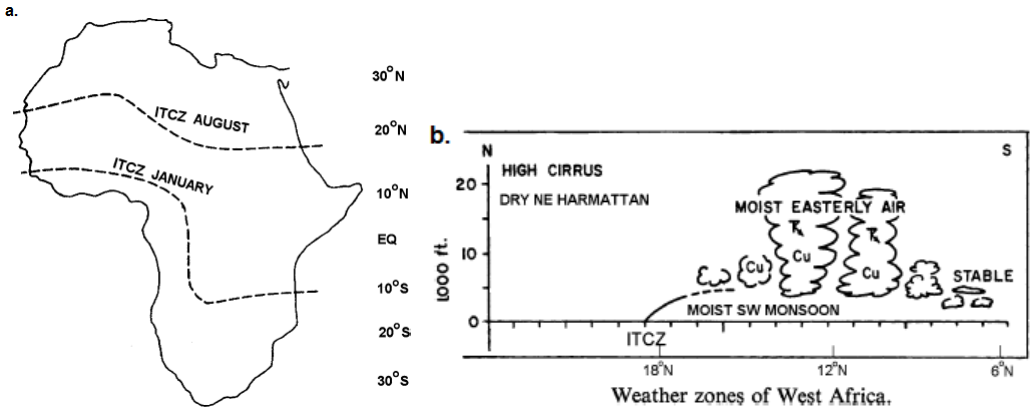

Figure 3.3: **a:** Location of the ITCZ over Africa during August and January, showing the non-uniformity in the direction the ITCZ traverses, as well as the more northern position during Boreal summer. **b:** How the classic view of the ITCZ is expected to develop over tropical Africa. The structure of the deep convective cloud with respect to its location over this region in August can be seen. All images are taken from Nicholson (2009).

3.1.2 African Easterly Waves

Apart from the ITCZ, the phenomenon with the largest scale influence on deep convection over tropical Africa is the African easterly jet (AEJ) (figure 3.4a). The AEJ is associated with the development of convective systems over this region through its influence on the development of squall lines and mesoscale convective systems (Bechtold, 2009; Nicholson, 2009; Wu *et al.,* 2009). The AEJ is a jet found in the mid troposphere between 500-700 hPa (4000-5000 m) in the region north of the monsoon trough, where the wind speed is easterly and maximum. Maximum easterly velocities are found between 500 and 650 hPa (Burpee, 1972; Cook, 1999). The core of this jet is found around 15°N at the West coast, moving southwards over land, with a width of 5-10° (Cook, 1999). The vertical windshear associated with this jet enhances the development

of mesoscale convective systems. Figure 3.4b shows the resulting vertical structure associated with the AEJ and the associated deep convection and precipitation representative of Northern tropical Africa. The region south of the AEJ is an area of intense convective activity and associated intense rainfall, and the AEJ has long been believed to be the main control on the inter annual variability of precipitation and deep convection over tropical Africa as a whole (Kanamitsu and Krishnamurti, 1978; Nicholson, 2009). The intraseasonal movement of the AEJ largely controls the movement of MCS's over tropical Africa, with these systems following its position (Besson and Lemaître, 2014).

Associated with the jet and acting as a possible mechanism in the development of convective systems are African easterly waves (AEW). These waves generally form north of the equator and over western Africa and occur directly south of the core of the AEJ (Diongue *et al.,* 2002). They have a period of 2-6 days with wavelengths of 2500 km (Nicholson, 2001; Tompkins *et al.,* 2005; Bechtold, 2009), and are a result of the barotropic (meridional shear) and baroclinic (vertical shear) instability of the African Easterly Jet (AEJ). These waves are well known modulators of deep convection, with an enhancement of convection ahead of the trough axis (Diongue *et al.,* 2002).

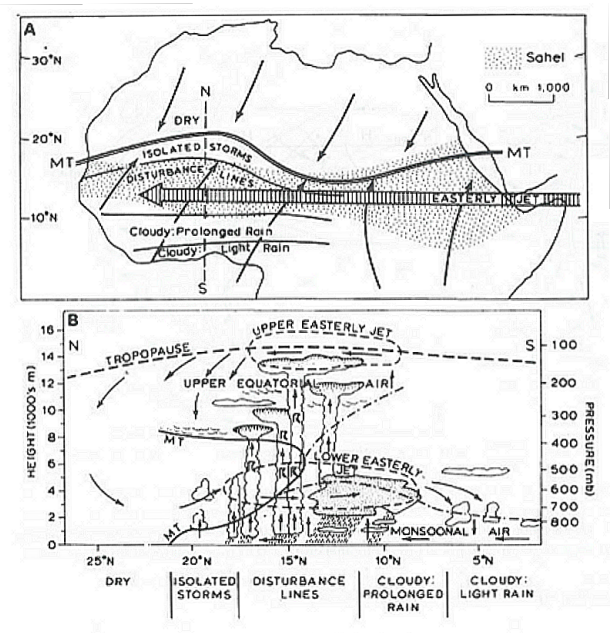

Figure 3.4: **A:** Surface flow and the AEJ over Northern tropical Africa in August. MT is the Monsoon trough, the area within ITCZ where the trade winds converge (represented by the arrows). **B:** The resulting vertical structure, between 0 and 16 km in the vertical and 0° to 25° N in the horizontal over Northern tropical Africa. Arrows represent the circulation of air. From: Barry and Chorley (2003).

3.2 Deep Convection over Tropical Africa - June and December 2010

In order to understand the response of UTH and OLR to deep convection and to aid in the development of cloud detection methods in chapter 4, an analysis of cloud top height is given. This is also followed by an analysis of the vertical clear sky relative humidity profile to characterise the atmospheric state of the region of interest. Using ERA-Interim data introduced in chapter 2, cloud variables are analysed over 6-hourly

periods for June and December 2010. The use of ERA-Interim at 6 hourly time steps is conducted to obtain insight into the diurnal cycle associated with deep convection as manifested in the ERA-Interim record.

As discussed in chapter 1, it is expected that deep convection over tropical Africa follows a distinct lifecycle over the diurnal cycle and also a seasonal pattern due to the large scale influences discussed above. As discussed, cloud top heights are representative of convective intensity, with the greatest intensity seen when the atmospheric state is suited to convection and values of CAPE are high. We therefore expect to see some seasonality relating to cloud top heights and also cloud frequency.

In this study, deep convection is defined as continuous cloud cover in the vertical extent, having a maximum cloud base height of 1.5 km, a minimum thickness of 5 km and a minimum cloud top height of 6 km, following the definition by Suzuki *et al.,* (2011) and the MetOffice (2013a). Cloud variables including cloud top and thicknesses are presented for both June and December 2010 at hourly time intervals as probability and cumulative density functions (PDF and CDF respectively) as well as box and whisker diagrams. This will give a representation of the diurnal and seasonal variation in deep convection over the study region. The box and whisker diagrams show the median (middle line in the box) and the upper and lower quartiles (UQ and LQ; top and bottom lines of the box respectively, the difference being the inter quartile range (IQR)). The whiskers are representative of the maximum and minimum values of the data, or 1.5 times either the 0.25 or 0.75 quartile ranges. The outliers are therefore representative of any values more than 1.5 times either the 0.25 or 0.75 quartile ranges. The clear sky vertical RH and temperature profiles are also shown and discussed to give an understanding of the study environment.

In order to test for differences in the cumulative distribution of cloud top heights and the distribution around the median value, the Kolmogorov-Smirnov test and Mann-Whitney U test are used. Both tests are non-parametric, meaning no assumption about the distribution is made, and both tests give a P-value - a confidence interval of 0.05, such that if a small P value is calculated (<0.05) the null hypothesis (that the data shows no difference in its distribution) is rejected with 95% confidence, and it is assumed that there is a significant difference in the distribution at this confidence level.

The two sample Kolmogorov-Smirnov (KS) test is a test of the shape of the cumulative probability distributions (i.e. differences in skewness) of two populations (Sheskin, 2003). The KS test quantifies a difference value, D, which describes the maximum vertical deviation between two cumulative frequencies of the two datasets (ranging from 0 to 1, with a large D value meaning a large deviation, significant at 0.05). Therefore the KS test cares only for the distribution of the data, and can determine whether two datasets differ significantly in their distribution, with no prior assumption about the distribution. In this study the KS test is used to determine whether variables such as cloud top height possess a significantly different distribution dependent on season. If there is no significant difference between the shape of the distributions the D value will equal zero, or will be very low if the distributions differ slightly.

The Mann-Whitney U test is an alternative to the parametric Student's T-test. It is a test of the difference in the distribution, or medians, between two groups of data (Kirk, 2008). The Mann-Whitney U test ranks the data in order from low to high, and then calculates the P value based on the distribution around the median. As with the KS test, in this study the Mann-Whitney U test is used to determine whether the distribution around the median of cloud top heights differ with season.

Though using the KS test alone will give an idea of the difference in the distribution, the Mann-Whitney test tests for changes in the location of the data around median. Using both tests gives a strong idea about the

differences between two datasets, allowing for more robust assumptions to be drawn. A significant difference in the distribution around the median is likely to be caused by the difference in the shape of the distributions. The D statistic given by the KS test will then give a quantified scale of the difference in the distributions.

3.3 Cloud Variables

3.3.1 Frequency of Deep Convection

Based on the discussion above and in chapter 1, it is expected that deep convection over tropical Africa will show a greater frequency when solar heating is greatest - in the early afternoon - with the frequency of convection lowest in the early morning hours. It is also expected that the effect of the ITCZ's movement and the associated greater frequency of convection following the ITCZ, as discussed above will also be seen.

Figure 3.5 shows the frequency of convection at 6 hourly UTC intervals for June and December 2010. This shows a much greater frequency of clouds in June 2010 than December 2010. Based on the definition of deep convection above, 5528 profiles are found to represent deep convection over the study area in June 2010 compared to 1251 profiles in December 2010 for the same region. This is representative of the effect of the ITCZ's movement and the associated greater frequency of convection following the ITCZ, as discussed above. When comparing the frequency of deep convection between seasons, the cloud follows a typical cycle of less convective frequency in the early morning hours, with the greatest frequency seen at 1200 UTC (1841 cloud profiles in June, 589 in December). In June, the lowest frequency is found at 1800 UTC (783 clouds), whilst the lowest is found at 0000 UTC in December (182 cloud profiles).

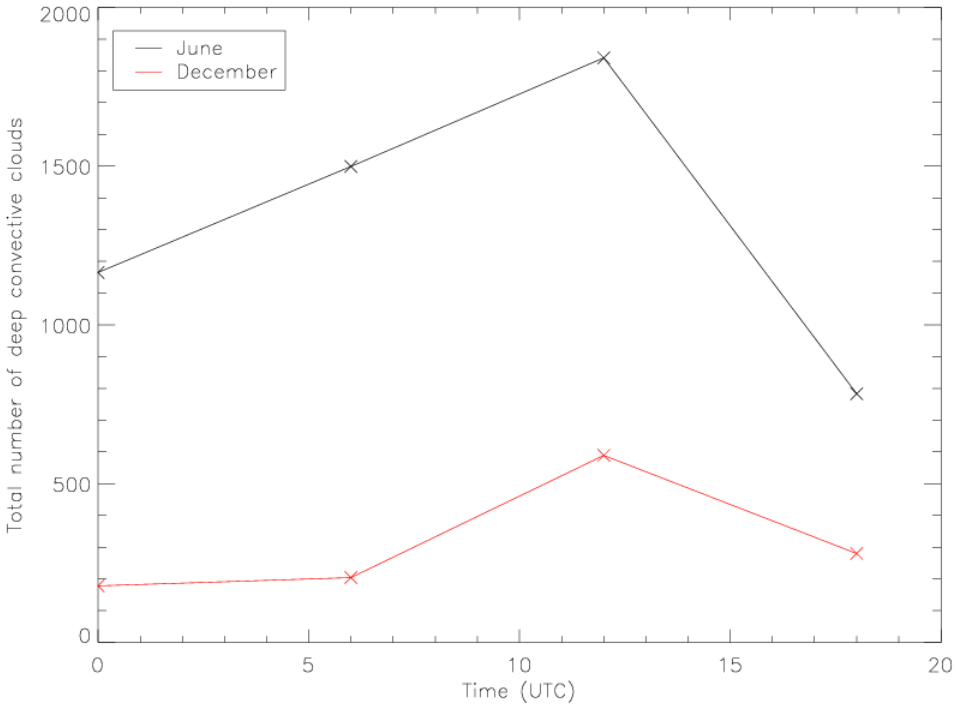

Figure 3.5: Frequency of deep convection in June and December 2010 from ERA-Interim.

The frequency of convection is also presented spatially as a function of local standard time (LST) at each ERA-Interim time period. Figure 3.6 shows the convective frequency in 0.7° longitude bins at each UTC for June and December, with the corresponding LST also shown. With a major control on convection being the radiative heating of the surface, the region covered in this study is likely to show a spatial response which is not evident when analysed purely at UTC.

As expected from figure 3.5, at all time periods more convection is present in June (figures 3.6a and c; 3.7e and g), with this difference being especially marked during the early morning hours. In December (figures 3.6b and d; 3.7f and h), areas of higher frequency are found closer to the equator than in June, as expected due to the position of the ITCZ at this time of year. A marked diurnal pattern in the frequency is evident in June with the frequency of convection greatest in the early afternoon, similar to what has been found by Schröder *et al.*, (2009). A slightly different but just as marked diurnal pattern is also seen at ~5° N, ~10°E in June.

This pattern of convective frequency is likely to be influenced by the orography of the region (figure 3.8). This is seen especially in June where the two areas with the greatest frequencies correspond to the region near the Cameroonian highlands, especially to the lee of the Adamawa highlands and the Joss plateau, a region of west Africa around ~5° N, ~10°E. The maximum frequencies of convection are seen to correlate well with these higher regions. Some effect is also seen towards the north west of the Great Rift Valley (from ~0° to 5° N, ~30°-40°E) where no convection is found in the shadow of these mountains. This is especially seen in the late hours and early morning hours. Similarly, the aridity of the region also correlates well with the frequency of convection. The need for uniformly high relative humidity for the offset and development of deep convection is clearly seen in the spatial pattern of convective frequency, with the areas of high humidity coinciding with those of high frequency (figure 3.9). In figure 3.9, a climatological zones over the study region as defined by the aridity of the region. The climatology is based on data provided by the Third Assessment Report of the IPCC (2001). In this climate zone classification, regions of high aridity are seen around 5° N and 40° E. This coincides with areas of minimal and non existent convection. There is a marked lack of deep convection closer to the Sahel, where the region is drier and less intense convective clouds would be expected to form based on figure 3.3b.This is also seen for the most northerly regions of the study area, where the beginning of the Sahel is found and is also classified as arid, as well as mountainous regions.

Temporally, the greatest frequency of convection is found at around 1330 LST in June (between 3 and 5° N, 17 and 25° E), slightly earlier than the times of greatest convective frequency found by Schröder *et al.,* (2009). The same pattern is seen in December though closer to the equator. This temporal pattern in convective frequency agrees with that found by both Laing and Fritsch (1993) and Chung *et al.,* (2007), who find convection maxima in the early afternoon, with topographically induced convection a key feature of this temporal signature.

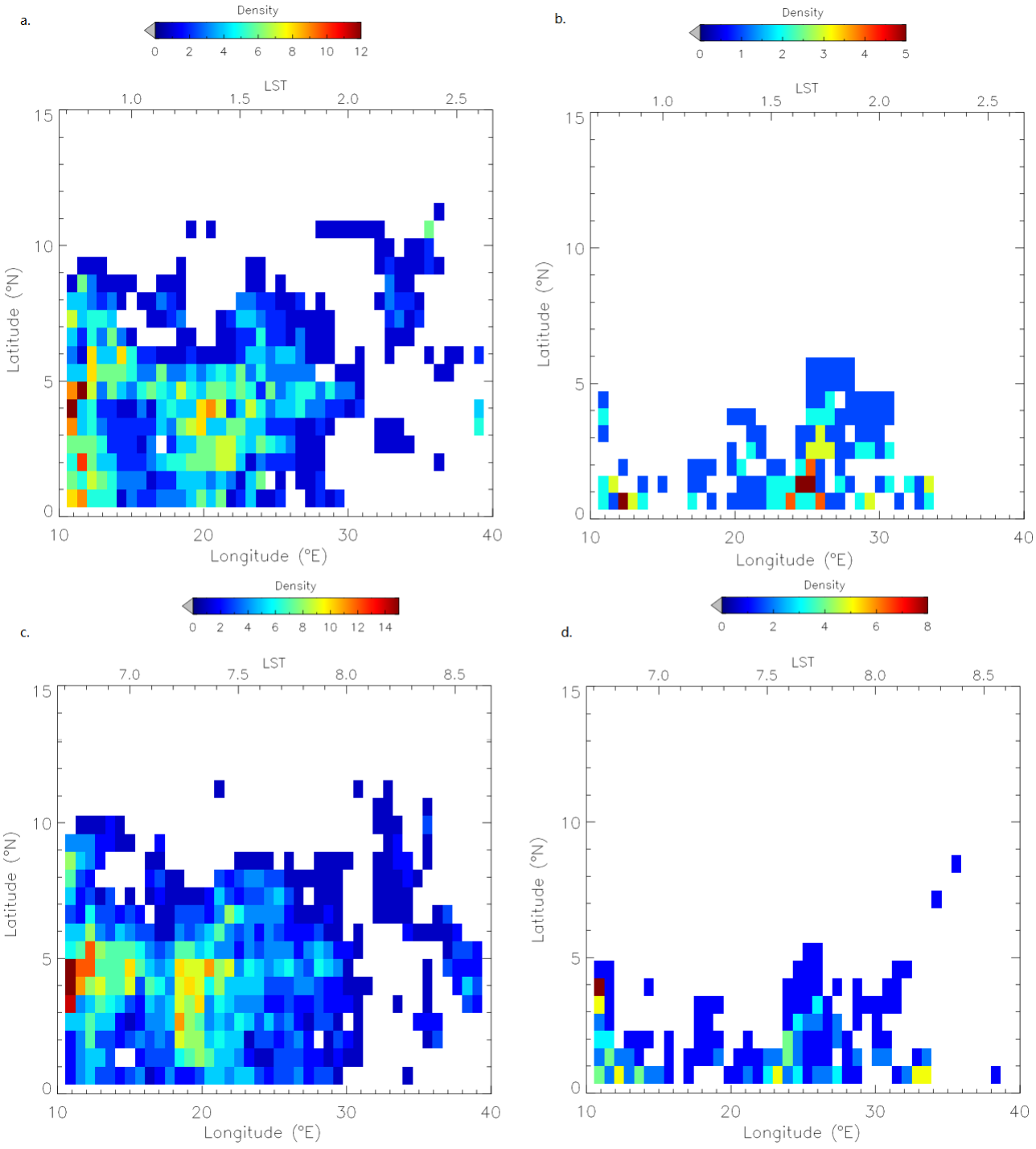

Figure 3.6: Frequency of convection in June 2010 (**a, c**) December (**b, d**) at 0000 UTC (**a** and **b**) and 0600 UTC (**c** and **d**) in relation to LST. Convective frequency is binned by longitude in 0.7 degree bins. Note the changing scale between each plot.

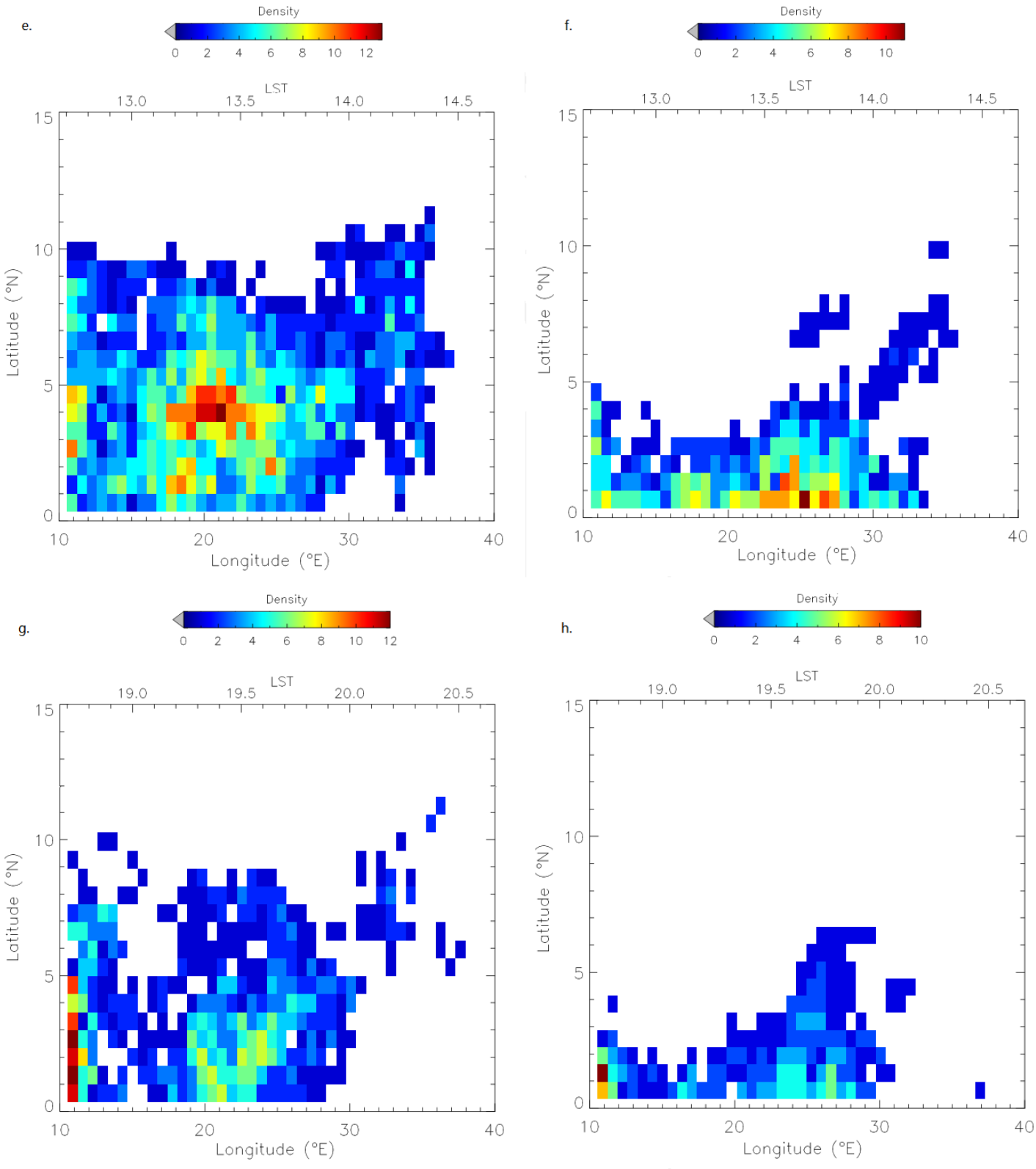

Figure 3.7: Frequency of convection in June 2010 (**e, g**) December **(f, h**) at 1200 UTC (**e** and **f**) and 1800 UTC (**g** and **h**) in relation to LST. Convective frequency is binned by longitude in 0.7 degree bins. Note the changing scale between each plot.

Figure 3.8: Relief map of the study region. Source: Berens (2013)

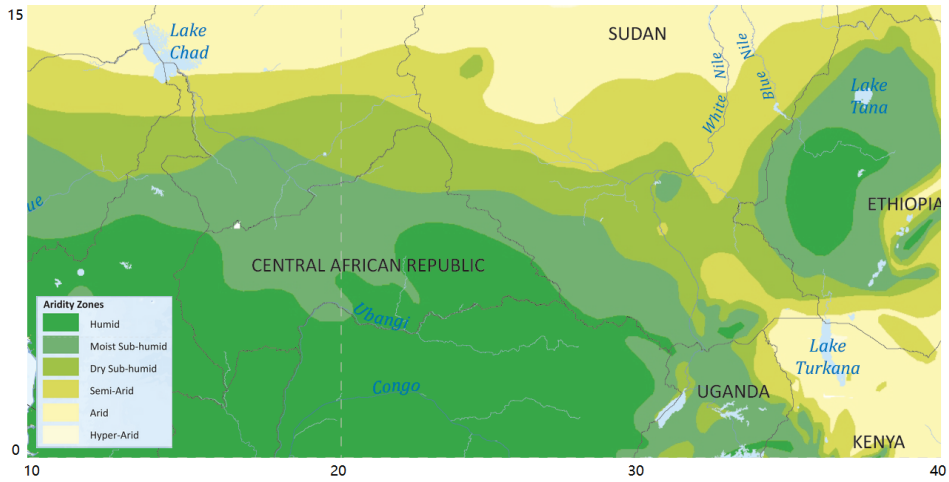

Figure 3.9: Map of aridity over the study region. Source: UNEP (2015)

3.3.2 Cloud Top Heights (CTH)

Overall mean cloud top heights for June and December show a difference of 882 m between the two periods (12.96 km in June; 12.14 km in December), suggesting that the convective intensity does differ, though not greatly, between the two seasons. Moreover, from tables 3.1 and 3.2, it is clearly evident that cloud top height at each UTC period is consistently higher at each period in June. This relates to the convection being more intense during this period, as discussed in chapter 1. Mean cloud top heights in June range from 12.5 km at 0600 UTC to 13.6 km at 1800 UTC, compared to December where mean cloud top heights range from 11.9 km at 0600 UTC to 12.5 km at 1800. A slightly larger range in cloud top heights is also seen in June compared to December. This likely suggests that there is a larger range of clouds spread over a range lifecycle stages in December, compared to the more intense and therefore higher convection seen in June. A consistent maximum cloud top height is seen for all periods in June 2010, with only a small variation over the

same periods in December. This suggests that intense convection may prevail over the entire day. A higher median is seen for June 2010, which suggests a more negative skew in June, even though a the minimum cloud top heights in December are considerably larger than that in June.

Time	Number of clouds	Mean (km)	Median (km)	Max (km)	Min (km)
0000	1165	13.5 (σ=1.35)	13.9	15.5	6.1
0600	1499	12.5 (σ=1.66)	12.7	15.5	6.3
1200	1841	12.7 (σ=1.54)	12.8	15.5	6
1800	783	13.6 (σ=1.5)	13.9	15.5	6.4

Table 3.1: Statistics for cloud top heights at 6 hourly periods in June 2010. Time given in UTC.

Time	Number of clouds	Mean (km)	Median (km)	Max (km)	Min (km)
0000	178	12 (σ=0.9)	12.3	14.2	8.4
0600	204	11.9 (σ=1.27)	12.2	14.3	6.1
1200	589	12.1 (σ=0.9)	12.4	14	7.6
1800	280	12.5 (σ=0.7)	12.4	14.2	10.1

Table 3.2: Statistics for cloud top heights at 6 hourly periods in December 2010. Time given in UTC.

The results shown above are summarised in figure 3.10. The range of maximum cloud top heights in June show no time dependent difference, whilst minimum cloud top heights show a small time dependent difference, suggesting that only a small difference in the range of cloud top heights exists in June though the range of mean cloud top height is smaller in December than in June. December shows a smaller range in cloud top heights between maximum and the respective minimum cloud tops at each time step and also a time dependent difference in cloud top heights. The time dependent range in December shows a smaller range at 1800, whereby convection is most intense and newer convection is unlikely to be developing. This suggests the mean is masking the range of cloud top heights between minimum and maximum seen at each timestep in each month.

The median cloud top heights in June range from 12.7 km at 0600 UTC (figure 3.10b) to 13.9 km at 0000 UTC (figure 3.10a). The difference in medians in December is much smaller, with the medians ranging from 12.2 km at 0600 UTC to 12.4 km at 1200 UTC. A large number of outliers are found below the lower quartiles. Outliers represent the cloud top heights over 1.5 standard deviations from the lower quartile. This is due to the high frequency of the higher cloud tops and the small number of low cloud tops at all periods in June and December creating a more negatively skewed dataset.

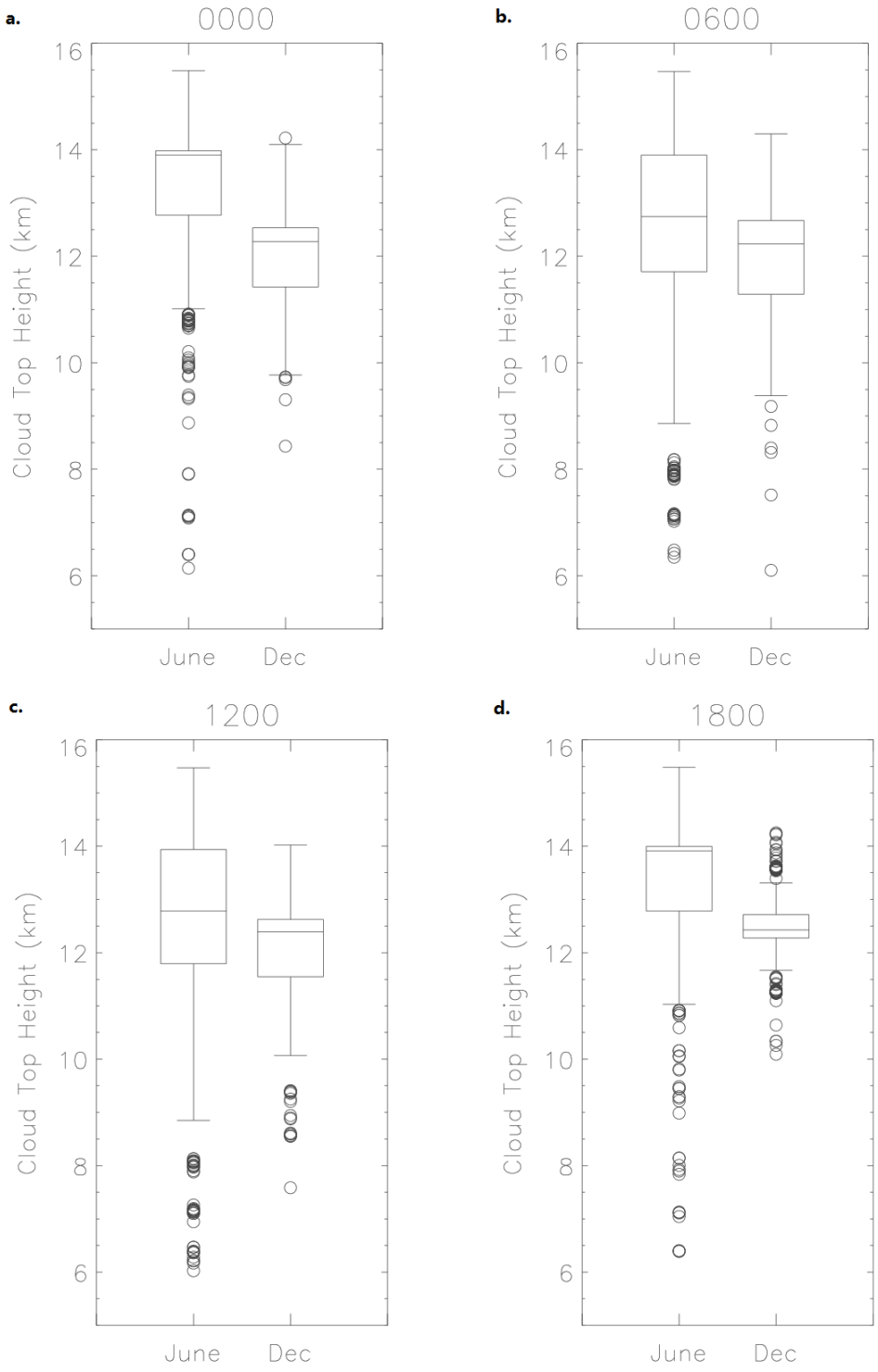

Figure 3.10: Box and whisker diagrams of deep convective cloud top heights (km) in June and December 2010 over the study region at **a)** 0000 **b)** 0600 **c)** 1200 **d)** 1800

Figure 3.11 shows the probability and cumulative distribution function of cloud top heights for June and December 2010. The PDF shows a higher frequency of higher cloud tops in June, with no clouds over 14.5 km high in December. The two sample KS test shows the maximum difference in the cumulative distribution (D value) to be 0.48 between the two months at the 5% confidence interval, suggesting a significant difference between the two populations.

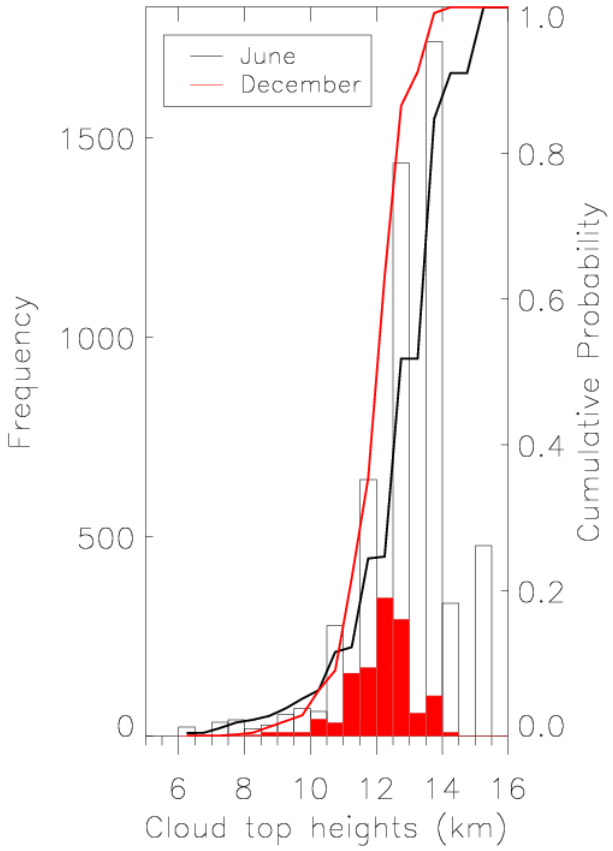

Figure 3.11: PDF and CDF of cloud top heights for June and December 2010 over the study region. Data is taken from ERA-Interim vertical profiles.

This negative skew in the distribution and frequency of cloud top heights is also seen at each UTC period (figure 3.12 a to d). The probability density functions of CTH in figure 3.12, again highlight that there is a much greater frequency of deep convective clouds in June than December over the study region at all periods. From figure 3.12, as in figure 3.11, it is evident that all periods show a negative skew, more so for June, due to the higher frequency of high cloud tops evident in June, for example, at 00:00 there are 181 clouds between 15-15.5 km in June but no clouds being higher than 14.5 km in December at 00:00. At 06:00 and 12:00 UTC (figure 3.12, b and c) the highest frequency of clouds are found with cloud top heights of 12.5-13 km for both months.

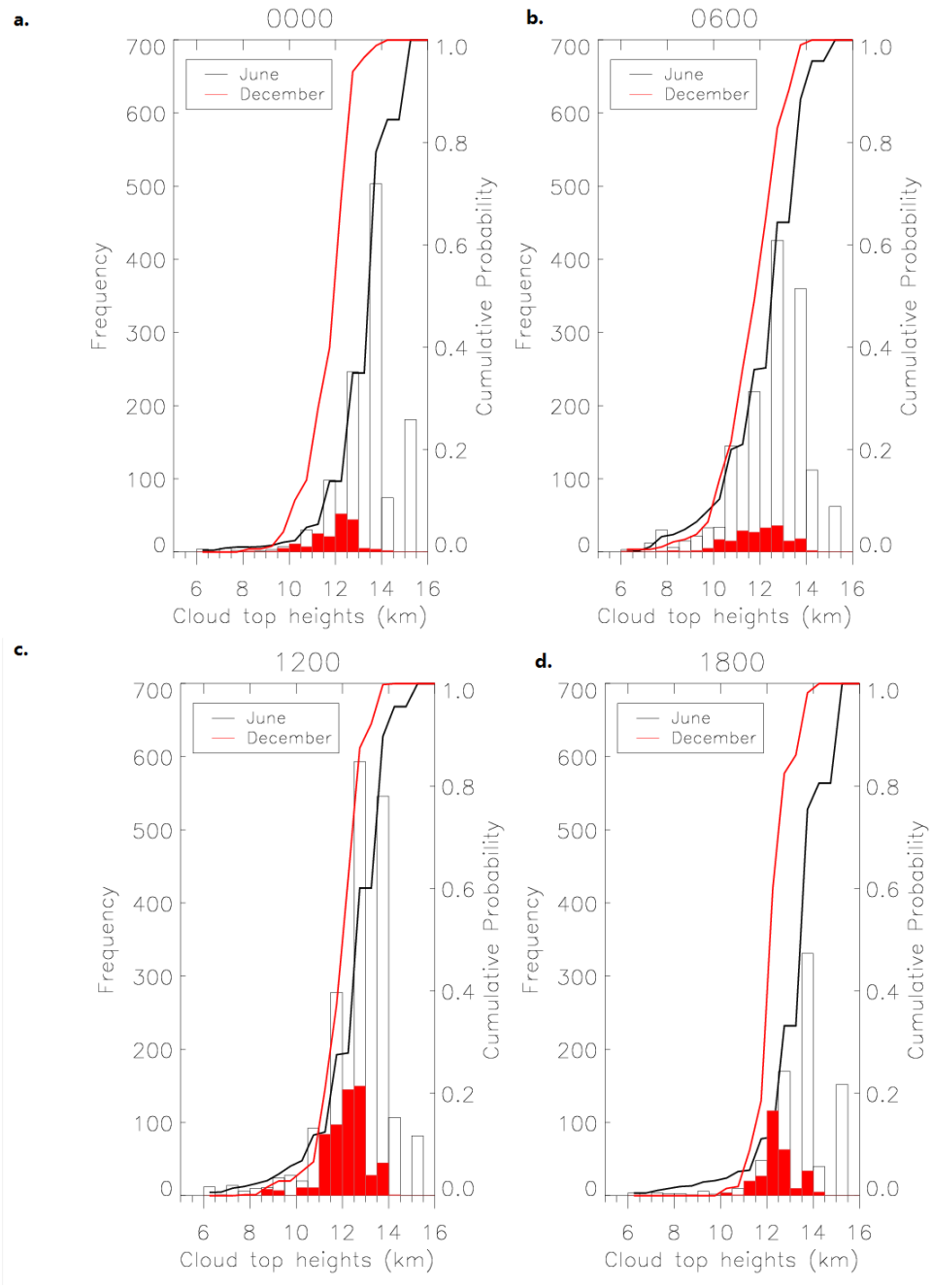

Figure 3.12: Probability and cumulative density functions of deep convective cloud top heights (km) in June (black) and December (red) 2010 over the study region. Cloud top heights are compared at each 6 hourly UTC time interval from **a.** 0000 UTC to **d.** 1800 UTC.

For all periods, we see a statistically significant difference in the median cloud top heights using the Mann-Whitney U test, with the range being higher in the summer, as confirmed by a large KS statistic for all periods. Applying the non-parametric Mann-Whitney U test (table 3.5) shows deep convection in June and December to have a significantly different medians ($P = < 0.005$). This is supported by the KS statistic,

which also shows the data to have large differences in their distributions (large D values) at the 5% confidence interval, an artifact of the much higher frequency of cloud tops heights in June. The largest D value is found at 0000. When compared to the boxplots in figure 3.10a, it can be seen that lower quartile in June at 0000 is higher than the upper quartile in December, causing this high D value. This likely relates to the expected more intense convection in June than December.

Time	**Mann-Whitney *P* value**	**KS test *D* value**
0000	< 0.005	0.69
0600	< 0.005	0.37
1200	< 0.005	0.47
1800	< 0.005	0.63

Table 3.3: Mann-Whitney and KS statistics for cloud top heights at 6 hourly periods in June and December 2010

3.3.3 Relative Humidity profiles

Mean vertical clear sky relative humidity profiles are plotted for June (black) and December (red) (figure 3.13) to characterise the study region in order to give background for the analysis in chapters 4 to 6. The vertical profiles are taken from the 6 hourly ERA-Interim profiles classified as being clear sky (0% cloud in the vertical). 5733 completely clear sky profiles are found in June 2010 over the study region, compared to 34008 in December 2010, representative of the much greater cloud frequency in the summer season. Mean relative humidity is presented with one standard deviation.

In June, the vertical profile generally shows an increase in RH with height up until ~600 hPa, whereas an increase is seen up to ~700 hPa in December. Above this, the RH profile shows a strong decrease over a short distance in both June and December up to ~400 hPa in June and ~550 hPa in December. From these points an increase in RH is seen up to ~100 hPa in both profiles. A peak is seen in both months at all time periods at 100 hPa. Overall, at all time periods, below 150 hPa vertical RH is higher in June than December. This may be due to the higher frequency of convective events and subsequent dissipation of these clouds in June than December acting as a greater source of water vapour. Relative humidity is higher in December than June in all time periods above 150 hPa. It was found by Seidel *et al.*, (2001) that the tropical tropopause is found to be higher and at a lower pressure in December than June over the tropics. With December being the dry season, the relative humidity profile is drier, but due to a higher tropopause height, the ~150 hPa level in June is likely to be found in the stratosphere. The fact that this region of higher humidity in December between the two profiles may be due to the stratosphere being drier. Further, above this region, at ~100 hPa, the profiles tend towards the same value, suggesting both are now occupying the drier stratosphere. At most points in the vertical profiles there is some overlap in standard deviations, though this minimal overlap would suggest the general pattern to be robust.

The difference between the RH profiles at each time step are shown in figure 3.14. The largest difference in the peak mean humidity between the two months is at 1200 (figure 3.14c). In June, peak humidity is 69% ($\sigma = 21\%$) at 1200, compared to 84% ($\sigma = 23\%$) in December. The largest difference is found at 0600, where we see a difference of 36% at 550 hPa. This results from the shape of the vertical RH profile, where between ~600 hPa and ~300 hPa we see a decrease in RH with height, with this occurring higher in the atmosphere in June than December.

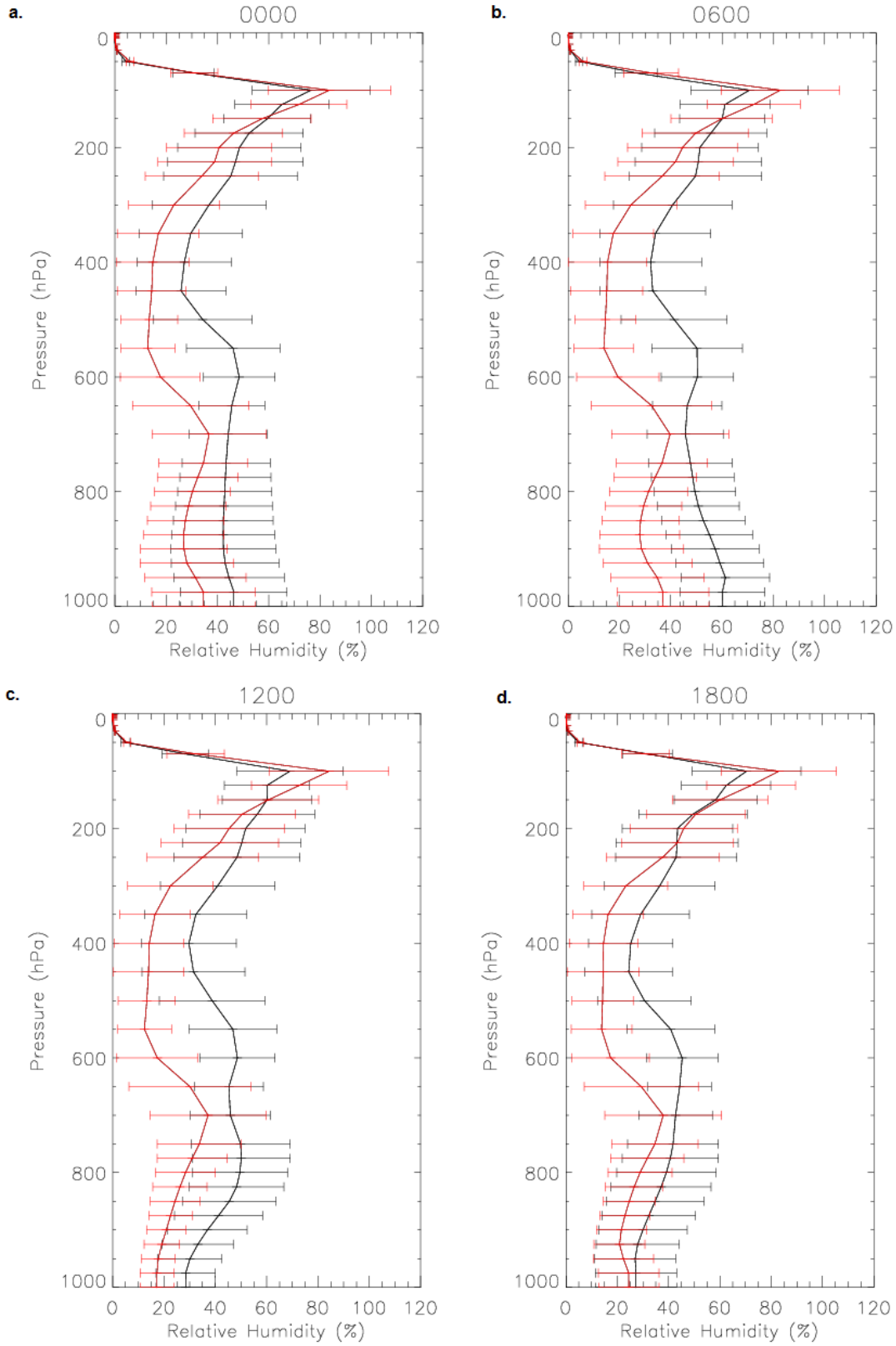

Figure 3.13: Vertical mean clear sky relative humidity profiles for June (black) and December (red) 2010 at 6 hourly intervals from **a.** 0000 UTC to **d.** 1800 UTC. The error bars are one standard deviation.

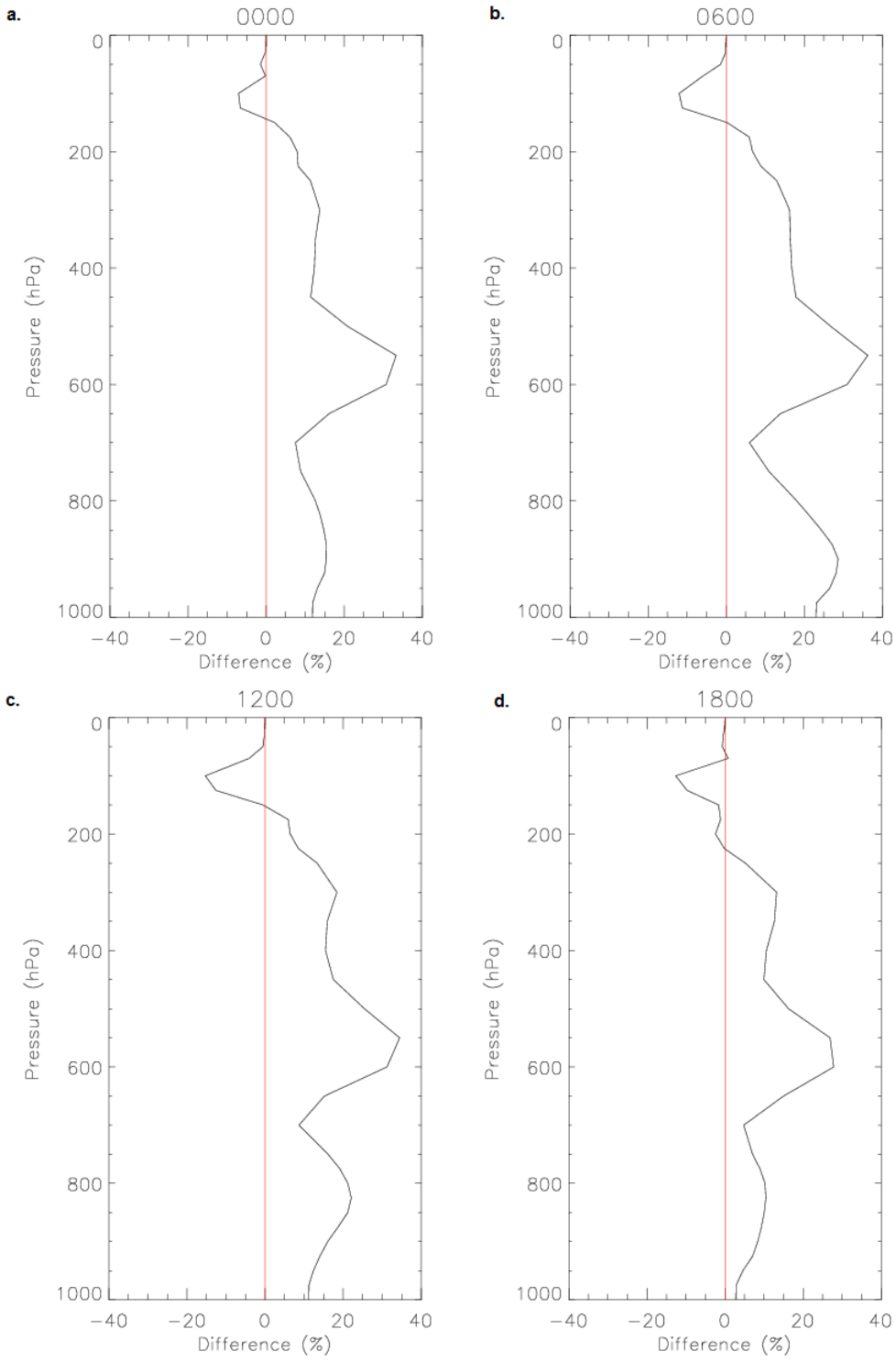

Figure 3.14: Differences in the vertical mean clear sky relative humidity profiles between June and December 2010 at 6 hourly intervals from **a.** 0000 UTC to **d.** 1800 UTC.

3.4 Summary

A summary of the large scale meteorological controls on deep convection over Tropical Africa has been given and the seasonality of these controls. The temporal and spatial patterns of deep convection in ERA-Interim are shown and confirm their agreement with findings by Chung *et al.,* (2007) and Schröder *et al.,* (2009). Temporally, a peak in convective frequency was found at ~1400 LST, whilst the spatial pattern broadly correlated with the orography of the region and the large scale dynamics of this region. This has been followed by a characterisation of the cloud top heights over the study region and the intensity of the deep convection here, in relation to the time of day and seasonality. The findings broadly confirm the diurnal and seasonal behavior expected from chapter 1.

Finally, a characterisation of the clear sky relative humidity profiles over the diurnal cycle for both June and December have been given to diagnose any differences as a function of time of day and season. This has allowed for a baseline with which to compare the results of the observation based study to follow.

Chapter IV

Detecting Deep Convection

4 Cloud Detection

A prerequisite to understanding the response of UTH and OLR to deep convection is the ability to detect this cloud type. Detection schemes are often applied to satellite imagery to isolate particular atmospheric phenomena, including deep convective cloud and associated detraining cirrus.

Top of atmosphere (TOA) radiances measured by geostationary satellites such as SEVIRI are particularly useful for tracking fast moving or developing phenomena such as clouds. As discussed in chapter 2, geostationary satellites have the advantage of a high temporal resolution, potentially providing detailed information on the lifecycle of clouds, but have a relatively low spatial resolution. The combination of radiances measured by these types of satellites, with information from low Earth orbiting satellites (LEO's) such as CloudSat and CALIPSO with their different spatial and temporal characteristics, provide the opportunity for robust analysis of cloud properties.

In order to detect deep convective and cirrus clouds in this study, brightness temperature difference (BTD) thresholding techniques are used. A brief discussion on the theory and background of this method is given in this chapter. To understand the sensitivity of TOA brightness temperatures to some key deep convective cloud properties such as cloud top height, thickness and optical depth, and the implications of changes in these for the BTD thresholds used in this study, a sensitivity test of the response of the TOA brightness temperatures to these is conducted. The brightness temperature modelling is initially conducted for a representative case study in June 2010 to determine the sensitivity of brightness temperatures to a change in viewing zenith angle. Based on the results of this sensitivity test, TOA brightness temperatures are also modelled for all deep convective profiles in June 2010. This is followed by an analysis and discussion of the results. The modelled thresholds are then used as a guide to determine BTD thresholds through colocated spatial and temporal matching between SEVIRI BTD's and CloudSat cloud classifications, using the cloud classification dataset described in chapter 2. The most appropriate threshold for deep convection detection is determined using probability tests including skill scores and receiver operating characteristic (ROC) curves similar to Roebber (2009). These are based on the results of a colocated match-up, with a characterisation of the convective cloud properties detected by CloudSat given as context for the thresholds chosen. The same method of probability testing is also applied to CloudSat and SEVIRI matchups in December 2010 to determine the robustness of the detection method to a season with a markedly different convective regime (see chapter 3). To determine the response of clear sky UTH and the corresponding clear sky OLR to deep convection, cirrus cloud also need to be detected and masked to minimise the contamination of clear-sky pixels by upper level cloud. To determine suitable thresholds for cirrus detection and the sensitivity of TOA brightness temperatures to cirrus cloud properties, the same method of modelling, colocated matchup and threshold determination is applied to the 10.8 and 12.0 μm wavelength band differences.

4.1 Background and Theory

High clouds tops in geostationary satellite images are characterised by lower temperatures in the thermal infrared and higher reflectivity in the solar radiation channels than clear sky areas (as can be seen in figure 2.5, section 2.2.3). Optically thick clouds, such as the core of deep convective clouds, can be considered to radiate as a blackbody with emitted and measured radiances coming from the cloud top. Hence optically thick clouds, such as a deep convective core have a brightness temperature that can be assumed to be the thermodynamic cloud top temperature. Measurement of satellite received channel radiances, conversion into brightness temperatures (BT) using equation 2.11, and application of the appropriate channel filter function allows for the detection of a number of different cloud types and their microphysical properties through the development of brightness temperature thresholds.

Early detection studies have shown that through using the infrared brightness temperature in the window region (10.8 to 12.0 μm) a brightness temperature threshold can be set, typically between 208 K and 260 K depending on the spatial resolution of the instrument and the time of the analysis, to act as a proxy for deep convective cloud detection (for example: Shenk *et al.,* 1976; Maddox, 1980; Chen and Houze Jr., 1997). Vila *et al.,* (2008) claim the setting of such a threshold to be arbitrary, but most studies using this method have set thresholds below 260 K. Chen and Houze Jr. (1997) find the threshold to be temporally variable dependent on the time of day. The brightness temperature varied between <208 K for clouds developing in late afternoon and peaking in extent in the early hours of the morning. The brightness temperature threshold was found to increase for clouds maturing in the early afternoon, having a threshold of 208-235 K, agreeing with the temperature threshold found by Velasco and Fritsch (1987). The threshold then increased further with clouds maturing in the early evening having a threshold range of 235 K-260 K. This method is still commonplace in cloud detection studies (e.g. Fiolleau and Roca, 2013; Konduru *et al.,* 2013). For example Konduru *et al.,* (2013) use a probability distribution of 10.8 μm infrared brightness temperatures to determine cloud type (deep convective or not deep convective).

The BT's at two different wavelengths can also be used to develop BTD thresholds. Use of the difference between the water vapour channels is a common method used for detecting intense deep convection reaching the upper troposphere and overshooting into the lower stratosphere. This method is used in this study to detect deep convection, using the difference between 6.2 μm and 7.3 μm water vapour channels of SEVIRI ($BTD_{6.2\text{-}7.3}$).

The ability of BTD thresholds to act as a detection method for cloud types is a consequence of the weighting functions of each wavelength band in SEVIRI, making the temperature threshold less arbitrary. Each wavelength band of SEVIRI is sensitive to certain atmospheric constituents such as gases, cloud and aerosol, and their vertical distribution, as well as temperature and pressure (Soden and Fu, 1995). Specifically, in a clear sky the radiances measured in the 6.2 μm channel are emitted mostly in the upper troposphere, relating to the water vapour present between 200 and 500 hPa as it is located at the centre of a strong water vapour absorption band (Soden *et al.,* 2005). In clear sky conditions, this channel can be used to infer the spatial and temporal distribution of water vapour in the clear sky surrounding cloudy regions (chapter 6) (Tian *et al.*, 2004). In a clear sky, radiances measured in the 7.3 μm band are contributed to mostly by the middle troposphere by water vapour between 400 and 600 hPa (Ackerman, 1996).

Both the 6.2 and 7.3 μm bands are strongly attenuated by clouds, and the BT measured by SEVIRI will be affected to a different degree in each band dependent on the cloud height and thickness (Shenk *et al.,*

1976). This threshold is based on the near blackbody appearance of optically thick and vertically deep clouds. As the cloud grows in the vertical extent reaching the tropopause the emitted TOA radiances will be roughly equal meaning the $BTD_{6.2\text{-}7.3}$ will tend towards zero. Optically thinner clouds will be less representative of a blackbody and hence at TOA one would expect a contribution to the 7.3 μm band from a lower, warmer level in the atmosphere resulting in a more negative $BTD_{6.2\text{-}7.3}$. Analysis of brightness temperature differences between the water vapour bands by Lensky and Rosenfeld (2008) and Barbosa *et al.,* (2011) using SEVIRI suggest a difference of -2 K or greater between the 6.2 μm and 7.3 μm bands will allow for detection of intense deep convective clouds. For comparison, clear sky $BTD_{6.2\text{-}7.3}$ will tend towards -20 K.

In this study, the analysis of the temporal response of UTH and OLR to deep convection will require a consideration of the cloud lifecycle, as discussed above. A -2 K threshold will allow for detection of intense convection in the mature stage of the clouds lifecycle as the clouds vertical extent reaches the tropopause, but to understand the UTH and OLR response over the clouds lifecycle we need to consider the growth/development stage of the cloud as discussed in chapters 1 and 3. Santurette *et al.*, (2009) find a $BTD_{6.2\text{-}7.3}$ of between -10 K and -5 K to be representative of this stage due to the cloud not reaching the tropopause at this part in its lifecycle. A threshold of a similar magnitude is also found by Mecikalski *et al.,* (2010) who find a mean $BTD_{6.2\text{-}7.3}$ of -6.6 K with a standard deviation of 5.94 K to be suitable for detecting growing deep convective clouds in the earlier stage of their lifecycles. If the intensity of the vertical updraft creating the deep convection is strong, the cloud may be found to overshoot into the stratosphere. In this instance a positive $BTD_{6.2\text{-}7.3}$ will be necessary to detect overshooting deep convection. This relates to the vertical temperature profile of the atmosphere, which increases with height in the stratosphere and the presence of stratospheric water vapour absorbing radiation emitted from the cold cloud top re-emitting infrared radiation at a warmer stratospheric temperature. This BTD method therefore provides a good indicator of the age and presence of the deep convective core where the strongest updrafts are occurring, and the possible height/strength of the convection based on the proximity of the $BTD_{6.2\text{-}7.3}$ to 0 K.

Another potentially important control on UTH is cirrus cloud, due to the evaporation of ice particles as discussed in chapter 1. Cirrus clouds are generally found above an altitude of 6 km and cover between 21 to 33% of the tropics at any one time (Wylie *et al.*, 2005; Mace *et al.,* 2006; Krebs *et al.*, 2007). Due to the semi-transparent nature of cirrus clouds, the BTD between the infrared 10.8 μm and 12.0 μm bands can be used for their detection. Known as the split-window method, the $BTD_{12.0\text{-}10.8}$ is a common method for the detection of the aforementioned cloud type (for example, Inoue, 1987; Kriebel *et al*, 2003; Krebs *et al.*, 2007; Lensky and Rosenfeld, 2008).

Physically, the $BTD_{12.0\text{-}10.8}$ method is based on the difference between the single scattering properties of ice and differential water vapour absorption at these wavelengths (Inoue, 1987; Krebs *et al.*, 2007). If the 10.8 μm and 12.0 μm channels are used in isolation there is a lack of contrast between clear sky and clouds within the satellite imagery. Cirrus detected in the infrared channels may have a high brightness temperature due to their low effective emissivities making the discrimination between the surface, low level cloud and cirrus difficult in a single band (Roca *et al.,* 2002). Therefore the difference between the 12.0 μm and 10.8 μm bands is used to differentiate clear from cloudy pixels. Cirrus cannot generally be considered as blackbodies and a contribution from the surface emissivity is seen, and has to be considered in radiative transfer modelling of cirrus.

Studies show a range of $BTD_{12.0\text{-}10.8}$ have been found for cirrus detection. Inoue (1987) finds a $BTD_{12.0\text{-}10.8}$

of -2.5 K or less to be representative of all cirrus, with $BTD_{12.0\text{-}10.8}$ above this representative of clear skies whilst Lensky and Rosenfeld (2008) show a difference of -4 K and below will allow for detection of cirrus cloud using this method. Negri *et al.,* (2012) find a range based on the cirrus type, with $BTD_{12.0\text{-}10.8}$ between -1 and -4 K found for thick cirrus and -5 K and less being thin cirrus. As with the $BTD_{6.2\text{-}7.3}$, a $BTD_{12.0\text{-}10.8}$ of 0 K indicates the top of a high, deep convective cloud, for the same reasons described above. The cirrus detection threshold can then be applied along with $BTD_{6.2\text{-}7.3}$ to SEVIRI imagery in an effort to mask cloud cover in the upper troposphere.

To determine a the sensitivity of TOA brightness temperatures and to determine a range of sensible threshold values, a sensitivity analysis is performed using the SBDART model introduced in chapter 2. SEVIRI waveband radiances are modelled for clear sky, deep convective and cirrus profiles to determine a likely appropriate range of BTD's for deep convection and cirrus detection.

4.2 Modelling of TOA Brightness Temperatures

To provide an understanding of the perturbation a deep convective cloud layer has on TOA radiances, both clear sky and cloudy TOA brightness temperatures were modelled using the SBDART model introduced in chapter 2. Total upward radiances between 4.0 μm and 15.0 μm in 0.1 μm increments were simulated at 50 km (taken to be the TOA). Radiances in the SEVIRI 6.2 μm, 7.3 μm, 10.8 μm and 12.0 μm bands were converted to brightness temperatures with the application of their respective SEVIRI filter functions using the equation 2.11. ERA-Interim profiles input to the model consisted of vertical pressure, height, temperature, water vapour density (g m^{-3}) and ozone density (g m^{-3}), taken from the Gaussian gridded ERA-Interim atmospheric pressure level profiles described in Chapter 2. For clear sky modelling all ERA-Interim profiles with a 0% cloud cover in the vertical in June 2010 at 1200 and 0000 UTC between 0°N to 15°N latitude and 10°E to 40°E longitude were used. For modelling deep convection, all profiles with continuous vertical cloud cover with a minimum height of 6 km was considered deep convection (based on Suzuki *et al.,* 2011). The vertical ERA-Interim profiles at 1200 and 0000 only were used due to temporal constraints of the CloudSat 2B-CLDCLSS product that will be used within the BTD threshold testing process discussed later in this chapter.

4.2.1 Clear Sky

The results of the modelled clear sky BT's in the 4 SEVIRI channels used in this study are seen in table 4.1. A difference of 2.2 K is found between mean 12.0 μm and 10.8 μm band brightness temperatures. This is a result of the greater clear sky transmissivity of 10.8 μm brightness temperatures from the surface to the TOA, with greater preferential absorption of the 12.0 μm brightness temperatures by water vapour. The 6.2 μm brightness temperature is lower than that of the 7.3 μm brightness temperature, due to the peak of the 6.2 μm channel weighting function being in the upper troposphere.

Wavelength Band (μm)	Mean BT	Standard Deviation	Minimum	Maximum
6.2	242.6	2.6	238.2	248.3
7.3	264.9	3	259.9	270.3
10.8	299.2	5.1	294.9	316.3
12.0	297	5.4	291.8	314.6

Table 4.1: Modelled mean clear sky brightness temperatures (K) in the wavelength bands used in this study for all clear sky periods at 0000 and 1200 UTC June 2010.

As expected from table 4.1, a mean $BTD_{6.2\text{-}7.3}$ of -22.3 K (σ = 2.2) is seen for clear skies in June 2010 (table 4.2). The range of $BTD_{6.2\text{-}7.3}$ from -26.7 K to -19.5 K relate to the variations in clear sky humidity in the vertical profile, with a moister upper troposphere having a more negative $BTD_{6.2\text{-}7.3}$. From the vertical profiles presented in chapter 3 (figures 3.13 and 3.14), the little change evident in the profiles over the diurnal cycle suggest that small change will be seen in these values of $BTD_{6.2\text{-}7.3}$ over the day. It can also be surmised from the vertical profiles in chapter 3 that December may possess higher 6.2 μm and 7.3 μm values due to the lower humidity values, but similarly show less change over the diurnal cycle.

Mean $BTD_{6.2\text{-}7.3}$	Standard Deviation	Minimum BTD	Maximum BTD
-22.3	2.2	-26.7	-19.5

Table 4.2: Modelled clear sky $BTD_{6.2\text{-}7.3}$ (K) for June 2010.

When considering $BTD_{12.0\text{-}10.8}$ for clear-skies in June 2010, values range from -3.2 K to -0.78 K (table 4.3). This suggests that observed $BTD_{12.0\text{-}10.8}$ below -3 K may be indicative of the presence of cirrus cloud. This is similar to the value used by Lensky and Rosenfeld (2008) for cirrus detection with SEVIRI.

Mean $BTD_{12.0\text{-}10.8}$ (K)	Standard Deviation	Minimum BTD (K)	Maximum BTD (K)
-2.2	0.7	-3.2	-0.78

Table 4.3: Modelled clear sky $BTD_{12.0\text{-}10.8}$ for June 2010.

4.2.2 Modelled TOA Brightness Temperatures - Deep Convection

Firstly, a case study is analysed to test the sensitivity of the two thresholds to a change in the cloud properties at viewing zenith angles between 0° and 50° (50° being the greatest viewing zenith angle over the study region). The model baseline parameters are shown in table 4.4. For each simulation one parameter was varied per run, with all other parameters kept constant. Optical depth at 0.55 μm ($\tau_{0.55\mu m}$) was varied between 60 and 180 in increments of 10 with optical depth uniformly distributed over the cloud. $\tau_{0.55\mu m}$ values are taken from Fischer *et al.*, (2000) and the International Satellite Cloud Climatology Project (ISCCP) (2014). Cloud top heights were varied between 7 km and 16 km, with this covering the range of cloud top heights measured by CloudSat for this specific cloud (figure 4.1a).

Cloud top height (km)	Cloud base height (km)	$\tau_{0.55}$	r_e	Phase
10	1	100	33	Water

Table 4.4: Baseline model parameters for a deep convective cloud layer in SBDART.

4.2.3 Case Study - 2nd June 2010

The case study is of a large deep convective cloud in the mature stage of its lifecycle, evident from the shape of the cloud - the distinctive anvil shape seen on 2nd June 2010 at 23:54-23:57 (CloudSat overpass time) (figure 4.1a and b).

The anvil structure of the cloud is classified by the cloud classification algorithm as Altostratus (classified as blue in the classification imagery) rather than the same deep convective cloud (classified as pink in the classification imagery). The detraining high cloud, characteristic of the dissipation seen in the later stages of a clouds lifecycle is also seen further out from the core towards the end of the anvil. The TOA $BTD_{6.2\text{-}7.3}$ measured by SEVIRI is also shown for the same cloud system, with the CloudSat path represented by the black line (figure 4.1d). The $BTD_{6.2\text{-}7.3}$ of the deep convective core is around -3 K. In comparison to the MODIS 11 μm imagery (figure 4.1c) the highly reflective area (between 5° and 10°) is much larger than the part of the system classified as deep convection by CloudSat. This area, corresponding to a lower $BTD_{6.2\text{-}7.3}$ than that of the core in figure 4.1d, is thick anvil cloud. The more fibrous edges of the system seen in figure 4.1c have a $BTD_{6.2\text{-}7.3}$ of around -7 K and are likely to be detrained anvil or cirrus.

In order to gain a general understanding of the spectral response of TOA brightness temperatures to a deep convective cloud, a comparison is made with the brightness temperatures seen for a clear profile (figure 4.2). The clear sky profile is from the same CloudSat track. The spectral response functions (SRF) for the two SEVIRI water vapour bands are also shown. When compared to clear sky brightness temperatures over the spectral range shown, a much flatter spectral response is seen with the presence of deep convection.

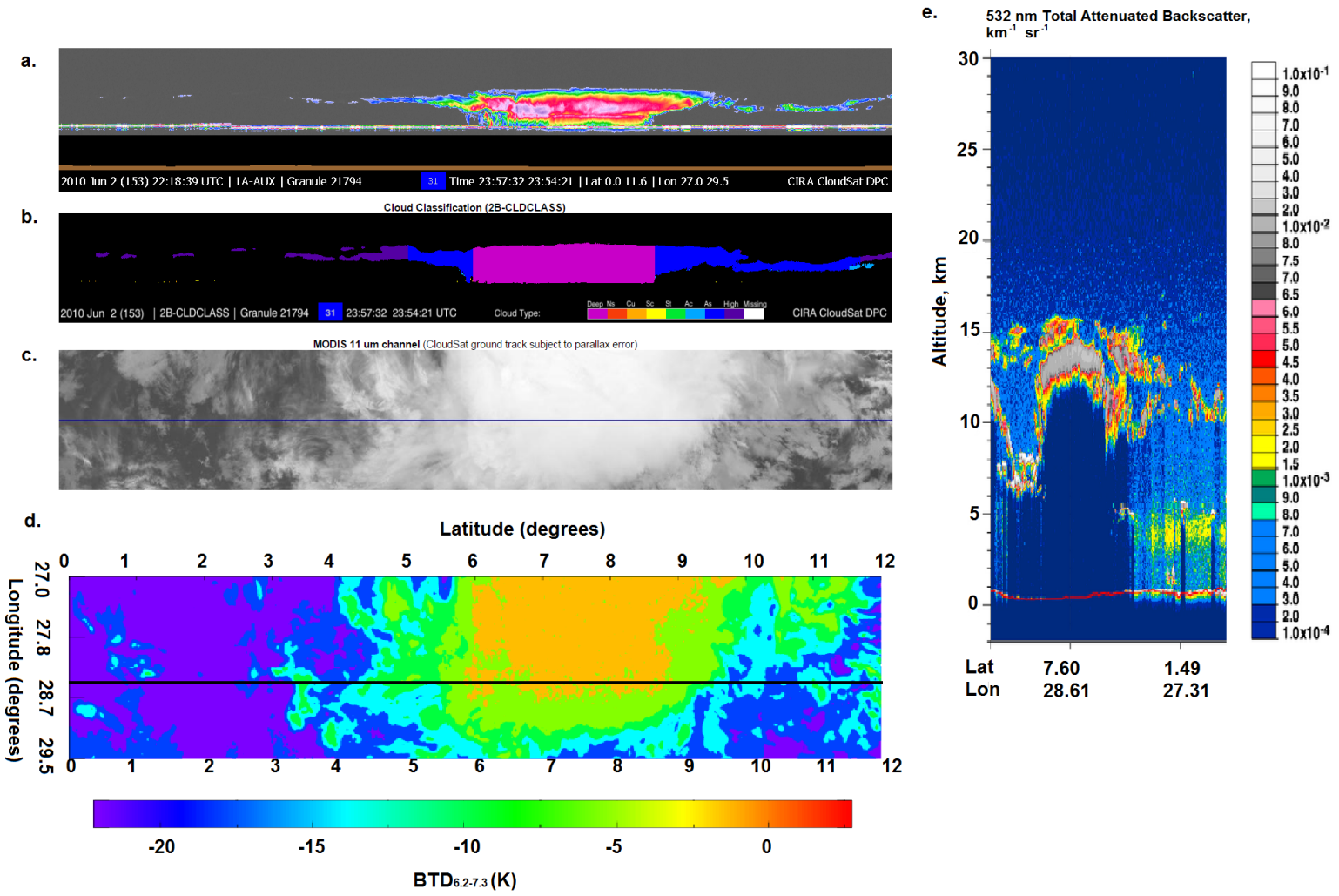

Figure 4.1: An example of a deep convective cloud system at 23:54-23:57 on June 2nd 2010, between 0°-11.6° N and 27°-29.5° E. **a)** The 'quicklook' along track CloudSat reflectivity profile of the cloud system as classified by CloudSat. The vertical dimension is the height, the horizontal dimension being the along track path. **b)** The same cloud system as classified into cloud types based on microphysical parameters by the CloudSat 2B-CLDCLASS algorithm. This shows the deep convective cloud (pink) with accompanying altostraus (blue) and high clouds (purple). The anvil shape of the cloud, with detraining altostratus around a core of deep convection, classifies this as cloud as being in the mature stage of its lifecycle. **c)** The MODIS 11 µm swath along the path giving a cloud top view of the deep convective system. This is provided with the quicklook imagery. The y-axis is the longitude, the x-axis is the latitude, both in degrees. **d)** SEVIRI TOA $BTD_{6.2\text{-}7.3}$ for the same cloud. The black line represents the direction of CloudSat's overpass path. The y-axis is the longitude, the x-axis is the latitude, both in degrees. **e)** The 532nm attenuated backscatter profile of the convective system as measured by CALIPSO. The y-axis is the vertical height in km. The x-axis the latitude and longitude of the CALIPSO track. Sources: CloudSat (2010), CALIPSO (2013).

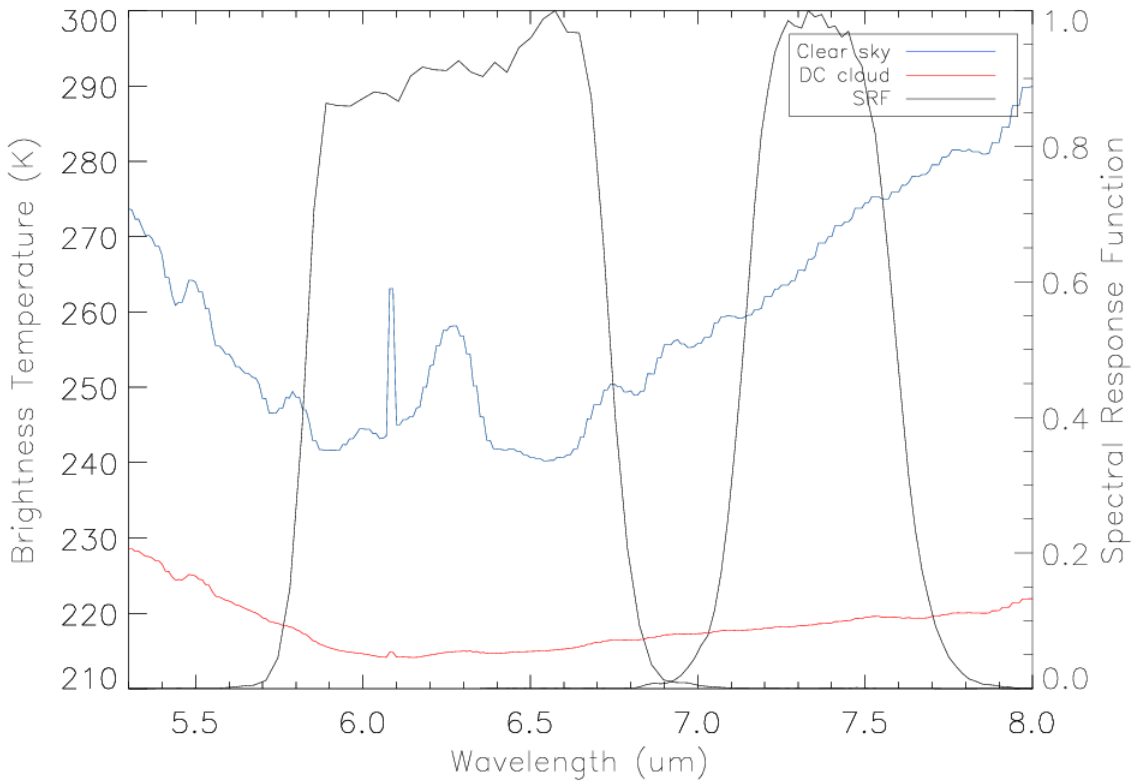

Figure 4.2: The response of modeled TOA brightness temperatures to a clear sky profile and a profile containing a deep convective cloud. Brightness temperatures are modelled between 4 and 15 µm. Both profiles were taken from 2nd June 2010. Red is deep convection, blue is the clear sky profile. The spectral response functions (SRF) of the two SEVIRI water bands are also given (black lines).

4.2.4 Cloud Top Height and Thickness

The response of TOA BT's to a change in cloud top height was modelled for the case study. From large negative thresholds with lower cloud top heights, $BTD_{6.2\text{-}7.3}$ becomes less negative with an increase in cloud top height, tending towards 0 and then becoming positive with increasing cloud top height (figure 4.3). These thresholds above 0 K are representative of overshooting deep convection reaching the stratosphere. Though still positive, $BTD_{6.2\text{-}7.3}$ becomes slightly less positive at a height of 16 km.

The range of $BTD_{6.2\text{-}7.3}$ found in this sensitivity test are in agreement with the majority of values found in the literature at cloud heights of 9 km and above. Below this height, $BTD_{6.2\text{-}7.3}$ becomes much more negative than that found by Lensky and Rosenfeld (2008). Based on the characteristic cloud lifecycle definition given in chapter 1 and the definition of deep convection from Suzuki *et al.,* (2011), continuous cloud with a cloud top height at 6 km is representative of deep convection in the early stage of its life cycle. This initial result suggests that a more negative $BTD_{6.2\text{-}7.3}$ may be necessary to detect deep convection from the early stages in the lifecycle when cloud tops are ~7 km.

When comparing the sensitivity of $BTD_{6.2\text{-}7.3}$ to cloud top heights and the viewing zenith angle it is clear that the strongest control on $BTD_{6.2\text{-}7.3}$ is the cloud top height. A range of 9.6 K is seen between $BTD_{6.2\text{-}7.3}$

at 7 km (most negative $BTD_{6.2\text{-}7.3}$) and 13 km (most positive $BTD_{6.2\text{-}7.3}$) at 0° viewing zenith. This range is slightly larger at a 50° viewing zenith, increasing to 10.26 K.

There is much less sensitivity in $BTD_{6.2\text{-}7.3}$ with respect to viewing zenith angle. The maximum range in $BTD_{6.2\text{-}7.3}$ as a result of different viewing zenith was seen at 7 km, where a 0.46 K difference between 0° and 50° was found, ranging between -8.5 K (σ = 2.07) at 0° viewing zenith angle and -8.96 K (σ = 2.24) at 50° viewing zenith angle. The smallest range over viewing zenith is seen at 13 km, with a difference of 0.2 K found over a range of 50°. This is also the most positive $BTD_{6.2\text{-}7.3}$, ranging from 1.1 K (σ = 0.05) at 0° viewing zenith to 1.3 K (σ = 0.03) at 50°. The $BTD_{6.2\text{-}7.3}$ is seen to become less negative as zenith angle is increased. The increases in path length with an increase in zenith leads to differential absorption and re-emission, which results in the $BTD_{6.2\text{-}7.3}$ tending towards less negative values.

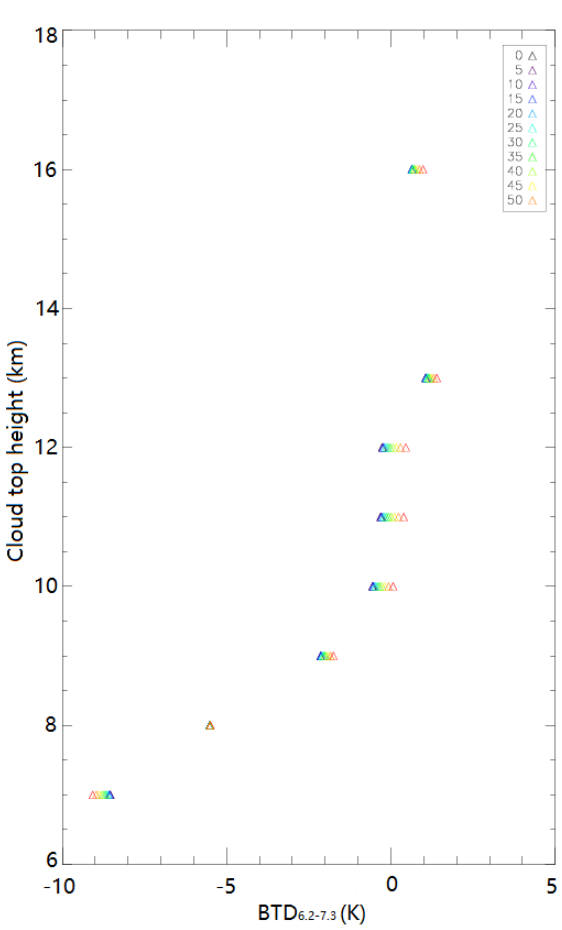

Figure 4.3: The response of modelled $BTD_{6.2\text{-}7.3}$ to a change in cloud top height (km) for a single convective event on June 2nd 2010 (CloudSat overpass: June 2nd at 23:54-57), with a changing zenith angle in increments of 5° between 0° and 50° (see legend, where the number represents the viewing zenith angle in degrees).

4.2.5 Cloud Optical Depth

Little sensitivity in TOA $BTD_{6.2\text{-}7.3}$ is seen with a change in both optical depth and zenith angle (figure 4.4). The maximum range in $BTD_{6.2\text{-}7.3}$with a change in optical depth is found at a viewing zenith angle of 0°.

The $BTD_{6.2\text{-}7.3}$ ranges from -1.09 K with an optical depth of 60 to -0.25 K at 180, a range of 0.84 K. Due to the range of optical thickness of the modelled cloud, ranging between 60 and 180, almost no variation in $BTD_{6.2\text{-}7.3}$ would be expected. This is due to the exponential relationship between optical depth and transmissivity. It is therefore evident that the brightness temperatures are much more sensitive to a change in cloud top height when optical depths are this large. $BTD_{6.2\text{-}7.3}$ found in the range of optical depth tested in this sensitivity analysis are within the range expected from the literature and similar to that found by Lensky and Rosenfeld (2008).

As before, $BTD_{6.2\text{-}7.3}$ becomes less negative with increasing zenith angle. For an optical depth of 60, $BTD_{6.2\text{-}7.3}$ ranges between -1.08 K (σ = 0.21) at 0° viewing zenith and -0.43 K (σ = 0.21) at 50° viewing zenith. For an optical depth of 180, $BTD_{6.2\text{-}7.3}$ ranges between -0.25 K (σ = 0.15) at 0° viewing zenith and 0.14 K (σ = 0.18) at 50° viewing zenith (figure 4.4).

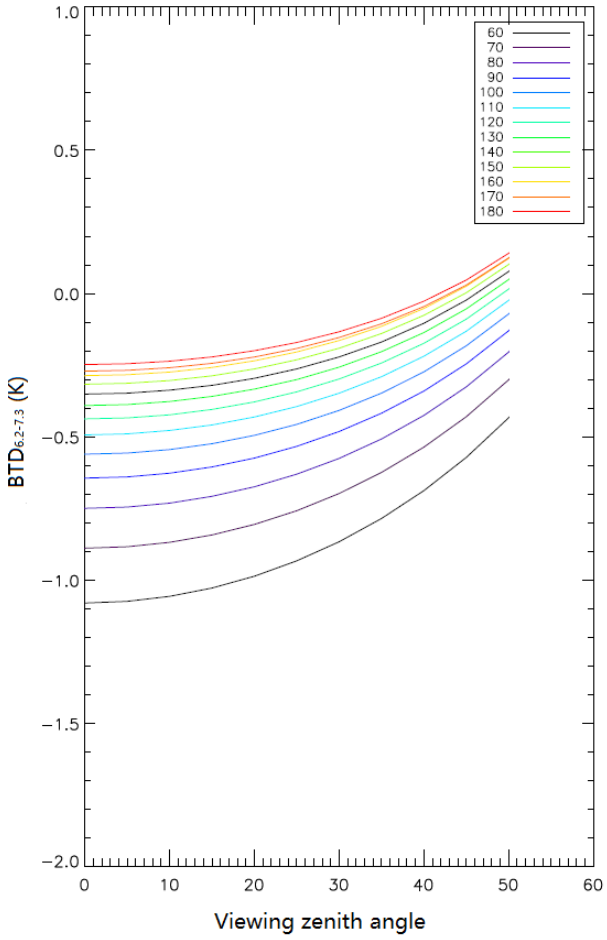

Figure 4.4: The response of $BTD_{6.2\text{-}7.3}$ over a range of viewing zenith angles, for a change in cloud optical depth (see legend) for the single convective event on June 2nd 2010 (CloudSat overpass: June 2nd at 23:54-57), with a changing zenith angle.

It is expected that due to the cloud being so optically thick the $BTD_{6.2\text{-}7.3}$ would show very little sensitivity

with a change in optical depths. This is not seen in the modelling study above where some, albeit very small, variation is seen with optical depth. To further test the sensitivity of TOA $BTD_{6.2\text{-}7.3}$ to a change in optical depth, $\tau_{0.55}$ of 5, 10 and 20 were also modelled (figure 4.5). $BTD_{6.2\text{-}7.3}$ was found to increase from -8.9 K to -4.5 K with a change in optical depth between 10 and 20 at a viewing zenith of 0°, representing a change 4.4 K. This shows that at lower optical depths there is much greater sensitivity to cloud optical thickness than at the larger optical depths found with deep convective clouds.

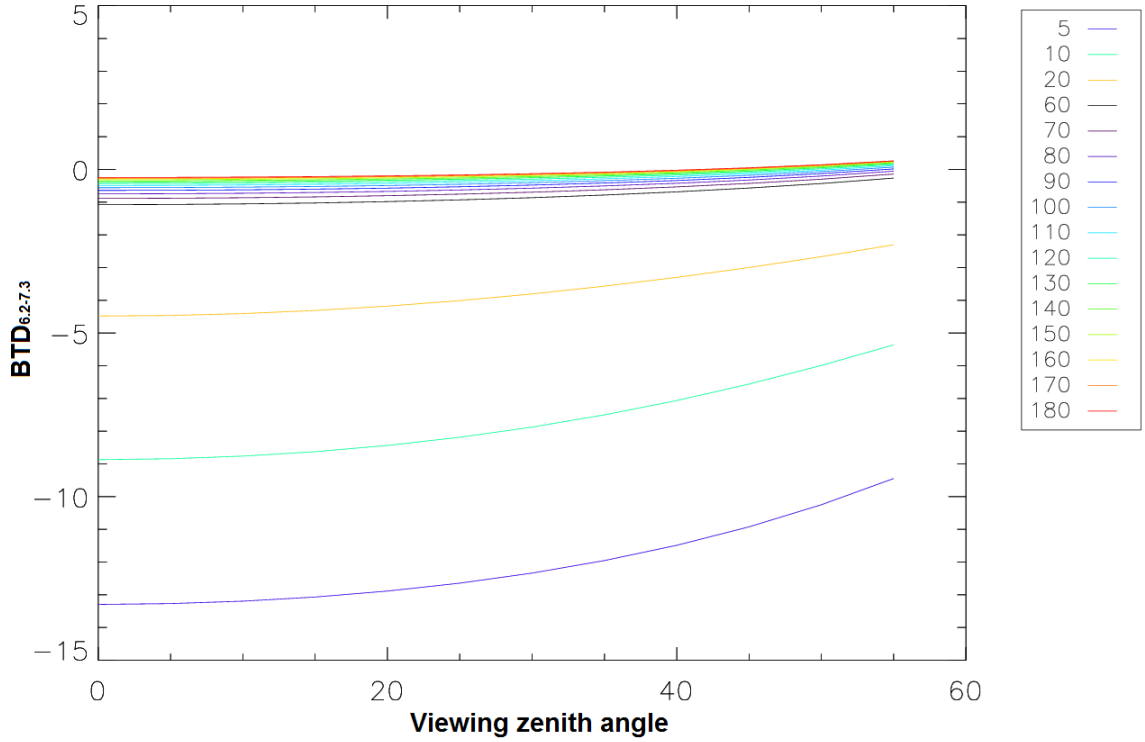

Figure 4.5: The response of $BTD_{6.2\text{-}7.3}$ over a range of viewing zenith angles, for a change in cloud optical depth as shown before (see legend) with further smaller optical depths modelled for the single convective event on June 2nd 2010 (CloudSat overpass: June 2nd at 23:54-57), with a changing zenith angle.

It may also be assumed that the small changes in $BTD_{6.2\text{-}7.3}$ may be due to the cloud not being at the tropopause. The modelled cloud top height was lower than that of the tropopause, which can be assumed to be at the temperature inversion at 12 km seen in figure 4.6. An optically and vertically thick deep convective cloud with a cloud top at this height would be expected to possess a $BTD_{6.2\text{-}7.3}$ of ~0 K. Therefore at a slightly lower cloud top height the water vapour in the layer above the cloud is expected to absorb and re-emit at a lower 6.2 μm band brightness temperature. This effect would cause the 7.3 μm band brightness temperature measured at the cloud top to be slightly larger than that of the 6.2 μm band, creating a small negative $BTD_{6.2\text{-}7.3}$.

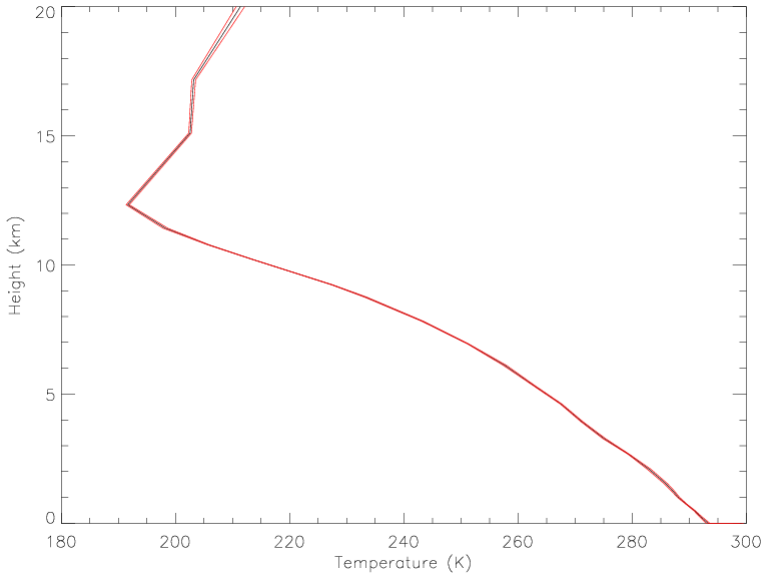

Figure 4.6: Mean vertical temperature profile for the case study on June 2nd 2010 (black line) with ± one standard deviation (red line).

It is evident from the response of the TOA $BTD_{6.2\text{-}7.3}$ to a change in cloud top height, optical depth and viewing zenith angle that $BTD_{6.2\text{-}7.3}$ is most sensitive to a change in cloud top height. Minimum $BTD_{6.2\text{-}7.3}$ for this deep convective cloud was -8.96 K. This is below that found by Lensky and Rosenfeld but similar to that expected for younger, developing cloud. In relation to optical depth the $BTD_{6.2\text{-}7.3}$ is most sensitive to a change in viewing zenith angle rather than further increases in optical depth. Optically thicker clouds do show a cloud $BTD_{6.2\text{-}7.3}$ tending more towards 0 with an increase in viewing zenith angle, but the range in $BTD_{6.2\text{-}7.3}$ between 60 and 180 shows only a small difference when compared to a perturbation in cloud top height. However, in general there is little sensitivity to a change in viewing zenith angle between 0° and 50°. This relates to the thickness of the cloud, whereby the TOA brightness temperatures of thick clouds are contributed to mostly by the cloud top. Note that simulations were also performed to assess the sensitivity of $BTD_{6.2\text{-}7.3}$ to realistic variations in the cloud effective radius but the impact was even smaller than the changes reported due to increasing optical depth. This agrees with previous sensitivity studies by Lensky and Rosenfeld (2008).

4.2.6 June 2010

Since the above results are based on a single case study, it is considered informative to determine whether the same results hold over a range of atmospheric profiles. The $BTD_{6.2\text{-}7.3}$ is modelled for all ERA-interim atmospheric profiles in June 2010 at 0000 and 1200 containing deep convection. Modelling was conducted at a viewing zenith angle at 0° due to the minimal sensitivity to a change in viewing zenith angle shown in the case study above. The relative impact on TOA BT's with the addition of a cloud layer for different cloud top heights and optical depths was modelled following the same method as above and using the same parameter values as displayed in table 4.4. $BTD_{6.2\text{-}7.3}$ was again modelled with respect to r_e (varied between 20 and 33) but again, no sensitivity was shown between these values.

4.2.7 Cloud Top Height

The modelled $BTD_{6.2\text{-}7.3}$ in response to a change in cloud top height followed a similar profile to the case study (figure 4.7). $BTD_{6.2\text{-}7.3}$ is found to become less negative with an increase in cloud top height. Similar to the case study, the minimum mean $BTD_{6.2\text{-}7.3}$ of -7.4 K ($\sigma = \pm 2.4$) is found at a cloud top height of 7 km. The more negative $BTD_{6.2\text{-}7.3}$ found is similar to Santurette *et al.,* (2009), and follow what is expected from deep convective cloud tops earlier in their lifecycles. Based on the earlier ERA-Interim climatology of cloud top heights (chapter 3), it is excepted that these larger negative $BTD_{6.2\text{-}7.3}$ values may allow for the detection of deep convection, confirming the results found in the case study.

The maximum mean $BTD_{6.2\text{-}7.3}$ of 0.89 K ($\sigma = \pm 0.06$) is found at a cloud top height of 13 km. The $BTD_{6.2\text{-}7.3}$ is positive above 13 km, though again, at a height of 16 km a movement of $BTD_{6.2\text{-}7.3}$ back towards 0 K is seen.

All standard deviations are large below 9 km. The small increases in standard deviation at heights above this, particularly those in excess of 13 km are due to small variations in stratospheric water vapour and associated stratospheric emission in the 6.2 micron channel. At lower cloud top heights standard deviations are large due to the influence of tropospheric being water vapour variability in the clear sky profiles above the cloud. Above 9 km, the smallest standard deviations found at a cloud top height of 11 km (mean $BTD_{6.2\text{-}7.3}$ = 0.06 K; $\sigma = \pm 0.04$). This suggests these cloud tops to be close to the tropopause, whereby minimal absorption and re-emission occurs.

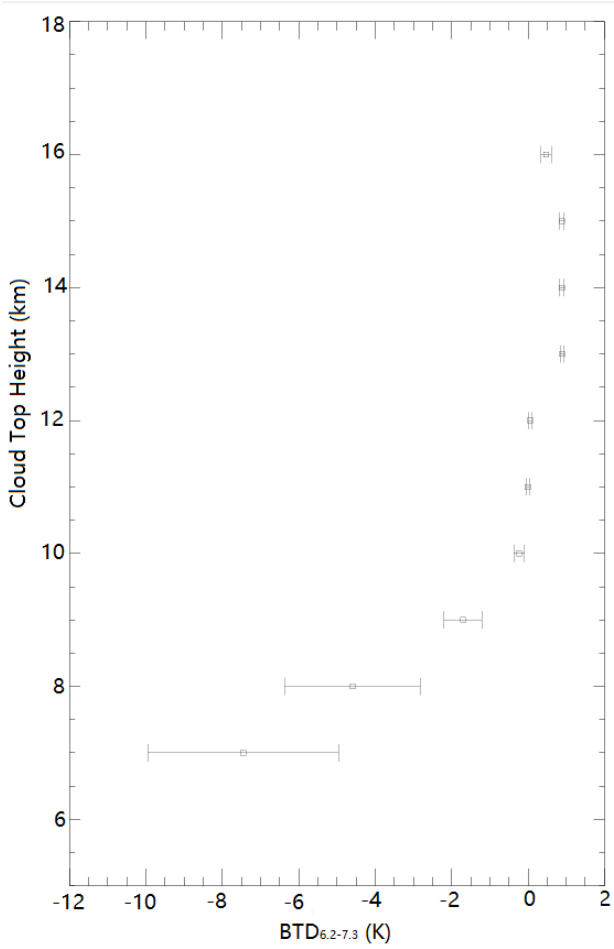

Figure 4.7: $BTD_{6.2\text{-}7.3}$ with one standard deviation for all deep convection profiles in June 2010, modeled with a changing cloud top height.

4.2.8 Cloud Optical Depth

Again, the response of $BTD_{6.2\text{-}7.3}$ to a change in optical depth is similar to that seen for the June case study (figure 4.8). It is again evident that there is only a small difference in the sensitivity of $BTD_{6.2\text{-}7.3}$ to a change in optical depth. The $BTD_{6.2\text{-}7.3}$ tends to 0 K with an increase in the optical depth but overall the sensitivity is very small to any change. As expected, the largest magnitude mean $BTD_{6.2\text{-}7.3}$ were found at an optical depth of 70 (mean = -0.4 K; $\sigma = \pm 0.15$) and smallest at an optical depth of 180 (mean = -0.063 K; $\sigma = \pm 0.13$). The modelled mean $BTD_{6.2\text{-}7.3}$ is higher for all optical depths when averaged over the month of June than for the case study.

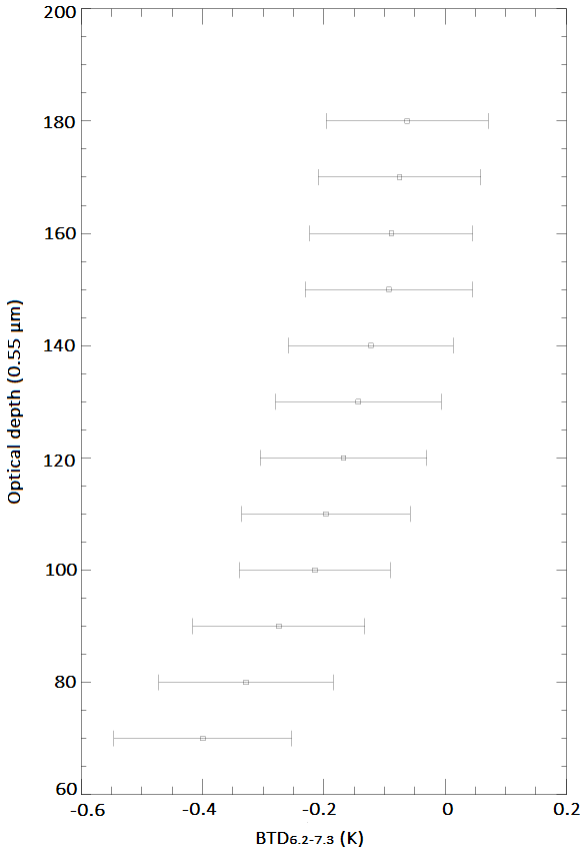

Figure 4.8: $BTD_{6.2\text{-}7.3}$ with one standard deviation for all deep convection profiles in June 2010, modeled with a changing optical depth between 70 and 180.

The sensitivity test confirms that the greatest sensitivity of the $BTD_{6.2\text{-}7.3}$ is seen with a change in cloud top height when optical depths are already very large. Given the range of deep convective cloud top heights over the study region seen in chapter 3, the modelling results show a a $BTD_{6.2\text{-}7.3}$ of -10 K and above would be representative of deep convective cloud over all stages of the cloud lifecycle discussed in chapter 1. This confirms that a response in $BTD_{6.2\text{-}7.3}$ is seen in relation to the stage of the clouds lifetime, with lower thresholds applicable to younger cloud development.

4.3 $BTD_{6.2\text{–}7.3}$ Threshold Determination with CloudSat

The results of the sensitivity study in the previous section highlight the main factors that would be expected to affect the $BTD_{6.2\text{-}7.3}$ and give an idea of the magnitude of the $BTD_{6.2\text{-}7.3}$ thresholds that might be expected. In order to compare the modelled thresholds to an independent set of cloud observations, a colocated spatial and temporal match-up between SEVIRI and CloudSat is performed. The CloudSat 2B-CLDCLASS algorithm cloud classifications discussed in chapter 2 are used as a basis of comparison with SEVIRI BTD's to determine realistic thresholds based on the results of the sensitivity test. The most appropriate threshold to detect deep convection is determined using receiver operating characteristic (ROC) curves and four probability statistics, discussed below. The same method of threshold determination is also applied to deep convective cases in

December. This allows for the robustness of the $BTD_{6.2\text{-}7.3}$ method to be tested on a different season, characterised in chapter 3 as having a markedly different convective regimes in terms of both frequency and cloud top height.

Although the co-located validation allows for a statistical representation of the ability of SEVIRI to detect deep convection when compared to the CloudSat cloud classification data, CloudSat possesses limitations as discussed in chapter 2. Further to these, due to sun-synchronous orbit of the A-Train constellation, CloudSat makes roughly 32 equatorial overpasses each day with the equivalent number of day and night time crossings. These occur at roughly 1:30 am and 13:30 pm local time. As seen in chapters 1 and 3, deep convective cloud frequency and development peaks in the late afternoon between 2 and 4 pm LST (Futyan and Del Genio, 2007), with the mature and decaying stages of the cloud life cycle coming towards the early hours of the morning. Hence using CloudSat in the match-ups as a guide may not allow for the detection of either developing convection in the early stage of its life or the most intense and developed deep convection (cloud tops at their coldest points) and may lead to a $BTD_{6.2\text{-}7.3}$ being developed that may not be representative of all deep convection. For example, the application of a more negative $BTD_{6.2\text{-}7.3}$ may cause a higher number of clouds to be detected which are not deep convection, but are included in the detection as a deep convective cloud based on this classification.

4.3.1 Skill Scores

To quantify the ability of SEVIRI to detect deep convection based on comparisons with CloudSat 2B-CLDCLASS cloud classifications, four key predictability skill scores were calculated. These are based on 2x2 contingency tables (example in table 4.5) and gave a quantification of the agreement between observed (the assumed to be 'truth') data (CloudSat) and the predicted values (SEVIRI $BTD_{6.2\text{-}7.3}$). Here, hits are 'yes' events that were observed and correctly predicted using SEVIRI; false alarms are events that were not observed but were predicted as 'yes'; misses are events that were missed by the prediction but actually occurred in CloudSat; and correct negatives are events that were correctly predicted as not occurring and did not occur.

		Observed Values	
		Y	N
Predicted Values	Y	*Hit*	*False Alarm*
	N	*Miss*	*Correct Negative*

Table 4.5: Description of a 2x2 contingency table used for skill scores. This allows a comparison of agreements and disagreements between predicted and observed values. When an event either occurs or is predicted it is a Yes event; when no event occurs or is not predicted, this is a No event. Y = Yes, N = No.

Use of the contingency table allows for the calculation of the Probability Of Detection (POD, equation 4.1), False Alarm Ratio (FAR, equation 4.2), the Success Ratio (SR, inverse of FAR) and the Critical Success Index (CSI, equation 4.3) for each $BTD_{6.2\text{-}7.3}$ threshold. Through the relationship between hits, misses and false alarms, POD and FAR allows for an understanding of how likely it is that the $BTD_{6.2\text{-}7.3}$ threshold will provide a correct prediction. For events like deep convection the hits are rare compared to the non-events and correct negatives, so the dataset is unbalanced and correct predictions of the correct negatives can be easily made, causing the contingency table to become saturated with high values of correct negatives. These

skill scores were therefore chosen to limit this effect.

The commonly used equations to calculate POD, FAR and CSI are mathematically related and the relationship between them can be geometrically represented in a single chart, allowing for the relationship between them to be easily understood (Roebber, 2009). POD and CSI are positively oriented (the more successful a threshold the higher the POD and CSI), whilst FAR is negatively oriented (the more successful a threshold, the lower the FAR). POD ranges from 0-1, with a perfect forecast equaling 1, and is the fraction of cases where an observed yes-event was both predicted and observed:

$$POD = \frac{Hits}{Hits + Misses} \tag{4.1}$$

A limitation of this statistic is its tendency to reach 1 when the threshold becomes unrealistic. This situation would create a high false alarm rate by over predicting the occurrence of events. For example, for a $BTD_{6.2\text{-}7.3}$ of -20 K and above will detect all deep convection in CloudSat as can be seen from the modelling results of cloudy TOA $BTD_{6.2\text{-}7.3}$, yet be an unrealistic threshold to use as this is representative of a clear sky $BTD_{6.2\text{-}7.3}$ (table 4.2), therefore giving a high false alarm rate. FAR also ranges between 0-1, with 0 being a perfect forecast, i.e. no false alarms.

$$FAR = \frac{FalseAlarms}{Hits + FalseAlarms} \tag{4.2}$$

This statistic allows us to determine the number of false alarms - where deep convection is predicted by SEVIRI but not observed by CloudSat and is the fraction of cases where a yes-event was predicted but not observed. The inverse of this is plotted on the ROC curve, and is known as the success ratio (SR).

The CSI allows us to calculate the number of deep convective cases that were correctly forecast from the fraction that were either forecast or observed. This measure of forecast accuracy does not include correct negatives and is a useful scalar attribute when events are rare:

$$CSI = \frac{Hits}{Hits + Misses + FalseAlarms} \tag{4.3}$$

The objective of this sensitivity testing of the BTD thresholds with skill scores is to increase POD, whilst reducing FAR. When this is not possible, and both begin to increase simultaneously (for example, when the threshold becomes more extreme and more false alarms are given as well as correct positives), the threshold that will be chosen will have the highest CSI. An increase in POD accompanied by an increase in FAR with a higher threshold may give an overestimation of deep convection, but an overestimation of cloud cover will decrease the likelihood that a cloud contaminated pixel is assumed to be clear sky.

To determine the best $BTD_{6.2\text{-}7.3}$ threshold for the purpose of this study, an approach similar to receiver operating characteristic (ROC) curves by Roebber (2009) are used (figure 4.9). These are plots of POD against SR and are used as a test of performance of modeled output against actual values through exploiting the relationship between the POD and FAR. They allow for an a visual inspection of the most successful threshold as well as a statistical representation. Using the success ratio (SR), a perfect forecast will lie in the top right of the plot, with an increase in the accuracy of the prediction represented by a movement of 45° towards the top right corner (POD increasing with a corresponding decrease in FAR). The ROC space represents the trade off between correct predictions and false alarms.

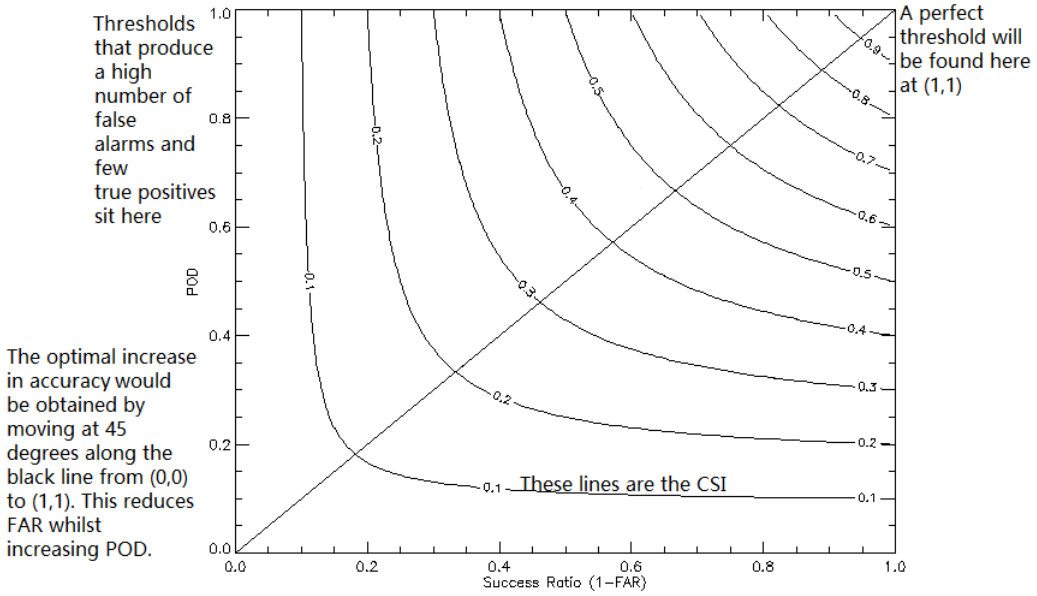

Figure 4.9: Example of a ROC curve used for the determination of the most successful threshold. POD is plotted against SR. A perfect choice of threshold would result in a cluster of points in the top right hand corner of the plot.

4.3.2 Initial Colocated Matchup

An initial colocated matchup was conducted for all periods in June 2010 when CloudSat passed over the study region. CloudSat overpasses were co-located spatially and temporally with SEVIRI data, with the closest SEVIRI pixels compared with the CloudSat cloud classifications. A spatial matchup of the closest pixel within 0.125° of a CloudSat overpass was first used although further sensitivity tests have been performed perturbing the distance between the CloudSat passover and the matched SEVIRI pixel. It was found that fractionally more cases were analysed when the distance between co-locations was increased to 0.25° but no improvement was found in the accuracy in the detection of deep convection.

A range of the $BTD_{6.2\text{-}7.3}$ thresholds consistent with the modelling results shown previously (-3.5 K to -1.5 K) were used for the initial matchup for the whole of June 2010. As expected with this type of skill score, POD increases as $BTD_{6.2\text{-}7.3}$ becomes more negative, classifying more cloud as deep convection, reaching 0.62 at -3.5 K (table 4.6 and figure 4.10). The initial matchup shows that in all cases FAR is always higher than POD (FAR = 0.63 at -3.5 K), suggesting an over estimation of deep convection by SEVIRI. CSI shows that of all cases that were predicted by SEVIRI, whether incorrect or correct predictions, the number of correct predictions never rises above 30%, suggesting that using a BTD threshold approach (given the assumption that CloudSat cloud classifications are perfect) is limited when using these thresholds.

In comparison to other studies, Henken *et al.,* (2011) found a POD of 0.65 and a FAR of 0.32 for a convective cloud mask developed using the visible brightness temperature bands of SEVIRI and cloud physical properties. It is also highlighted by Henken *et al.,* (2011) that an automated radar based convective cloud warning algorithm used by the Amsterdam Airport Schiphol has a POD of 58% and an FAR of 70%, much higher than that seen in this study. Moisselin and Autonès (2013) calculated a POD of 0.66 and FAR

of 0.44 when detecting convection using the Rapid-Detection Thunderstorm Convective Warning (RDT-CW) product, whilst Mosher (2002) finds a POD of between 0.39 and 0.44 when using the 6.7-11 μm band brightness temperature difference to detect deep convection.

$\mathbf{BTD_{6.2\text{-}7.3}}$	**POD**	**FAR**	**CSI**	**SR**
-3.5	0.62	0.63	0.29	0.37
-3	0.58	0.61	0.3	0.39
-2.5	0.53	0.59	0.3	0.41
-2	0.49	0.56	0.29	0.44
-1.5	0.43	0.54	0.28	0.46

Table 4.6: POD, FAR and CSI for June 2010, for co-located matchup of SEVIRI and CloudSat over a range of $BTD_{6.2\text{-}7.3}$.

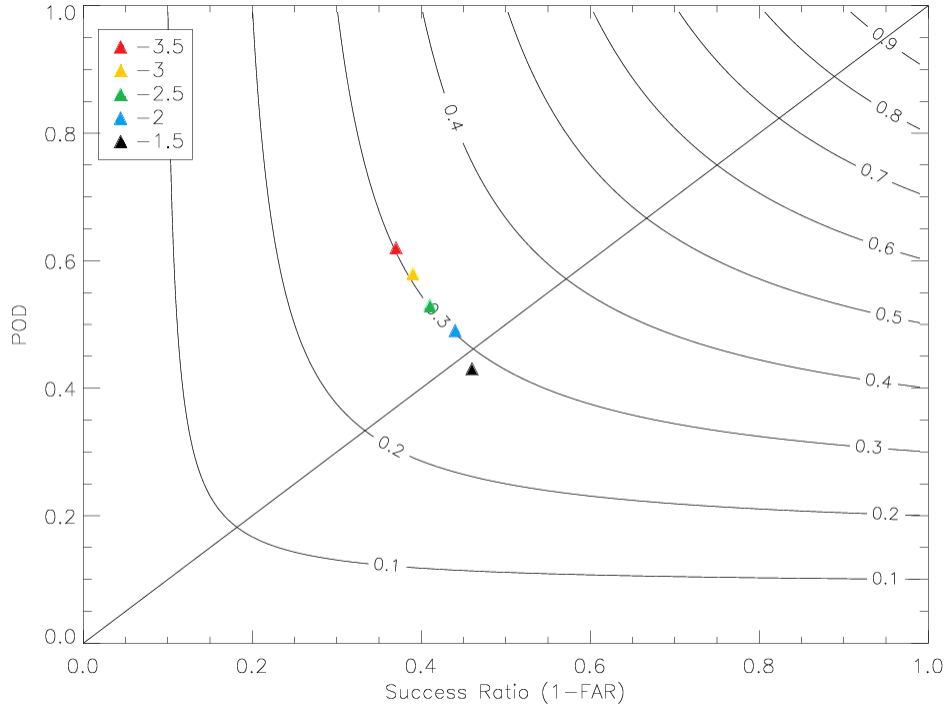

Figure 4.10: ROC curve for the initial matchup. The legend (top left) shows the $BTD_{6.2\text{-}7.3}$ range.

4.4 Reclassification of CloudSat Cloudclass Data - Altostratus

From the initial matchup of the $BTD_{6.2\text{-}7.3}$ thresholds with CloudSat cloud classifications, it is evident that large overestimation's of deep convection occur, represented by the large FAR for each threshold tested. The large overestimation may be caused by the classification of vertically and optically thick detraining anvil close to the core as Altostratus within the CloudSat classification dataset. The detraining anvil clouds may possess a range of microphysical characteristics similar to that of Altostratus and be classified as such in the 2B-CLDCLASS algorithm. Properties that may be similar include the reflectivity factor, cloud top heights

and thickness, and the TOA $BTD_{6.2\text{-}7.3}$of the two cloud types. These properties are likely to be similar to that of deep convection when in close proximity and when at similar heights to the convective core. Deep convection is also sometimes embedded within Altostratus cloud and convective cloud can sometimes develop from Altocumulus Castellanus, but may possess an unusually high cloud base (MetOffice, 2014). Detraining anvil from deep convective clouds also contain overshooting convection into the stratosphere, which will have a $BTD_{6.2\text{-}7.3}$ representative of intense deep convection (> 0 K) but may be classed as Altostratus by the CloudSat classification. This classification issue was also found by Yuan and Houze Jr. (2010) and Young *et al.* (2013). Those studies found that cloud classified as Altostratus cloud in the CloudSat dataset within 1.5-2 cloud radii of deep convection and with a thickness of 4-5 km was likely to be anvil cloud detraining from mature deep convection.

Given the high FAR's shown above for the initial co-located matchup, and based on the findings of Yuan and Houze Jr. (2010) it is expected that the $BTD_{6.2\text{-}7.3}$ threshold is classifying some of the contiguous anvil (classified as Altostratus) as deep convection, causing the FAR to increase. This underestimation of deep convection can be seen in figure 4.12, where a CloudSat overpass on June 25th shows a clear core of deep convection with some altostratus on either side of the core (figure 4.11a).

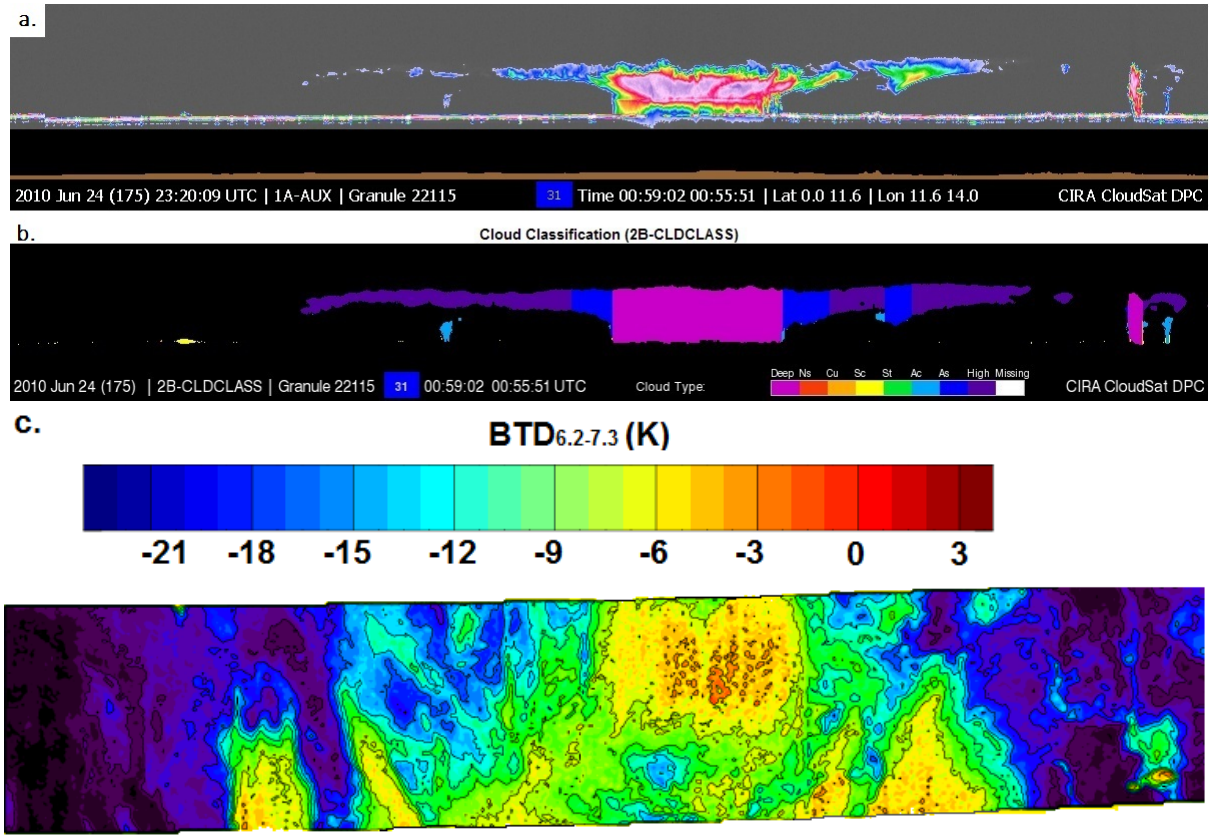

Figure 4.11: A comparison between the CloudSat 2B-CLDCLASS classification of deep convection and SEVIRI $BTD_{6.2\text{-}7.3}$ of the same cloud system at 01:00 on June 25th 2010, between 0°-11.6° N and 11.6°-14° E. **a)** The 'quicklook' CloudSat reflectivity profile of the cloud system. **b)** The same cloud system as classified into cloud types based on microphysical parameters by Sassen and Wang's (2008) CloudSat 2B-CLDCLASS algorithm. This shows the deep convective cloud in pink with accompanying altostratus (dark blue) and high clouds (purple) (see key). CloudSat imagery taken from: CloudSat (2010). **c)** Representation of SEVIRI TOA $BTD_{6.2\text{-}7.3}$ for the convective event seen from above the cloud system. The contours are at 3 K intervals.

To improve the probability of detecting deep convection when using $BTD_{6.2\text{-}7.3}$ whilst reducing the FAR, contiguous cloud classified as Altostratus in the CloudSat dataset is reclassified as deep convection based on the anvil thickness and cloud radii ranges found by Yuan and Houze Jr. (2010). POD, FAR and CSI are calculated for each of the variations of distance from cloud edge (contiguous Altostratus falling within 1, 1.5 and 2 cloud radii from the cloud edge) and anvil thickness (anvil thickness between 4 and 5 km) and the reclassified CloudSat classifications are validated against SEVIRI to examine the agreement between the two independent datasets. POD, FAR and CSI are calculated for each iteration at -3K, -2K and -1K $BTD_{6.2\text{-}7.3}$ to characterise the sensitivity of the POD, FAR and CSI to each change. Radius is calculated along the track of the dataset as CloudSat only provides a 2D representation of the cloud.

A comparison with the POD, FAR and CSI before and after reclassification shows a much lower FAR after reclassification for each $BTD_{6.2\text{-}7.3}$ threshold and reclassification class, confirming the cause of the high FAR in the original matchup to be contiguous Altostratus. This is also accompanied by an increase in CSI, which is expected due to the relationship between the three statistics. A reclassification of anvils within 1

cloud radii and with an anvil thickness of 5 km or less (in bold, table 7) show the highest POD (0.62) and CSI (0.47) at a $BTD_{6.2\text{-}7.3}$ of -3 K. The POD value is slightly higher than obtained in the original matchup using the same $BTD_{6.2\text{-}7.3}$ threshold, but there is an accompanying strong decrease in FAR (to a value of 0.33) compared to 0.61 before the reclassification. CSI has increased from 0.3 to 0.47. Although this is clearly not perfect it represents a marked improvement and suggest that the detection method has some skill given the differences in sensor type and resolution.

These values found in this study are similar to that found in other studies discussed above, suggesting these are the expected range of POD and FAR values. The range of POD in the literature may be a result of the methods used to detect convection, or the need to be less or more conservative with the thresholding based on the needs of each study. Given these results, a reclassification of anvil to deep convection within 1 cloud radii and with a thickness of 5 km or less was applied to all anvils and altostratus within the CloudSat dataset before the final thresholds for $BTD_{6.2\text{-}7.3}$ were determined based on further POD, FAR and CSI calculations.

BTD	**Cloud Radii**	**Anvil thickness (km)**	**POD**	**FAR**	**CSI**
-3	1	4	0.52	0.31	0.42
-2	1	4	0.43	0.26	0.37
-1	1	4	0.27	0.22	0.26
BTD	**Cloud Radii**	**Anvil thickness (km)**	**POD**	**FAR**	**CSI**
-3	1.5	4	0.51	0.31	0.41
-2	1.5	4	0.41	0.26	0.36
-1	1.5	4	0.26	0.22	0.24
BTD	**Cloud Radii**	**Anvil thickness (km)**	**POD**	**FAR**	**CSI**
-3	2	4	0.51	0.31	0.41
-2	2	4	0.42	0.26	0.36
-1	2	4	0.27	0.22	0.24
BTD	**Cloud Radii**	**Anvil thickness (km)**	**POD**	**FAR**	**CSI**
-3	**1**	**5**	**0.62**	**0.33**	**0.47**
-2	1	5	0.51	0.28	0.42
-1	1	5	0.33	0.23	0.3
BTD	**Cloud Radii**	**Anvil thickness (km)**	**POD**	**FAR**	**CSI**
-3	1.5	5	0.59	0.32	0.45
-2	1.5	5	0.48	0.27	0.41
-1	1.5	5	0.31	0.23	0.28
BTD	**Cloud Radii**	**Anvil thickness (km)**	**POD**	**FAR**	**CSI**
-3	2	5	0.59	0.33	0.46
-2	2	5	0.48	0.28	0.41
-1	2	5	0.31	0.23	0.28

Table 4.7: POD, FAR and CSI for the matchup between colocated SEVIRI $BTD_{6.2\text{-}7.3}$ and reclassified CloudSat cloud classification data from June 2010. The matchup is conducted over a small range of $BTD_{6.2\text{-}7.3}$, from -1 to -3 K. Tables are based on a change of cloud type from contiguous Altostratus to deep convection based on the distance from the cloud edge, measured in deep convective cloud radii and anvil thickness between 4 and 5 km.

4.5 Receiver Operating Characteristics - Threshold Determination

Given the difference in the cloud top heights over course of a day shown in chapter 3, and with cloud top heights exerting the greatest influence over $BTD_{6.2\text{-}7.3}$, the CloudSat data was split into day and night, aligning with the instrument flyover times. In order to provide a context for the $BTD_{6.2\text{-}7.3}$ thresholds determined using the ROC approach, in the next section the characteristics of deep convective cloud top heights during night and day as derived from CloudSat after the reclassification described above, are provided.

4.5.1 June - Day and Night

Probability and cumulative density functions of cloud top and base heights are provided for June day and night time cases (figure 4.12). It is evident from the PDF's that there is a greater frequency of convective clouds at night in June than at day time, with there being 1202 vertical profiles during the day compared to 1416 at night. In comparison to the frequency of convection found using ERA-Interim (chapter 3), a similar pattern is seen in that a greater frequency is found at night, though the actual frequency between the two datasets does differ. This may be due to constraints put on the definition of deep convection in ERA-Interim during the analysis (e.g. base height) and also the difference in resolution between the two datasets (both temporal and spatial).

A greater frequency of clouds with a higher cloud top are found at night. Again this is similar to the pattern found in ERA-Interim. Mean cloud top heights measured by CloudSat at night are 11.8 km (σ= 3), compared with 10.5 km (σ= 2.5) during the day. This is somewhat less than the mean cloud top height found in ERA-Interim, which suggests some discrepancy between modelled and observed convection. This may be due to the convective parameterisation in ERA-Interim possibly overestimating the intensity of the convection or the definition used to detect deep convection in ERA-Interim. The lowest cloud top heights in June were found during the day, with the lowest being 4.7 km - much lower than that classified as deep convection in ERA-Interim, again due to the definition used to detect deep convection in ERA-Interim (chapter 3). The lowest cloud top height found at night was 5.9 km.

The histogram of the cloud top heights for June night time cases show a distinct bimodal shape, creating a distinct step in the CDF. A Kolmogorov-Smirnov test shows a statistically significant difference in deep convective cloud top heights detected by CloudSat. A maximum difference between the cumulative density functions of the two cloud top height distributions (day and night) is 0.357 (P = <0.005), suggesting the clouds have significantly different distributions, from which it can be inferred that a more negative $BTD_{6.2\text{-}7.3}$ will be needed for detecting day time convection.

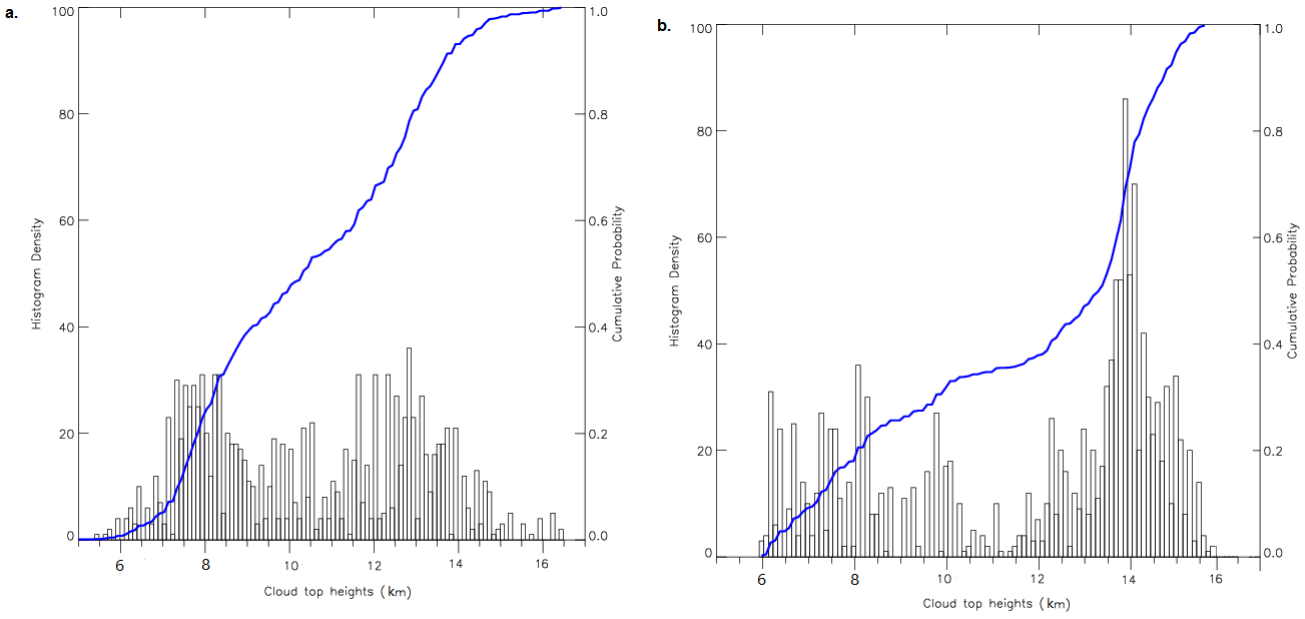

Figure 4.12: **a)** Frequency distribution (bars) and cumulative density functions (blue line) of cloud top heights (top) (m) for day time cases during June 2010 **b)** For night time cases during June 2010 Data is taken from CloudSat.

Box and whisker diagrams of cloud top heights are also presented in figure 4.13. The median cloud top height is higher at night for June cases (13.3 km, compared to 10.3 during the day). This is representative of the cloud lifecycle discussed in chapter 1, with deep convection reaching maturity, and therefore highest cloud top heights, in the later hours. This is the same pattern that is seen in ERA-Interim, with a similar median cloud top height at night, though the median is over 2 km lower during the day in CloudSat. The highest cloud top in June is found during the day (16.5 km).

Cloud top heights show a larger range for day time cases with the median and mean being lower than at night (figure 4.13). The upper quartile at night is much higher than that of day time convection, with a similar pattern seen in ERA-Interim. The fact that there is a small difference between median cloud top height and the upper quartile at night in June suggests that generally higher cloud tops are seen at this period and is caused by the bimodal peak seen in figure 4.12.

As convection reaches its most intense in the late afternoon to early evening, this allows SEVIRI and CloudSat night time cases to measure more developed and dissipating convective clouds if they are following the expected convective cloud lifecycle. This is also seen in the ERA-Interim analysis, whereby the median is much closer to the maximum cloud top height. Interestingly, there are no outliers in the CloudSat data, whilst there are several in ERA-Interim. This suggests there is a more even spread around the median in CloudSat than in ERA-Interim. This can be seen from there being a negative skew in the frequency distribution of ERA-Interim that is not apparent in CloudSat. This may be due to the resolution of the datasets, with CloudSat having a much greater spatial resolution than ERA-Interim.

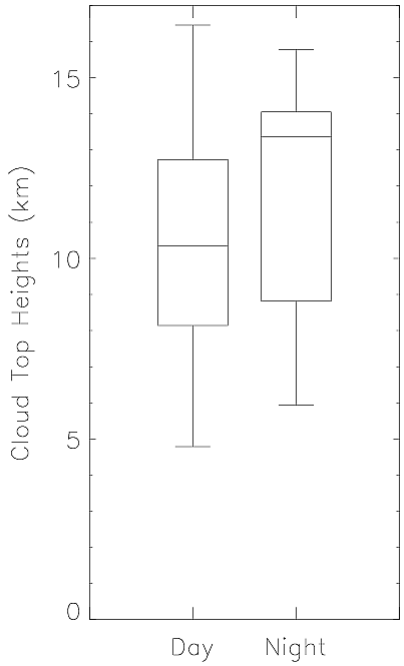

Figure 4.13: Box and whisker diagrams of cloud top heights (km) for day (~1300) and night (~0100) time deep convection events in June 2010. Convective events are split into day and night time cases based on CloudSat overpass times. The boxplots show median (middle line) and upper and lower quartiles. The tails represent the the maximum and minimum values within 1.5 standard deviations of the upper or lower quartile.

4.5.2 Threshold Determination

The matchup is conducted again to determine the results the POD, FAR and CSI for the separate $BTD_{6.2\text{-}7.3}$ thresholds for day and night time cases in June. The thresholds are varied between 0 K and -12 K at 0.5 K increments, based on the range of $BTD_{6.2\text{-}7.3}$ seen in the results of the modelling study. This will compensate for the lower cloud top heights found in CloudSat shown above. The results of the matchup are plotted as receiver operating characteristic curves (figure 4.15).

The ROC curves show similar patterns for both periods, with FAR increasing and POD flattening out with the more negative thresholds. This is expected as a threshold is reached where the majority of deep convective events have been detected, with any further cloud detected with SEVIRI becoming a false alarm. A comparison between POD, SR and CSI for June day time $BTD_{6.2\text{-}7.3}$ thresholds show a $BTD_{6.2\text{-}7.3}$ of -9 K is most successful for detecting day time convection, whilst for night time convection we see a $BTD_{6.2\text{-}7.3}$ of -3K is the most successful threshold. The skill scores show the same FAR and CSI for both periods, but a very small difference in POD, even with a $BTD_{6.2\text{-}7.3}$ difference of -6 K. This is summarised in table 4.8.

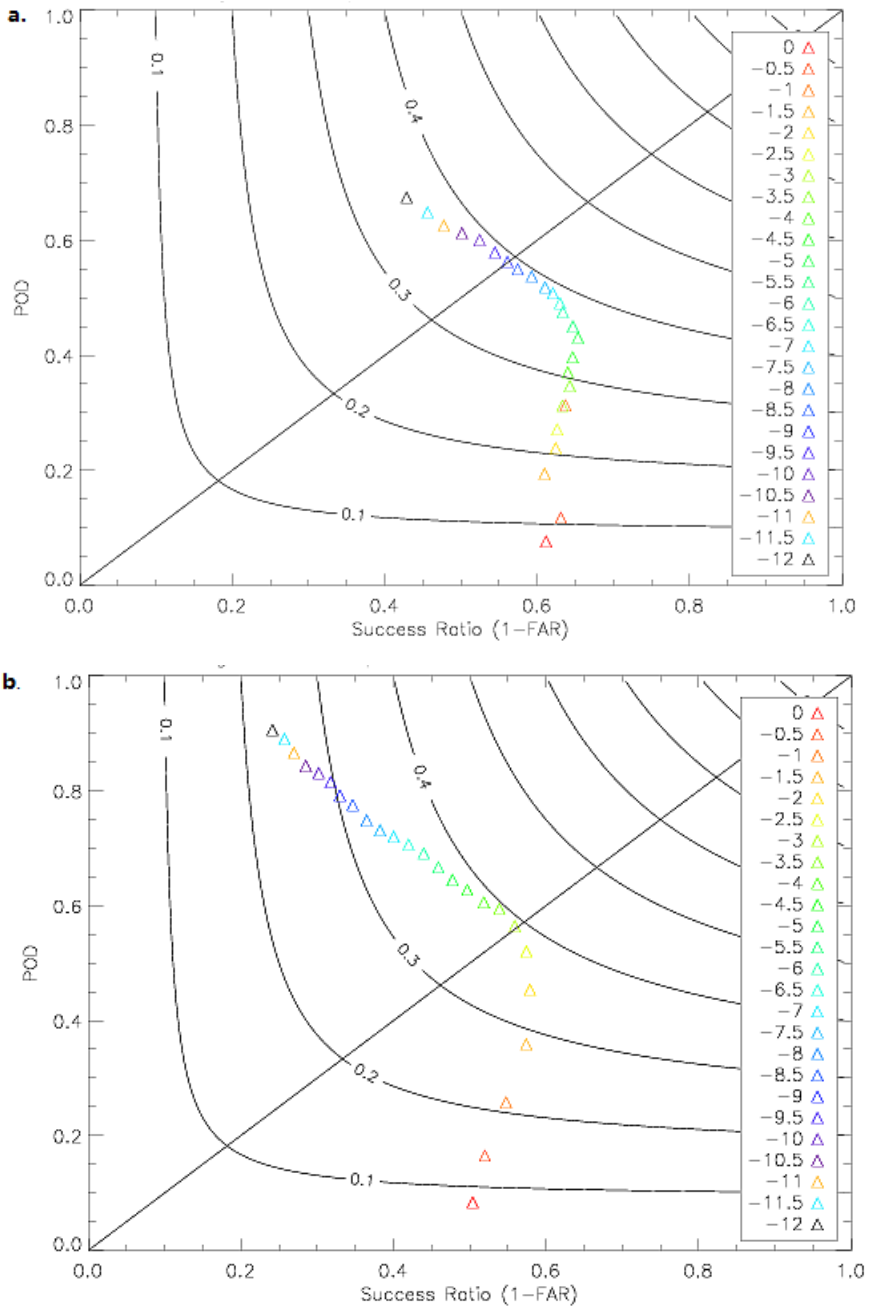

Figure 4.14: Receiver operating characteristic curves for June day and night classifications. **a)** POD vs success ratio for June 2010 day time $BTD_{6.2\text{-}7.3}$ thresholds. **b)** POD vs success ratio for June 2010 night time $BTD_{6.2\text{-}7.3}$ thresholds.

	$BTD_{6.2\text{-}7.3}$	POD	FAR	SR	CSI
Day	-9 K	0.56	0.44	0.56	0.39
Night	-3 K	0.57	0.44	0.56	0.39

Table 4.8: POD, FAR, SR and CSI for most successful $BTD_{6.2\text{-}7.3}$ for June day and night time deep convection

Although the values of POD, FAR, SR and CSI for the most successful thresholds are very similar for both day and night cases, the threshold itself is different by 6 K. The difference in the best $BTD_{6.2\text{-}7.3}$ thresholds between day and night is representative of the cloud top heights found at these times. As seen from the analysis of cloud top heights in CloudSat, there was a much greater frequency of high cloud tops at night, with a higher mean and median cloud top height than during the day. This lends itself to a less negative $BTD_{6.2\text{-}7.3}$, which would detect a large number of deep convective clouds at this time. This is compared to the the distribution of cloud top heights seen during the day time, whereby a lower frequency of high cloud tops is found. A lower mean and median cloud top height is also found during the day than at night. This distribution of cloud top heights during the day would therefore result in a more negative $BTD_{6.2\text{-}7.3}$ needed for the detection of these clouds.

Though a FAR of 0.44 is found for the most successful threshold (defined as having the highest POD and CSI combination) the aim is to produce a threshold for $BTD_{6.2\text{-}7.3}$ which does not underestimate the amount of deep convection found as this may result in cloud contaminated pixels being classified as cloud free. A -9 K threshold for day time cases and -3 K threshold for night time cases of convection satisfy this criteria.

4.5.3 December Day and Night

To test for any seasonal differences and to test the robustness of this $BTD_{6.2\text{-}7.3}$ threshold, the same process of using the the reclassified CloudSat data to probe relevant thresholds is applied to winter time convection in the same region. From the analysis of ERA-Interim data in chapter 3, it is evident that although December convection is charaterised by lower cloud top heights, the range of height is also much smaller, with June possessing many more clouds with a lower cloud top height. Therefore it is expected that the $BTD_{6.2\text{-}7.3}$ thresholds for December may not be as negative as that of June, resulting from there being less low clouds and therefore less of a need to reduce the $BTD_{6.2\text{-}7.3}$ accordingly to detect them.

PDF's and CDF's of deep convective cloud top heights detected by CloudSat are shown in figure 4.16. The frequency of convection is, as expected, much less than that in June (172 profiles for day time periods, 264 at night). Similar to June, a large spread of heights is seen between a minimum of 5.8 km and a maximum of 15.6 km during the day (figure 4.16a). Day time convection in December has a higher mean than summer time convection (10.8 km during the day, 12 km at night). The distribution of night time cloud top heights in CloudSat is characterised by two distinct peaks between 7 and 9 km and higher cloud tops between 13 and 16 km, creating a large step in the CDF of December night time cases (figure 4.16b) The KS statistic for this month is lower than that of June, with a maximum difference of 0.29 ($P = <0.005$), though the distributions are still significantly different enough to infer a different BTD6.2-7.3 will be needed for each time period.

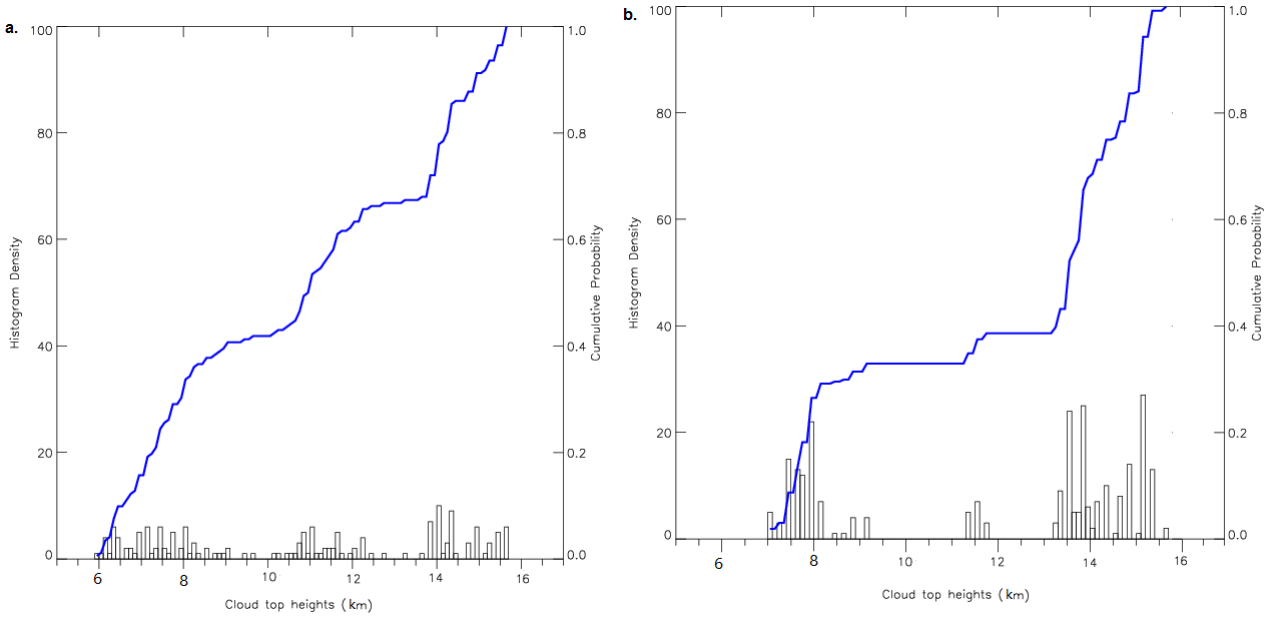

Figure 4.15: **a)** Frequency distribution (bars) and cumulative density functions (blue line) of cloud top heights (top) (m) for day time cases during December 2010 **b)** For night time cases during December 2010 Data is taken from CloudSat.

A similar range of cloud top heights are found for both December day and night time periods in CloudSat (figure 4.17). Deep convective cloud top heights in CloudSat range from a minimum of 5.8 km to a maximum of 15.7 km during the day, and a minimum of 7 km to a maximum of 15.2 km at night. A much higher median cloud top height is seen at night in December (13.6 km) than compared to day time (11 km), representative of the greater frequency of higher cloud tops at night.

In comparison to the deep convection found in ERA-Interim, there are some differences in the distribution of the cloud top heights. For day time convection, a larger range is seen in CloudSat, though a lower median is found. In ERA-Interim, no cloud tops lower than 8 km are found during the day, whilst those in CloudSat are much lower. At night, cloud top heights in CloudSat again show a larger range than in ERA-Interim, though they also show a higher median. This may be due to the ability of ERA-Interim to represent convection when compared to more detailed observations such as CloudSat.

In comparison to cloud top heights detected by CloudSat in June, a smaller range is seen for both day and night in December. June day time convection detected by CloudSat has a maximum cloud top height of 16.5 km compared to 15.7 km in December, whilst night convection reaches a maximum of 15.9 km in June compared to 15.2 km in December. The median cloud top height is higher in December than June for both day and night time convection, a result of the greater frequency of lower cloud top heights in June. The higher median and mean cloud top heights detected by CloudSat in December would suggest a less negative $BTD_{6.2\text{-}7.3}$ threshold than that found for June would be appropriate to detect winter convection.

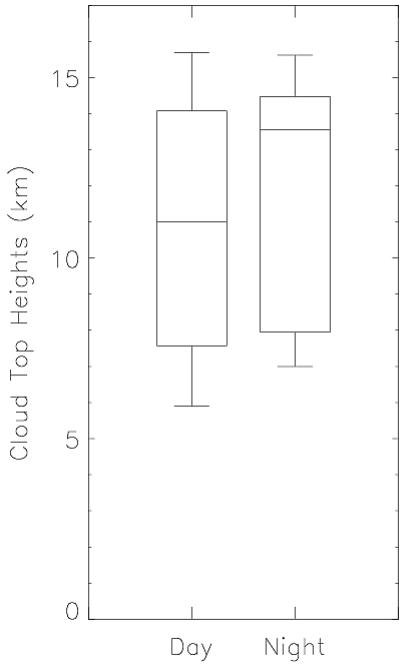

Figure 4.16: Box and whisker diagrams of cloud top heights (km) and cloud thicknesses (km) for day (12:00 UTC) and night (00:00 UTC) time deep convection events in December 2010. Convective events are split into day and night time cases based on CloudSat overpass times. The boxplots show median (middle line) and upper and lower quartiles. The tails represent the the maximum and minimum values within 1.5 standard deviations of the upper or lower quartile.

As before, the thresholds used for deep convection detection are split into 0.5 K increments and are varied between 0 K and -12 K to compensate for possible lower cloud top heights measured by CloudSat (figure 4.18). The resulting ROC curves show dissimilar shapes. A $BTD_{6.2\text{-}7.3}$ of -3 K is found to be the most successful threshold for day time deep convection in December (figure 4.18a). FAR is above 50% for this case and almost equal to POD. Given the distribution of cloud top heights shown in figures 4.16 and 4.17 and in ERA-Interim, the high $BTD_{6.2\text{-}7.3}$ during the day is somewhat unexpected. Low cloud top heights would typically be expected to result in more negative $BTD_{6.2\text{-}7.3}$ because of the weighting functions. When compared to the sensitivity study of the response of $BTD_{6.2\text{-}7.3}$ to cloud top heights, this threshold of -3 K is representative of cloud top heights between 8 and 9 km and above. Given the distribution of CloudSat cloud top heights this threshold will detect most deep convective cases.

The night time threshold shows little change in the SR with an increase of $BTD_{6.2\text{-}7.3}$ between 0 and -7 K (figure 4.18b). In this case, CSI was instrumental on the determination which threshold was most appropriate. The highest CSI is seen at -7 K so this value is chosen as the threshold. This shows a much higher POD (0.74), but has a higher FAR (0.59), suggesting this is a liberal threshold which satisfies the need to be more liberal with cloud detection. Though a high FAR is seen for both thresholds, the high POD and the need to ultimately make sure there is no cloud contamination when performing the analysis of clear sky UTH and OLR ultimately outweighs the need for a low false alarm rate.

This pattern in the direction of $BTD_{6.2\text{-}7.3}$ from day to night in December is the opposite to what is expected from the vertical growth of clouds over the cloud lifecycle. A possible explanation for this apparent threshold discrepancy may be due to the shape of the distribution of cloud top heights at these times. Night time cloud top heights appear to be centered on two strong maxima at ~7.5 K and ~14.5 K, with this distribution in cloud top heights needing a more negative $BTD_{6.2\text{-}7.3}$ for detection.

	$BTD_{6.2\text{-}7.3}$	**POD**	**FAR**	**SR**	**CSI**
Day	-3 K	0.52	0.51	0.49	0.34
Night	-7 K	0.74	0.59	0.41	0.35

Table 4.9: POD, FAR, SR and CSI for most successful $BTD_{6.2\text{-}7.3}$ for December day and night time deep convection

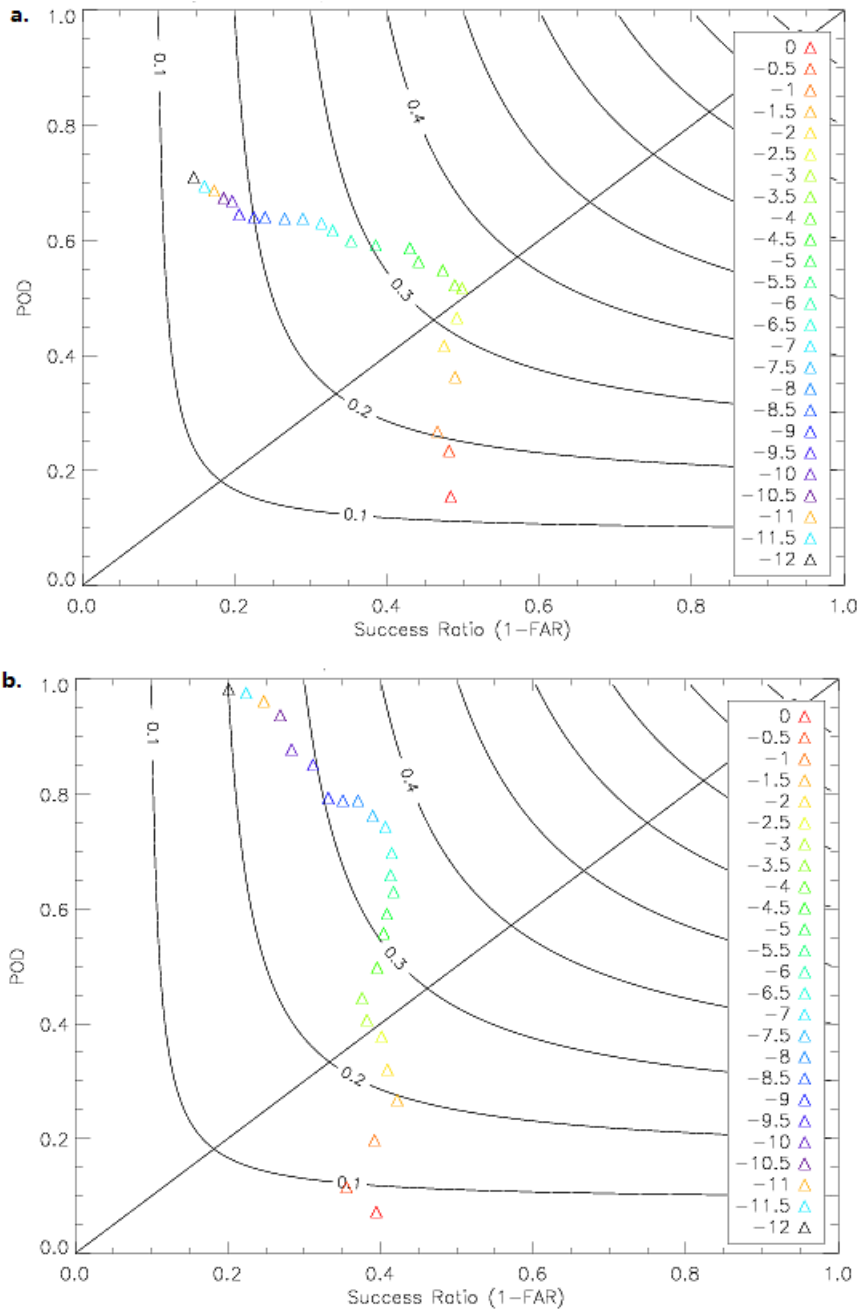

Figure 4.17: Receiver operating characteristic curves for June day and night classifications. **a)** POD vs success ratio for December 2010 day time $BTD_{6.2\text{-}7.3}$ thresholds. **b)** POD vs success ratio for December 2010 night time $BTD_{6.2\text{-}7.3}$ thresholds.

4.5.4 Cirrus clouds

In order to analyse the spatio-temporal response of clear sky UTH and OLR to deep convection, detrained cirrus cloud developing in the dissipating stage of the clouds lifecycle also need to be detected and masked.

The detection of cirrus is conducted using the difference between the 12.0 and 10.8 μm infrared bands. This method was developed by Inoue (1985) and is based on an empirical relationship based on the effective emissivity at these two wavelengths. Though being effective at detecting cirrus and a common method used for cirrus detection, limitations in its application exist in the assumption of a fixed relationship between the two emissivities at these wavelengths, which may not hold for all microphysical properties of cirrus (Bantges, 2000). The sensitivity of the $BTD_{12.0\text{-}10.8}$ to a change in key cirrus cloud properties are modelled following the same method as used for modelling the $BTD_{6.2\text{-}7.3}$ to determine a range of possible thresholds for cirrus detection.

The cold nature of these clouds means the emission of longwave radiation are low (Houze, 1993). Unlike deep convective clouds, cirrus clouds are not considered 'black' in the infrared spectrum. Cirrus optical depths are generally low, typically below 5 in the visible, with sub visual cirrus possessing optical depths less than 1. Thick cirrus associated with the detraining anvils of deep convection are optically thicker than other cirrus types especially when close to the convective core, creating a net cooling effect (Baran and Francis, 2004). The radiative properties of cirrus depend largely on the cirrus ice particle size and shape, with cirri often composed of bullets and hexagonal columns. This poses difficulties in modelling studies when using models such as SBDART which includes the scattering parameters for spherical ice grains (Ricchiazzi *et al.,*, 1999). This along with the the application of Mie theory may cause the modelled absorption to be overestimated (Bantges, 2000). Aside from the ice crystal shape, the main controls on the cirrus radiative properties are the optical depth (τ) of the cloud and the effective radius (*re*) of the ice crystal within the cloud (Krebs *et al.*, 2007). Ice cloud effective radius is a fundamental control on the radiative properties of cirrus cloud and is proportional to the ratio of ice water content to the extinction coefficient (Heymsfield *et al.,* 2006). The particle effective radius is usually derived from empirical relationships due to the shape, size and the distributions of these ice particles varying over the cloud. Further effects on the sign of the radiative effect come from the height of the cloud within the atmosphere and the solar zenith angle.

Using the thresholds representative of cirrus clouds in the sensitivity study as a guide, a colocated matchup is made between SEVIRI $BTD_{12.0\text{-}10.8}$ and the 2B-CLDCLASS-Lidar cloud classifications described in chapter 2. Threshold determination of SEVIRI detected cirrus with the high cloud classification in the 2B-CLDCLASS dataset alone may introduce further uncertainty into the determination of a suitable threshold through an underestimation of cirrus by CloudSat, as discussed in chapter 2.

4.5.5 Modelled TOA Brightness Temperatures - Cirrus clouds

The sensitivity of $BTD_{12.0\text{-}10.8}$ to cirrus cloud properties is modeled for two separate cirrus cloud profiles on June 4th 2010 at 0000 and December 6th 2010 at 0000. Jensen *et al.,* (1996) showed, theoretically, that there are two formation mechanisms for thin cirrus - that detraining from deep convective cloud as anvil, or nucleation near the tropical tropopause. The June case is a thick cirrus with no attachment to a deep convective cloud seen in the profile, whilst that of December is a detraining cirrus from a deep convective cloud, likely to be dissipating from an anvil. Figures 4.19 and 4.20 show the CALIPSO Lidar backscatter and the CloudSat quicklook images of each scene. The December cirrus (figure 4.20), found at a height of 16-17 km and at a latitude of 0°-~1° N, is a vertically thinner cloud than that of the June case. This cirrus in December is overlying another cloud, classified as Cumulus in the CloudSat classifications. The June cloud has a higher attenuated backscatter, suggesting this cloud is optically thicker. This is expected to give a

different $BTD_{12.0\text{-}10.8}$ for each cloud, representative of different cirrus types. For the December profile, the MODIS 10.6-12.05 μm band brightness temperature differences are also provided with the available quicklook imagery (figure 4.20c). The direction of change using this method is positive rather than negative when a cirrus cloud is present due to the way the difference is calculated. It can be seen that in the presence of cirrus cloud along the track that the BTD ranges between 10 and 5 K. This provides some guidance as to what the range of $BTD_{12.0\text{-}10.8}$ may be from the following modelling study.

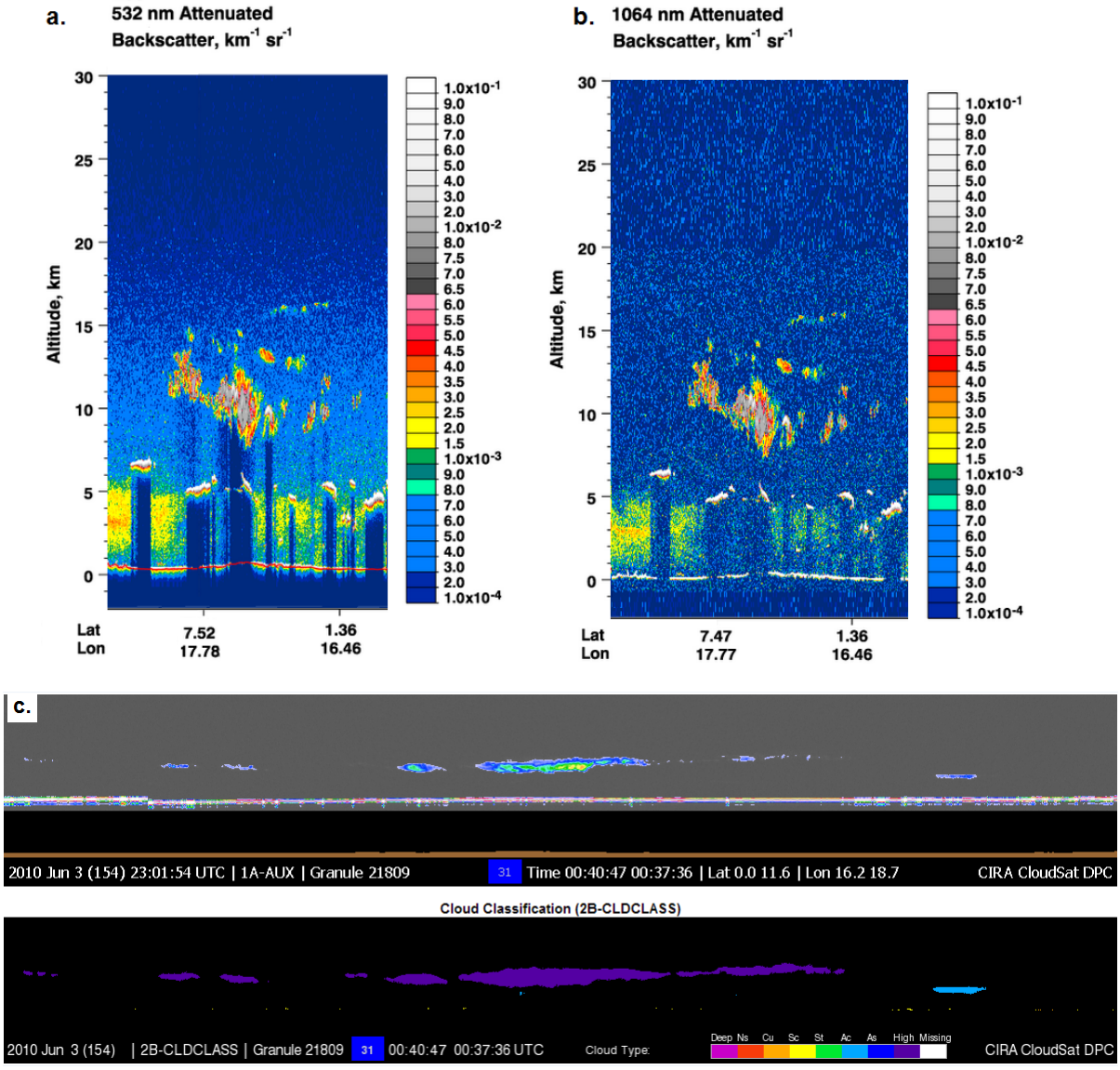

Figure 4.18: **a)** 532 nm attenuated backscatter used in the 2B-CLDCLASS classification at 00:37-00:40 on June 4th 2010, between 0°-11.6° N and 16.2°-18.7° E. **b)** 1064 nm attenuated backscatter. **c)** The 'quicklook' CloudSat reflectivity profile of the cloud system and the same cloud system as classified into cloud types based on microphysical parameters by the CloudSat 2B-CLDCLASS algorithm. This shows the cirrus cloud, classified as high cloud by CloudSat.

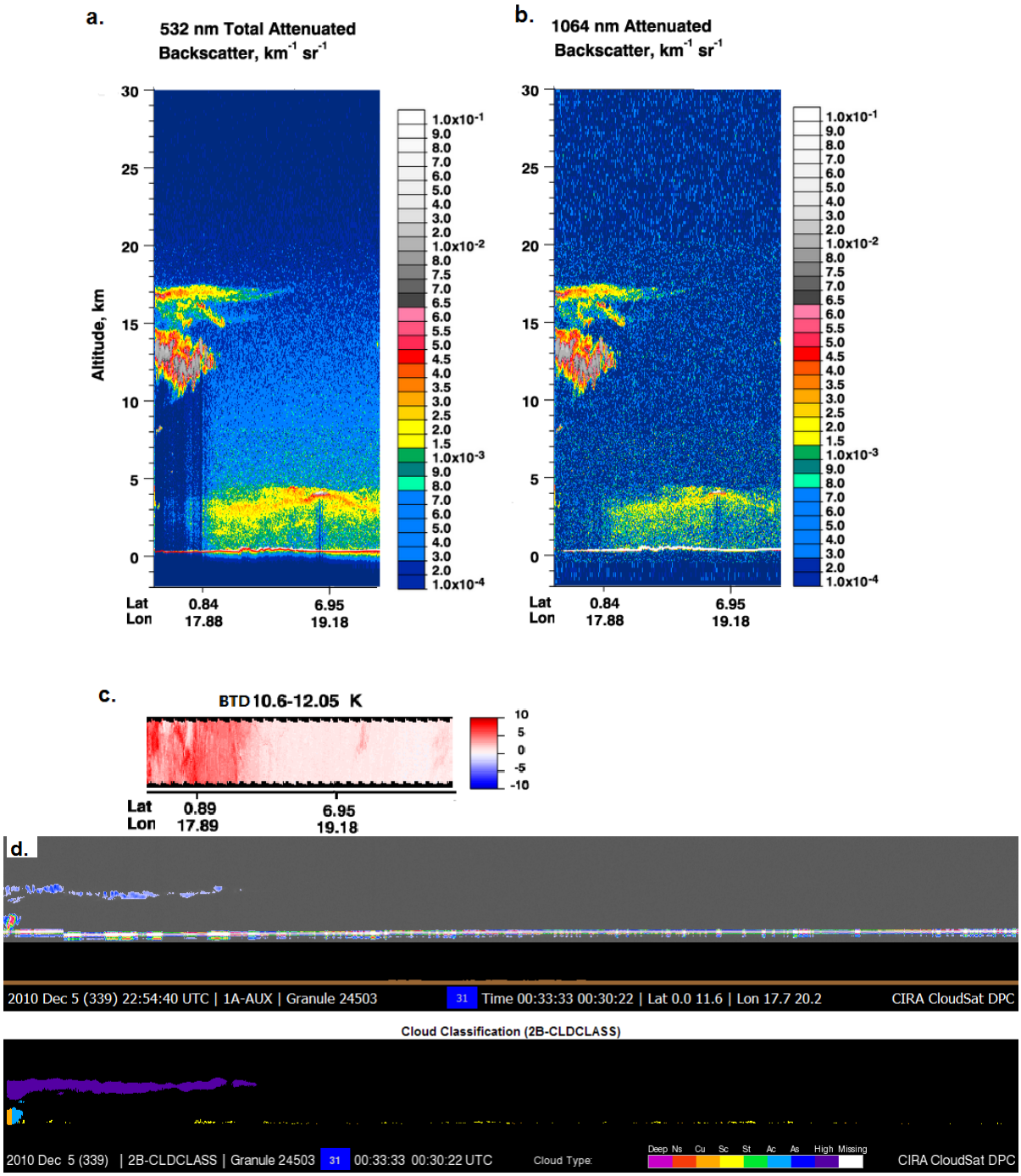

Figure 4.19: **a)** 532 nm attenuated backscatter of used in the 2B-CLDCLASS classification at 00:30-00:33 on December 6th 2010, between 0°-11.6° N and 17.7°-20.2° E. **b)** 1064 nm attenuated backscatter. **c)** The MODIS 10.6-12.05 µm brightness temperature difference (K) along track for the cloud system. **d)** The 'quicklook' CloudSat reflectivity profile of the cloud system and the same cloud system as classified into cloud types based on microphysical parameters by the CloudSat 2B-CLDCLASS algorithm. This shows the cirrus cloud, classified as high cloud by CloudSat.

The mean vertical temperature and relative humidity profiles of the atmospheric profiles input to SBDART are given for the two cases (figures 4.20 and 4.21). The vertical relative humidity profile for the cirrus case on June 4th 2010 (figure 4.20 b) shows a high relative humidity throughout most of the vertical profile in the tropopause (taken as the region below the temperature inversion in figure 4.20 a). In the region of the tropopause where the cirrus is found (8-11km, shown in figure 4.18) the relative humidity is above 90%, reaching supersaturation between 8 and 10 km. The vertical relative humidity profile for the cirrus case in December 6th 2010 (figure 4.21 b) shows a much drier profile in the region below the cloud (below 12 km). Mean relative humidity shows a high supersaturation in the region where the cloud exists, reaching a mean RH of 128%.

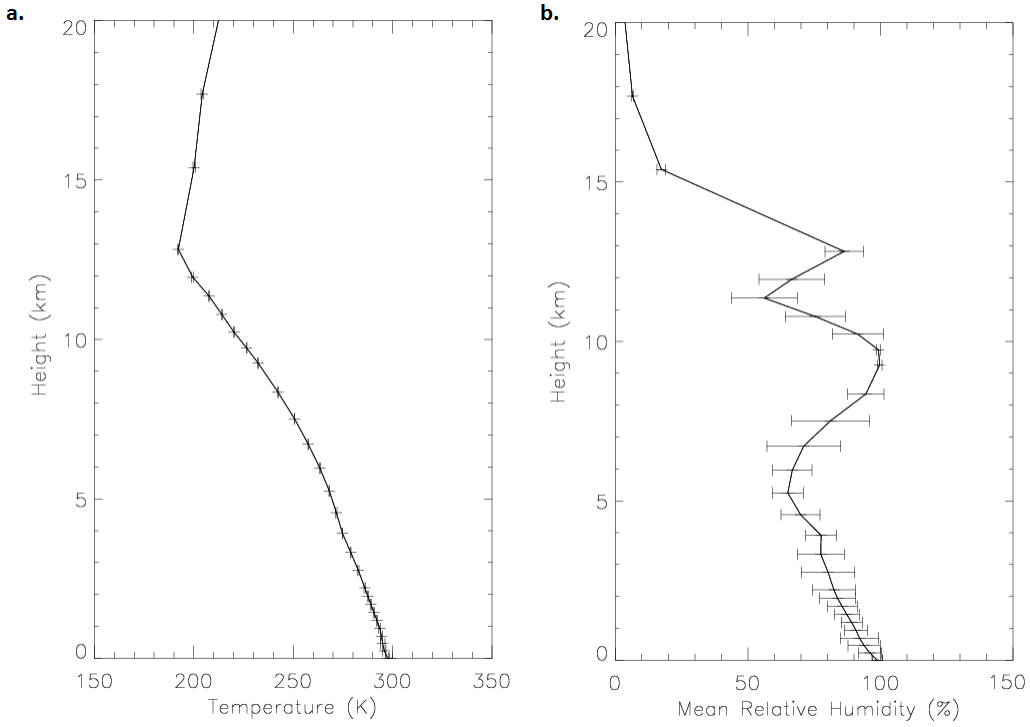

Figure 4.20: Vertical mean temperature (**a**) and relative humidity (**b**) of the cirrus profiles input to SBDART from June 4th 2010. ±1 standard deviation is given at each point in the vertical.

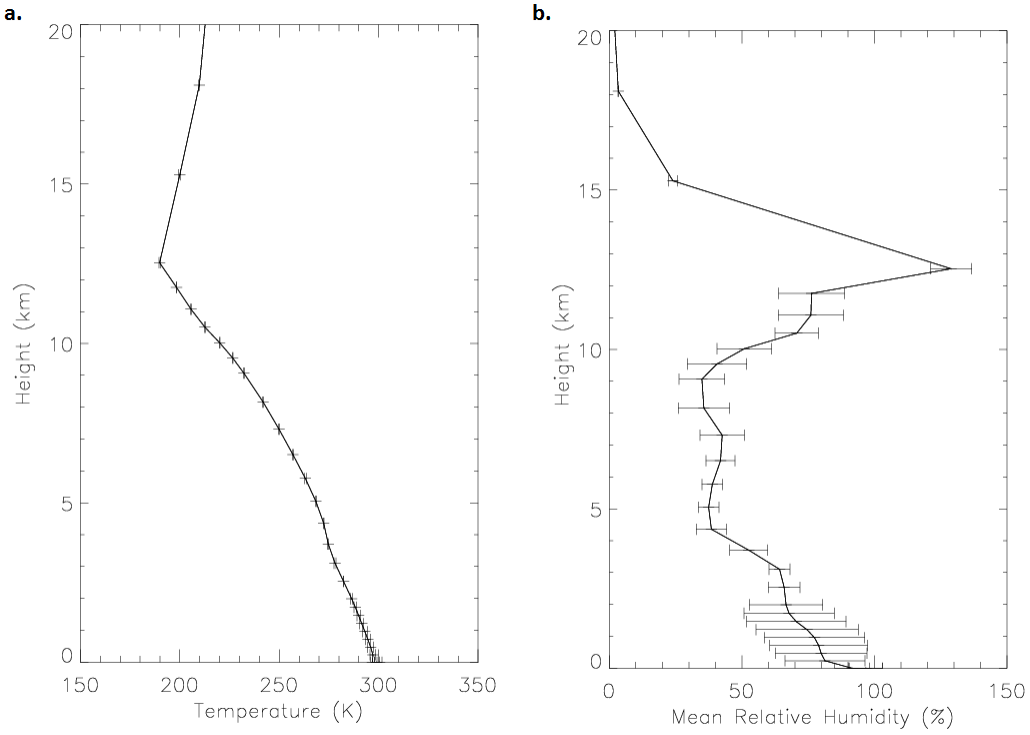

Figure 4.21: Vertical mean temperature (**a**) and relative humidity (**b**) of the cirrus profiles input to SBDART from December 6th 2010. ±1 standard deviation is given at each point in the vertical.

To simulate $BTD_{12\text{-}10.8}$ for the two representative case studies the baseline parameters were varied. Four variations in cloud properties were made, where one property was varied and all others kept constant - including cloud top height (constant base, increasing vertical thickness), cloud height, optical depth ($\tau_{0.55\mu m}$) and effective radius (r_e) of the ice particle. The corresponding vertical profiles from ERA-Interim were used as input to the model atmospheres for those profiles covering the profile. Mean spectral surface emissivity for the study region was taken from Cooperative Institute for Meteorological Satellite Studies (CIMSS, 2010) monthly means.

The optical depth was varied between 0.03 and 5 to represent sub-visual cirrus, thin cirrus and thick cirrus (with a constant effective radius of 20 and cloud geometrical thickness of 1 km, cloud base height at 7km and top at 8 km, shown in table 4.10). The optical depth and effective radius values were taken from Lynch *et al.,* (2002) and a cirrus radiative transfer modelling study by Ewald *et al.,* (2013). Cloud top heights were varied between 8 km and 12 km. Cloud vertical extents were taken from Massie *et al.,* (2010). Cloud height was varied for a one layer cirrus between 7 km base height and 17 km base height to cover the range seen in the above profiles. The effective radius was varied between 10 µm and 40 µm. Brightness temperatures were modeled at viewing zenith angles of between 0° and 80°. Baseline parameters for the model runs are shown in table 4.10.

Cloud top height (km)	Cloud Base Height	$\tau_{0.55}$	r_e	Phase
8	7	3	20	Ice

Table 4.10: Baseline model parameters for a cirrus cloud layer in the simulations.

4.5.6 Cirrus Optical Depth

Similar ranges in $BTD_{12.0\text{-}10.8}$ are seen for both June and December over the range of optical depths and viewing zenith angles used in the modelling study. At a viewing zenith angle of 0° $BTD_{12.0\text{-}10.8}$ ranged between -2.4 K to -5.2 K in June (figure 4.22a), with a similar range of -2.3 K to -5 K seen for the December case (figure 4.22b). The $BTD_{12.0\text{-}10.8}$ seen at the lower viewing zenith angles are similar to the range seen in the quick-look imagery in figure 4.19.

When comparing $BTD_{12.0\text{-}10.8}$ at low viewing zeniths over the range of optical depths, a decrease in $BTD_{12.0\text{-}10.8}$ is seen with an increase in optical from subvisual clouds at 0.03 to thicker clouds at an optical depth of 2. Interestingly, an increase is seen in $BTD_{12.0\text{-}10.8}$ at optical depths greater than 2. This is caused by a reduction in the transmissivity of the 12.0 μm and 10.8 μm radiances from the surface and through the cloud as the optical depth increases due to the exponential relationship between optical depths and transmissivity, and causes the $BTD_{12.0\text{-}10.8}$ to tend towards 0 at larger optical depths.

In relation to the viewing zenith angle, between 0° and 50° the $BTD_{12.0\text{-}10.8}$ increases with an increase in viewing zenith angle for optical depths of 2 and above. Below and optical depth of 2, $BTD_{12.0\text{-}10.8}$ is found to decrease with an increase in viewing zenith angle. For example, at an optical depth 0.5, the June case shows a decrease in $BTD_{12.0\text{-}10.8}$ from -3.7 K at a viewing zenith angle of 0° to -4.8 K at 50°. $BTD_{12.0\text{-}10.8}$ decreases with an increase in viewing zenith angle to 70°, above which the $BTD_{12.0\text{-}10.8}$ begins to increase with viewing zenith angle. When examining the response of each band separately to a change in viewing zenith angle (figure 4.22c), the trend towards a more negative $BTD_{12.0\text{-}10.8}$ around 60°-70° viewing zenith is due to the $BT_{12.0}$ falling at a faster rate than that of $BT_{10.8}$.The movement of $BTD_{12.0\text{-}10.8}$ toward 0 K at higher viewing zenith angles is also due to the reduction in transmissivity as the viewing zenith angle is increased, as can be seen from the equation describing transmissivity in chapter 2. As the angle increases towards the horizon, i.e 80° and above, transmission of radiation is very low due to the radiation travelling through more atmosphere.

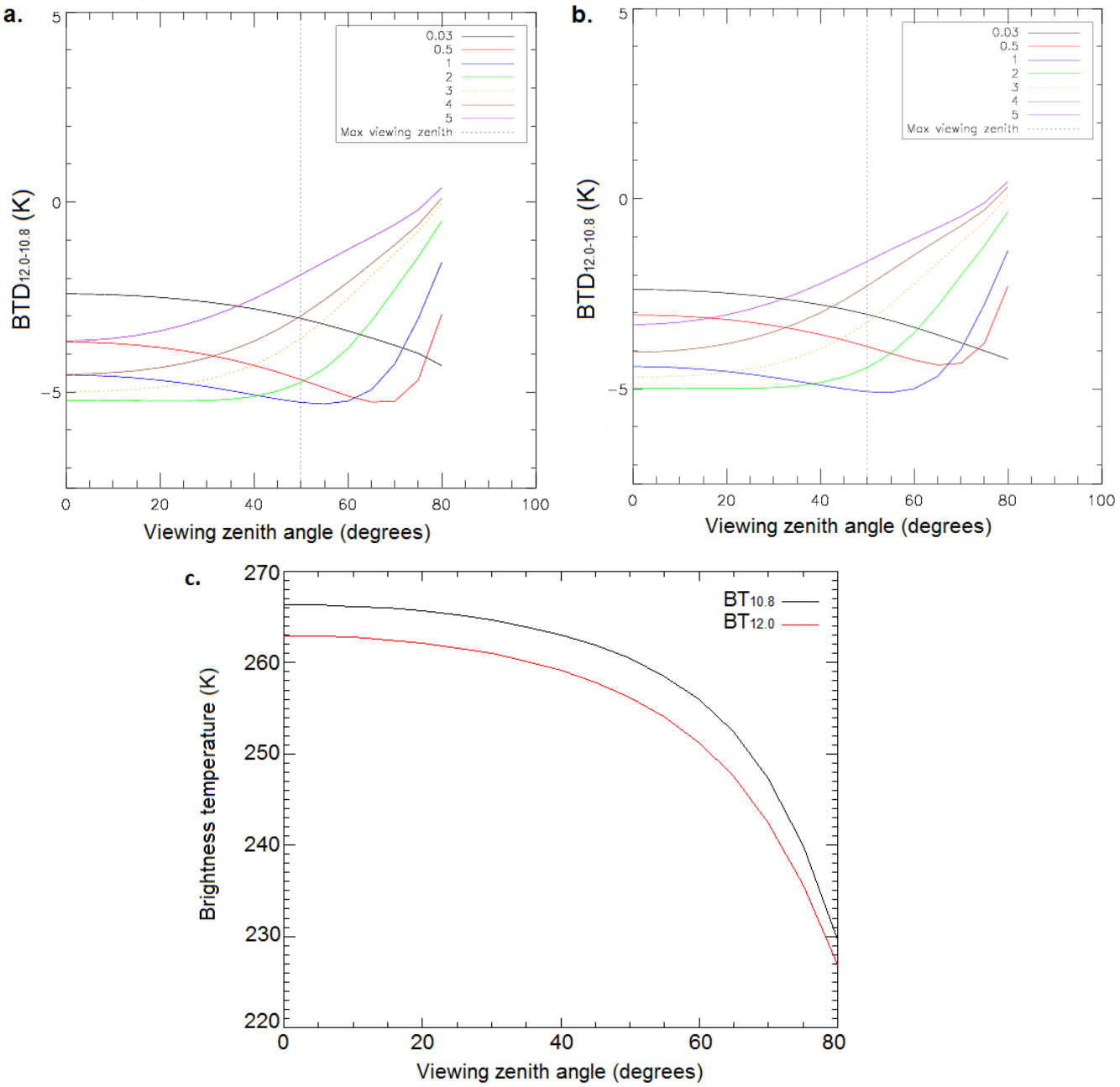

Figure 4.22: **a)** $BTD_{12.0\text{-}10.8}$ for single a single cirrus cloud with a changing $\tau_{0.55\mu m}$ for June 4th at 00:00 UTC. **b)** December 6th at 00:00 UTC (right), with a changing zenith angle. Maximum viewing zenith angle seen by SEVIRI over the study region is represented by the dotted line at 50°. **c)** The mean 10.8 and 12.0 μm brightness temperatures for the 0.5 optical depth cirrus clouds simulated above.

4.5.7 Cloud Height

Cirrus cloud $BTD_{12.0\text{-}10.8}$ was modelled with a constant geometrical thickness of 1 km and with a varying cloud top and base height (figure 4.23). In June (figure 4.23a), the $BTD_{12.0\text{-}10.8}$ shows little variability with a

change in the height of the cloud. For example, the $BTD_{12.0\text{-}10.8}$ found for the June case ranged between -1.86 K at 0° viewing zenith and -1.34 at 50° viewing zenith at 8 km - the lowest point (rounded to the nearest km) at which cirrus was found in the June case study (see figure 4.18). At a cloud height of 18 km $BTD_{12.0\text{-}10.8}$ varies between -3.1 K at a 0 ° viewing zenith angle and -1.9 K at a viewing zenith angle of 50°. The lowest $BTD_{12.0\text{-}10.8}$ was found at a height of 13 km, where a $BTD_{12.0\text{-}10.8}$ of -4.6 K was found at at 0° viewing zenith angle. The response of $BTD_{12.0\text{-}10.8}$ shows that as the cloud height is increased the $BTD_{12.0\text{-}10.8}$ decreases until the cloud reaches 13 km, after the $BTD_{12.0\text{-}10.8}$ becomes less negative.

For the December case (figure 4.23b) the range of $BTD_{12.0\text{-}10.8}$ is found to be larger and more negative than that of the June case. At 8 km a $BTD_{12.0\text{-}10.8}$ of -4.7 K is found at a viewing zenith angle of 0°, and -3.3 at at a 50° viewing zenith angle. At 18 km $BTD_{12.0\text{-}10.8}$ ranged from -6.4 K to -3.6 K between 0° and 50° viewing zenith angles. The most negative $BTD_{12.0\text{-}10.8}$ of -12.9 K is found at a height of 12 km. The difference between the least and most negative $BTD_{12.0\text{-}10.8}$ values at 0° viewing zenith angle represent a range of 8.1 K.

In both June and December cases, $BTD_{12.0\text{-}10.8}$ is relatively constant between viewing zenith angles of 0° and 40°, after which it rapidly tends to towards less negative values. For example, in June at a cloud height of 8km a range of 0.2 K is found between viewing zenith angles of 0° and 40°, compared to a range of 0.27 K between 40° and 50°. Similar increases towards 0 K are found in the December case, though this becomes a more rapid increase beyond 50°. At a cloud height of 12 km, where the most negative $BTD_{12.0\text{-}10.8}$ is found, a difference of 0.6 K is found between 40° and 50°. The rapid increase in $BTD_{12.0\text{-}10.8}$ at zeniths greater than 50° is similar to the response of seen above for a change in optical depth due to the control of viewing zenith angle on atmospheric transmission.

The difference in the sensitivities between the June and December case are also a result of the differing vertical humidity profiles. The vertical relative humidity profile for June (figure 4.20 b) shows a high relative humidity in the region between 8 and 11 km and another peak at 13 km. The stronger absorption of 12.0 μm band radiances than that at 10.8 μm by water vapour would result in a larger $BTD_{12.0\text{-}10.8}$ in regions of higher humidity. The relatively small change in UTH with height in June when compared to December between the modelled cloud top heights results in a less negative $BTD_{12.0\text{-}10.8}$. When considering the thresholds at 13 and 14 km in December, it can be seen that this corresponds to a region of high supersaturation, which would result in a stronger absorption of 12.0 μm band radiances, creating the much more negative threshold.

The sensitivity found in response to both the change in the cloud height and the viewing zenith angle are all in agreement with the thresholds found by Negri *et al.*, (2012) and Inoue (1987) who finds differences of -1 K and -2.5 K respectively to be representative of all cirrus, and is similar to that shown in the MODIS BTD imagery in figure 4.19.

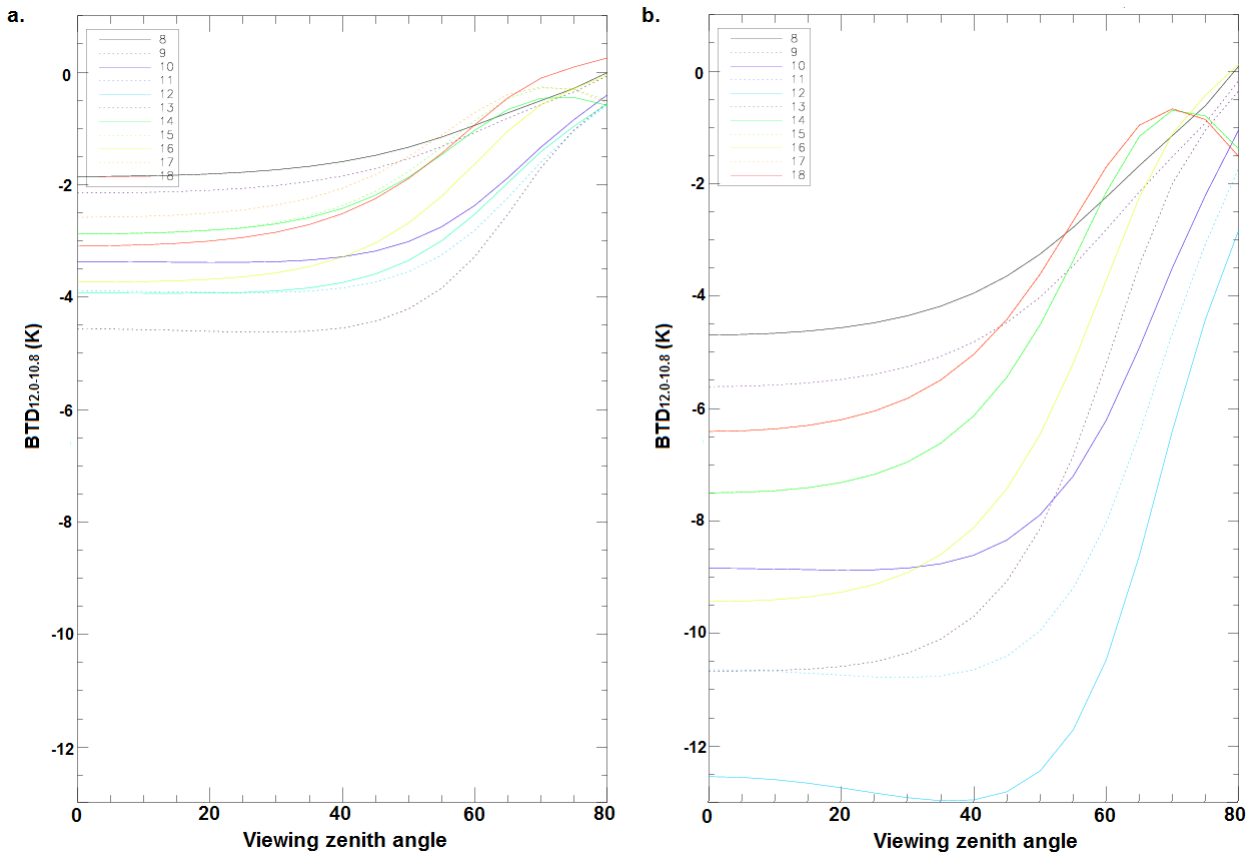

Figure 4.23: The sensitivity of $BTD_{12.0\text{-}10.8}$ to a change in the vertical cloud height between 8 km and 18 km. $BTD_{12.0\text{-}10.8}$ is shown as a function of viewing zenith angle between 0° and 80°. The colours represent cloud heights, as shown in the legend. **a)** $BTD_{12.0\text{-}10.8}$ for single a single cirrus cloud of 1 km thickness and changing cloud top heights for June 4th at 0000. **b)** December 6th at 0000 (right).

4.5.8 Cloud Top Height

When keeping the cloud base height at 7 km and increasing the cloud top height, the $BTD_{12.0\text{-}10.8}$ becomes more negative. This is seen in both the June and December profiles. The least negative $BTD_{12.0\text{-}10.8}$ on June 4th is seen at a cloud top height of 8 km, varying between -5 K at 0° viewing zenith angle and -3.3 K at 50° viewing zenith angle (figure 4.24a). The largest $BTD_{12.0\text{-}10.8}$ is found with a cloud top height of 12 km, varying between -10.4 K at 0° viewing zenith and -11.1 K at 50° viewing zenith. It is also seen that the $BTD_{12.0\text{-}10.8}$ shows very little variation with height above 10 km, with the difference in $BTD_{12.0\text{-}10.8}$ between 10 km and 12 km at 0° viewing zenith angle being 0.22 K. The least negative $BTD_{12.0\text{-}10.8}$ on December 6th is also seen at 8 km, varying between -4.7 K at 0° viewing zenith and -3.3 K at 50° viewing zenith, again decreasing to a minimum at 12 km varying between -13.4 K at 0° viewing zenith and -16.4 K at 50° viewing zenith, larger than that seen in the June case (figure 4.24b).

More negative values of $BTD_{12\text{-}10.8}$ are seen with an increasing cloud top height due to the geometrical path becoming longer as the cloud is extended in the vertical. The radiation traversing the cloud from the surface has a longer path length through the cloud as the geometrical thickness is increased, though the

density of the absorbing medium decreases. This results in the radiation at TOA coming from a lower region in the atmosphere. The TOA BT's measured for geometrically thinner clouds will be more representative of those at cloud top, compared to the geometrically thinner clouds which will have a greater contribution from the surface and absorption by water vapour in the vertical column. As seen with a change in the optical depth and cloud top height, the least negative $BTD_{12.0\text{-}10.8}$ is seen at larger viewing zeniths and is due to the approach towards blackbody behaviour at these higher viewing angles.

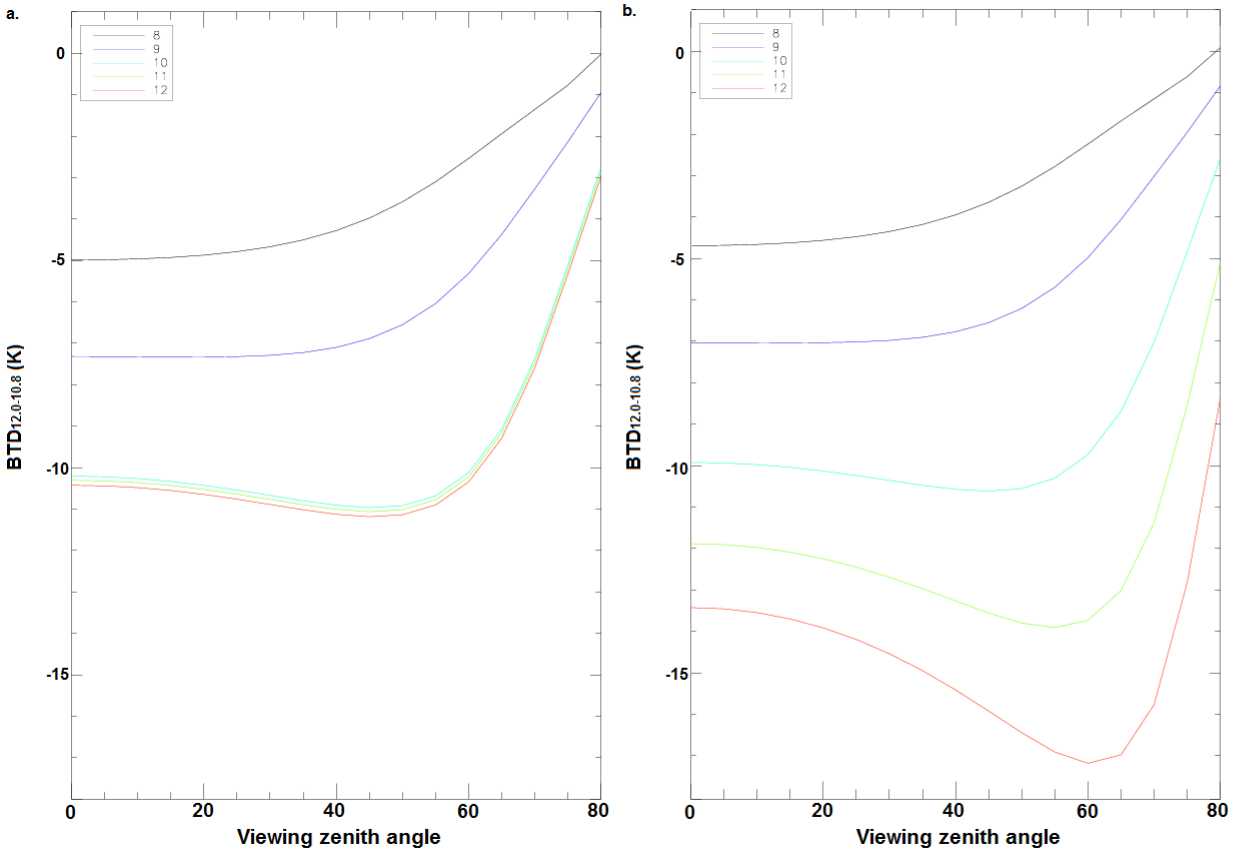

Figure 4.24: The sensitivity of $BTD_{12.0\text{-}10.8}$ to a change in the cloud top height between 8 km and 12 km, with a constant base height and a constant optical depth **for a)** a single cirrus event on June 4th at 0000. **b)** December 6th at 0000, as a function of viewing zenith angle. The colours represent cloud top heights, as shown in the legend.

4.5.9 Effective Radius

An important control on the radiative response of cirrus is the effective radius of the cirrus ice particle. The effective radius of a cirrus particle can range between 5 and 50 microns. The sensitivity to a change in effective radius was modelled between 10 and 40 microns at intervals of 5 microns (figure 4.25). In both cases, a decrease in the size of the effective radius results in greater absorption at 12.0 μm than 10.8 μm, creating a more negative $BTD_{12.0\text{-}10.8}$. In June, at 0° viewing zenith angle, a mean $BTD_{12.0\text{-}10.8}$ of -2.46 K is seen for an effective radius of 10. This increases to a mean of -1.59 K for an effective radius of 40. The

$BTD_{12.0\text{-}10.8}$ in December is lower at a viewing zenith angle of 0°, ranging from -4 K at an effective radius of 40 to -6.3 K at an effective radius of 10. This decrease in the $BTD_{12.0\text{-}10.8}$ with an increase in the effective radius is caused by the smaller particles presenting a larger cross sectional path compared to larger particles when keeping the geometrical thickness and optical depth constant. When viewed spectrally rather than as a channel radiance (figure 4.26), a steep gradient is seen between the two wavelength channels for smaller effective radii. This is shown in figure 4.26 for a cirrus profile in the June 2010 case study at a viewing zenith angle of 0°. The spectral response of brightness temperatures is shown for cirrus with effective radii of 10 microns (black line) and 40 microns (red line).

In relation to the viewing zenith angle, the $BTD_{12.0\text{-}10.8}$ for each effective radius tend to 0 with a viewing zenith angle above 10°. This shows more sensitivity to the change in the viewing zenith angle than with other cirrus cloud properties. The $BTD_{12.0\text{-}10.8}$ is lower for December at 0° and relates to the profile used in SBDART being representative of a thinner cirrus, as can be seen from the attenuated backscatter profiles (figure 4.19).

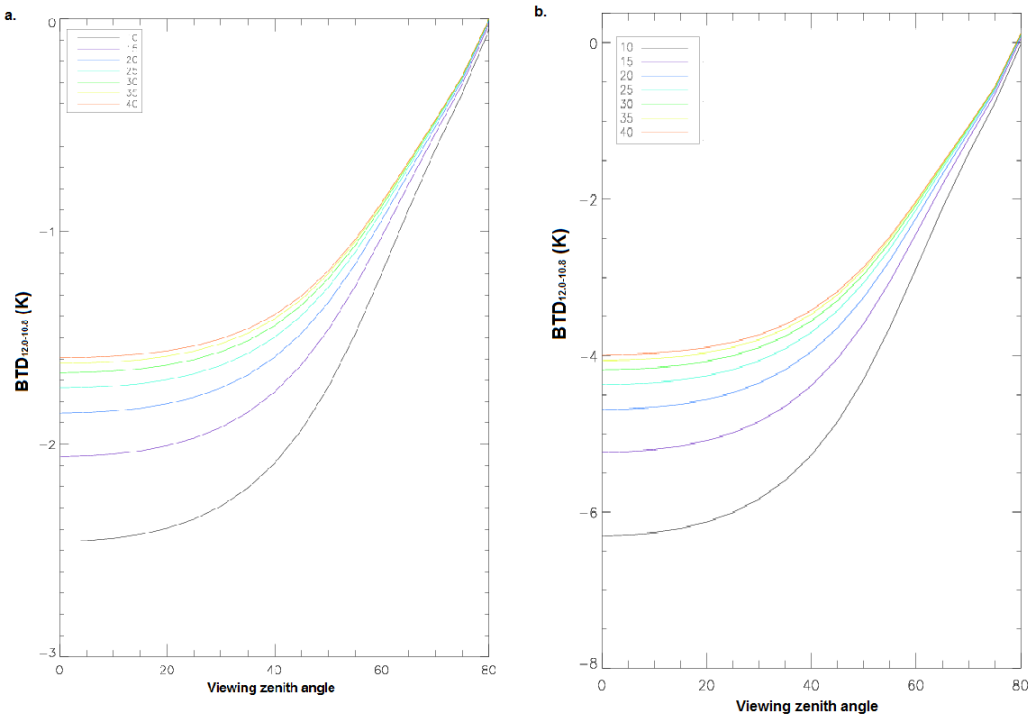

Figure 4.25: **a)** $BTD_{12.0\text{-}10.8}$ for a single cirrus cloud with a changing effective radius for June 4th at 0000. **b)** and December 6th at 0000 with a changing zenith angle. Effective radii are shown in the legend. Note the change in scale of the Y-axis.

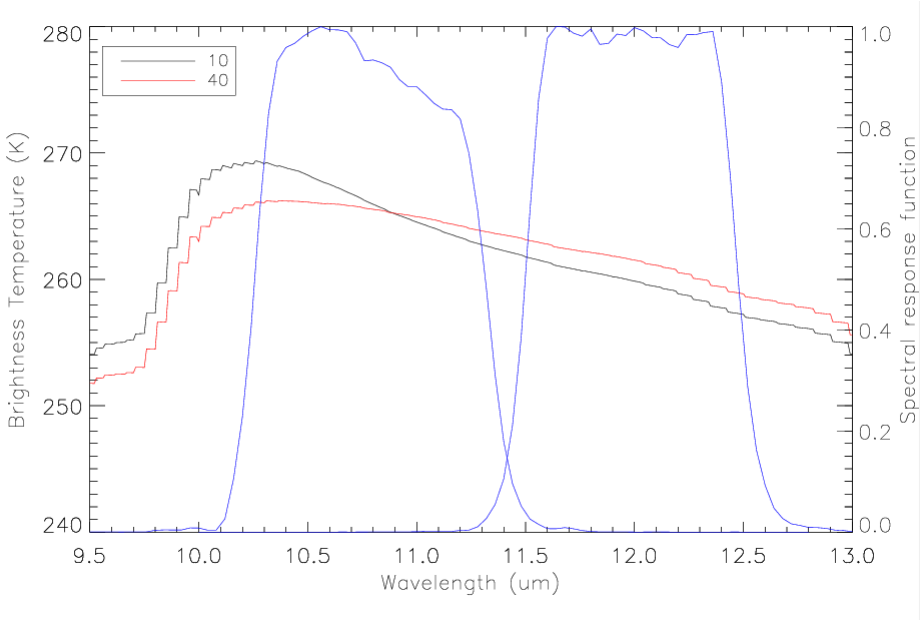

Figure 4.26: The spectral response of brightness temperatures to a profile containing a cirrus cloud in the June 2010 case study. The spectral brightness temperatures are modelled with an effective radius of 10 microns (black line) and 40 microns (red line) at a viewing zenith angle of 0°. The spectral response function for the 10.8 and 12.0 SEVIRI channels are also shown (blue).

From the sensitivity studies of $BTD_{12.0\text{-}10.8}$ above it is evident that little response is seen to a change in viewing zenith angle between 0° and 50°, though a greater sensitivity is seen when modelling the response to a change in the effective radius over viewing zenith angle. Above 50° a strong increase from negative $BTD_{12.0\text{-}10.8}$ to less negative thresholds are seen. $BTD_{12.0\text{-}10.8}$ are found to be most sensitive to changes in cloud height in the vertical when the cloud is kept at a constant thickness, and cloud top height when the cloud base is kept constant. The sensitivity of $BTD_{12.0\text{-}10.8}$ is also largely controlled by the atmospheric profile used as input into SBDART. The ranges modelled above are similar to the ranges found in the literature and inform the range of $BTD_{12.0\text{-}10.8}$ used when determining an appropriate threshold with ROC curves.

4.6 Receiver Operating Characteristics - Threshold Determination

The sensitivity study conducted above is used to inform the determination of POD, FAR and CSI for $BTD_{12.0\text{-}10.8}$ thresholds for the detection of cirrus. Colocated matchups are conducted between SEVIRI $BTD_{12.0\text{-}10.8}$ and the 2B-CLDCLASS-LIDAR cloud classifications of cirrus over the study region in June and December 2010. The matchups are conducted at both day and night constrained by the CloudSat and CALIPSO fly over times. Thresholds are calculated at intervals of 0.5 K between 0 and -5 K.

It is seen that all but December night time cases (figures 4.28a and b, figure 4.29a) tend towards a POD of 1 with a 0 K threshold. A POD of 1 at 0 K means all clouds are detected at this threshold though a large overestimation will also occur due to the classification of all high or optically thick cloud tops as cirrus, including deep convection, where BT's are emitted from the cloud top. For example, a success ratio of 0.45 is seen for December day time when POD is 1. From the earlier SBDART modelling of clear sky brightness temperatures a mean $BTD_{12.0\text{-}10.8}$ of -2.2 K and a minimum of -0.7 K was found (table 4.3), suggesting a

$BTD_{12.0\text{-}10.8}$ of 0 K will severely overestimate the the number of cloud covered scenes.

The most successful thresholds are determined based on the maximisation of CSI, whilst keeping a reasonable POD and success ratio and are also chosen due to their proximity to the 1-1 line in the ROC curve, with the most successful thresholds generally closest to this line (Roebber, 2009). . The most successful thresholds for June are shown in tables 4.11. The most successful threshold for June day time cases is -3 K. This threshold has a SR of 0.48 with POD of 0.59, and a CSI of 0.36.

For June night time cases (figure 4.28b), the most appropriate threshold was determined to -1 K. This threshold has a SR of 0.85, with a POD equaling 0.81. CSI was 0.72 for this threshold.

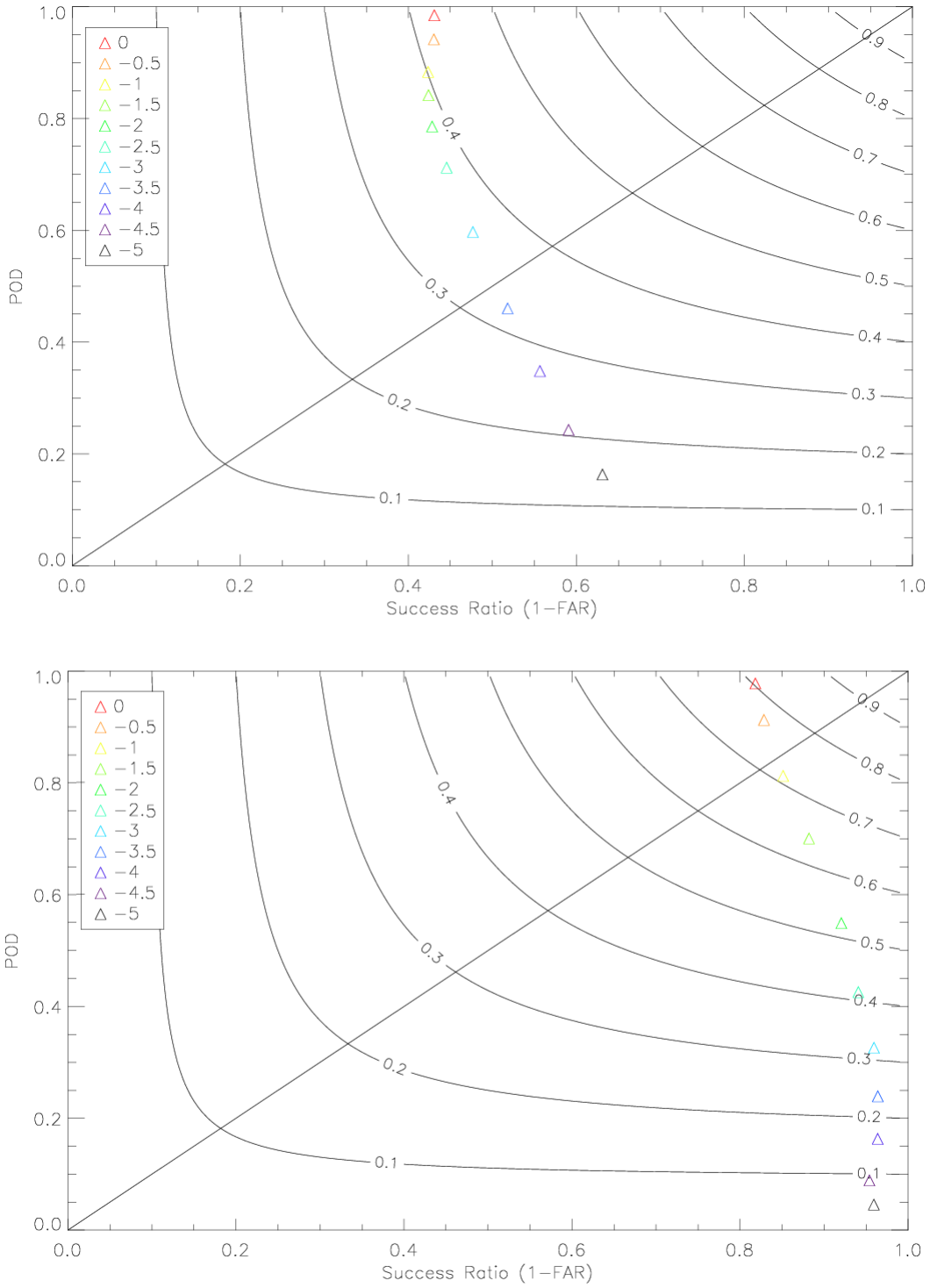

Figure 4.27: **a)** POD vs success ratio for June 2010 day time $BTD_{12.0\text{-}10.8}$ thresholds. **b)** POD vs success ratio for June 2010 night time $BTD_{12.0\text{-}10.8}$ thresholds.

	$\mathbf{BTD_{12.0\text{-}10.8}}$	POD	FAR	SR	CSI
Day	-3 K	0.59	0.52	0.48	0.36
Night	-1 K	0.81	0.15	0.85	0.71

Table 4.11: POD, FAR, SR and CSI for most successful $BTD_{12.0\text{-}10.8}$ for June day and night time cirrus

The most successful threshold for December day time cases of -2.5 K possesses a CSI of 0.4 with a SR of 0.59 and POD of 0.56 (figure 4.28a). For December night time cases (figure 4.28b) the most successful threshold is found to be 0 K. CSI is 0.55, SR is 0.65 with a POD of 0.79. Similar to June night time cases the POD for the most successful threshold is high with a low FAR. In order to analyse a clear UTH and OLR response to deep convection, this high POD gives confidence in the ability to mask high level clouds.

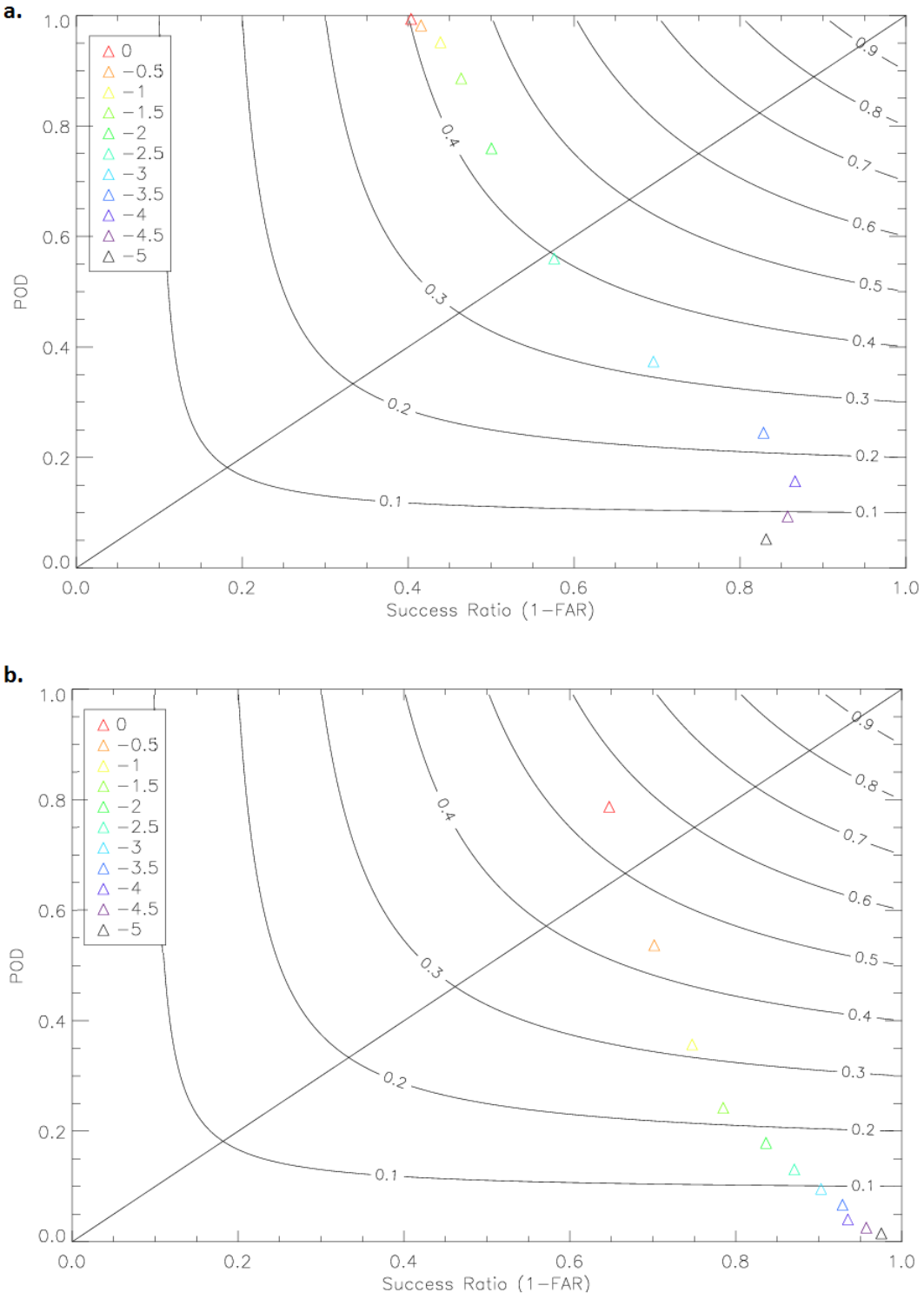

Figure 4.28: **a)** POD vs success ratio for December 2010 day time BTD12.0-10.8 thresholds. **b)** POD vs success ratio for December 2010 night time BTD12.0-10.8 thresholds.

	$\mathbf{BTD_{12.0\text{-}10.8}}$	POD	FAR	SR	CSI
Day	-2.5 K	0.56	0.31	0.59	0.4
Night	0 K	0.79	0.35	0.65	0.55

Table 4.12: POD, FAR, SR and CSI for most successful $BTD_{12.0\text{-}10.8}$ for December day and night time cirrus

4.7 Conclusion

The sensitivity of SEVIRI $BTD_{6.2\text{-}7.3}$ and $BTD_{12.0\text{-}10.8}$ to changes in key cloud properties are modelled. These cloud parameters were cloud top heights, thicknesses effective radius and optical depths. The $BTD_{6.2\text{-}7.3}$ sensitivity to deep convection is modelled using both a case study to determine the sensitivity of $BTD_{6.2\text{-}7.3}$ to a change in viewing zenith angle and all deep convective profiles in June 2010. $BTD_{6.2\text{-}7.3}$ is found to be most sensitive to a change in cloud top height. Little sensitivity is seen to both optical depth, due to the large optical depths characteristic of this cloud type, and viewing zenith angle, due to the satellite received radiances at both wavelengths primarily being measured at cloud top. The range of $BTD_{6.2\text{-}7.3}$ found in the sensitivity tests are within that found in the literature, and based on these earlier studies and the theoretical understanding of weighting functions, are representative of deep convection in both the early stage and the mature stage of its lifecycle. This gave a guide as to which thresholds are most sensible for detecting deep convection.

To determine sensible $BTD_{6.2\text{-}7.3}$ thresholds, colocated matchups between SEVIRI $BTD_{6.2\text{-}7.3}$ and CloudSat cloud classifications are conducted. The most effective thresholds are found using four key statistics - POD, FAR, SR and CSI. These are geometrically related and allow for an understanding of how a change in a threshold will create more false alarms or have a greater probability of detecting the deep convection. Initial tests showed an overestimation of deep convection by SEVIRI, represented by a high FAR. It was found that this overestimation was due to classification of deep convective anvil as Altostratus by the CloudSat algorithm. Based on previous studies by Yuan and Houze, jr. (2010) the contiguous anvil surrounding the cloud was reclassified as deep convection and the colocated matchup conducted again. The probability statistics were recalculated and showed that the contiguous anvil within 1 cloud radii and with a thickness of 5 km or less, when reclassified as deep convection provided the most successful $BTD_{6.2\text{-}7.3}$ thresholds. In comparison with other studies using SEVIRI such at that of Schroder *et al.,* (2013), this study includes anvil as well the deep convective cores in the masking of the clouds. This allows for a much higher confidence that only clear sky pixels will be seen. This also confirms findings by Yuan and Houze, jr. (2010) that the CloudSat algorithm is limited in its ability to determine cloud types when just using microphysical parameters.

The CloudSat classifications are further split into day and night time cases based on the over pass time of CloudSat. Thresholds are calculated for June and December to allow for any seasonal differences to emerge from the differences in the distribution of deep convective cloud top heights between these two periods.

The determination of thresholds with the four probability statistics show the most successful thresholds for the detection of deep convection to be -9K for June day time; -3 K for June night time; -3 K for December day time and -7 K for December night time. These thresholds are representative of the cloud profiles at these time periods and the life cycle of deep convective clouds.

The sensitivity of $BTD_{12.0\text{-}10.8}$ to a change in cirrus cloud properties were also modelled using SBDART. The key cirrus cloud properties included cloud top height, cloud height in the vertical, optical depth and effective radius of the cirrus ice particle. This was also modelled over a range of viewing zenith angles to

understand the response of $BTD_{12.0\text{-}10.8}$ at higher viewing zenith angles. The greatest sensitivity is found when changing cloud geometrical thickness, whilst little sensitivity is found in relation to the viewing zenith angle between 0° and 50°.

SEVIRI $BTD_{12.0\text{-}10.8}$ thresholds were matched with colocated 2B-CLDCLASS-LIDAR cloud classifications. This product is a combination of both CloudSat and CALIPSO measurements and provides a more accurate representation of cirrus than CloudSat alone. The sensitivity study provided a guide as to the range of $BTD_{12.0\text{-}10.8}$ thresholds to use in the colocated matchup. The thresholds were again determined using the POD, FAR, SR and CSI. The most successful thresholds found for cirrus detection were -3 K for June day time; -1 K for June night time; -2.5 K for December day time and 0 K for December night time. These thresholds show good agreement with those found by Negri *et al.,* (2012) and Lensky and Rosenfeld (2008) who also used similar thresholds for cirrus detection. This provides a method for determining clear skies based on two different methods of cloud detection and masking, whilst most previous studies have relied upon a single temperature threshold. Though this has been sufficient for those studies, the use of two separate thresholds based on the response of brightness temperatures to the distribution of water vapour in the vertical column ($BTD_{6.2\text{-}7.3}$) and differential water vapour absorption ($BTD_{12.0\text{-}10.8}$) in the troposphere gives a higher degree of confidence that upper level and thick clouds will be masked in the analysis of clear sky pixels.

Chapter V

Cloud Tracking Algorithm

5 Overview

In order to understand the effect of deep convection on variables such as clear sky UTH and OLR over a clouds lifetime, a method of cloud tracking needs to be implemented alongside a cloud detection method like that developed in chapter 4. Similar to this study, methods of cloud detection and tracking have generally employed brightness temperature thresholds to identify and track clouds. Early cloud tracking methods using satellite data were conducted manually, with Aspliden *et al.,* (1976) and Martin and Schreiner (1981) manually tracking MCS's during GATE (Global Atmospheric Research Program Atlantic Tropical Experiment), whilst Laing and Fritsch (1993) also manually tracked mesoscale convective systems over India and over Africa using data from the Meteosat satellite. Manual tracking methods are subjective and hard to replicate, with the user also limiting the temporal range of the study, due to the lengthy time involved in the process.

To overcome such constraints, automated cloud tracking algorithms were developed, with early examples including that of Woodley *et al.,* (1980), who developed an algorithm based on the identified convective system meeting a propagation speed criterion. Using an automated tracking technique based on area overlap only, Williams and Houze (1987) developed a tracking system for MCS's, with Arnaud *et al.,* (1992) developing a similar system with additional checks on cloud splitting and merging. This method was developed further by Machado *et al.,* (1998) to track MCS's, with additional criteria on the temperature gradient over the cloud, the radius of the cloud and the shape and orientation of the cloud. The area overlap method was further tested by Machado *et al.,* (1998) with a weighted average of 28 cloud properties including the area overlap that may add information to the tracking algorithm, but no change in the accuracy of the algorithm was found when compared to a combination of tracking and visual inspection by a meteorologist. For this reason, and for its simplicity, the area overlap method has become the most common method of cloud tracking, with recent examples including that of Zinner *et al.,* (2008) who use an area overlap method to track deep convection using SEVIRI. This method is also applied to atmospheric phenomena other than clouds, with more recent studies including that of Ashpole and Washington (2013) using this method to detect and track dust events over the Sahara.

Using the cloud detection thresholds and masking methods developed in chapter 4, a cloud tracking algorithm has been developed based on the previous methods already discussed - area overlap, and a further criteria - the midpoint displacement. The splitting and merging of cloud systems is also accounted for. In order for this tracking algorithm to allow for a robust quantification of the response of both clear sky UTH and the corresponding OLR to deep convection in the spatio-temporal domain, SEVIRI data is interpolated to the GERB high-resolution (HR) scale (9*9 km at nadir) with the method involved described in section 5.1. This interpolation allows for a direct comparison between UTH and OLR at the same resolution.

The effect a change in the $BTD_{6.2\text{-}7.3}$ threshold between the two thresholds selected has on the frequency of deep convection detection is subject to a sensitivity test, whereby the algorithm is applied to the GERB HR scale 6.2 μm and 7.3μm data and clouds are tracked through their lifecycles over the study period. The cloud tracking algorithm is then developed and discussed with examples given of the effect of each criteria in

the algorithm. The implementation of the cloud tracking algorithm is then applied to a case study, whereby several clouds are tracked over their lifetime. This then allows for the analysis of the response of UTH and OLR to deep convection over the clouds lifetime, discussed in chapter 6.

5.1 SEVIRI to GERB HR Interpolation

To robustly quantify the response of UTH and OLR to deep convection, the four SEVIRI channels used in this study are interpolated to the GERB scale, known as GERB HR. This is conducted to allow for a direct comparison between the GERB and SEVIRI pixels when a cloud is being tracked.

The conversion to GERB HR scale from SEVIRI causes the number of deep convective systems detected to reduce. Due to the use of 9 SEVIRI pixels in one GERB HR resolution pixel, it is seen that a smaller number of larger convective systems are detected than when using SEVIRI. The intensity of the $BTD_{6.2\text{-}7.3}$ is also seen to decrease at the extremes. This is shown in a probability density function of $BTD_{6.2\text{-}7.3}$, comparing SEVIRI and GERB HR scale $BTD_{6.2\text{-}7.3}$ on June 2nd 2010 at 00:00 UTC (figure 5.1). Based on this time step, maximum $BTD_{6.2\text{-}7.3}$ at the SEVIRI scale was found to be 4.2 K, compared to 2.3 K at the GERB HR scale. A peak in the distribution of $BTD_{6.2\text{-}7.3}$ can be seen between -17 K and -15 K. From the modelling study in chapter 4, it is likely that this relates to clear sky, whilst the small peak between -2 K and 0 K may be representative of deep convection.

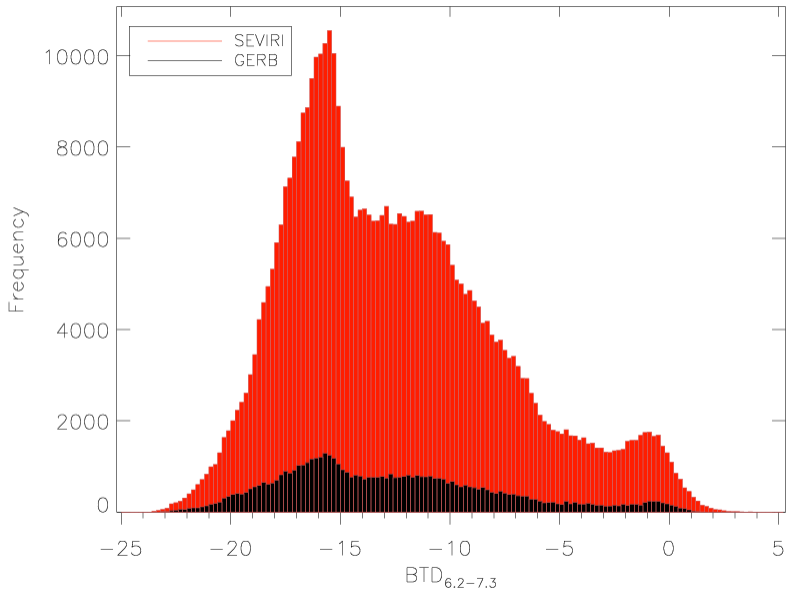

Figure 5.1: Distribution of the SEVIRI (red) and GERB HR scale (black) $BTD_{6.2\text{-}7.3}$ on June 2nd 2010 at 00:00 UTC.

In context of the spatial analysis conducted in chapter 4 for the matchup between SEVIRI and CloudSat, it was found that with an increase in the distance allowed from the CloudSat point to the corresponding SEVIRI pixel, no change in accuracy (POD and FAR) was found. POD and FAR were calculated to be the same at each $BTD_{6.2\text{-}7.3}$ threshold tested for each spatial difference. Based on this result, the thresholds

developed at the SEVIRI scale will not have to be changed when moving from SEVIRI scale pixels to GERB HR scale.

5.2 Cloud Tracking Algorithm

Based on the need to track deep convection in both the temporal and spatial domains, a cloud tracking algorithm is developed and implemented, based on two criteria - area overlap and the midpoint displacement.

Firstly, deep convection is identified in the SEVIRI water vapour channels using the $BTD_{6.2\text{-}7.3}$ threshold developed in chapter 4. The $BTD_{6.2\text{-}7.3}$ used allows for the core of the deep convective cell as well as the contiguous anvil attached to core within 1.5 cloud radii to to be identified. Clouds are identified and labelled as being an individual cell using a nearest neighbour technique, whereby any consecutive pixels classed as deep convection in the image with the $BTD_{6.2\text{-}7.3}$ method are labelled as the same cloud.

Secondly, once a cloud is detected in the first timestep, the tracking algorithm is implemented. The labelling technique is applied to the second timestep, allowing the clouds in timestep 1 to be matched to those in timestep 2. The criteria and process involved in the tracking algorithm is shown in a simplified flow diagram in figure 5.2. All clouds that satisfy the $BTD_{6.2\text{-}7.3}$ detection threshold are tracked. The cloud tracking algorithm follows the same process for each cloud detected in each timestep until the cloud is no longer classified as deep convection using the $BTD_{6.2\text{-}7.3}$ threshold. When the cloud tracking algorithm has analysed all detected clouds in timestep 1 using the criteria above, it will move onto timestep 2, where the process is repeated on newly detected clouds.

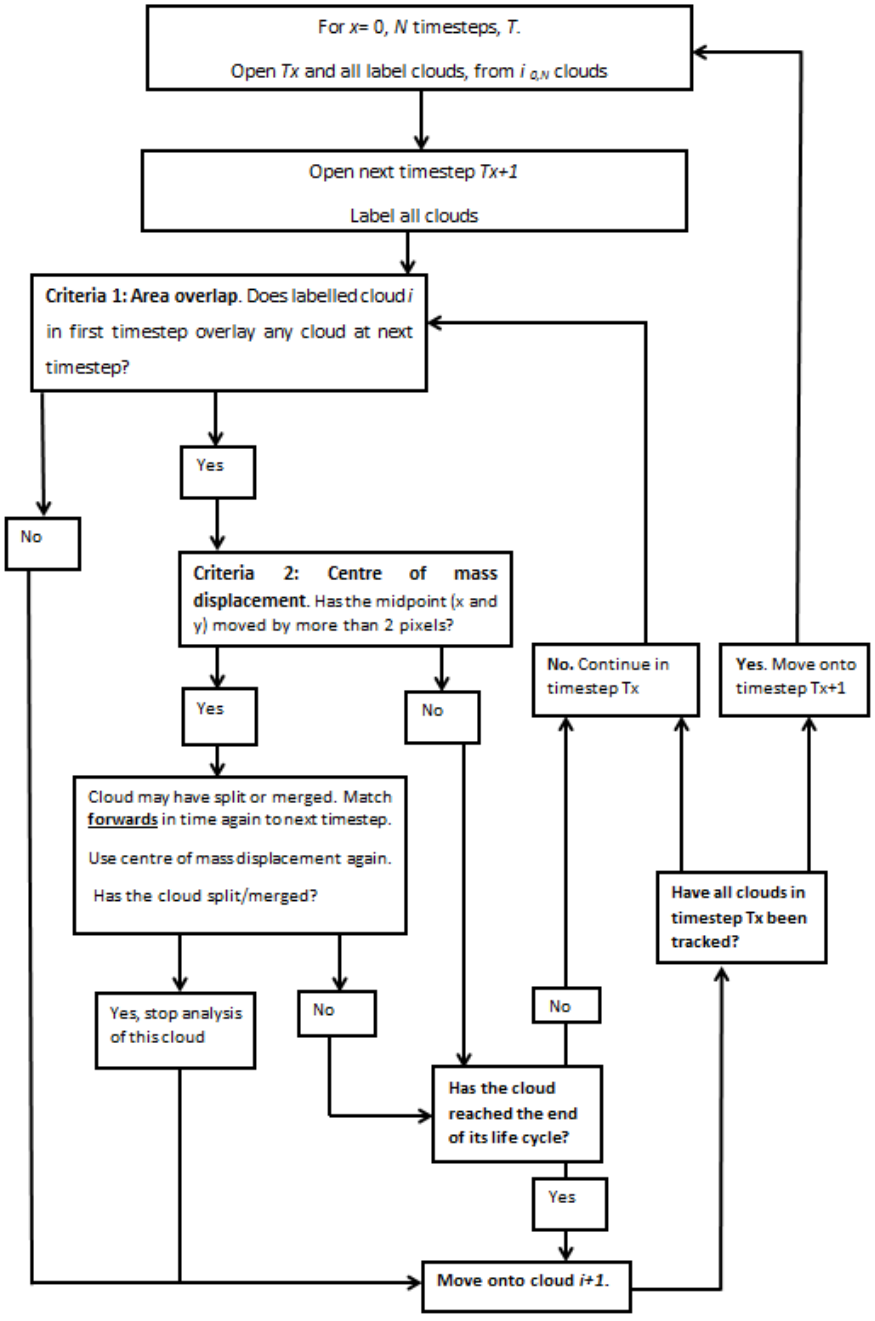

Figure 5.2: Flow chart describing the cloud tracking algorithm developed to track clouds over study area. The flow chart shows the tests that are considered for each cloud. The cloud tracking algorithm is described in more detail below.

For each tracked cloud, the mid-point is taken, along with the cloud 'radius', cloud area, perimeter, and the average, maximum and minimum $BTD_{6.2\text{-}7.3}$. These parameters are used in the analysis to provide criteria which can be used to compare the effects on UTH and OLR between different cloud sizes and lifecycle lengths in chapter 6. In order to measure cloud radius, the clouds are not assumed to be circular due to there

not being an equal distance between the cloud centre point and the edge. The cloud 'radius' is calculated as the distance between the centre of the cloud (x0, y0) and the furthest point away that is still classified as being the same cloud (x1, y1) (figure 5.3).

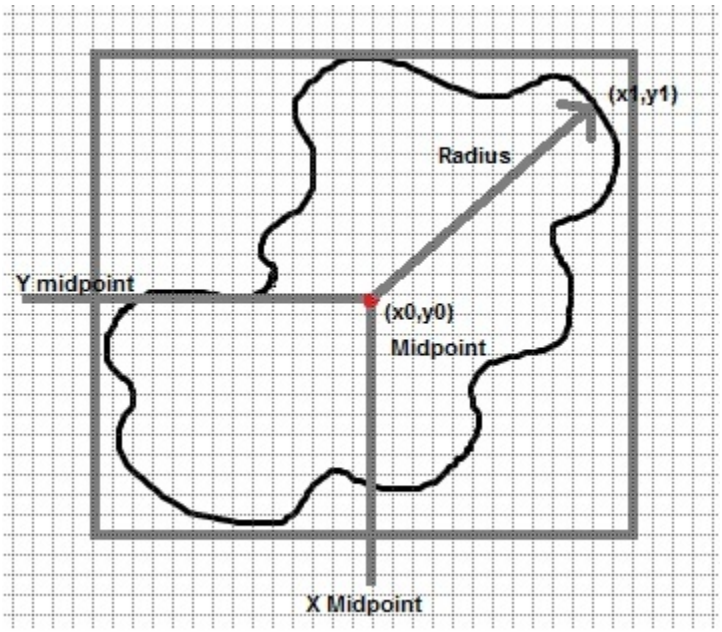

Figure 5.3: Cloud radius calculation. The radius is taken as the distance between the centre, (x0,y0) (red dot) and the furthest edge (x1,y1).

All clouds were analysed from the beginning of their life cycle - defined as the point at which they are first classified as deep convective clouds, until the point where this classification no longer applies - when the cloud top $BTD_{6.2\text{-}7.3}$ is below the threshold or they have split/merged. Any clouds that had already developed and were detected in the first timestep (00:00 UTC on June 1st 2010 and December 1st 2010) were masked and not tracked, allowing for only newly developed clouds in the following timesteps to be tracked and analysed. The cloud tracking algorithm is described in more detail below.

5.2.1 Criteria 1: Area overlap

The first criteria is based on the need to analyse clouds that are the same cloud in each following time step. This criteria was first used by Williams and Houze (1987) and forms the basis of most cloud tracking algorithms as discussed above, and when using a high temporal resolution dataset such as SEVIRI it provides a simple but effective way of detecting which clouds are the same in each following timestep. In their original study, Williams and Houze (1987) used a temporal resolution of 3 hours and an area overlap minimum of 50%. The use of SEVIRI, with a 15 minute temporal resolution allows for less ambiguous matching process between timesteps, negating the need for a fractional overlap in this criteria.

The criteria is the first step in determining if the cloud N1 in T1 is the same cloud in T2. The area overlap method assumes the labelled cloud N_1 at timestep T1 could be the same cloud in the next timestep, T2, if any of the newly labelled cloud in T2 overlaps a cloud at T1. If there is overlap it could be the same

cloud, or a split/merged cloud and is then passed to criteria 2 where this is determined. If the cloud in the first timestep, T1, does not overlap another in the second timestep, T2, this criteria is not satisfied and the cloud is assumed to have ended its lifecycle. This shown in a simple schematic in figure 5.4.

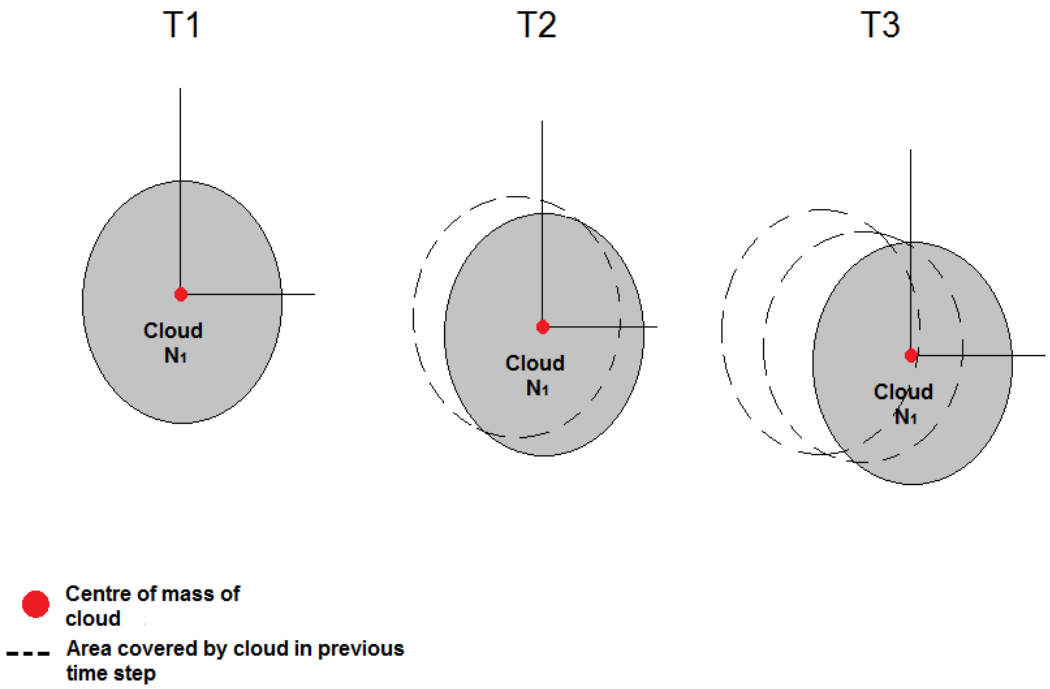

Figure 5.4: Schematic of the area overlap method used in the cloud tracking algorithm. A cloud is first detected in T1. The cloud is then also detected in T2. The dashed line at T2 shows the area occupied by the cloud in T1. If the cloud overlaps it is assumed to be the same cloud and is passed on to criteria 2 in the cloud tracking algorithm. If this passes criteria 2, the area overlap is calculated for T3. this process is repeated until the clouds lifetime is determined to have ended.

5.2.2 Criteria 2: Midpoint displacement

If a cloud has been classified as overlying, it is passed on to criteria 2 - the midpoint displacement. For a cloud labelled in T2 to be classified as the same cloud in T1, the clouds midpoint (taken as the midpoint from which the radius was calculated) must have moved less than 18 km. This distance is based on Mathon and Laurent (2001), who found convective propagation speed to be less than 22 m s^{-1}. If a cloud in T2 is overlying the area occupied by a cloud in T1, and the midpoint displacement was less than 18 km between 15 minute timesteps it is classified as the same cloud. This is shown schematically in figure 5.5.

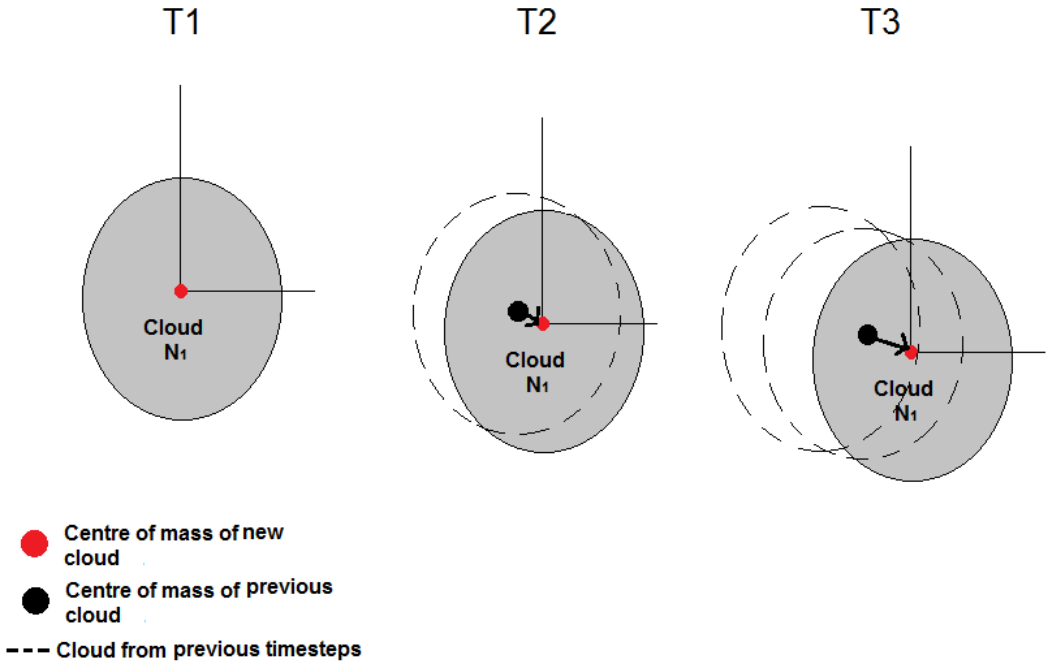

Figure 5.5: Schematic of the area overlap method used in the cloud tracking algorithm. A cloud is first detected in T1 and the midpoint is calculated. The cloud is then also detected in T2 and the new midpoint is calculated. The dashed line at T2 shows the area occupied by the cloud in T1. If the cloud overlaps and the centre off mass displacement is less than 18 km it is assumed to be the same cloud by the cloud tracking algorithm. The cloud is then tracked through to T3 and this process is repeated until the clouds lifetime is determined to have ended.

5.2.3 Splitting and merging

As a cloud develops, dissipation and splitting of smaller clouds from the main system becomes a common feature, especially when a cloud is in the mature stage of the life cycle. In order to track a cloud over its lifecycle, this splitting and merging has to be considered with regards to which part of the system is to be tracked through time.

If the cloud in T2 overlies a cloud in the previous timestep T1 it is possible that this cloud is a 'split cloud'. A split cloud is defined as any smaller, newly formed cloud (either a newly formed convective cell or part of the older system that has split away) that overlies the area previously occupied by a cloud in the previous time step. The cloud is defined as newly formed because the labelling method will classify this a new cloud. The splitting of clouds introduces an unrealistic midpoint displacement (Vila *et al.*, 2008). The 'split cloud' is the cloud with the largest midpoint displacement when more than one cloud overlies the area occupied by a cloud in the previous timestep. This can be seen in a schematic in figure 5.6. When a cloud splits from the system in T1 and is classified as a new cloud in T2, the midpoint of the new 'split cloud' will be based on the smaller area that the new cloud covers and this will have changed significantly to the midpoint in T1 (figure 5.6). This invokes a new tracking criteria, whereby the two clouds (the original cloud and the split cloud) in timestep T2 are tracked forwards in time again to T3. This uses the midpoint displacement and

area overlap criteria forwards in time to allow the tracking algorithm to decide which cloud to follow. If a new cloud is classified as a split cloud by the algorithm and overlies a cloud from the previous time step it is not tracked, as the algorithm recognises the area previously occupied by a cloud and that it was part of a previous, already maturing system. This area will have already been tracked and masked by the algorithm so the split cloud is not tracked or analysed.

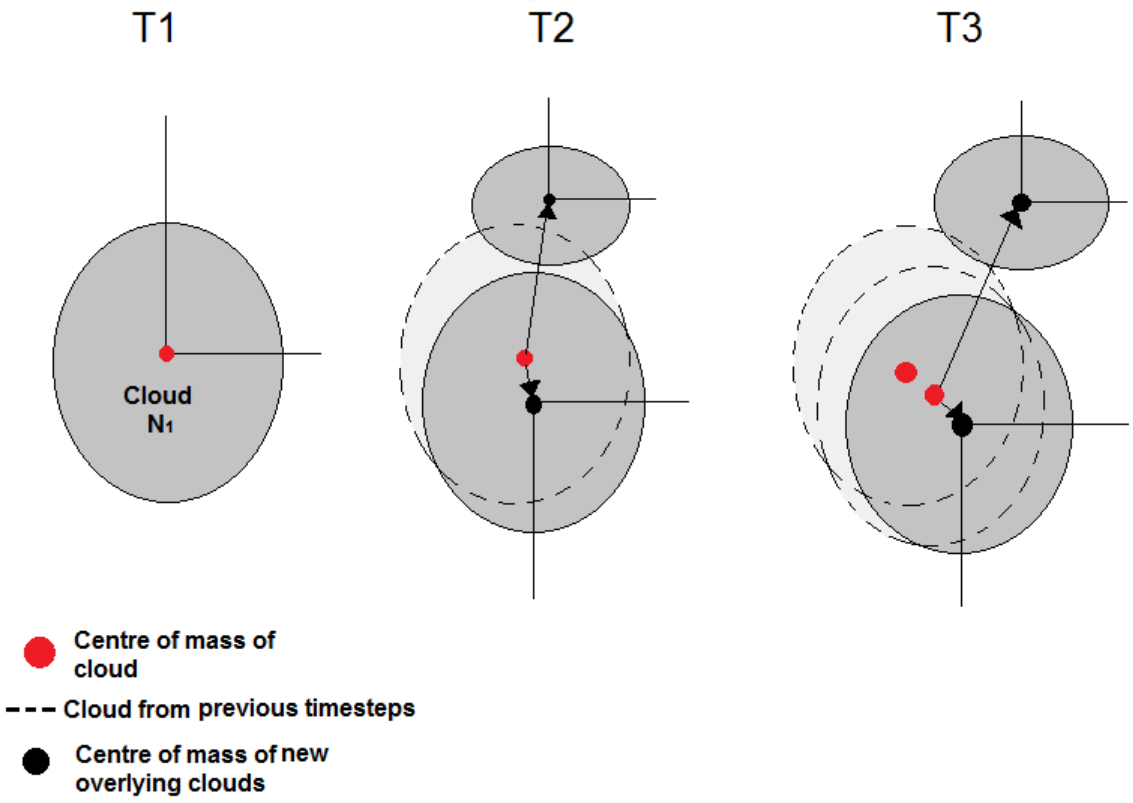

Figure 5.6: The forward tracking of clouds when a cloud may have split. At timestep T2 we see two clouds are overlying the area previously occupied by N_1 at T1. If there is more than one cloud overlying the area cloud N_1 occupied at T1 (e.g. when a cloud has split), the algorithm will search T3 to decide which cloud to track. This is decided through the calculation of the midpoint displacement. The cloud with the smallest midpoint displacement is taken as the cloud to follow (the larger cloud at T3) because clouds with a large midpoint displacement are assumed to be splitting from a larger cloud (the smaller cloud at T3).

An example of a splitting cloud is also given in figure 5.7. Splitting can be seen at 14:45 UTC on the 7th June 2010 (shown at half hourly intervals in figure 5.7). Cloud 1, a larger system, splits into two clouds at 15:15 UTC, number 2 being a smaller cloud than cloud 1. In this case, the cloud tracking algorithm continues to track cloud 1, whilst cloud 2 is not tracked as it part of an older system. Cloud 1 then splits again at 15:45 into cloud number 1 and 3. Again, like cloud 2, cloud 3 is not tracked but cloud 1 is. Cloud splitting generally forms smaller clouds compared to the larger system it has split from. Split clouds are masked in the subsequent time steps so no analysis will occur on these.

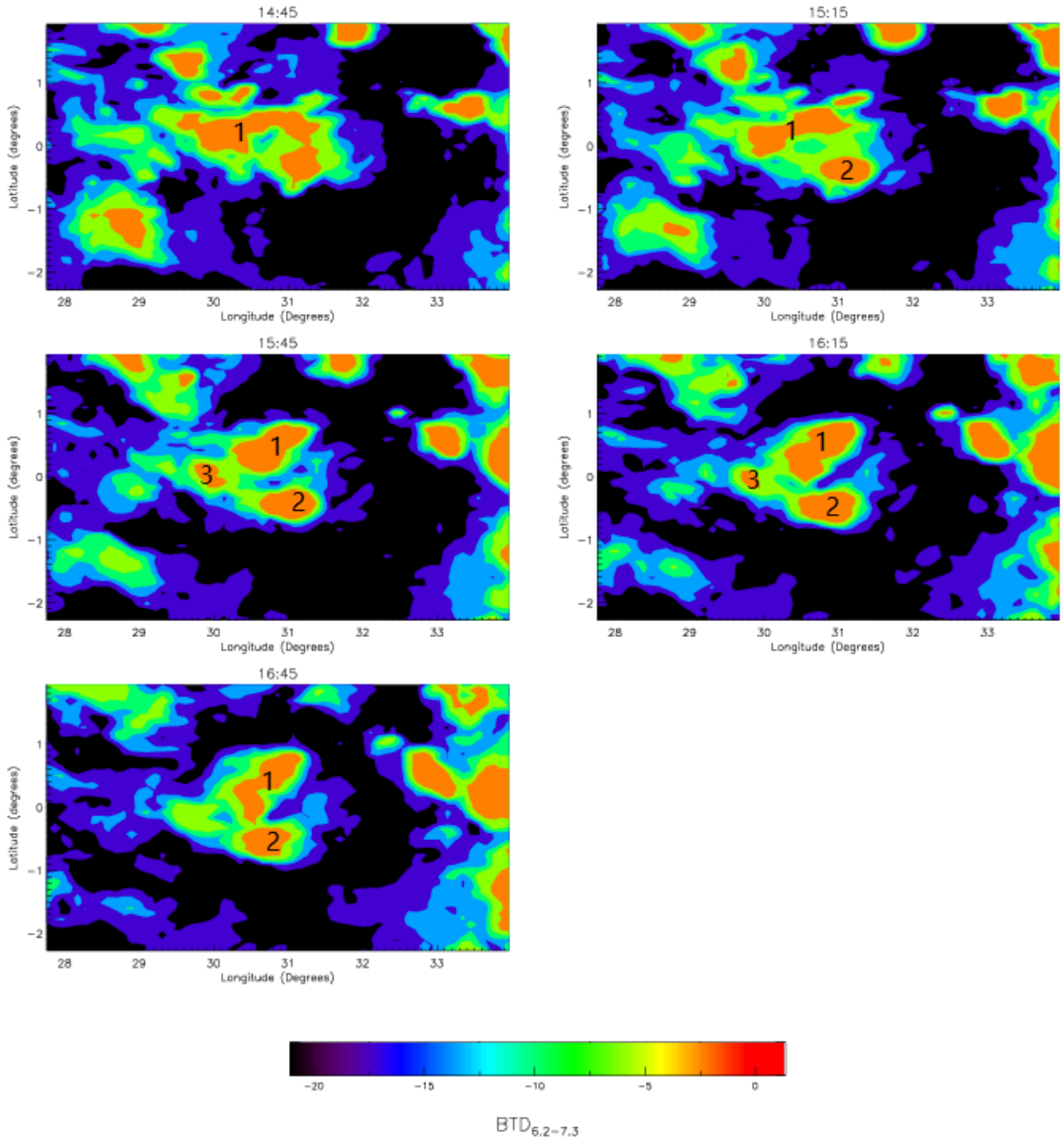

Figure 5.7: An example of clouds splitting (shown at half hourly intervals). This example is from the 7th June 2010 at 14:45. The cloud are numbered 1, 2 and 3. At 15:15 cloud 1 splits into clouds 1 and 2. In this case, only cloud 1 is tracked, as cloud 2 has split off the larger system. Cloud 3 then splits off of cloud 1 at 15:45, which again, is not tracked due to this splitting off the larger system.

A merged cloud is defined as a previously classified cloud that has a large midpoint displacement between timesteps based on the joining of two clouds and the greater area on which to base the calculation of the cloud centre on. An idealised schematic of a merged cloud is shown in figure 5.8. Two clouds are labelled in the first timestep, T1. In the second timestep, T2, these clouds begin to merge. By the third timestep, T3, the smaller cloud has merged with the larger cloud, creating one larger cloud. The midpoint has shifted due to the merging of the two systems and is calculated at the red dot. This red dot is furthest from the midpoint of cloud N_2. Therefore the algorithm continues to track cloud N_1.

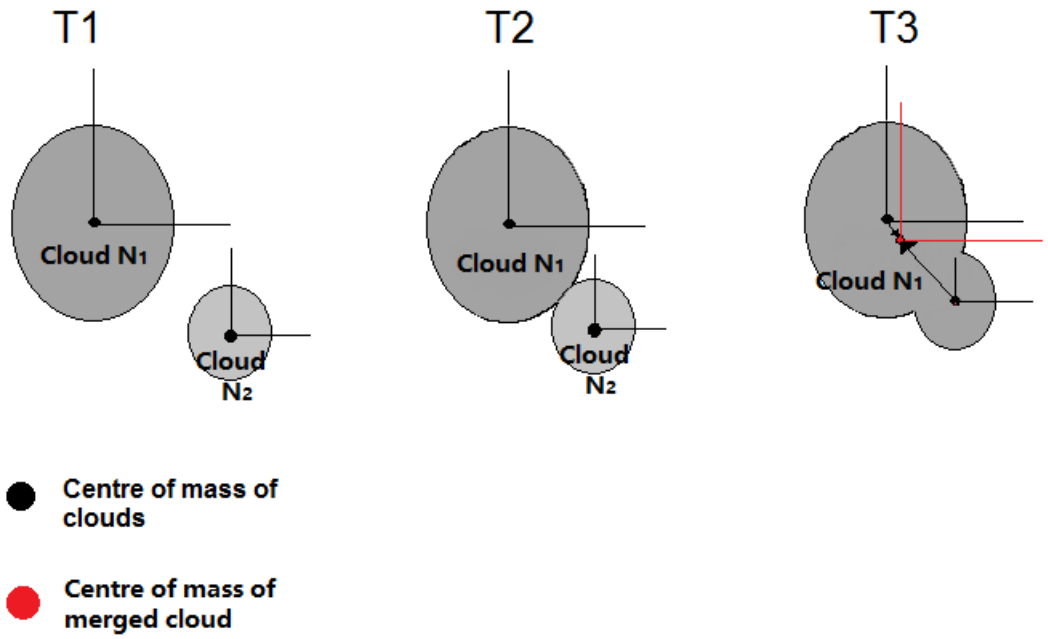

Figure 5.8: A diagram to depict two clouds merging. Two clouds, N_1 and N_2 are detected at timestep T1. These clouds begin to merge in timestep T2. As the cloud merges in timestep T3, the midpoint fro each cloud shifts. The greatest distance between the two original centres and the new centre is between that of cloud N_2 and the new centre. Therefore the tracking algorithm continues to track cloud N_1, not N_2.

The merging of larger systems also occurs as clouds grow and expand, creating larger mesoscale systems. This can be seen in an example given in figure 5.9. At 23:30 UTC on 6th June 2010 two larger systems, numbered 1 and 2, are detected. As the clouds evolve, they begin to merge with each other (01:00 UTC) and becoming one larger cloud (01:30). Based on the algorithm discussed above, as cloud 2 merges with cloud 1, this is classed as the end of that clouds lifecycle, whilst cloud 1 is defined as the cloud to be tracked.

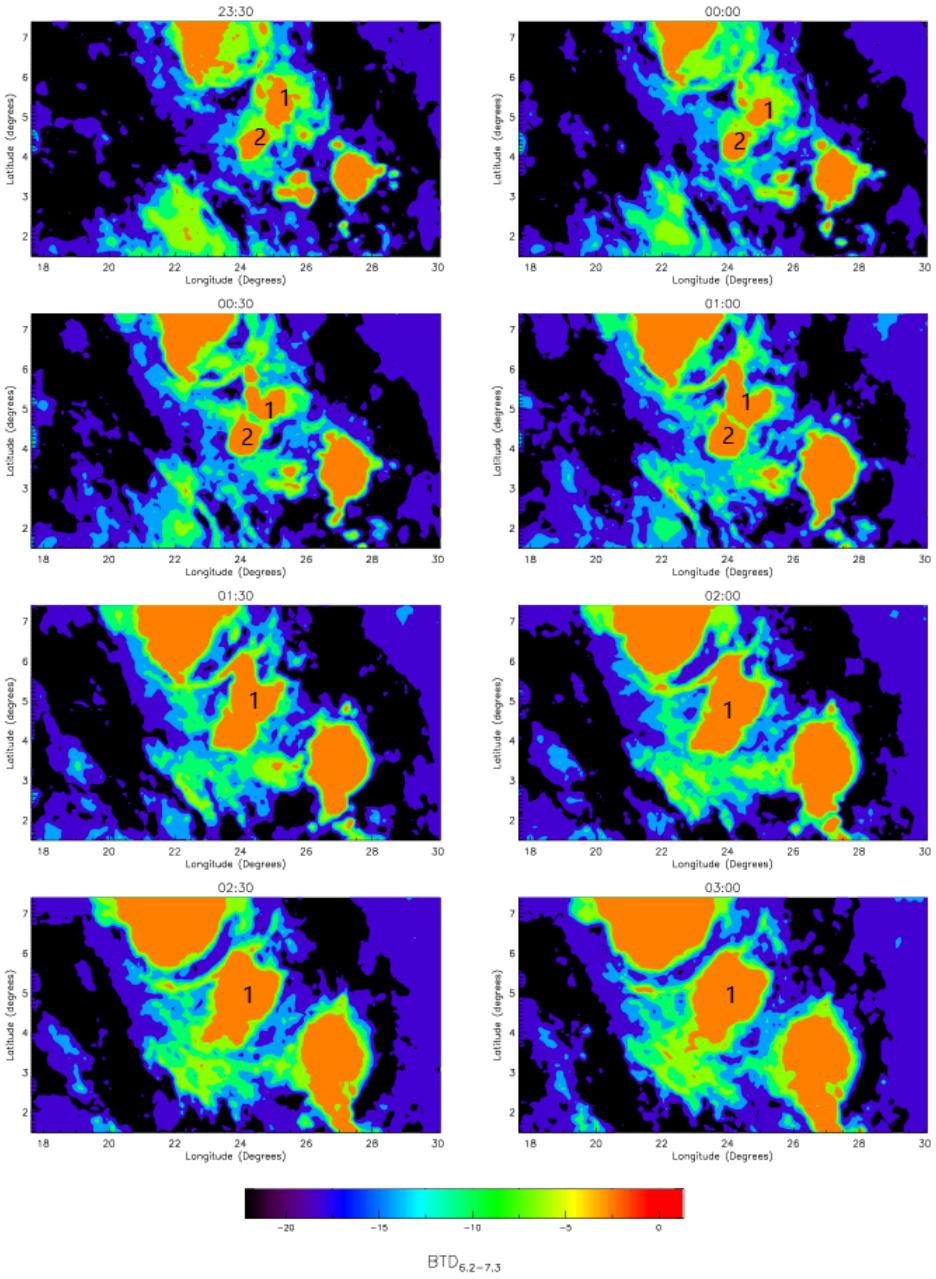

Figure 5.9: An example of two clouds merging (shown at half hourly intervals) . This example is from the 6th June 2010 at 23:30. The cloud are numbered 1 and 2. As cloud 2 merges with cloud 1 at 01:30, cloud 2 can no longer be tracked as the midpoint displacement is larger for cloud 2 than cloud 1. This is the end of cloud 2's life and the larger merged cloud 1 continues to be tracked.

5.3 Sensitivity Test

The $BTD_{6.2\text{-}7.3}$ threshold used for the detection of deep convection was validated at the native SEVIRI resolution in the previous chapter against CloudSat tracks between 11:00-13:00 and 23:00-01:00 due to the

orbital characteristics of this instrument. As discussed in chapter 4, the validated thresholds are a reflection of the $BTD_{6.2\text{-}7.3}$ at these times only. Due to there only being two time periods available for determining the most effective threshold, the effect of using a step change in $BTD_{6.2\text{-}7.3}$ between the two validated BTD's is compared to a sinusoidal change in temperature between the two thresholds found (figure 5.10). A sensitivity test is conducted between 5 days, from the 10th June 2010 to 15th June 2010. The frequency of convection, defined as the number of newly detected deep convective clouds, is shown against time of day. This is compared to the temperature threshold used in the sensitivity test. The step change temperature threshold is set at -3 K between 18:00 and 06:00, and -9K for the period 06:00 to 18:00. The sinusoidal change reaches -3 K at 00:00 and -9 K at 12:00. The frequency of newly detected deep convective clouds is shown at both universal time coordinates (UTC) and local sidereal time (LST). This comparison is made to determine the frequency of convection given the control of solar heating on deep convection.

Figure 5.10 shows a peak in deep convective cloud frequency in both distributions at around 14:00 UTC. The cloud frequency is also at a minima in the early hours of the morning, as expected due to the control of solar heating on deep convection. This pattern is similar for both the step change and sine change in the $BTD_{6.2\text{-}7.3}$ threshold. This is consistent with with the discussions in chapter 1 and 3. However, using a step change in the temperature threshold results in an unnatural jump in the frequency of convection at 06:00 UTC from 72 new deep convective events to 305 at 06:15 UTC (figure 5.10a). This large jump is still evident for several time steps after this change in the temperature threshold, until a natural increase in the detection of new convective events is seen at around 09:00 UTC. The frequency of convection begins to follow the patterns of convective frequency found by Schröder *et al.,* (2013) (an early afternoon increase in convection peaking around 15:00 LST) and that found in ERA-Interim (chapter 3). The step change also shows a sudden drop in the frequency of convection to 280 at 18:00 UTC from 490 at 17:30 UTC. The maximum frequency of newly detected deep convective events is at 14:00 UTC, with 721 newly detected events at this time over the 5 days period. The minimum in the frequency of newly detected convective events is found at 05:45 UTC, the timestep before the step change in $BTD_{6.2\text{-}7.3}$ threshold. The total amount of clouds found over the 5 days test period detected using the step change function was 30472 separate events. When presented with respect to the local sidereal time (LST), the peak in the frequency is seen at 14:45 LST, with a frequency of 719 new clouds detected at this time.

In contrast, the sinusoidal change temperature threshold (figure 5.10b) shows a more natural increase in the frequency of newly detected deep convective events with no sudden jump or dip. Although the use of a sinusoidal change assumes all cloud $BTD_{6.2\text{-}7.3}$ will follow this curve, an increase in convective frequency over the 24 hour period is found similar to that discussed in chapter 1 and 3 with convection following solar heating. The general pattern is also similar to that of the frequency when using the step change in the temperature threshold. This is especially the case when convective frequency is shown as a function of LST. As a function of UTC, the peak in convective frequency is seen at 13:45 UTC, earlier than the peak found with the step change $BTD_{6.2\text{-}7.3}$, and showing a 1 hour 45 minute lag between the the minimum BTD (-9 K at 12:00 UTC) and maximum frequency. Peak convective frequency at 13:45 was 688 newly detected events. As a function of LST, we again see the same shift to later times in the frequency of convection. The maximum frequency of deep convection is seen at 14:45 LST, the same as when implementing the step change in $BTD_{6.2\text{-}7.3}$, with 709 clouds detected at this point. The minima in deep convective frequency was found at 05:45 with 131 new clouds detected. This is the same time as the step change function. Using a sinusoidal

temperature threshold, a total of 29765 newly detected deep convective clouds are detected over the 5 day period. When comparing the frequency of convection detected using SEVIRI to that in ERA-Interim in chapter 3, it can be seen that the peak convective frequency is found at a later time using SEVIRI. This may be due to the resolution of ERA-Interim, limiting the comparison to 4 periods in the day, though the peak in convection in SEVIRI does coincide with the 'early afternoon' (12:00 UTC) in ERA-Interim.

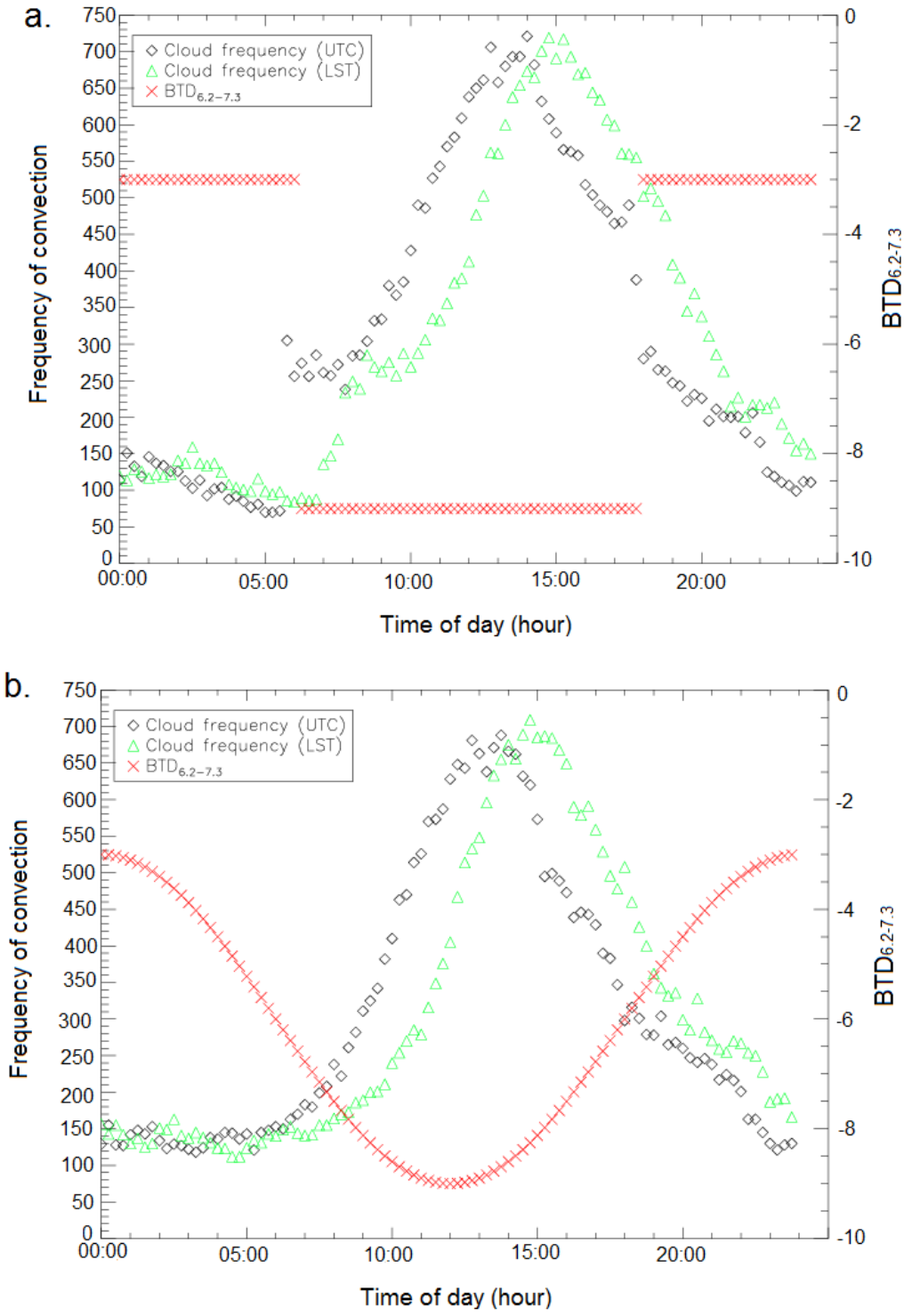

Figure 5.10: The frequency of newly detected deep convection over a period of 5 days between 10th June 2010 and 15th June 2010. This shows the sensitivity of the frequency of deep convection detection to a change in $BTD_{6.2\text{-}7.3}$. Frequency of convection is shown as a function of UTC (black) and LST (green) to account for the effect of solar heating on the frequency of convection. **a)** Using a step change function (red) between the two validated $BTD_{6.2\text{-}7.3}$ thresholds. **b)** Using a sine wave temperature change function (red) between the same two thresholds.

Based on the results of this sensitivity test, particularly the jump and dip in convective frequency seen between $BTD_{6.2\text{-}7.3}$ when using a step change, the sine function is selected as the preferred method of changing the $BTD_{6.2\text{-}7.3}$ threshold over the course of a 24 hour period.

5.4 Cloud Tracking - Case Study

To test the ability of the cloud tracking algorithm to detect and track deep convection from the point of initial detection to the point where the cloud is no longer classified as deep convection, a case study of three individual clouds with life times longer than two hours is presented below (figure 5.11 and 5.12). The clouds detected by the algorithm in this case study are found at 18:30 on 4th June 2010 (figure 5.11). The three clouds - labelled 1 to 3 - are tracked for over their lifetime as defined by the $BTD_{6.2\text{-}7.3}$ threshold. The clouds are detected and tracked over 15 minute intervals, but shown at hourly intervals in figure 5.12.

The clouds are first detected using the $BTD_{6.2\text{-}7.3}$ threshold and then labelled using the nearest neighbour labelling method at 18:30 UTC. Each cloud is then tracked in time following the criteria set out above, with the labelling conducted and variables collected at each timestep. The $BTD_{6.2\text{-}7.3}$ is shown within a box of 3 cloud radii from cloud edge in the latitudinal and longitudinal direction. In figure 5.12 it is evident that the box used for analysis may not be entirely within the study region, for example, clouds 1 and 2. In this case, the box is extended past the edge of the study region, as the cloud is still within the area of interest.

The three clouds are tracked over the period of time in which the $BTD_{6.2\text{-}7.3}$ threshold is satisfied and the tracking criteria are met. It can be seen from each cloud tracking box that the clouds change shape and grow in each timestep until they no longer pass the $BTD_{6.2\text{-}7.3}$ threshold. The tracking case study here shows a successful translation of methods used in earlier studies which used a much lower temporal resolution, for example Machado *et al.*, (1998) who use a 3 hour temporal resolution.

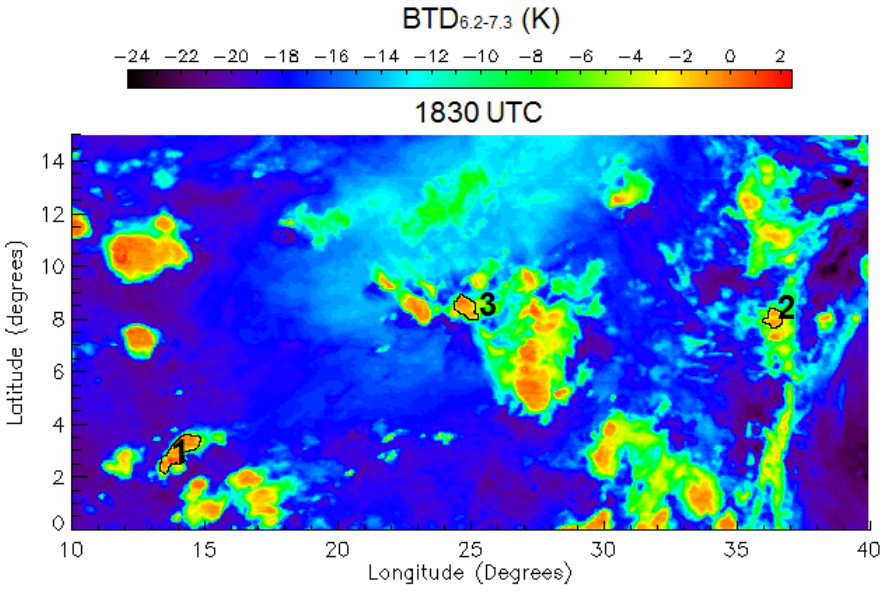

Figure 5.11: $BTD_{6.2\text{-}7.3}$ over the study region at 18:30 UTC on June 4th 2010. 3 clouds are labelled and outlined in black in this first timestep.

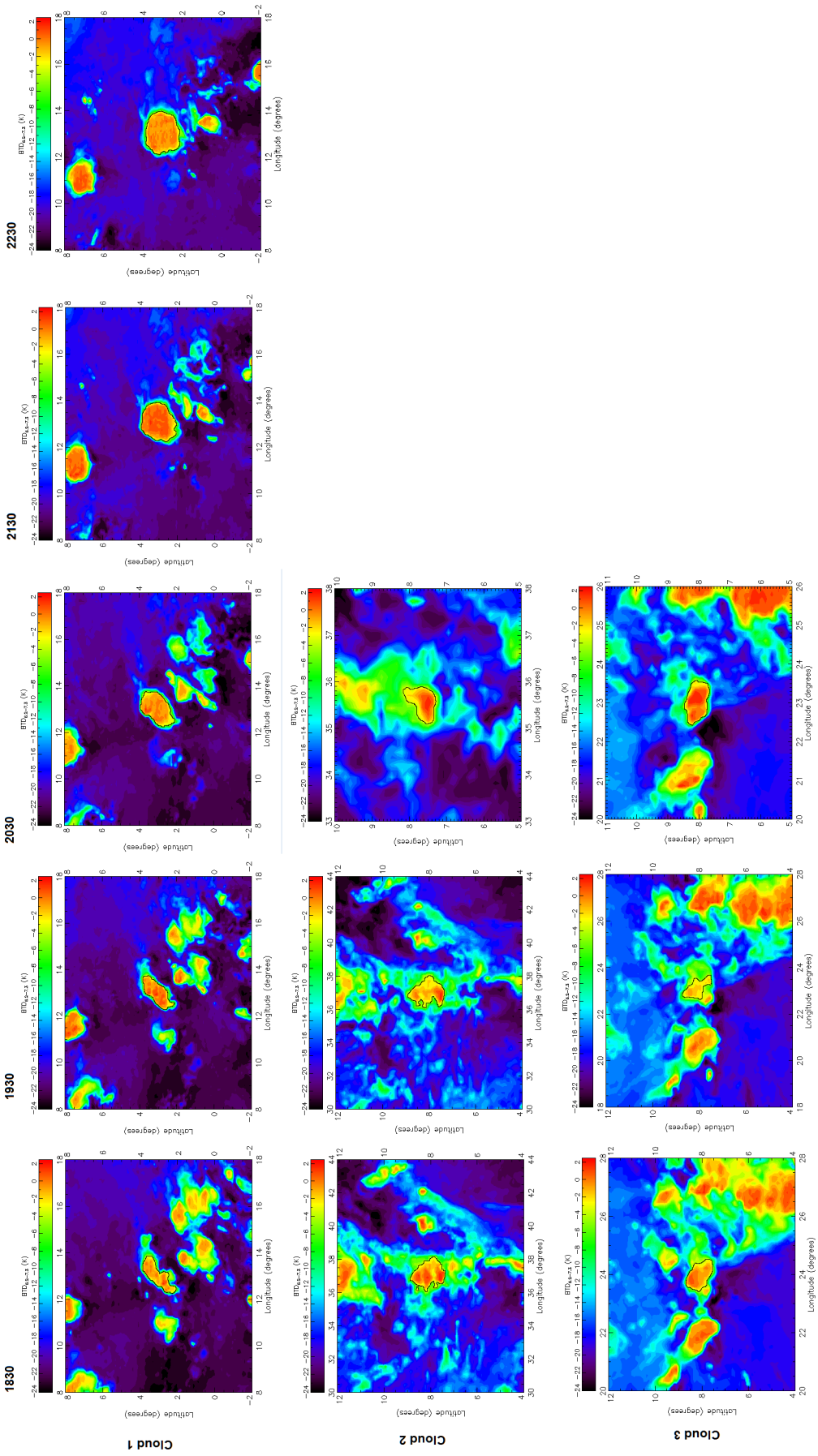

Figure 5.12: Example of cloud tracking using the cloud tracking algorithm. 3 clouds from figure 5.11 are tracked over their lifetimes. $BTD_{6.2\text{-}7.3}$ in the region surrounding the 3 labelled clouds. The $BTD_{6.2\text{-}7.3}$ is shown at hourly timesteps over each clouds lifetime. The tracked clouds are outlined in black.

5.5 Summary

A cloud tracking algorithm has been developed to track clouds based on two criteria - area overlap and midpoint displacement. The area overlap method is the most common method used for cloud tracking. This criteria requires that clouds overlap in subsequent timesteps in order to be potentially classified as the same cloud. If this criteria is passed, the second criteria, the midpoint displacement, requires that clouds move no more than 18 km between pixels. This criteria also determines whether the overlying cloud is a split or merged cloud. The classification of a cloud as split or merged is dependent on the same two criteria. If a cloud is overlying the area previously classified as cloud but a large midpoint displacement has occurred, this cloud is classified as split or merged, and the tracking ceased for this cloud (if merged) or not started (if split).

The tracking algorithm is implemented over a period of 5 days to determine the sensitivity of number of clouds detected to a change in the $BTD_{6.2\text{-}7.3}$. The $BTD_{6.2\text{-}7.3}$ is implemented with a step change and compared to a sinusoidal change in the threshold between the day and night time $BTD_{6.2\text{-}7.3}$. The sensitivity test shown to have a similar shape in the frequency distribution for both implementations. The sinusoidal method will be used in conjunction with the tracking algorithm as no unnatural jump in convective frequency occurs between changes in $BTD_{6.2\text{-}7.3}$.

The cloud tracking algorithm was implemented to track 3 individual clouds first detected in the same time step. This shows the successful translation of methods used in earlier studies to SEVIRI imagery and will allow for clouds to be tracked when they are above the required $BTD_{6.2\text{-}7.3}$ threshold at this point.

Chapter VI

UTH, OLR and the Response to Deep Convection

6 Overview

As discussed briefly in chapters 1 and 2, clear sky OLR is highly sensitive to perturbations in UTH in regions of low ambient UTH. Though water vapour in upper troposphere represents a small fraction of the total column amount, it significantly controls the OLR (Udelhofen and Hartmann, 1995; Soden, 1998; Houshangpour *et al.,* 2005). To improve our understanding of the control of UTH on the net outgoing radiation budget, it is important to understand the spatial and temporal variation of UTH in response to deep convection.

To be able to quantify the spatio-temporal response of UTH to deep convection, a quantifiable and understandable measure of water vapour is needed. An early scarcity of upper tropospheric humidity measurements led to Soden and Bretherton (1993) developing a relationship between the more widely available TOA water vapour band brightness temperature and vertically averaged UTH, based on a simple theoretical radiative transfer model. The weighting function of the 6.2 μm rotational-vibrational emission band of water vapour is highly sensitive to a broad layer of UTH between 200 and 500 hPa under clear sky conditions as discussed in chapters 1 and 2 (Soden, 2000; Bates and Jackson, 2001). With the recent increase in the availability of geostationary spectrally resolved satellite measurements of water vapour band radiances such as that of SEVIRI, the implementation of Soden and Bretherton's method allows for a more convenient way of quantifying water vapour radiances into UTH. The availability of geostationary satellite observations of spectral and broadband TOA radiances, such as that of SEVIRI and GERB, has also provided the opportunity for the response of UTH and OLR to deep convection to be analysed at an unprecedented high temporal resolution.

In order to calculate UTH from the relationship developed by Soden and Bretherton (1993), clear sky TOA radiances are modelled using MODTRAN and converted to 6.2 μm brightness temperatures. Regression analysis is then conducted to determine the relationship between these modelled clear sky 6.2 μm brightness temperatures and the corresponding UTH in order to determine regression coefficients, a and b, that can be applied to the linear relationship between SEVIRI 6.2 μm brightness temperatures and the logarithm of UTH. An error analysis is also conducted on this relationship, based on known SEVIRI instrument errors and systematic biases found before flight and inflight.

This linear relationship is then applied to the SEVIRI water vapour channel data over the study location for each 15 minute period of June and December 2010, along with the cloud detection thresholds (chapter 4) and the cloud tracking algorithm (chapter 5) to analyse the response of clear sky UTH to deep convection over the lifetime of each tracked deep convective cloud. The corresponding GERB HR OLR data is also analysed at each clear sky point over the same tracking period for each cloud. The clear sky UTH and OLR response is analysed with respect to the cloud lifetime and the distance from the edge, measured in cloud radii in both the zonal and meridional directions. The perturbations to UTH and OLR are then calculated with respect to the mean UTH and OLR measured at the first time step. The temporal lag is defined in terms of the difference between the point at which maximum $BTD_{6.2\text{-}7.3}$ is seen and the point in the time series at

which a significant positive perturbation occurs in mean clear sky UTH (section 6.5). The three questions introduced in chapter 1 are then revisited and analysis is conducted in order to provide a quantification of these questions of interest.

6.1 UTH and 6.2 μm Brightness Temperature Relationship

Clear sky TOA radiances were modelled at wavelengths between 4 μm and 15 μm, at 0.01 μm increments using MODTRAN. These were converted to the corresponding 6.2 μm brightness temperatures using the appropriate filter function following the method introduced in chapter 3. ERA-interim profiles with 0% cloud in the vertical column were used as input into MODTRAN, consisting of the vertical temperature and RH profiles, the vertical water vapour density profile (g m^{-3}), the vertical ozone concentration (ppm), and CO_2 (constant 397.8 ppm in the vertical (data taken from the Carbon Dioxide Information Analysis Centre, 2014)) at 37 pressure levels at 0000, 0600, 1200 and 1800, temporally constrained by the availability of ERA-Interim data. 0% cloud cover in the vertical is needed due to the sensitivity of the method to any cloud cover in the profile when applying this method to 'real' SEVIRI data (Soden and Bretherton, 1993). It is suggested by Soden *et al.*, (1994) and Park *et al.,* (2007) that this approach may introduce a warm bias due to there being no overcast pixels considered in the UTH estimation and due to the lower water vapour content of these vertical columns. This may effect the accuracy of the UTH estimates near cloud edges where the SEVIRI spatial resolution allows for the clear sky-cloud border to be detected more easily than when using ERA-interim profiles.

The clear sky vertical RH in these profiles between 200 and 500 hPa is vertically averaged to give the upper tropospheric humidity. The corresponding brightness temperatures of these clear sky profiles are then calculated for the 6.2 μm band using equation 2.11 in section 2.1.1 with the respective SEVIRI filter function applied.

Following the method by Soden and Bretherton (1993), it is possible to determine the coefficients, a and b, of the linear relationship between the logarithm of clear sky UTH and the corresponding modelled 6.2 μm water vapour band brightness temperatures:

$$a + bBT_{6.2} = \ln\left(\frac{UTH * P'}{cos\theta}\right) \tag{6.1}$$

where θ is the viewing zenith angle, P' is a normalised pressure variable ($P' = p_0/p_*$) accounting for the temperature effect on the weighting function (p_0 is a variable base pressure where the air temperature is 240 K and $p*$ is 300 mb - a fixed reference pressure point for UT water vapour absorption line width (Soden and Fu, 1995)). p_0 is estimated for every vertical profile using a least-squares polynomial fit between 200 and 500 hPa in each vertical temperature profile. The mean value of p_0 for the month is used to calculate P'. P' is calculated to be 0.96 for June 2010 and 0.99 for December 2010. This is similar to the value found by Geer *et al.,* (1999) who find P' to be approximately 1. θ is the satellite viewing zenith angle (between 0^o and 50^o for this study) and accounts for the change in the path traversed by the radiation.

To test the sensitivity of the modelled UTH to a change in viewing zenith angle, the coefficients are then applied to a range of viewing zenith angles. Then, in order to understand the sensitivity of the 6.2 μm band to possible instrument errors and systematic bias associated with SEVIRI, a sensitivity study is conducted.

6.1.1 Regression Analysis

To obtain the a and b coefficients, clear sky UTH and the corresponding modelled 6.2 μm band brightness temperatures were split into two randomly chosen subsets - the calibration and validation subsets. The calibration dataset was used to calculate the regression coefficients a and b. As expected from equation 6.1, a non-linear relationship is found between modelled 6.2 μm brightness temperature and UTH (figure 6.1, a and c). For December, there is a much greater frequency of clear sky profiles (17004 profiles) compared to June (5738) and a larger spread of modelled UTH. The regression coefficients of the linear relationship between the logarithm of UTH and the 6.2 μm brightness temperatures are shown in figure 6.1 (b and d) for both June and December. The values found in June are similar to that found by Soden *et al.,* (1994), Soden (1998) and Soden and Lanzante (1996) who find a to be 31.5 and b to be -0.1136. The lower intercept found for December may be due to the greater frequency of lower UTH found in this month. Although Soden (1998) suggests that generally no seasonality is seen in the UTH coefficients, a similar range in the intercept is found by Jedlovec *et al.,* (2000) when using this same method of UTH estimation.

The maximum clear sky UTH in the ERA-Interim profiles in June used to calculate the a and b coefficients was 88.3%, where the TOA 6.2 μm brightness temperature was calculated to be 237 K. 100% humidity corresponds to a brightness temperature of 235.28 K in June. This lower limit of 235 K was also found by Jedlovec *et al.*, (2000). Although it is expected that UTH would be close to 100% near cloud edges, with the possibility of supersaturation (UTH >100%), the use of completely cloud free vertical profiles from ERA-Interim has limited the range of UTH that is used in the calibration. A lower maximum UTH in December of 76.5% is found to correspond to 238 K. The higher frequency of lower values of UTH in December relate to the influence of the ITCZ on the humidity distribution at this time of year. As shown in chapters 3 and 4, the study region is within the region of subsidence of the ITCZ. This is therefore likely to reduce the number of deep convective clouds found in this region and in turn create a drier upper troposphere.

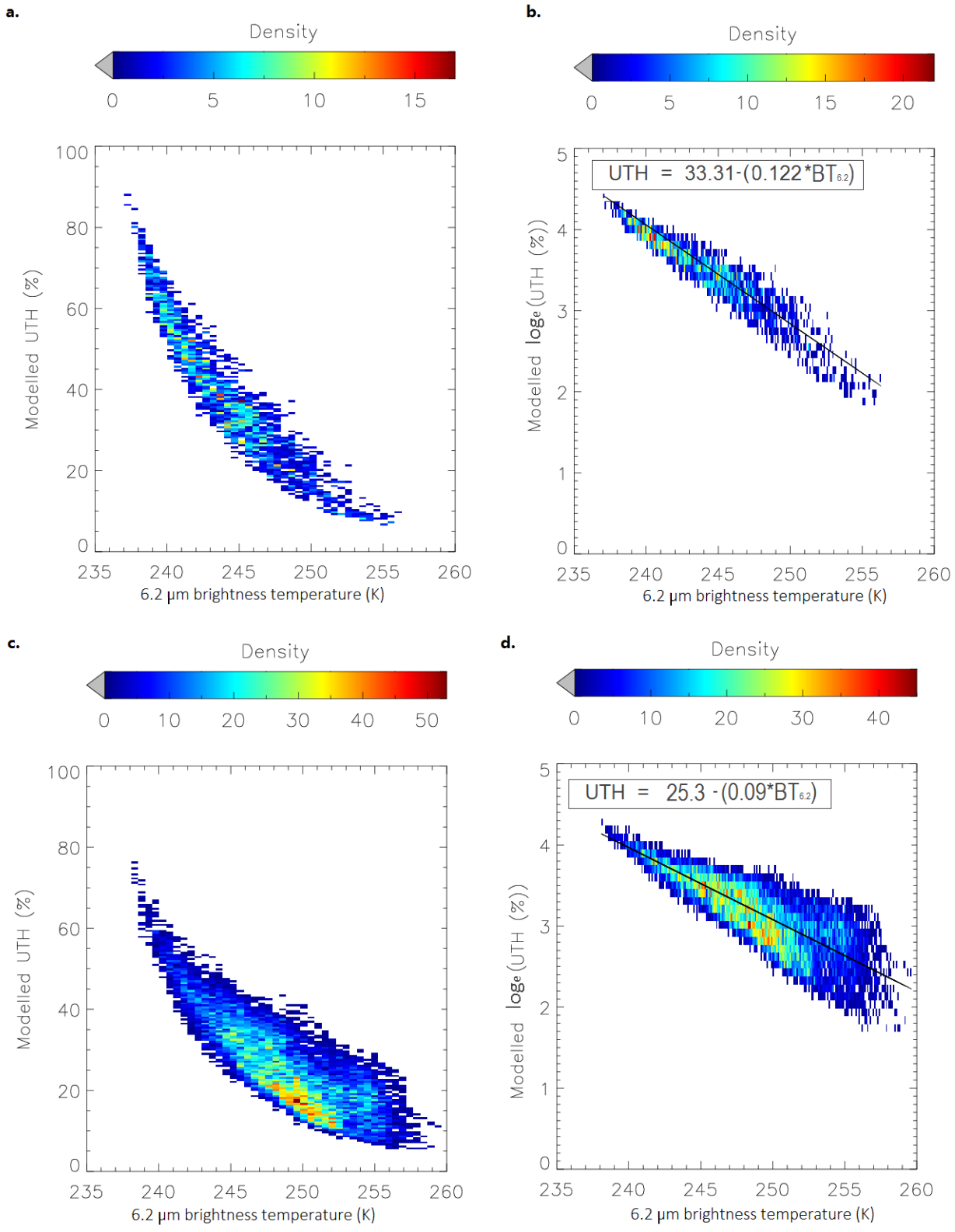

Figure 6.1: The relationship between mean UTH (%) and modelled 6.2 μm band brightness temperatures **a)** June 2010 **b)** Log linear response June 2010 **c)** December 2010 **d)** Log linear response December 2010.

Using the a and b coefficients derived from the calibration subset, UTH values were estimated from the validation subset and compared to the corresponding true UTH from ERA-Interim. Histogram density plots of estimated against 'true' UTH are shown for June and December 2010 at 0° and 50° viewing zenith angle (figure 6.2). It is seen from the density plots that there is good correlation between estimated and true UTH. The Pearson's product-moment correlation coefficient, R, for June are 0.963 at 0° viewing zenith and 0.959 at 50° viewing zenith (table 6.1). The R coefficient for these viewing zenith extremes in June suggest that these coefficients well reproduce the relationship between the two variables across the full range of geometries within the study region in this month. Similarly, the bias between estimated and true UTH values shows little variation with view zenith.

The density plots of estimated versus true UTH for each of the extremes in viewing zenith angle in December (figure 6.2 c and d) both show a much larger spread than the corresponding June plots. The low humidities during this month show a relatively scattered BT response which dominates the overall regression fit. This results in a general underestimation of higher UTH values and is reflected in the lower value of R and a higher RMSE and bias in December when compared to June. The RMSE and Bias values in each month are similar to that found by Soden (1998) who calculated UTH for July and January 1987 using the GOES instrument.

June	**R**	**RMSE (%)**	**Bias (%)**
0° VZA	0.963	4.35	0.19
50° VZA	0.959	4.57	0.23

December	**R**	**RMSE (%)**	**Bias (%)**
0° VZA	0.87	5.23	0.615
50° VZA	0.89	5.47	0.63

Table 6.1: Correlation statistics for June and December 2010 measured vs modelled UTH at the extreme viewing zenith angles, 0° and 50°.

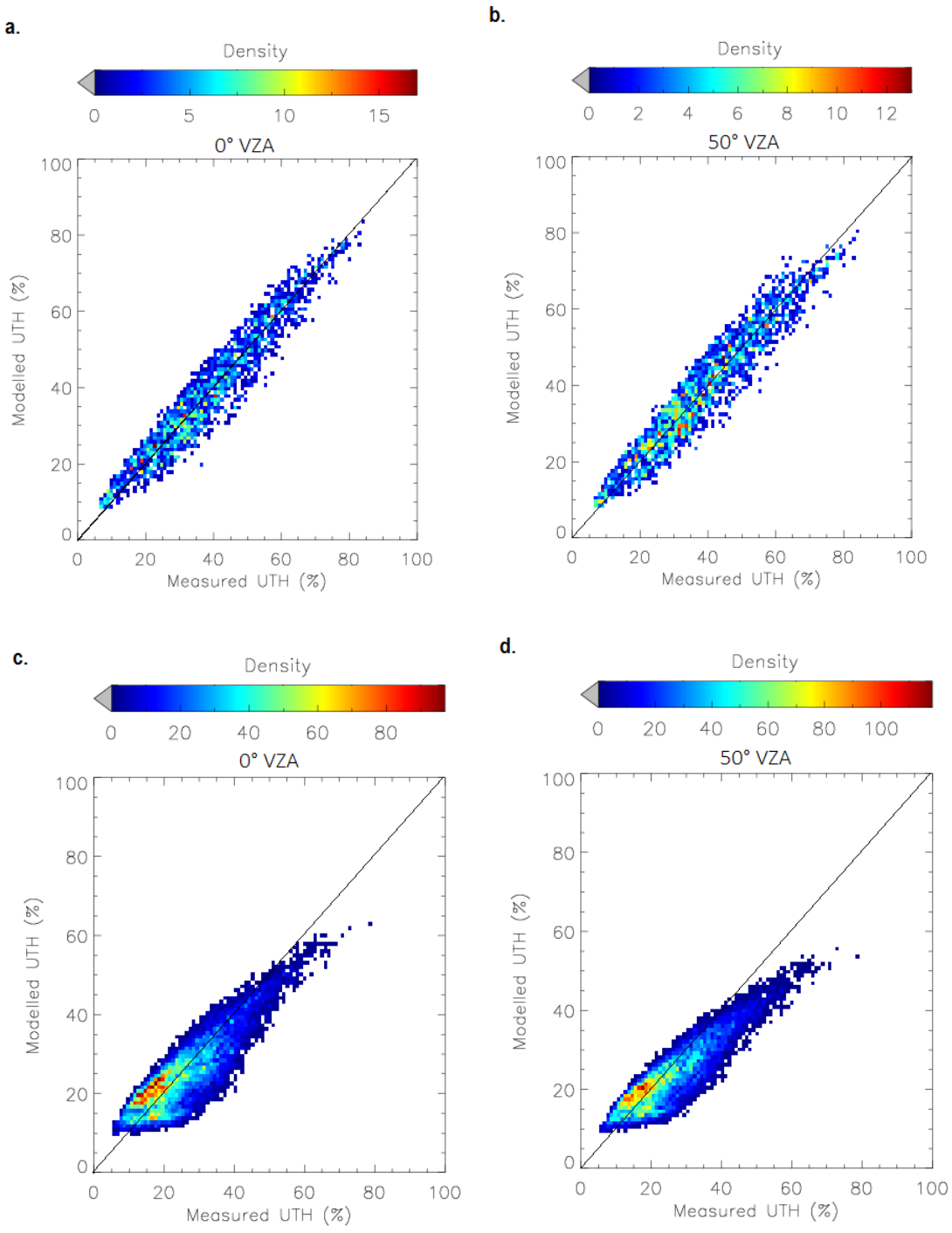

Figure 6.2: Histogram density plots of the measured UTH (calculated in MODTRAN) and the modelled UTH (Using the a and b coefficients applied to $BT_{6.2}$ data from MODTRAN) for June and December 2010. **a)** June 0° viewing zenith. **b)** June 50° viewing zenith. **c)** December 0° viewing zenith. **d)** December 50° viewing zenith.

6.1.2 Error analysis

A problem with using a satellite instrument for the measurement of radiances is that the instrument will have pre-flight and inflight errors and systematic biases due to the drift in the instruments calibration accuracy over its lifetime (Schmetz *et al.,* 2002). Systematic biases - long term errors in the observations of a fixed amount - can usually be corrected for. The accuracy of SEVIRI radiance measurements is expected to be within 1K in the IR channels due to the onboard calibration of the instrument. A range of random errors in were found by Schmetz *et al.,* (2003) of 0.25 K (best case scenario found in flight) and 0.75 K (based on accepted calibration accuracy preflight). A -1.7 K bias was found by Szyndel *et al.*, (2005) in the difference between ERA-Interim clear sky 6.2 μm band water vapour channel radiances and SEVIRI 6.2 μm band radiances. To test the sensitivity of the a and b coefficients to these random instrument errors and the systematic bias, the UTH was re-modelled with the random errors applied as a RMS error and instrument bias applied to the modelled 6.2 μm brightness temperatures. The errors were randomly distributed with a mean of 0 (or -1.7 K when the bias was applied), and a standard deviation of the applied error (0.25 K or 0.75 K). The UTH is modelled for both June and December at 0° and 50° to again determine the sensitivity of changing the satellite viewing zenith angle at the extremes of the study area zeniths. It is noted that the bias found by Szyndel *et al.*, (2005) will contain both the effect of any real SEVIRI $BT_{6.2}$ offset and the impact of any error in ERA-I UTH profiles. However, we take this estimate as a 'worst case' scenario for SEVIRI bias errors in this channel.

6.1.3 June

The range of random errors and instrument biases are applied to the modelled 6.2 μm brightness temperatures for June (tables 6.20 and 6.21, figures 6.3 and 6.4). For random errors alone (0.25 K and 0.75 K) relatively little overall change is seen in the estimated UTH. A decrease in R is seen with an increase from 0.25 K error to 0.75 K. With an error of 0.75 K, as might be expected, more spread is seen in the true vs estimated UTH (figure 6.3c and d) as reflected in the associated RMSE. The bias also decreases with an increase in the error, though this is very small (0.04 %). This suggests, from the little sensitivity seen with the addition of the error, the modelled UTH is robust in its response to any realistic random errors that may occur.

Applying the -1.7 K instrument bias systematically decreases the estimated UTH such that both the resulting bias and RMSE in these estimates are substantially inflated, by a factor of approximately 2, and a much more negative statistical bias is found. Subsequently adding the 0.25 K and 0.75 K random errors has a secondary effect, marginally increasing both the RMSE and bias (Table 6.2). A marginal increase in RMSE and bias also seen with viewing zenith angle (Table 6.3).

Random error/bias	R	RMSE (%)	Bias (%)
0.25 K random error	0.961	4.55	0.1
0.75 K random error	0.937	5.88	0.06
0.25 K random error and -1.7 K bias	0.961	10.82	-8.81
0.75 K random error and -1.7 K bias	0.937	11.93	-9.02

Table 6.2: Correlation statistics for the error analysis of UTH at a viewing zenith of 0°, in June 2010

Random error/bias	R	RMSE (%)	Bias (%)
0.25 K random error	0.956	4.76	0.14
0.75 K random error	0.932	6.01	0.1
0.25 K random error and -1.7 K bias	0.957	10.68	-8.76
0.75 K random error and -1.7 K bias	0.932	11.79	-8.97

Table 6.3: Correlation statistics for the error analysis of UTH at a viewing zenith of 50°, in June 2010

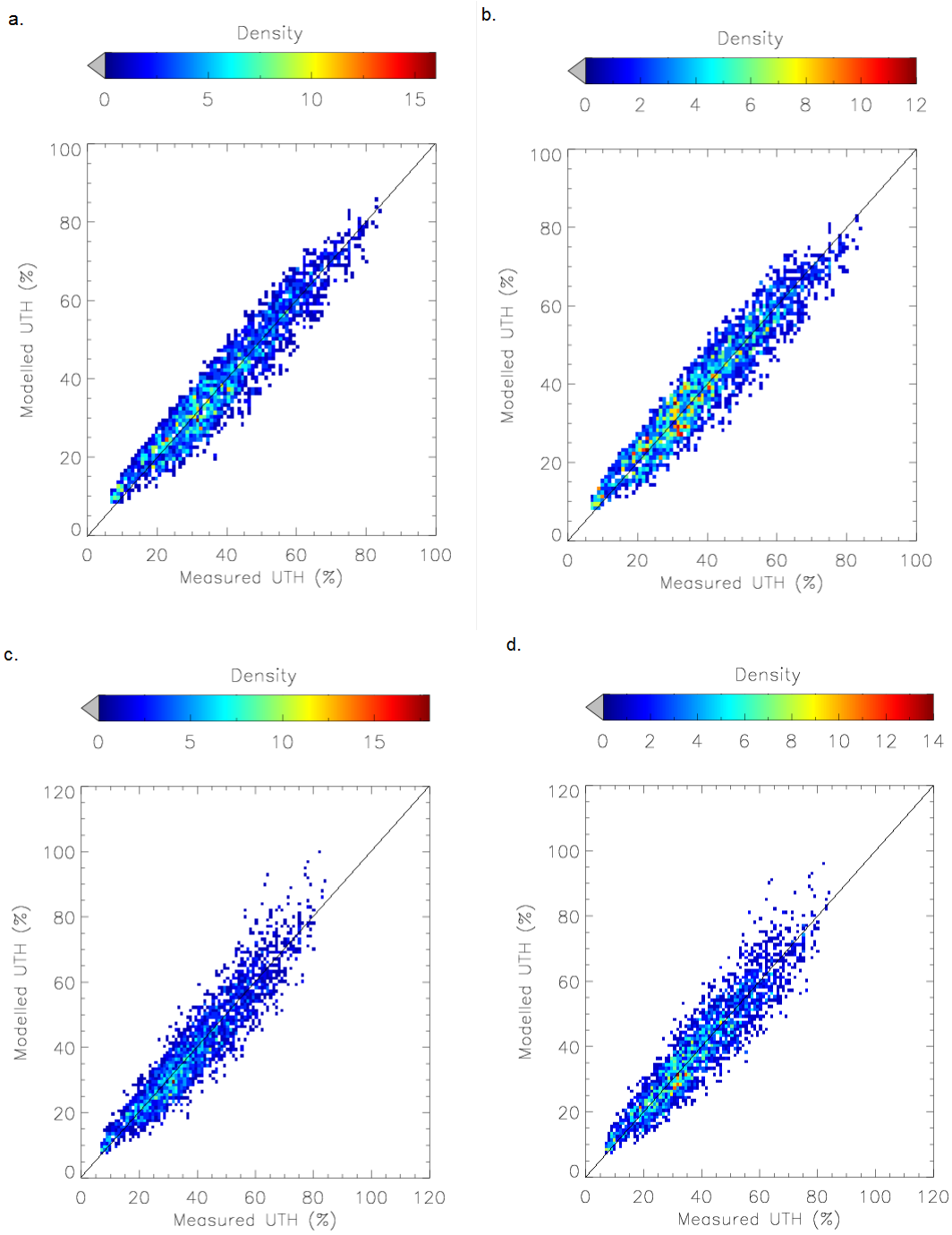

Figure 6.3: Histogram density plots of the measured UTH (calculated in MODTRAN) and the modelled UTH (Using the a and b coefficients applied to $TB_{6.2}$ data from MODTRAN) for June 2010. **a)** with a 0.25 K random error at 0° viewing zenith angle. **b)** at 50° viewing zenith angle. **c)** with a 0.75 K random error at 0° viewing zenith angle. **d)** at 50° viewing zenith angle.

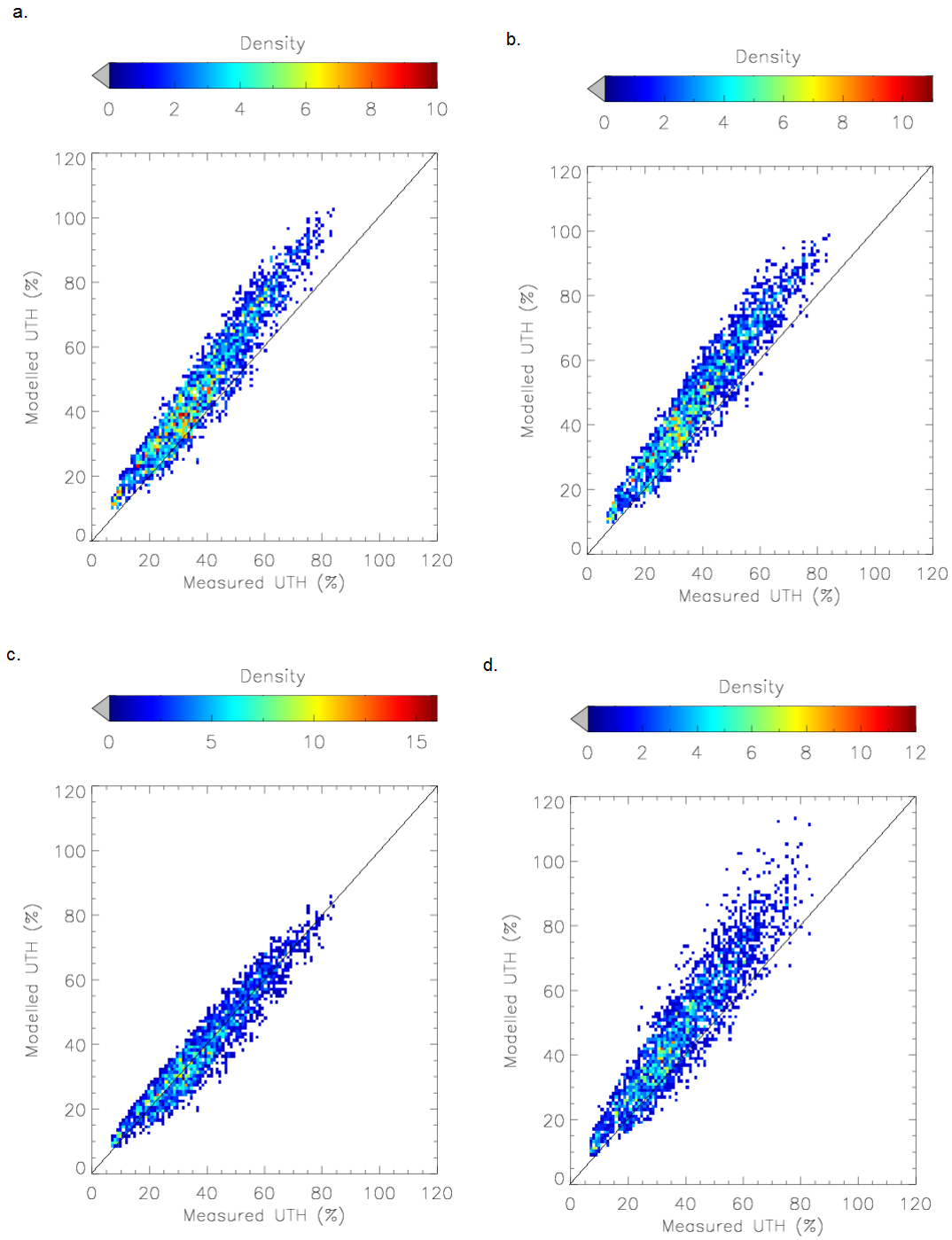

Figure 6.4: Histogram density plots of the measured UTH (calculated in MODTRAN) and the modelled UTH (Using the a and b coefficients applied to $TB_{6.2}$ data from MODTRAN) for June 2010. **a)** with a 0.25 K random error and -1.7 K standard deviation at 0° viewing zenith angle. **b)** at 50° viewing zenith angle. **c)** with a 0.75 K random error and -1.7 K standard deviation at 0° viewing zenith angle. **d)** at 50° viewing zenith angle.

6.1.4 December

The same method of error analysis was conducted for the clear sky UTH modelled for December 2010. The range of random errors and instrument biases are applied to the modelled 6.2 μm brightness temperatures at either extreme of the viewing zenith angle over the study region. Similar to that of June, with only random errors applied, a small change in UTH is found. RMSE also increases as the random error is increased. Again, as above, the bias is seen to decrease with an addition of random error. This is the case for both extremes of the viewing zenith.

With the addition of both the random errors and the -1.7 K bias, we see the same R as that when no instrument bias is applied. A higher RMSE is found with both additions, though at 50° viewing zenith angle the RMSE decreases. The bias, though smaller than that of June 2010, is seen to become more negative with the increase in random error. Although a high correlation coefficient is seen with an addition of both random error and systematic bias the large RMSE shows a possible ~6% error when both random error and systematic bias are applied.

Random error/bias	R	RMSE	Bias
0.25 K random error	0.87	5.3	0.63
0.75 K random error	0.86	5.52	0.586
0.25 K random error and -1.7 K bias	0.87	6.38	-3.44
0.75 K random error and -1.7 K bias	0.86	6.72	-3.52

Table 6.4: Correlation statistics for the error analysis of UTH at a viewing zenith of 0°, in December 2010

Random error/bias	R	RMSE	Bias
0.25 K random error	0.89	5.48	2.2
0.75 K random error	0.88	5.68	2.16
0.25 K random error and -1.7 K bias	0.89	5.06	-1.6
0.75 K random error and -1.7 K bias	0.87	5.4	-1.66

Table 6.5: Correlation statistics for the error analysis of UTH at a viewing zenith of 50°, in December 2010

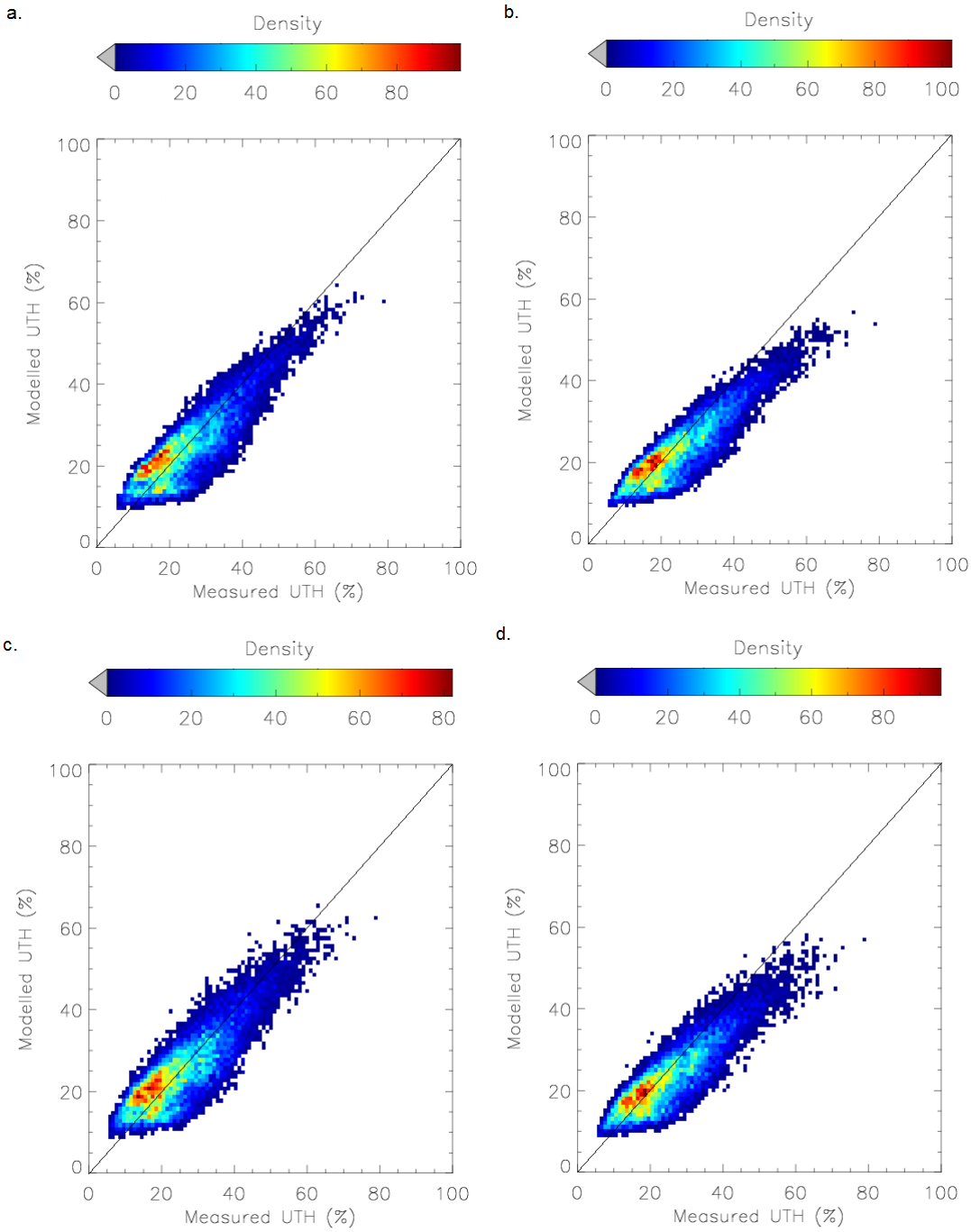

Figure 6.5: Histogram density plots of the measured UTH (calculated in MODTRAN) and the modelled UTH (Using the a and b coefficients applied to $TB_{6.2}$ data from MODTRAN) for December 2010. **a)** with a 0.25 K random error at 0° viewing zenith angle. **b)** at 50° viewing zenith angle. **c)** with a 0.75 K random error at 0° viewing zenith angle. **d)** at 50° viewing zenith angle.

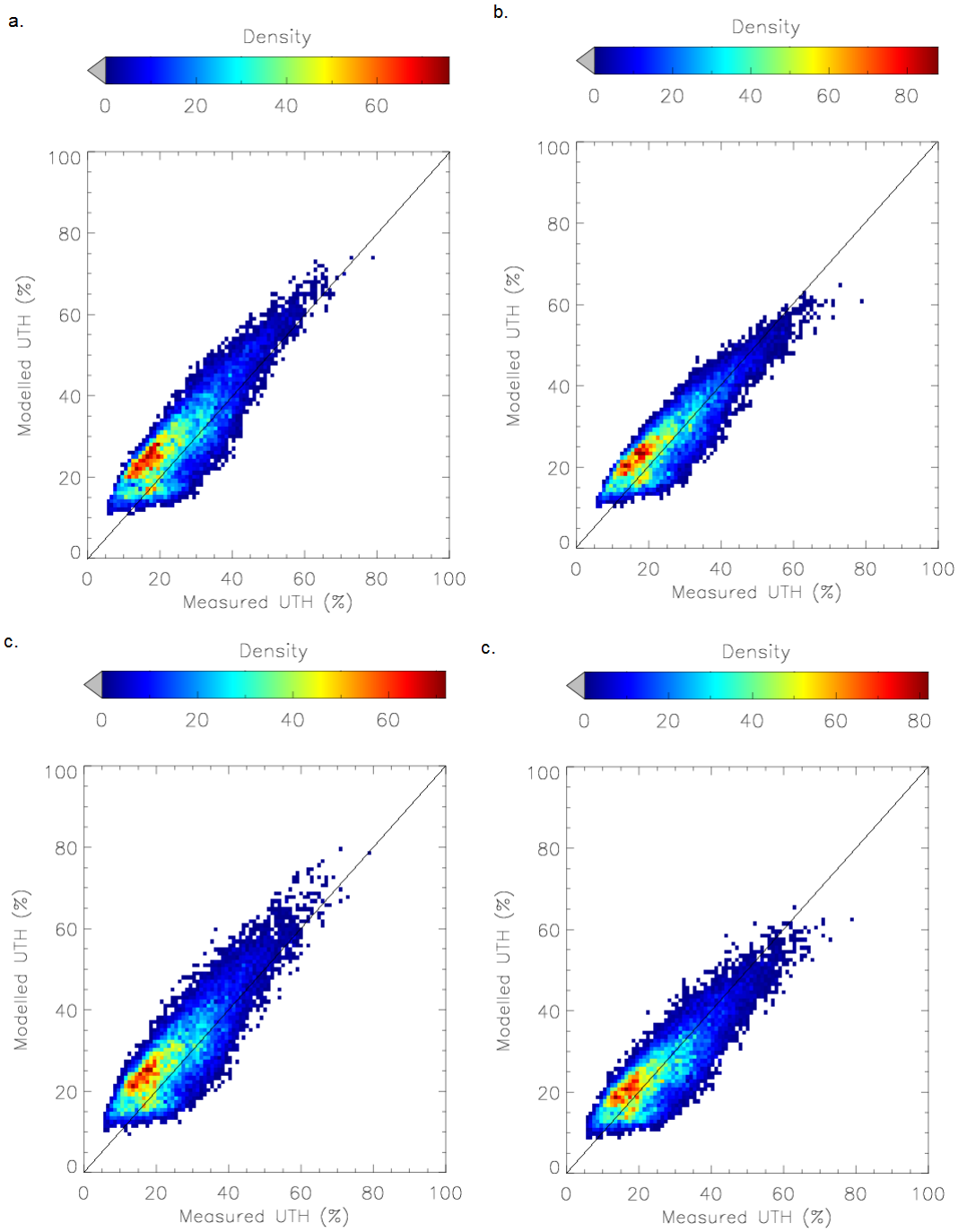

Figure 6.6: Histogram density plots of the measured UTH (calculated in MODTRAN) and the modelled UTH (Using the a and b coefficients applied to $BT_{6.2}$ data from MODTRAN) for December 2010. **a)** with a 0.25 K random error and -1.7 K standard deviation at 0° viewing zenith angle **b)** at 50° viewing zenith angle **c)** with a 0.75 K random error and -1.7 K standard deviation at 0° viewing zenith angle **d)** at 50° viewing zenith angle.

6.1.5 Limitations of the using 6.2 μm band - UTH and deep convection detection

The use of the 6.2 μm band in both the detection of deep convection and with the UTH relationship may introduce some erroneous UTH values. When using the $BTD_{6.2\text{-}7.3}$ method for detecting deep convection over the clouds lifetime, the 6.2 μm brightness temperature may be seen to decrease as the cloud dissipates and UTH increases, with the cloud top becoming thinner (through disspiation and the entrainment of cirrus) and absorption of longwave radiation by cloud droplets. A decrease in the 6.2 μm brightness temperature may result in a more negative $BTD_{6.2\text{-}7.3}$ and result in the cloud no longer being classed as deep convection when the threshold for the cloud is passed, even though the cloud itself is still in the region. A decrease in 6.2 μm brightness temperatures and non classification as deep convection will result in the region being classified as clear sky or cirrus. Due to the non-linear relationship between the 6.2 μm brightness temperatures and UTH, when pixel brightness temperatures are below 235 K an erroneously high humidity is estimated. In these cases it is assumed that the pixel is either supersaturated or cloud contaminated. Cloud contamination of pixels was found to bias UTH estimations by Soden and Bretherton (1993) due to their influence on the 6.2 μm bands weighting function. To eliminate these erroneous UTH values, a further threshold of 235 K was placed on the 6.2 μm channel, with any pixels below this threshold being masked out in June and December.

To visualise this relationship, a case study is analysed to determine whether the region in which a cloud used to exist but no longer does is determined to be cirrus or clear sky. Using the cloud tracking case study in chapter 5 (section 5.4), cloud number 1 is used as an example to test the response of each threshold to the cloud moving through the region. The region in which the deep convection is detected in T1 is taken and compared to that in T2, then T2 with T3 and so forth over the clouds lifetime. The deep convection and cirrus BTD thresholds used and $BT_{6.2}$ in the region in which cloud was not detected at T2 but detected in T1 (blue in T2) was found for each timestep over the clouds lifetime. An idealisation of the process is shown in figure 6.7.

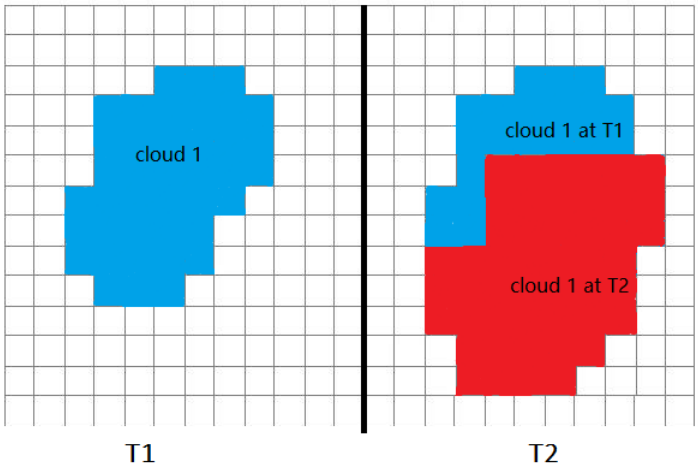

Figure 6.7: An idealisation of the comparison between the area overlaid by a cloud in T1 with that in T2. The blue shape in T1 represents a cloud. This is area classified as cloud is compared to the area in T2 classified as cloud. The $BTD_{6.2\text{-}7.3}$, $BTD_{12.0\text{-}10.8}$ and $BT_{6.2}$ of the area that was classified as cloud in T1 but not T2 (the blue area in T2) is taken to determine whether this region is classified as cirrus, clear sky or supersaturated/cloud contaminated.

In this case, over the clouds lifetime the $BTD_{6.2\text{-}7.3}$ threshold varied between -3.3 to -5.6 K. It is found that there were 26 pixels with a $BTD_{6.2\text{-}7.3}$ not classified as deep convection or cirrus in the region where the cloud existed in the previous timesteps over the clouds lifetime. Inspection of the 6.2 μm band shows these areas to have very low 6.2 μm brightness temperatures (figure 6.8), therefore creating spuriously high UTH values (e.g. a 6.2 μm brightness temperature of 225 K giving a UTH value of 350%). These values are therefore masked out in the analysis of the response of UTH to deep convection as being cloud contaminated.

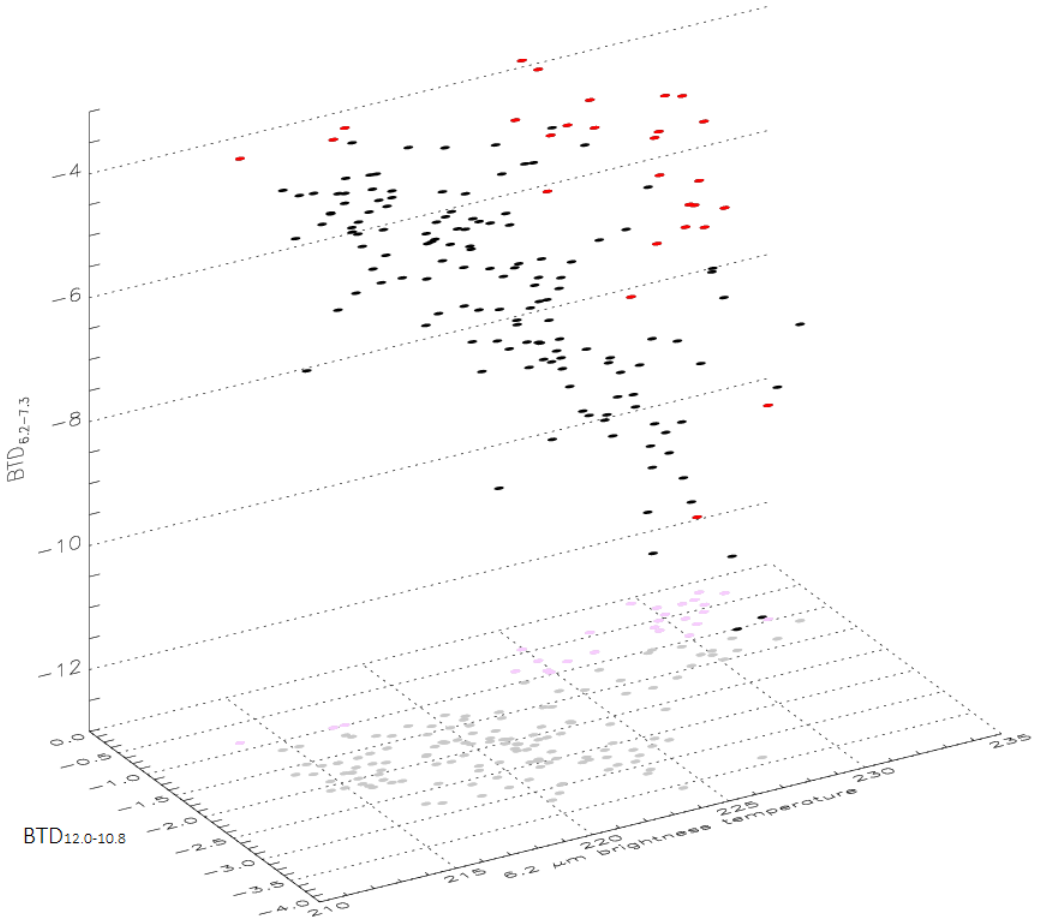

Figure 6.8: A 3D plot of the relationship between $BTD_{6.2\text{-}7.3}$ (the deep convective cloud threshold), $BTD_{12.0\text{-}10.8}$ (the cirrus cloud threshold) and the 6.2 μm brightness temperature. The black dots are those which represent the points that were once occupied deep convective cloud but are now masked as cirrus. The red dots are those that are were once occupied by deep convection and are not cirrus nor deep convection (above -1 K $BTD_{12.0\text{-}10.8}$ and below the corresponding $BTD_{6.2\text{-}7.3}$ threshold). The grey and pink dots represent the shadows of the black and red dots respectively, and show the relationship between the $BTD_{12.0\text{-}10.8}$ and the corresponding 6.2 μm brightness temperature for each point. From the UTH analysis in section 6.2, the pink dots are all considered to be either cloud contaminated or supersaturated due to them being less than 235 K and not classified as deep convection or cirrus.

6.2 Deep convection over tropical Africa - spatial characteristics and frequency-size distribution

The cloud detection thresholds and cloud tracking algorithm developed in chapters 4 and 5 are implemented with the UTH relationship over the periods of June and December 2010 to provide answers to the three questions introduced in chapter 1. The minimum life time under analysis is two hours - any cloud with a life time shorter than two hours was not considered in the analysis. This is based on similar tracking studies by Feng *et al.,* (2012) and Hagos *et al.,* (2013), whereby tropical convective systems were tracked and found on average to have a minimum life time of 2 hours. This is also shorter than the timesteps used in early cloud tracking studies such as that of William and Houze (1987) who use a minimum timestep of 3 hours between images. A spatial limit is not applied to the convection analysed due to cores of convective cells regularly ranging in sizes from 1-100 km (Roca *et al.,* 2002) and a GERB HR scale pixel being 9x9 km. Firstly, an analysis of the spatial distribution and the frequency-size distribution of the clouds detected in SEVIRI is given with qualitative comparisons to ERA-Interim in order to characterise the deep convection under analysis.

One key feature of the method used for deep convection detection in this study is that the $BTD_{6.2\text{-}7.3}$ threshold will detect the the most intense part of the convective cloud i.e. the core. Although this allows for a detection of the cloud during its most intense phase, this will affect the cloud lifetime that is measured. This will shorten the lifetimes of the measured lifetimes, with the cloud likely to still be in existence after the intense phase. The radius calculation is also based on the area exceeding the threshold, which may not include any detrained cirrus, though this is accounted for with the $BTD_{12.0\text{-}10.8}$ threshold.

6.2.1 Cloud frequency-size distributions

A comparison of the number of detected convective events in June shows 994 clouds found in SEVIRI, compared to 5288 in ERA-Interim. In December 283 deep convective events with lifetimes of 2 hours or greater were detected using SEVIRI with the same lifetime threshold, compared to 1251 in ERA-Interim. Due to the inherent differences in the temporal resolution between ERA-Interim and SEVIRI, and also the convection in ERA-Interim not being tracked in figures 3.6 and 3.7 (chapter 3), this difference in the number of detected deep convective clouds between SEVIRI and ERA-Interim is expected. The number of clouds detected and tracked in SEVIRI is largely influenced by the lifetime threshold of 2 hours or greater applied to deep convection in SEVIRI. The spatial resolution will also limit any quantitative comparison between the two datasets. Also, the number of convective events in ERA-Interim in the spatial distribution in chapter 3 does not account for the convection in neighbouring vertical profiles being the same cloud. This is not the case in the spatial distribution of SEVIRI detected deep convection due to the nearest-neighbour labeling method employed in the cloud tracking algorithm. Further the mean cloud radius size of deep convection in SEVIRI is 131 km in June (see next section), whilst the ERA-interim grid size is 0.7^{o} which may cause an overestimation of deep convection in ERA-Interim.

In their cloud tracking study of convective systems, Feng *et al.,* (2012) found a positive linear relationship between cloud radius size and lifetime. Taking the average cloud radius size over the clouds lifetime, no discernible pattern is found in the relationship between the lifetime and mean cloud radius in either June or December (figure 6.9). A large number of clouds with a small mean cloud radii and a short lifetime are detected. In June the distribution also shows a small number of clouds with a large mean radius but with

a short lifetime (figure 6.9a). This may occur when a large cloud system is present though the convective activity is not intense enough for the cloud top to be classified as deep convection. This pattern is not seen in December, where maximum mean cloud radii are a lot smaller than in June, confirming the seasonal effect of the ITCZ position on convective intensity, discussed in chapter 2 (figure 6.9b).

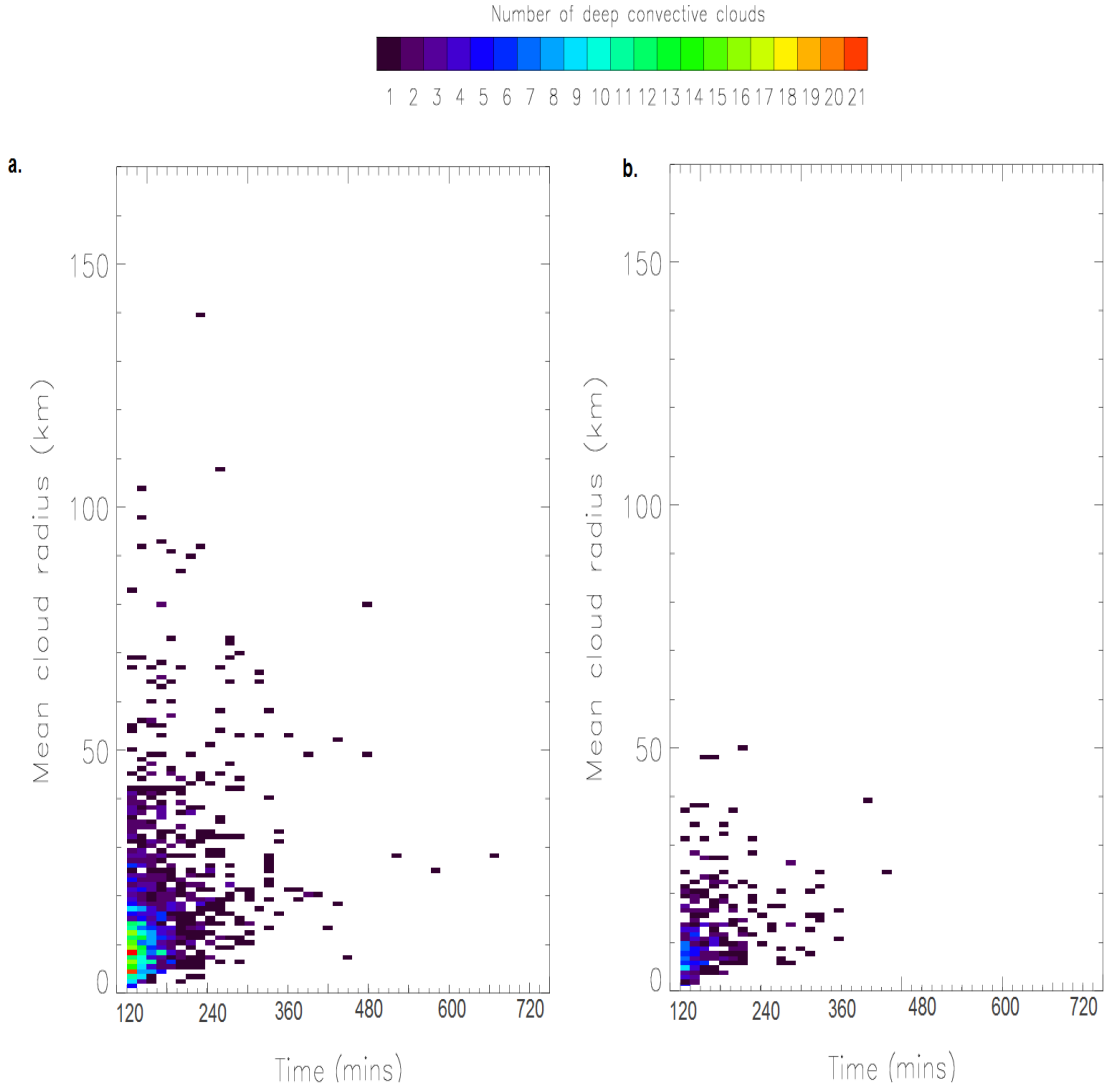

Figure 6.9: Lifetime size distributions of all clouds detected and tracked with a lifetime of 2 hours or greater in **a)** June 2010 and **b)** December 2010. Time (x-axis) is the length of the cloud lifetime.

When considering the frequency distribution of mean cloud radii, it is found to possess a log-normal distribution in both June and December 2010 (figure 6.10 and 6.11). This is similar to that found by Feng *et al.,* (2012), who find a log-normal distribution of both convective core sizes (with a maximum of 100 km found) and deep convective system radii (with a maximum of 300 km found). They also find a log-normal distribution in the convective core lifetime, with a maximum lifetime of 6 hours for the core during the intense

stage of the clouds lifecycle.

Using this log normal distribution, the cloud sizes were separated into 3 distinct size bins (small, medium and large), defined in relation to 1 standard deviation from the mean (figure 6.10b and 6.11b). The splitting of clouds into separate size bins is due to larger clouds being expected to have a greater perturbing effect on UTH due to the greater number of CCN present. This splitting into size bins allows for any size effects to be detected, rather than the effect of small clouds being over estimated if they are included in the same analysis as much larger clouds. In June 2010, the mean log normal cloud radii is 4.87 (131 km), with a standard deviation of 0.77. Therefore any cloud radius with a log normal size of greater than 4.1 (61 km) and less than 5.64 (292 km) are considered as medium sized clouds. This size bin includes 675 clouds. Those being less or more than this were classed small or large respectively. It was found that there were 160 small clouds and 159 large clouds using this method. The frequency distribution and the three size groups for June 2010 are shown in figure 6.10.

A similar shaped distribution is found for deep convection in December (figure 6.11). Small clouds in December were defined as those with a log normal cloud radii of less than 3.9 (51 km), with large clouds being those with a log normal cloud radii of greater than 5.2 (189 km).

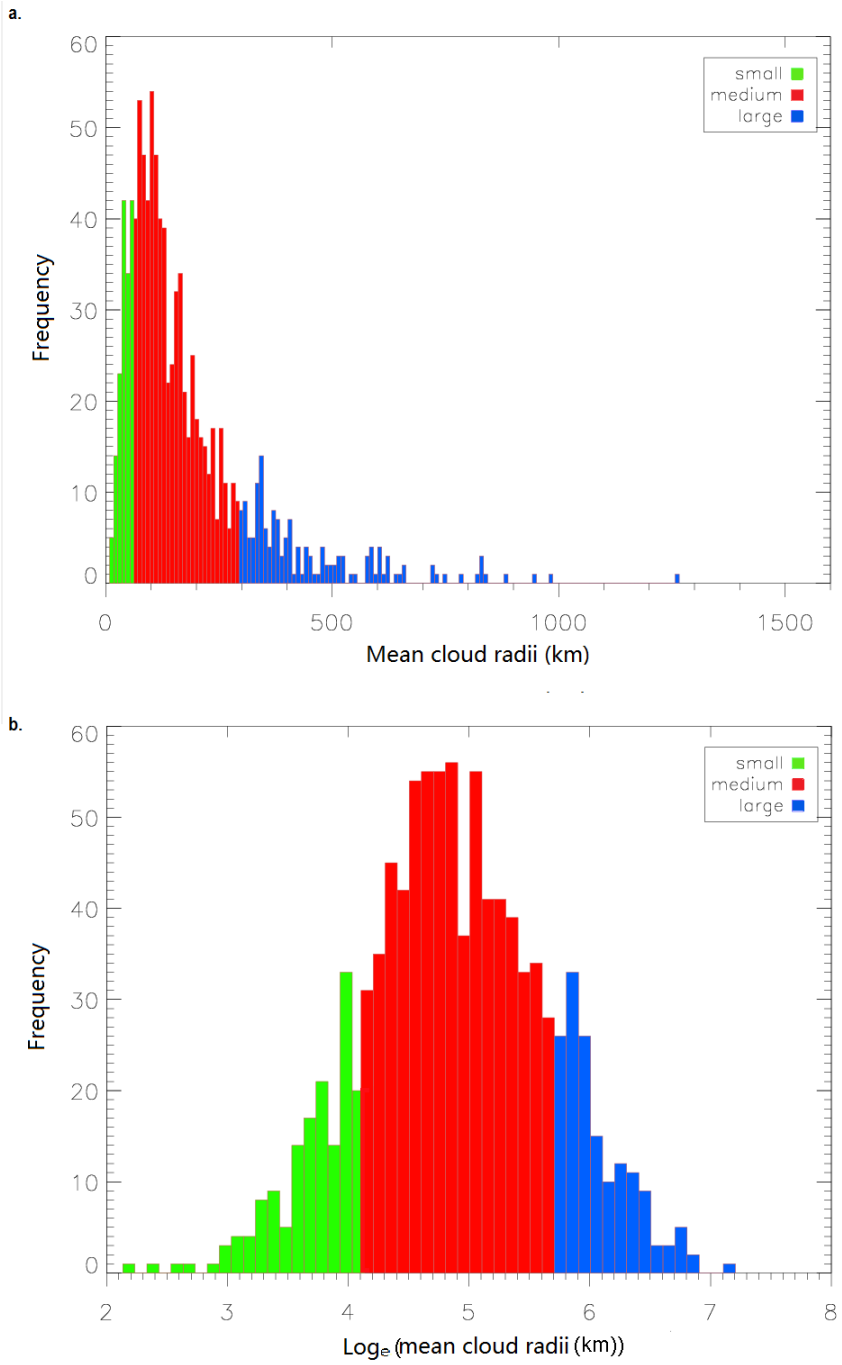

Figure 6.10: **a)** Frequency distribution of mean cloud radii (km) for all cloud with lifetimes over 2 hours in June 2010. **b)** Log-normal distribution. The colours represent the size bins small (green), medium (red) and large (blue).

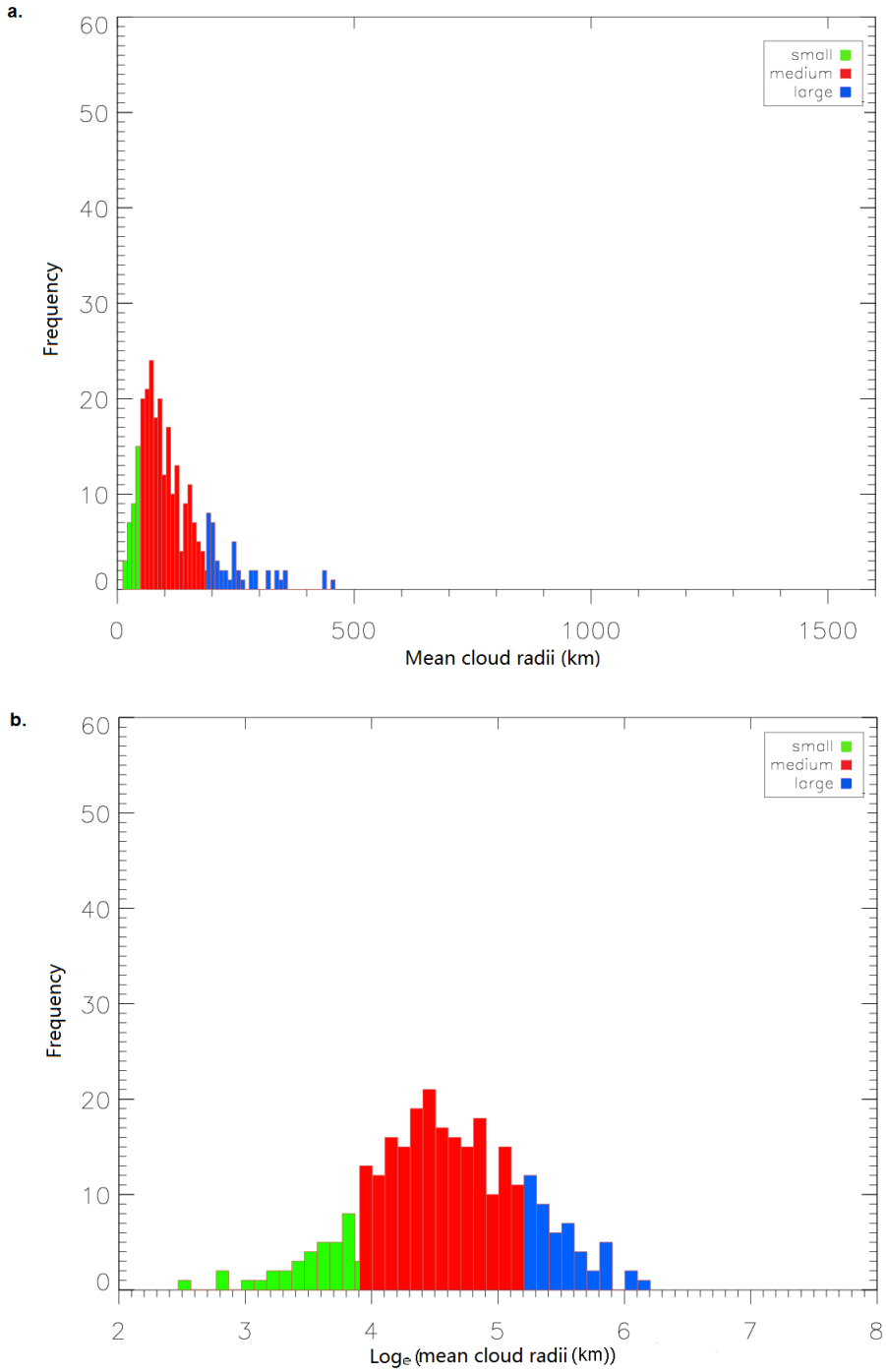

Figure 6.11: **a)** Frequency distribution of mean cloud radii (km) for all cloud with lifetimes over 2 hours in December 2010. **b)** Log-normal distribution. The colours represent the size bins small (green), medium (red) and large (blue).

The lifetime of the cloud may also effect the intensity to which the UTH and OLR is perturbed. To further

separate the clouds for analysis, clouds were separated into lifetime bins of half hourly intervals (figure 6.12 and 6.13). The separation into half hourly time bins from 2-2.5 hours to 6+ hours allows for a comparison between shorter lived clouds and those of a longer life span. Shown in figure 6.12 are the time bins up to 4-4.5 hours. In figure 6.13 are the time bins up to 3-3.5 hours. Bins of lifetimes above this were not included in the following analysis due to the frequencies of clouds in these bins being unlikely to give a robust representation of the UTH response to deep convection. For example, in June 2010 there were 11 clouds with a lifetime of 5 to 5.5 hours (0 small; 8 medium; 3 large). The highest frequency occurs in the 2-2.5 hour bin where 474 clouds were found as was evident in figure 6.10. When split into lifetime bins, the shape of the distribution of clouds in December shows a similar pattern to that of June 2010 (figure 6.13). 133 clouds were found with a lifetime of 2-2.5 hours in December, with the longest lifetime bin under analysis (3-3.5 hours) containing 37 clouds.

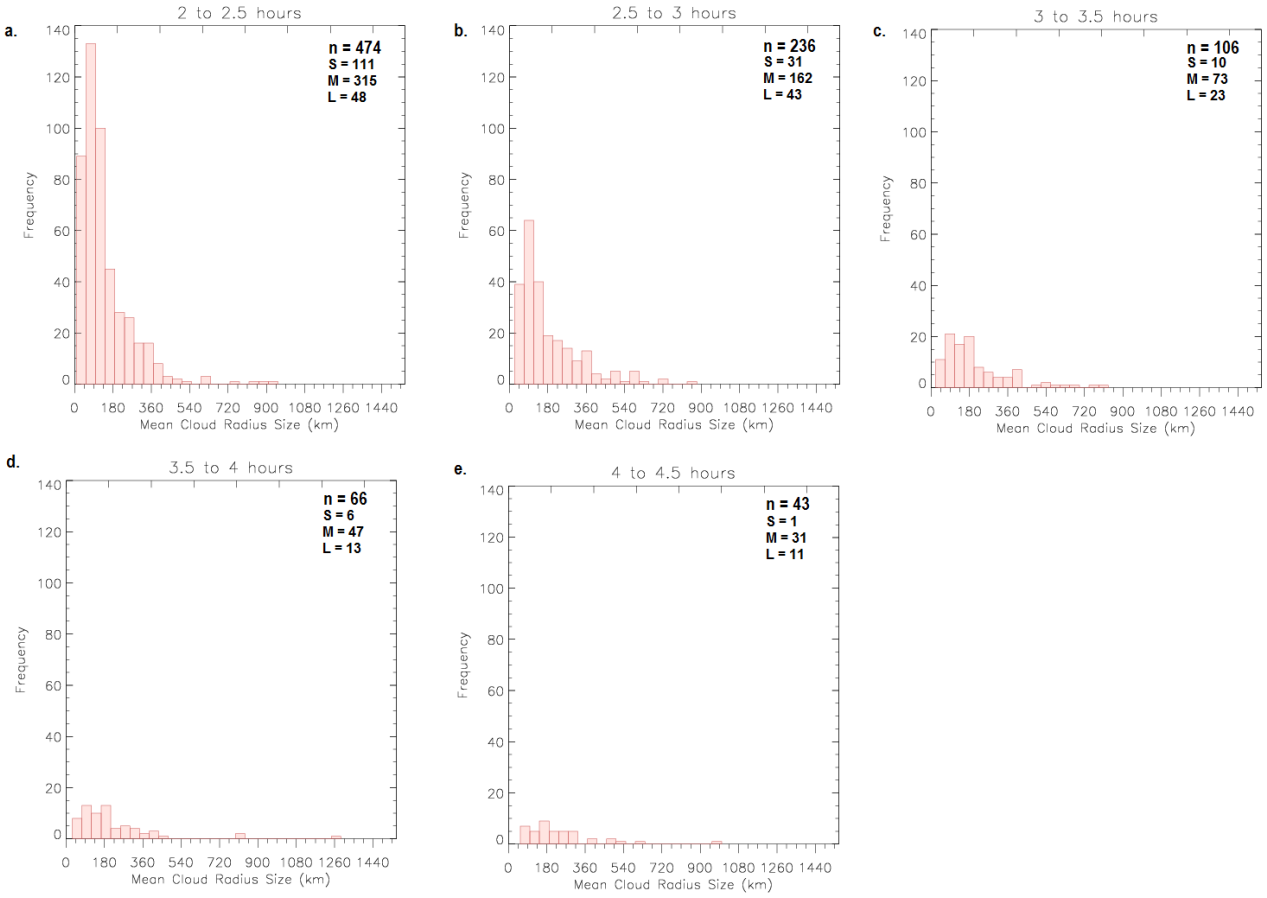

Figure 6.12: Frequency distributions of deep convective clouds in each half hourly time bin, between 2 to 2.5 hours and 4 to 4.5 hours for June 2010. n is the number of clouds in each lifetime bin. S, M and L represent small, medium, and large respectively.

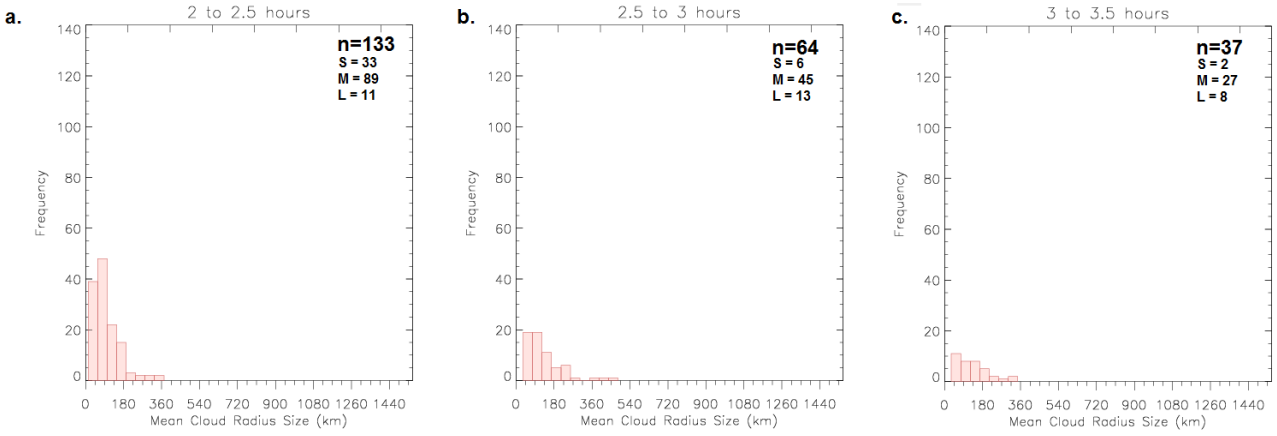

Figure 6.13: Frequency distributions of deep convective clouds in each half hourly time bin, between 2 to 2.5 hours and 3 to 3.5 hours for December 2010. n is the number of clouds in each lifetime bin. S, M and L represent small, medium, and large respectively.

6.2.2 Spatial distribution of deep convection

The spatial distribution of the deep convective clouds (the central latitude and longitude point of the cloud) detected using SEVIRI in both June and December 2010 are presented in 1˚x1˚ bins (figure 6.14). The spatial distribution shows the location where the cloud top $BTD_{6.2\text{-}7.3}$ is seen to first exceed the $BTD_{6.2\text{-}7.3}$ threshold.

Qualitatively, it can be seen that in some areas of the study region the number and location of convective events is similar to that seen in ERA-Interim in figures 3.6 and 3.7. These areas regions where the convection is largely influenced by the position of the ITCZ in both months, as expected from chapter 3. For example, no clouds are detected in the region between ~0° to ~6° N and ~38° to ~40° E. This is similar to the findings of Kayiranga (1991) and Ba and Nicholson (1998), who also find this region near Lake Turkana to be a region where the development of convection is minimal. This is also found by Roca et al., (2002) who prescribe this minimum in convection to the descending branch of the Walker circulation. In both months minimal convection is also found close to the Sahel, as expected due to this region being an area of vertical descent in the Hadley cell and a region of low humidity.

In June (figure 6.14a), the development of convection may also be influenced by the underlying relief. A comparison with the relief map in figure 3.8 shows the areas of peak convective activity to correlate with regions of high orography. This is found especially West/North-West of the Ethiopian highlands. Interestingly, the highest numbers of detected clouds are near the mountainous regions of Tondou Massif and Chaine des Mongos, a mountainous region in the Central African Republic (8° N, 22° E). Convection over Tropical Africa was found by Mohr and Thorncroft (2006) to occur within 0.5° of high terrain over the Cameroon highlands and the Tondou Massif. Similar patterns in convective frequency were found by Laing and Fritsch (1993) and Schröder *et al.,* (2009) over tropical Africa, with the Cameroon highlands found to correlate with the greatest frequency of convective events. Qualitatively, similar distributions in deep convection were found by Comer *et al.,* (2007), especially between 25°E-35°E and 0°N-5°N, and 34°E-37°E and 10°N-14°N. Using the principal component analysis of the diurnal cycle in GERB measured OLR as a diagnostic for deep convection, Comer *et al.,* (2007) find a similar spatial distribution in their 2nd empirical orthogonal function. This

was representative of deep convective cloud tops, which were found to strongly correlate with mountainous regions in tropical Africa, this being especially pronounced over the Ethiopian and Cameroon highlands.

The spatial distribution of deep convection detected in SEVIRI in December is also qualitatively similar to that of ERA-Interim (figure 6.14b). Little convection is seen above 8°N due to the southward movement of the ITCZ. Similar to June, no convection is seen at ~0° to ~6° N and ~38° to ~40° E. The region with the highest number of deep convective clouds in December is ~2°N, ~10°E, which is also seen in ERA-Interim. This region is close to the Gulf of Guinea and may experience enhanced convection due to convection being forced by the land-sea breeze. Both Desbois *et al.,* (1988) and Schröder *et al.,* (2009) find this to be particularly strong. As discussed in chapter 1 as a precursor to deep convection, Schröder *et al.,* (2009) find large values of specific humidity to coincide with this region possessing the local maxima of deep convective origin. In December, they find that over the Atlantic Ocean mean wind fields at near-surface exhibit a southeasterly trend. These then turn to south-westerly winds close to the coast of West Africa. This leads to a convergence over land, and with this region possessing high specific humidity, a local maxima in convective development is seen. This coincides with the peak in convection seen in this study in December.

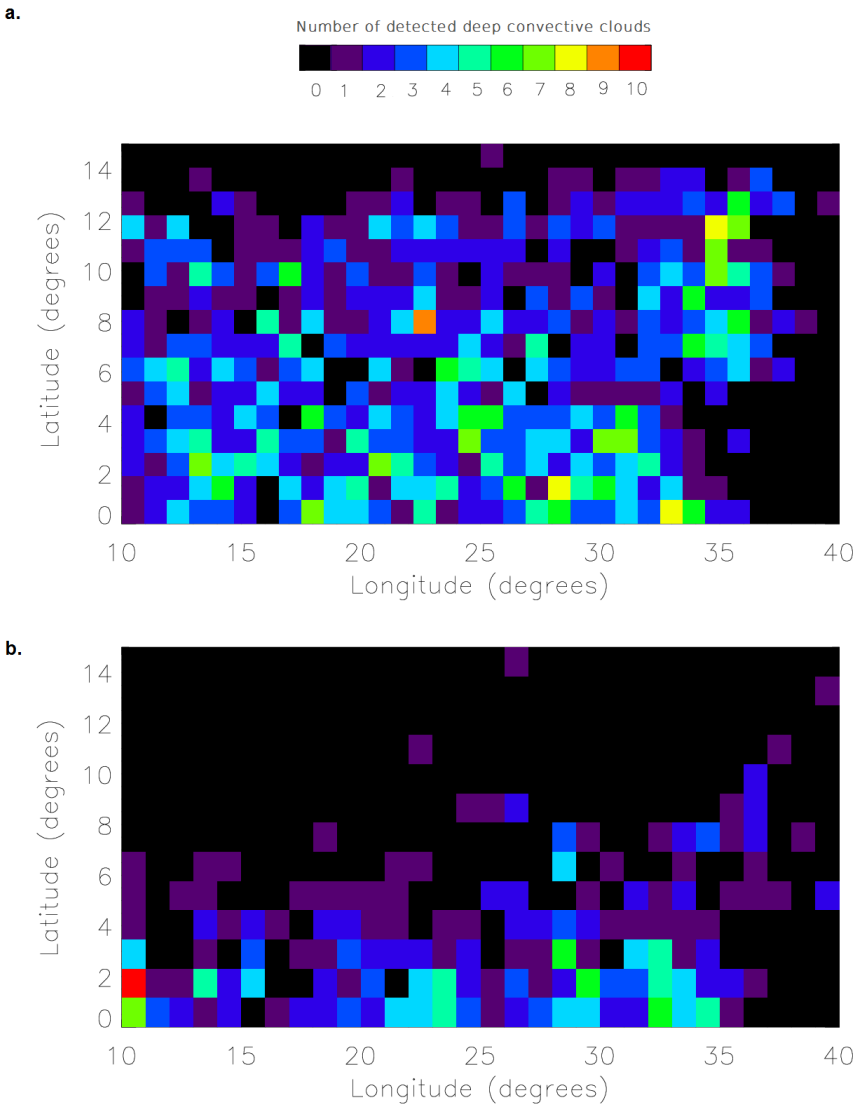

Figure 6.14: The spatial distribution of all deep convective clouds with lifetimes over 2 hours over the study region in 1°x1° bins, in **a)** June 2010 and **b)** December 2010.

6.3 The temporal and spatial scales of the UTH response associated with deep convection over tropical Africa

The mean clear-sky UTH and OLR in the region surrounding each tracked cloud in a 10 x 10 cloud radii box from the cloud edge was collected. This was analysed in boxes increasing in size by 1 cloud radii from the cloud edge, from 1-10 cloud radii. This allowed for a quantification of the spatial response of humidity to deep convection at a range of distances from cloud edge with respect to cloud radii. Time series analyses were conducted on the UTH in each analysis box (hereafter called analysis domain) for each tracked cloud over the range of distances from the cloud edge. This also allowed for a quantification of the temporal response both as the cloud was tracked over its lifetime, and the spatial response as this changes in time. For each

cloud analysis domain, mean clear sky UTH and OLR anomalies as a function of time over each cloud's lifetime were also calculated with respect to the mean UTH at the point of first detection to quantify any perturbation over the lifetime.

The box size is defined in the X and Y direction rather than a circle. This method follows a similar method of defining an area of analysis to Zelinka and Hartmann (2009). A box was used due to the original reclassification of altostratus following that of Yuan and Houze jr. (2010) in the orthogonal direction, rather than that in a circle surrounding the cloud. Further, though a circle may be a more natural shape to use when the definition of the distance from the centre of the cloud is based on the cloud radius, if a small cloud of, for example, 2 pixels diameter was detected, a box of 1 pixel would be used for 1 cloud radii. This would limit the ability to create a circle around the cloud. The use of a box rather than a circle around the cloud will also introduce errors in the UTH response when the UTH is not in of the two orthogonal directions from the cloud centre. The distance at the corners of each box will be further from the centre of the cloud than that in the orthogonal direction, which may distort the value of UTH assumed to be at a certain cloud radii distance away from the cloud edge when it is actually further away at the corners of the box.

6.4 Time series analysis

In order to quantify the response of UTH to deep convection in the spatio-temporal domain, time series analysis is conducted on each cloud size bin and for each lifetime bin given above. Time series of mean UTH are presented in 3D (figures 6.15, 6.17, 6.18, 6.20 and 6.21). The direction of the temporal response is in a leftward moving direction along the X-axis (away from the reader) in 15 minute intervals. The mean UTH response (Y-axis) over the clouds lifetime (from the point of first detection to the point where the $BTD_{6.2\text{-}7.3}$ threshold is no longer satisfied) is shown at increments of 1 cloud radii from cloud edge (Z-axis) to present the spatio-temporal response of mean clear sky UTH to deep convection. The coloured lines represent each cloud radii size analysis domain from 1 to 10, with black representing 1 cloud radii and red being 10 cloud radii. Deep convective clouds in both June and December are tracked and analysed to determine any seasonal effects based on cloud size and intensity. The UTH response is analysed and presented separately in the size bins small, medium and large.

For each individual cloud in the lifetime and size bin under analysis, mean UTH within each spatial analysis domain (from 1 to 10 cloud radii from cloud edge) is calculated at each timestep. This gives 10 mean UTH values at each timestep for each cloud. The overall mean UTH at each timestep presented in the timeseries is then the average of these mean UTH's in the respective lifetime and size bin. The standard error is also calculated at each timestep in the respective analysis domain to determine a measure of the spread of UTH in this bin. The standard error, *S.E.*, at each timestep (T) is calculated as:

$$S.E. = \frac{\sigma_{UTH'(T)}}{\sqrt{N}} \tag{6.2}$$

where N is the total number of samples, σ is the standard deviation of the overall mean UTH (*UTH'*) in the respective lifetime and size bin. The time series of UTH and OLR in June is analysed, followed by December for each lifetime bin with an appropriate number of samples in them.

6.4.1 June 2010 - small clouds

The mean UTH as a function of time in each cloud radii domain for small clouds with lifetimes of 2-2.5 hours is presented in figure 6.15. Spatially, it is seen that the UTH decreases with distance from the cloud edge, though this decrease is small. At the beginning of the clouds lifetime, the difference in mean UTH between 1 and 10 cloud radii represents a change in the spatial domain of 6.1%. The spatial difference in UTH is similar at all times over the lifetime, varying between a minimum difference of 5.6% at 75 minutes between 1 and 10 cloud radii and a maximum of 7.4% at the last timestep. The rate of change in UTH with time is not constant between cloud radii spatial domains (figure 6.16). Here a least-squares polynomial curve was fitted to each UTH time-series between 1 and 10 cloud radii from the point of first detection. Though the overall decrease in UTH within the spatial domain is small, the rate of change in the curves show that the UTH decreases at a faster rate closer to the cloud edge. For example, between 1 and 2 cloud radii in the first time step a decrease of -1.04% is found, compared to a decrease of -0.5% between the 6 and 7 cloud radii domain. As the cloud ages the difference in the rate of change between spatial domains changes. The rate of change closer to the cloud edge decreases, whilst at distances further form the cloud the rate of change increases. For example, after 90 minutes into the cloud lifetime UTH decreases by -0.46% between 1 and 2 cloud radii, and -0.55% between 3 and 4 cloud radii. This compares to the rate of change in UTH between 9 and 10 cloud radii of -0.9%. This suggests that as the cloud ages a propagation of UTH is seen from the cloud edge, reducing the spatial difference in UTH as the distance from the cloud increases.

Temporally, UTH generally shows a small increase over the clouds lifetime. Within 1 cloud radii (black line - figure 6.15), mean UTH ranges from a minimum of 58.6% to a maximum of 60.6%, a change of 2% over the lifetime. This small increase of ~2% over the clouds lifetime is seen for all cloud radii analysis domains, for example mean UTH in the 5 cloud radii analysis domain (light blue line) ranges from a minimum of 55.7% to a maximum UTH of 57.3%, whilst UTH in the 10 cloud radii domain (red line) ranges from 52.4% to 54.5%.

However, the standard error at each time step is large, with overlaps at each timestep from the beginning to the end of the time series. The standard error for the timesteps in the 1 cloud radii domain are found to be a maximum of 1.15 and a minimum of 1.11, which is approximately half of the range in mean UTH in this domain. Similar ranges and standard errors are found for all analysis domains, with the largest ranges (~2-2.5%) found within 3 cloud radii. Standard errors range between 0.9 and 1.2 over all analysis domains. Though this may suggest the small changes in UTH over the clouds lifetime are not robust, the general pattern emerging in the UTH response of an increase in UTH over the clouds lifetime is likely to be representative of the general pattern. Spatially, a more robust pattern in the UTH response is seen, with less of an overlap in standard error between subsequent timesteps (figure 6.16).

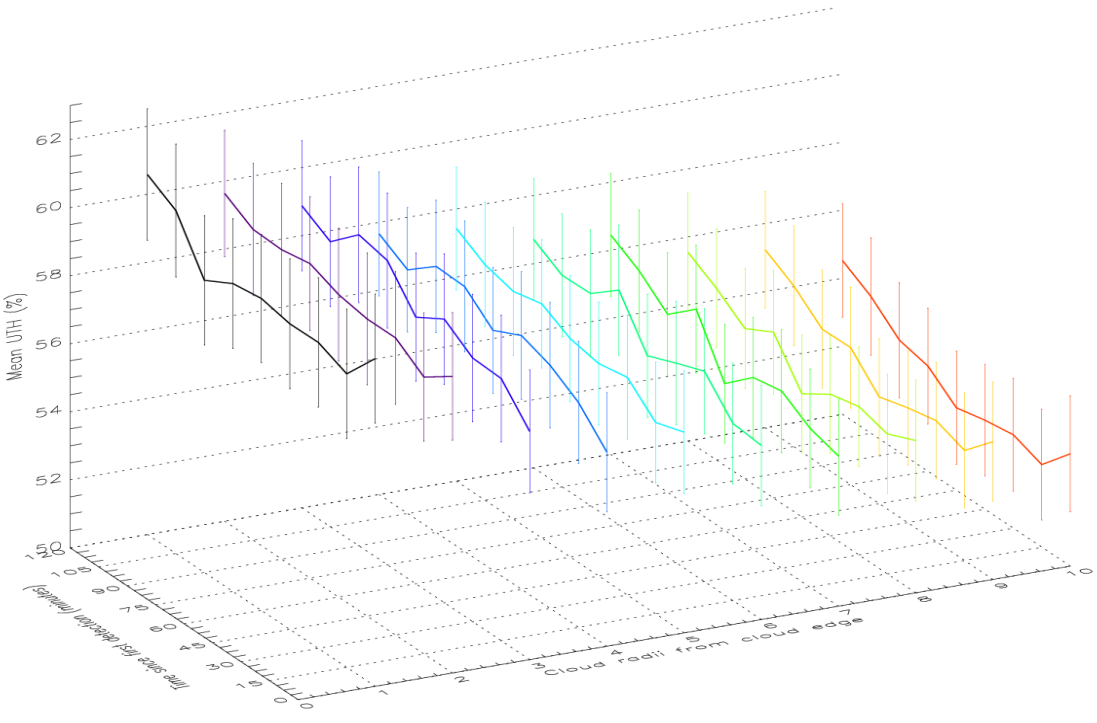

Figure 6.15: 3D plot of mean UTH (%) over time as a factor of the distance from cloud edge for small clouds in June, for clouds with a lifetime of 2 to 2.5 hours. One standard error is also given at each timestep. The colours represent each cloud radii domain, from 1 to 10. The black line is 1 cloud radii, the red line is 10 cloud radii, with increments of 1 cloud radii.

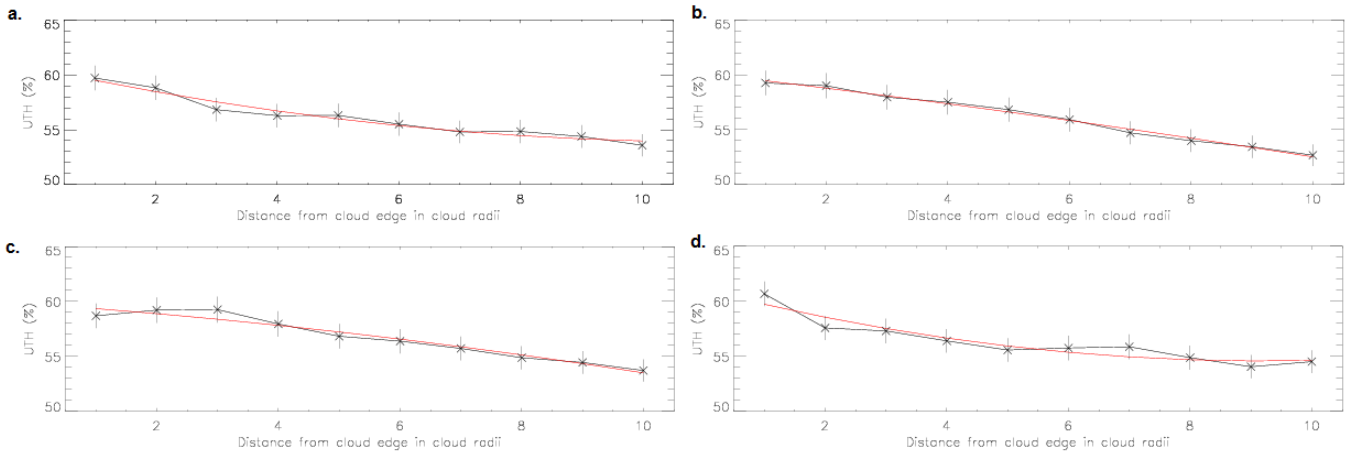

Figure 6.16: Response of UTH (%) over the spatial domain for small clouds in June 2010 with a lifetime of 2-2.5 hours. Mean UTH is presented for each cloud radii domain at **a)** 0, **b)** 60, **c)** 90 and **d)** 120 minutes into the clouds lifetime. The red line is a least squares polynomial fit to the UTH response. One standard error is given at each timestep.

6.4.2 Medium sized clouds

The mean clear sky UTH for all medium sized clouds shows a small increase in the clear sky UTH over time in all analysis domains. This increase in UTH over time is seen for all lifetime bins analysed.

An example of two 3D time series are given for clouds with a lifetime of between 2 to 2.5 hours (figure 6.17) and 3.5 to 4 hours (figure 6.18). Temporally, for clouds with a lifetime of 2 to 2.5 hours (figure 6.17), a smooth increase of approximately 4% in UTH is seen over the cloud lifetime. The mean UTH within 1 cloud radii in this lifetime bin ranges from a minimum of 61% to a maximum of 65%, compared to a minimum of 41.3% and a maximum of 45.5% at 10 cloud radii. Spatially, this is a difference of 20% in mean UTH between 1 and 10 cloud radii. This again shows that the greatest control on UTH in the region surrounding the deep convection is the distance from the cloud edge rather than the response over the cloud lifetime. This is similar to the pattern in the UTH response seen for small clouds. The spatial UTH response is ~3 times greater than the spatial difference seen for small clouds of the same lifetime (figure 6.15 and 6.16). With respect to the temporal response over the clouds lifetime, the change in UTH for medium sized clouds is twice that found for small clouds of the same lifetime.

For all analysis domains small standard errors are found for clouds with a lifetime of 2-2.5 hours, though the error is large enough that some overlap does occur between the UTH at each distance. The smaller standard errors are a consequence of the larger number of clouds in this size and lifetime bin. this would also suggest this to be a more robust representation of the UTH response in both the spatial and temporal domains.

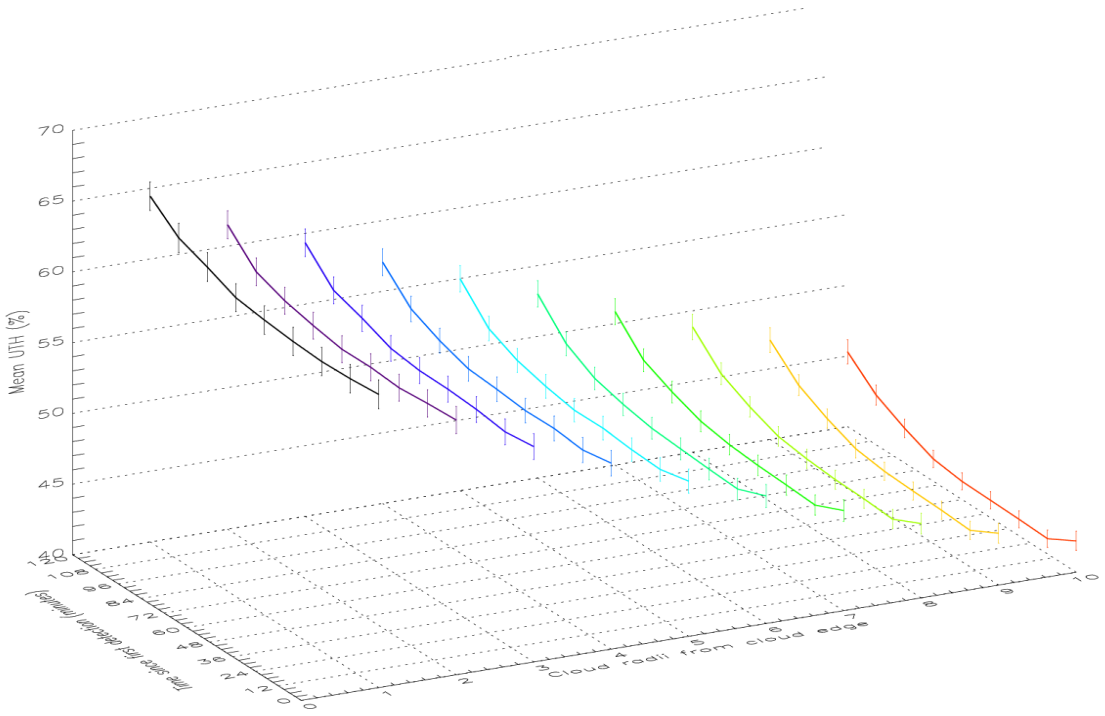

Figure 6.17: 3D plots of mean UTH (%) over time as a factor of the distance from cloud edge for medium sized clouds in June 2010, for 2 to 2.5 hours. One standard error is also given at each timestep. The colours represent each cloud radii domain, from 1 to 10. The black line is 1 cloud radii, the red line is 10 cloud radii, with increments of 1 cloud radii.

A greater perturbation to mean UTH over the clouds lifecycle can be seen for those clouds with a 3.5 to 4 hour lifetime (figure 6.18) compared to medium sized clouds with a shorter lifetime. An increase in mean UTH can be seen towards the end of the lifecycle, with the perturbation being greater with distance from the cloud edge.

For clouds with a lifetime of 3.5-4 hours, the mean UTH within one cloud radii ranges from a minimum of 65.2% to a maximum of 70.5%. Within 4 cloud radii mean UTH has decreased to a minimum of 55.7% and a maximum of 60.8% over the lifetime of the cloud, a decrease in mean UTH of ~10%. The mean UTH continues to decrease with an increase in the size of the analysis domain, with the lowest UTH found at 10 cloud radii. A minimum of 41.2% and a maximum of 51.2% is found at 10 cloud radii. This suggests the greatest rate of change occurs within the first 4 cloud radii. Interestingly, the difference between the maximum UTH between the 1 and 10 cloud radii analysis domains is ~20% for both lifetime bins shown. This is similar across all lifetime bins analysed for medium sized clouds (including those not shown here). This compares to small clouds, where a difference is ~6% is seen for the lifetime bin analysed. This suggests that a UTH response exists in relation to the cloud size.

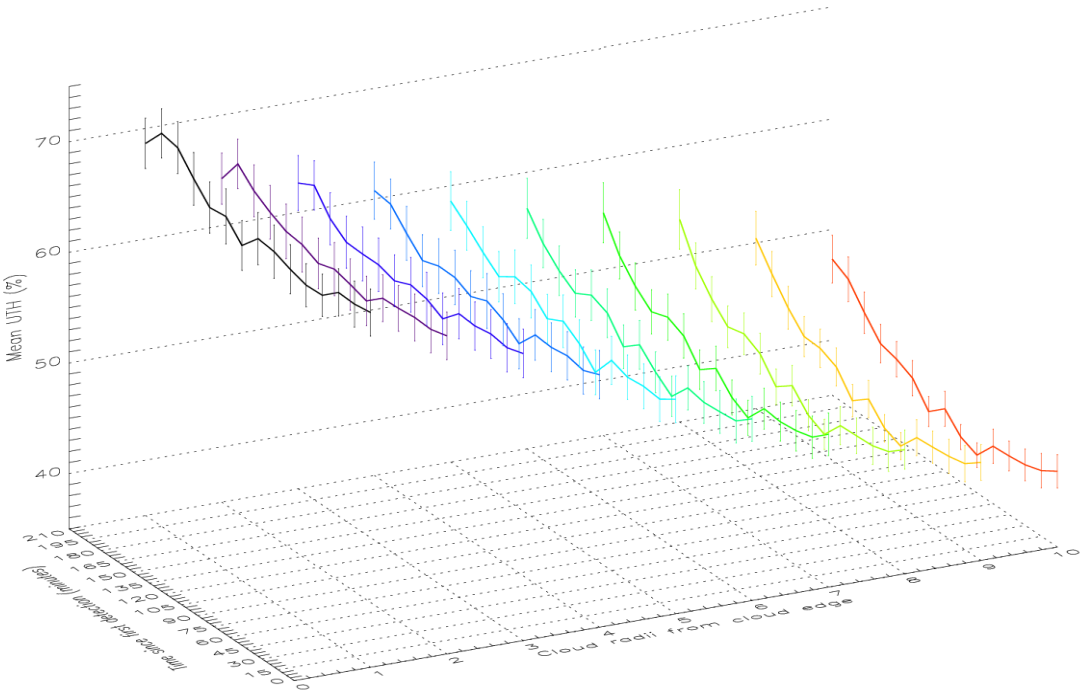

Figure 6.18: 3D plots of mean UTH (%) over time as a factor of the distance from cloud edge for medium sized clouds in June 2010, for 3.5 to 4 hours. One standard error is also given at each timestep. The colours represent each cloud radii domain, from 1 to 10. The black line is 1 cloud radii, the red line is 10 cloud radii, with increments of 1 cloud radii.

For medium sized clouds with a lifetime of 3.5 to 4 hours the rate of change between spatial domains shows a relatively constant decrease in UTH between each domain (figure 6.19). This pattern is found for all lifetime bins analysed for medium sized clouds in June 2010. This is in contrast to that found in for small clouds whereby a different rate of change was seen dependent on the distance from the cloud edge. The rate of change is steeper in the earlier stages of the clouds life time as the UTH has not propagated away from the cloud edge.

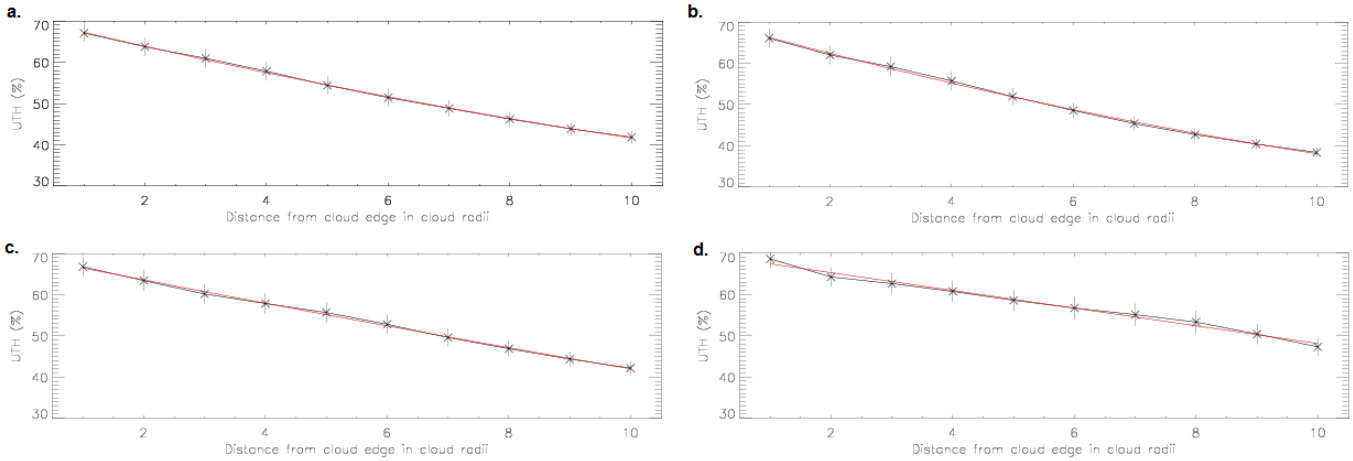

Figure 6.19: Response of UTH (%) over the spatial domain for medium sized clouds in June 2010 with a lifetime of 3.5-4 hours. Mean UTH is presented for each cloud radii domain at **a)** 0, **b)** 75, **c)** 150 and **d)** 210 minutes into the clouds lifetime. The red line is a least squares polynomial fit to the UTH response. One standard error is given at each timestep.

6.4.3 December 2010 - Medium sized clouds

3D time series are presented for medium clouds in December with lifetimes of 2-2.5 hours (figure 6.20) and 3-3.5 hours (figure 6.21). In comparison to clouds within the same lifetime and size bins in June, a difference of 12% in overall mean UTH is seen between months, with June having a higher mean UTH over all distances from the cloud edge.

For medium sized clouds with a lifetime of 2-2.5 hours, a definite spatial pattern emerges with UTH decreasing with distance from the cloud edge. The strongest decrease in UTH is seen within the first 3 cloud radii, with the UTH response becoming flatter with greater distance from the cloud edge. With regards to the spatial response of UTH, a stronger pattern emerges when compared to the temporal response. This is a similar relative pattern of behavior to that seen in June. A spatial difference of 12.9% is found within 10 cloud radii at the end of the lifecycle. When compared to the same lifetime and size group as June 2010, this is ~7% lower.

Temporally, within 1 cloud radii the mean UTH over the lifetime varies between an minimum of 50.3% at 30 minutes into the lifetime, increasing to a maximum of 52.9% at the end of the clouds lifetime, a change of ~2.5% over the clouds lifetime. At 10 cloud radii from the cloud edge a minimum mean UTH over the lifetime of 37.6% is found, again at 30 minutes into the clouds lifetime, suggesting an initial drying in the early stages of the clouds lifetime. This again increases to a maximum of 40% at the end of the lifetime as the cloud dissipates. Again, this is a change of ~2.5% over the clouds lifetime at this distance from the cloud edge, less than that for the medium sized clouds with the same lifetime in June 2010.

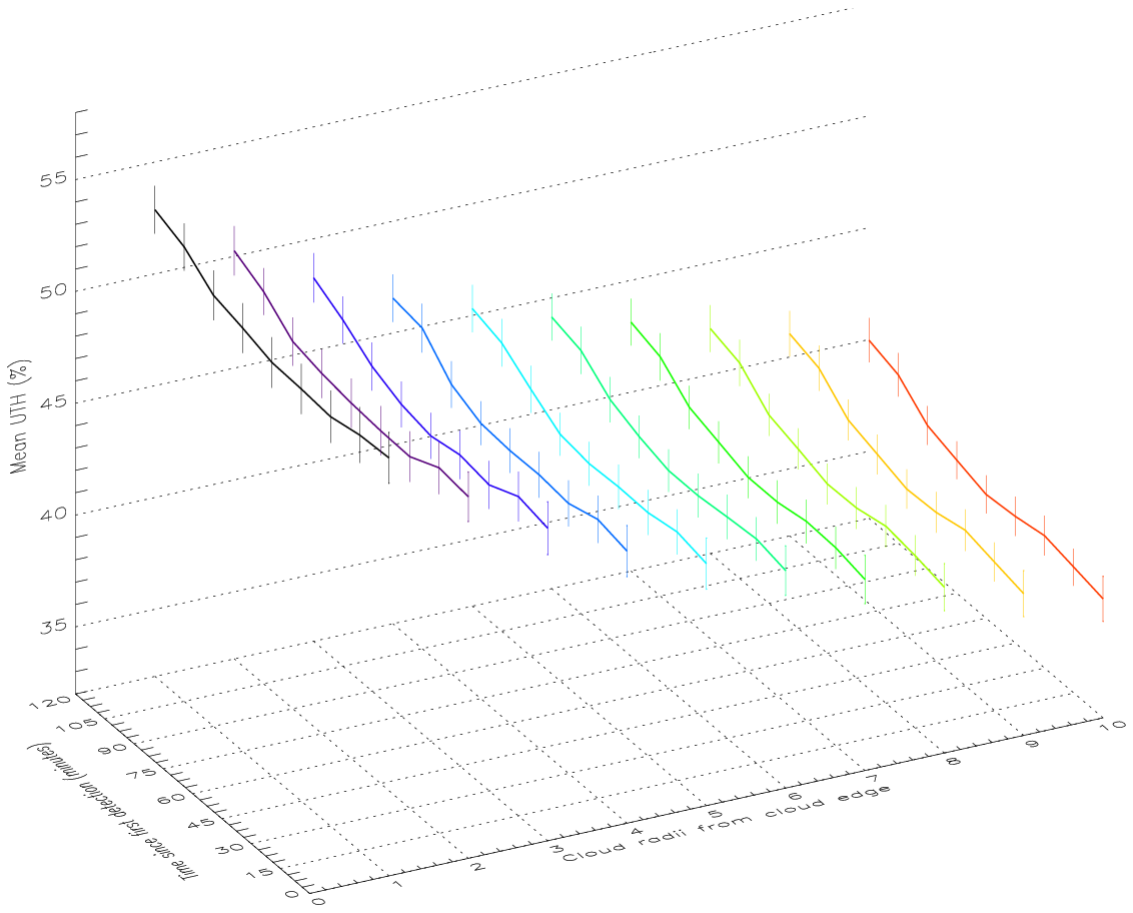

Figure 6.20: 3D plots of mean UTH (%) over time as a factor of the distance from cloud edge for medium sized clouds in December with a lifetime of 2 to 2.5 hours. One standard error is also given at each timestep.The colours represent each cloud radii domain, from 1 to 10. The black line is 1 cloud radii, the red line is 10 cloud radii, with increments of 1 cloud radii.

For clouds with a lifetime of 3-3.5 hours, similar patterns in the mean UTH response to the clouds presented in figure 6.20 emerge (figure 6.21). Temporally, UTH is initially seen to decrease suggesting a drying is occurring. This is followed by an increase over the clouds lifetime with a slightly stronger perturbation towards the end of the lifetime. Again, this perturbation is stronger towards the end of the lifetime in the larger analysis domains. Mean UTH within 1 cloud radii increases from a minimum of 50.6% to a maximum of 54.6% at the end of the lifetime. At 5 cloud radii, UTH decreases from 44.6% to 42.4% within 75 minutes, before increasing to 46.3% at the end of the lifetime. This initial decrease is stronger at distances further from the cloud edge. For example, At 10 cloud radii an initial decrease from 40% to 36% occurs within the first 75 minutes, increasing to 41% at the end of the lifetime.

Spatially, a decrease in mean UTH of ~13.5% occurs over the entire analysis domain. This is similar to the medium sized clouds in December with a shorter lifetime shown above, though it is smaller than that found in June 2010. This suggests the existence of a seasonal effect on UTH by deep convection in this region.

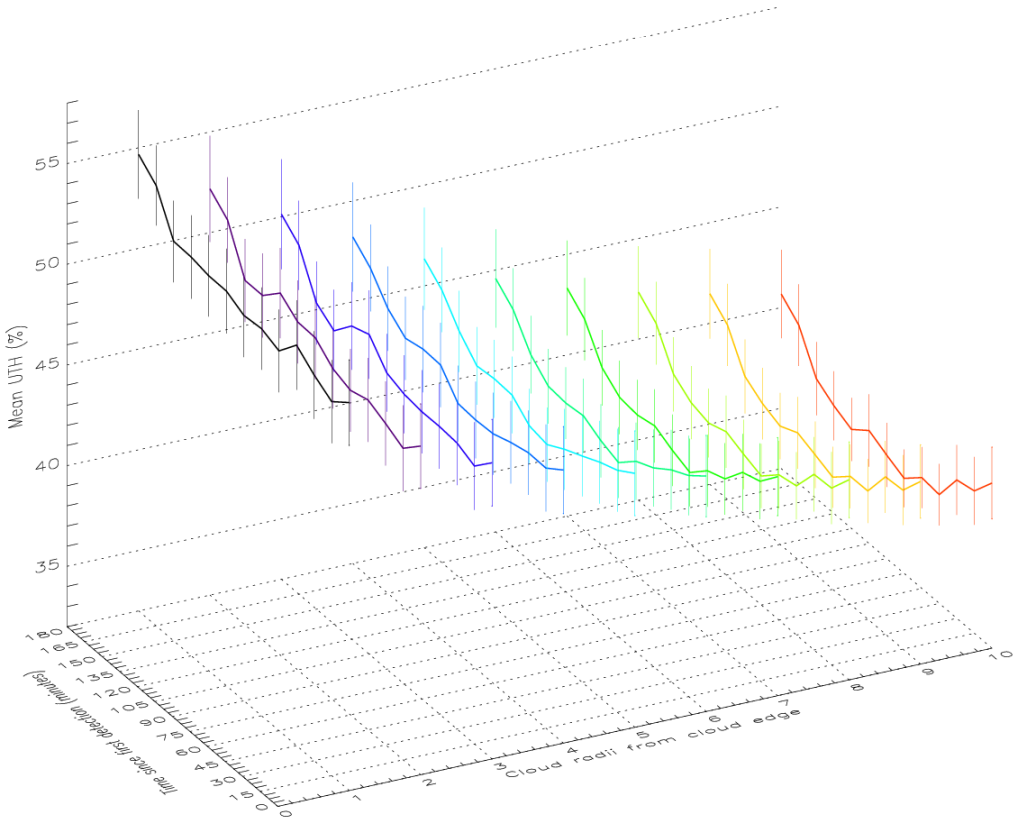

Figure 6.21: 3D plots of mean UTH (%) over time as a factor of the distance from cloud edge for medium sized clouds in December with a lifetime of 3 to 3.5 hours. One standard error is also given at each timestep. The colours represent each cloud radii domain, from 1 to 10. The black line is 1 cloud radii, the red line is 10 cloud radii, with increments of 1 cloud radii.

6.4.4 Discussion

Overall, a general temporal and spatial pattern in the mean UTH response is seen for each cloud size and lifetime bin analysed in both June and December. As shown above, although the standard errors show some overlap at all timesteps, a robust pattern emerges in which an increase in mean UTH is seen over the clouds lifetime. This is seen for all spatial analysis domains from 1 to 10 cloud radii. Overall, though an increase occurs over time, the increase in UTH found over time in all cases is small. For small clouds in June 2010 with a lifetime of 2-2.5 hours, an increase in UTH of only 2% was found, with this similar for each of the cloud radii domains analysed. A small increase of ~4% over the clouds lifetime is also seen for medium sized clouds with the same lifetime. The UTH change over time is similar to the patterns in the UTH response to deep convection found by both Zelinka and Hartmann (2009) and Johnston *et al.,* (2013) who find an increase of between 3% and 10% within 3 hours of detecting deep convection, the magnitude being dependent on the distance from the cloud. The UTH response over the clouds lifetime is found to be twice as strong in response to medium clouds when compared with small clouds. This suggests that a relationship exists between cloud size and the effect on UTH in the clear sky region surrounding the cloud. Temporally, the UTH response is

largest towards the end of the cloud lifetime as the cloud dissipates. This suggests that a time lag may exist in the response of UTH to deep convection.

Another pattern that emerges is a decrease in UTH with an increase in the size of the spatial analysis domain. This is consistent with the current understanding regarding convection as discussed in chapter 1, with the convection transporting water vapour to the upper troposphere and moistening the region surrounding it in the smaller analysis domains. This pattern is found to be stronger than the temporal response to UTH and is in contrast to Wright *et al.*, (2009) who found the UTH to respond greater to the time elapsed rather than distance from cloud edge. The spatial pattern in UTH in the region surrounding the cloud shows a greater perturbation of UTH for medium clouds. Medium clouds in June caused a ~20% change in UTH within a 10 cloud radii distance from the cloud edge compared to ~6% for small clouds for the same spatial domain. When comparing smaller clouds to medium sized clouds, a difference in the mean UTH response may be expected due to the more intense, larger systems transporting more hydrometeors to the upper troposphere. This agrees with the finding of Chung *et al.,* (2004), who find a positive correlation between UTH and the convective cloud area, attributed to the greater number of hydrometeors detraining from larger cores. Though, as seen from Sherwood (1999) a direct correlation may not exist due to other physical mechanisms controlling moistening, such as ambient RH and the updraft intensity.

Overall, the time series analyses suggests that in the vicinity of the cloud there is a constant strong influence on mean UTH, which may be due to mixing of the water vapour transported to the upper troposphere by the deep convection, and the increase in UTH from the evaporation of cloud hydrometeors. This pattern is expected from the discussion in chapter 1. The findings in this study add to further disagreement with Sun and Lindzen's (1993) suggestion that a drying effect is seen in the upper troposphere by deep convection. The UTH response found shows a form of 'cloud halo' close to the cloud edge, similar to that found by Perry and Hobbs (1996). When comparing the findings of this study to that of Wright *et al.,* (2009) the spatial extent of the UTH responses are found to be similar. Wright *et al.,* (2009) found moistening to be greatest within 300 km from the cloud edge. Given the size distribution of cloud radii in this study in June 2010, and the definition of medium clouds based on cloud radii size in figure 6.11, the spatial pattern found by Wright *et al.,* (2009) falls within 1 and 5 cloud radii for medium sized clouds. Their 300 km spatial moistening corresponds to a range of 1 cloud radii when medium clouds posses a radii of 292 km (the largest radii of medium sized clouds), and a maximum of 5 cloud radii when medium clouds have a radii of 61 km (the smallest medium cloud radii). This is within a similar spatial domain as that of the cloud halo effect found by Perry and Hobbs (1996). Luo and Rossow (2004) actually find the region moistened by convection to be much larger at 600-1000 km, which corresponds to a cloud halo for larger cloud systems.

UTH shows a weaker response to medium sized clouds in December than in June. Spatially, a difference of ~20% is found between 1 and 10 cloud radii for medium sized clouds in June, compared to ~13% for medium sized clouds in December. The overall clear sky UTH in the region surrounding deep convection is also higher in June than in December. UTH is found to be ~13% greater in June 2010 than December 2010. This may be a seasonal effect, related to the presence of the ITCZ in June, and consequently more cloud cover. Areas with a greater frequency of cloud cover, such as the study region in June, are found by Soden (1998) to have a greater UTH due to the influence of cloud condensate evaporation in enhancing UTH. This general pattern contrasts with the UTH response to deep convection found by Udelhofen and Hartmann (1995) and Roca *et al.,* (2002) who both found that moistening is greater in regions of lower ambient UTH, which suggests that

deep convection should have a greater perturbing effect on UTH in December than June.

The UTH in the spatial domain also shows an interesting pattern with regards to the rate of change in UTH with distance from the cloud edge. The rate of change, calculated using a least squares polynomial, for small clouds shows a stronger decrease between smaller analysis domains in the early stages of the clouds life time, though the actual change in UTH is small. As the cloud ages the rate of change gets larger for larger analysis domains. This represents a propagation of UTH away from the cloud with age. This pattern is less obvious for medium sized clouds whereby the rate of change is relatively constant between spatial domains over the clouds lifetime.

The overall robustness of these results can be assessed via the spread in the values of UTH found for each cloud class and timestep, as manifested by the associated standard error. This measure of spread will be affected by the sample size, typically becoming larger when fewer clouds fall within a given category. However, as the cloud ages, although some overlap occurs between the standard error in each timestep and the one proceeding it, no overlap is seen between the standard error at the beginning and end of the clouds lifetime. This suggests a significant perturbation in UTH does occur in both the temporal and the spatial domain at the end of the lifetime when compared to that at the beginning. Hence, the associated general increase in UTH in the temporal domain and decrease with distance from cloud is likely to be a robust pattern.

The mean UTH over the spatial and temporal domains for medium sized clouds shows a greater response to deep convection when compared to small clouds and is in agreement with Chung *et al.,* (2004). Due to the inherent control on the analysis domain being the cloud radii size, larger clouds will have larger analysis domains. A larger analysis domain would be expected to encompass a larger region of lower ambient UTH due to it encompassing a region further from the cloud edge. This issue was also analysed by Udelhofen and Hartmann (1995). They suggested that the UTH within an analysis region is dependent on the size of the analysis domain used. They analysed 3 domain sizes and found UTH to be range from 66.1% at the cloud edge, dropping to 39% within 50 km and 24% with 200 km. For small and medium sized clouds this would be within 1 to 5 cloud radii from the cloud edge. Therefore, given the size of the cloud radii detected in this study, the use of cloud radii as a metric for the analysis domain should accurately capture the UTH response to deep convection as the use of cloud radii in increments of 1 cloud radii from the cloud edge should adequately capture the spatial change in UTH. This is confirmed from an analysis of the rate of change in UTH with respect to distance from the cloud edge. For small clouds especially, the rate of change discussed above showed that the greatest change in the UTH occurs within the region closets to the cloud in the early stages of the cloud lifecycle. For medium clouds, the rate of change is relatively constant between all spatial domains, with this pattern consistent at all stages in the lifecycle.

6.5 UTH and OLR anomalies

From the 3D plots shown above, it is clear that some general spatial and temporal response of mean UTH to deep convection does exist. To determine whether any significant perturbation in the UTH and OLR is seen in this study and to remove the ambient component of the UTH and OLR response, anomalies of mean UTH and OLR are calculated with respect to that measured in the first time step, *T0*. The OLR is the broadband OLR measured by GERB and corresponds to the same clear sky pixels as the UTH retrievals. The anomaly is calculated for each individual cloud n of N clouds in the lifetime and size bin at timestep T. The anomaly,

$\triangle UTH(T)_n$, is the difference between $UTH(T)_n$ and the UTH at the point when the cloud is first detected $UTH(0)_n$:

$$\triangle UTH(T)_n = UTH(T)_n - UTH(0)_n \quad for\ n = 0, N \tag{6.3}$$

The anomaly is calculated at each point in each timestep for each cloud separately within the lifetime and size bin analysed. This is calculated for each analysis domain between 1 and 10 cloud radii. The overall mean anomaly for the lifetime and size bin within the analysis domain is then calculated as the mean of all N anomalies in the time bin:

$$\triangle UTH'(T)_n = \frac{\sum(\triangle UTH(T)_{n...N})}{N} \tag{6.4}$$

The standard error of the mean anomaly is calculated at each timestep using equation 6.2. As discussed in chapter 1, there is some agreement that a time lag may exist in the response of UTH and OLR to deep convection. The lag time is found to be a function of the metric from which the lag is measured. To further quantify the UTH response, the lag time is calculated. In this study, the maximum $BTD_{6.2\text{-}7.3}$ is considered the point of maximum convection. The lag time is considered to be the difference between the point at which the maximum $BTD_{6.2\text{-}7.3}$ is found over the clouds lifetime and the point at which the mean anomaly minus the standard error is greater than that measured at *T0*, as this is where some significant positive perturbation is considered to be seen in response to deep convection. This is calculated for each cloud in the respective cloud size and lifetime bin and given as an overall average for each bin. The anomalies are also calculated for the corresponding OLR to characterise the implications for the net outgoing radiative energy balance.

6.5.1 June 2010 - small clouds

The mean UTH (black) and OLR (red) anomaly with one standard error is presented in figure 6.22 for clouds with a lifetime of 2-2.5 hours. The UTH is represented by the left hand Y-axis and OLR by the right hand Y-axis. Although in each analysis domain some overlap is seen between the UTH standard errors at each time step, it is evident that a significant increase in mean UTH is seen over the clouds lifetime with respect to the UTH at *T0*. As suggested in the previous UTH analysis, in all cases in the early stages of the lifetime UTH decreases below the UTH at *T0*, suggesting a drying may be occurring in the early stage of the clouds lifetime. The magnitude of the initial drying is found to increase with an increase in the size of the analysis domain. UTH then increases, reaching a maximum towards the end of its lifecycle when the cloud is expected to be dissipating and hydrometeors evaporating.

Spatially, for clouds with a lifetime of 2-2.5 hours, UTH anomalies at the end of the clouds lifetime are found to increase with distance from cloud edge up to a distance of 4 cloud radii (not shown). For 1 cloud radii, UTH anomalies reaches 1.33% above that at *T0*. This compares to a maximum of 2.14% at 4 cloud radii. After this point, a smaller maximum UTH anomaly is found at the end of the clouds lifetime (1.28% at 5 cloud radii), ranging between 1% - 1.2% between 6 and 10 cloud radii from the cloud edge. This suggests the strongest influence of the cloud on UTH occurs within 4 cloud radii. When considering the standard error of the anomalies, the point of significant UTH perturbation occurs earlier in the lifetime for smaller analysis domains. Within 1 and 3 cloud radii (figures 6.22a and b) no overlap is seen with the standard errors at *T0* after 75 minutes into the clouds lifecycle, compared to 120 minutes at 6 and 10 cloud radii.

With regards to OLR, overall for clouds with a 2-2.5 hour lifetime, a simultaneous decrease in OLR anomalies are generally found with an increase in UTH anomalies. This pattern is seen in all cloud radii domains, though the OLR anomalies within 1 cloud radii shows a slight lag in response to the UTH anomalies. This may relate to the initial drying seen in the UTH anomaly. This lag is especially prevalent at 60 and 75 minutes where both UTH and OLR anomalies are seen to be increasing before a decrease in the OLR anomalies. As the analysis domain increases, the response of OLR with a change in UTH shows little negative perturbation from that at *T0*. This can be seen from the standard errors overlapping that at *T0*. Within 1 cloud radii no significant OLR perturbation is found and may be due to the lag in the OLR response to the UTH perturbation. Compared to that at *T0*, the largest OLR perturbations are found towards the end of the clouds lifetime. Within a 3 cloud radii analysis domain, a maximum OLR perturbation of -2.9 Wm^{-2} is found corresponding to the maximum UTH perturbation of 2% at the end of the clouds lifetime. Similarly, at 6 cloud radii a maximum OLR perturbation of -2.7 Wm^{-2} is found with a corresponding maximum UTH perturbation of 1.6%.

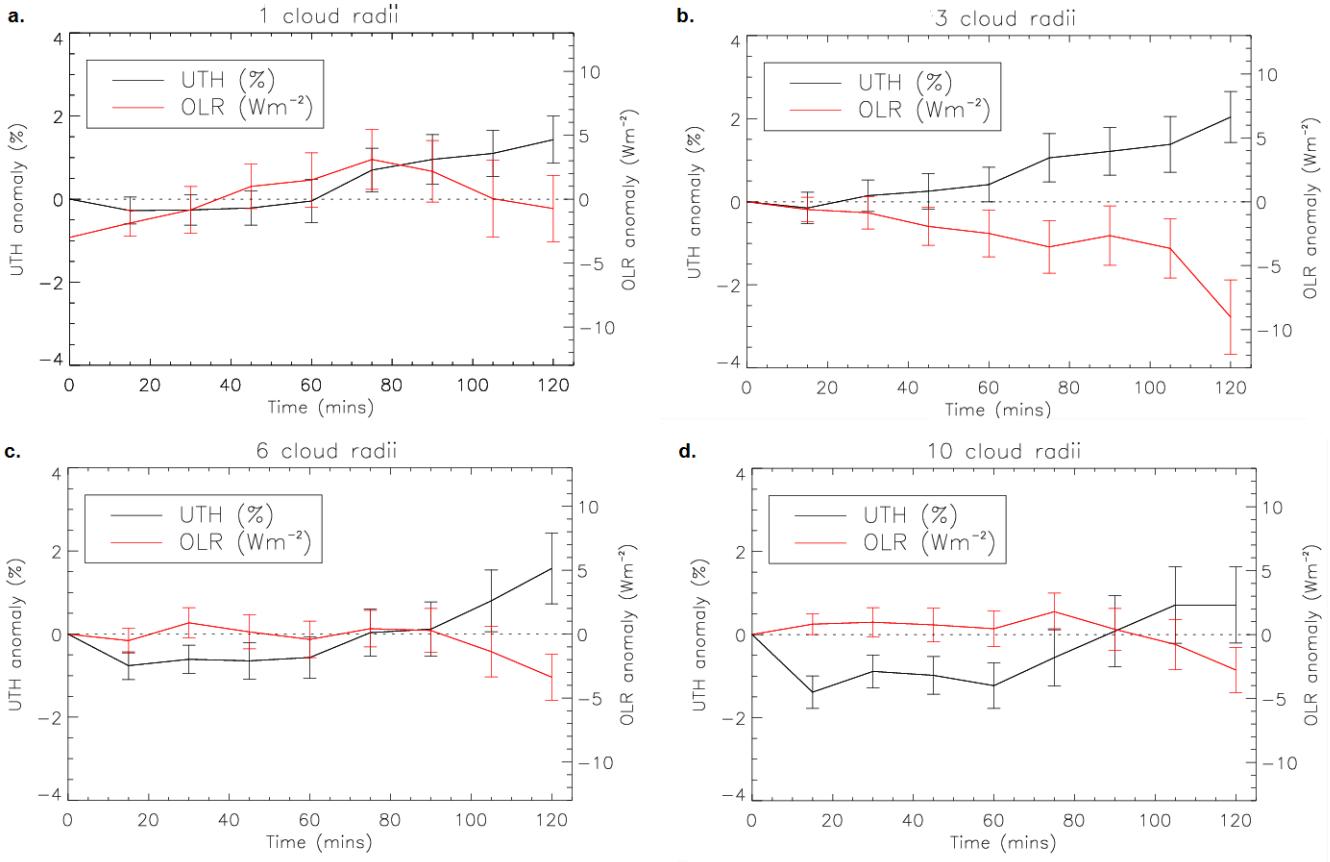

Figure 6.22: Clear sky UTH anomalies from the mean UTH (black) and OLR (red) at *T0*, for small clouds in June 2010 with a lifetime of 2 to 2.5 hours. The UTH anomalies are given over the life time of the cloud, in relation to distance from the cloud edge, for **a)** 1 cloud radii, **b)** 3 cloud radii, **c)** 6 cloud radii and **d)** 10 cloud radii. One standard error is also given.

The relationship between the UTH and OLR anomalies is plotted to determine the strength of the UTH

perturbation on the corresponding OLR perturbation (figure 6.23). The spatial domains are shown together to determine the overall spatial response of OLR to UTH. A linear least-squares fit with one sigma error of the slope and intercept is calculated for the relationship. A negative linear correlation of -0.64 is found to exist between UTH and OLR anomalies. A decrease in mean clear sky OLR of 1.59±0.28 Wm^{-2} is found with each increase in mean clear sky UTH of 1%.

Some outliers are seen resulting from the lag between UTH and the OLR response in the 1 cloud radii analysis domain (see legend), these being the UTH and OLR values at 60 and 75 minutes in the time series. The largest outlier is seen in the 3 cloud radii analysis domain and is a result of the large UTH anomaly of 2.08% towards the end of the lifetime seen in figure 6.22b. A large concentration of negative UTH anomalies representative of the initial drying larger early in the clouds lifecycle in the larger analysis domains, coupled with the largest UTH anomalies being found closer to the cloud edge (blue and purple points) suggests the existence of a spatial pattern of UTH in a localised region surrounding deep convection. It can also be seen that, overall, no time lag exists in the OLR response to UTH anomalies. The RMSE is calculated as 2.5 Wm^{-2}, which is relatively large given the range in OLR anomalies found. A two-tailed t-test shows the linear fit to be significantly different from 0 ($P = < 0.05$).

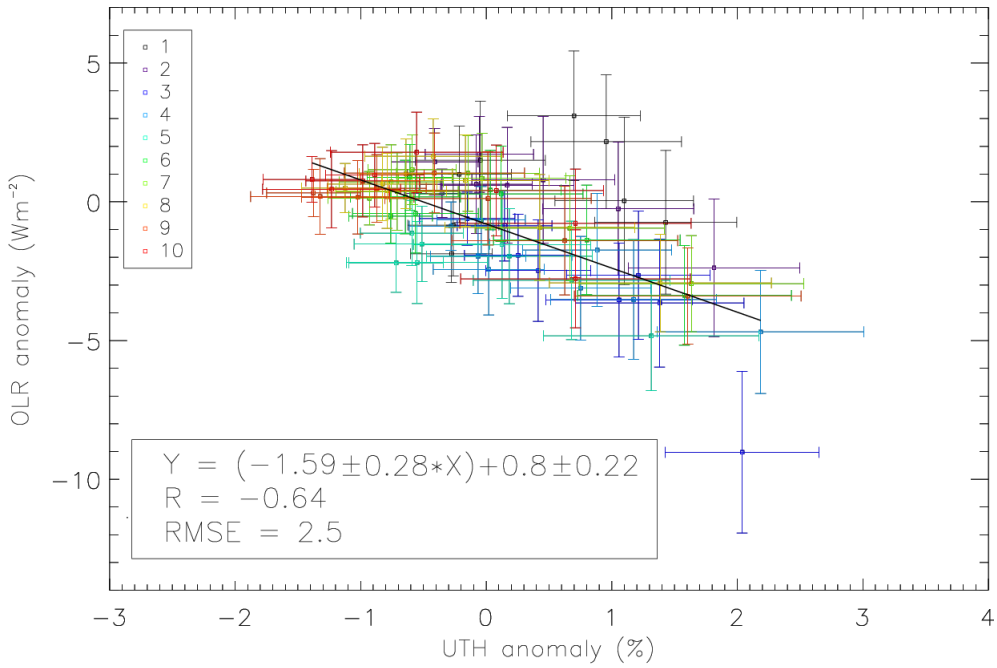

Figure 6.23: The linear least-squares relationship between UTH (%) anomalies and corresponding OLR (Wm^{-2}) anomalies for small clouds with a lifetime of 2-2.5 hours. One standard error is given for the UTH and OLR anomalies. Errors in the slope and intercept are one standard deviation. Analysis domains between 1 and 10 cloud radii are assigned a colour as shown in the legend.

6.5.2 Medium clouds

For clouds with a lifetime of 2 to 2.5 hours (figure 6.24), a significant increase in UTH above that at *T0* occurs towards the end of the clouds lifecycle as can be seen from the standard error overlap with the UTH

at *T0*. At 1 cloud radii, the range of anomalies found are between -0.2% (with a standard error of 0.16%) and 1.9% (with a standard error of 0.5%). This is again similar to the small clouds in June 2010 with the same lifetime in this analysis domain. The maximum perturbation in UTH of 3.8% is found at 6 cloud radii for medium sized clouds in this lifetime bin, which is a larger spatial influence than that for small clouds with the same lifetime. At 10 cloud radii (figure 6.24d), UTH anomalies range from -1.2 % to 3.4%, with standard errors of 0.27% and 0.74% respectively, ~3 times larger than for small clouds with the same lifetime, though the perturbation itself is small.

In comparison to small clouds with the same lifetime, within analysis domains between 1 and 5 cloud radii, the time difference between UTH at *T0* and that when the standard error no longer overlaps is the same. Within 1 cloud radii the standard errors at 75 minutes and later show no overlap with mean UTH at *T0* (figure 6.24a). Though the perturbation in UTH is more evident at larger cloud radii, the point where a significant difference is seen occurs later in the clouds lifetime, suggesting that a spatial pattern exists with regards to UTH propagation from the cloud edge.

Large perturbations can also be seen in the mean clear sky OLR response to deep convection. The OLR response shows an inverse relationship to UTH anomalies. This also suggests no time lag exists between perturbations between the two variables. Within 1 cloud radii a maximum OLR perturbation of -1.6 Wm^{-2} corresponds to the maximum UTH perturbation of 1.9%, with this increasing with distance from cloud edge. Due to the non-linear relationship between OLR and UTH, the maximum UTH anomaly, found at 6 cloud radii, does not correspond to the maximum OLR perturbation. A maximum perturbation of -4.4 Wm^{-2} is found at 10 cloud radii corresponding to a UTH perturbation of 3.4% (figure 6.24d), compared to -3.6 Wm^{-2} at 6 cloud radii for a UTH change of 3.8%. This is a response to the ambient UTH, whereby a bigger response in OLR is found for the same UTH change if the initial state is dry.

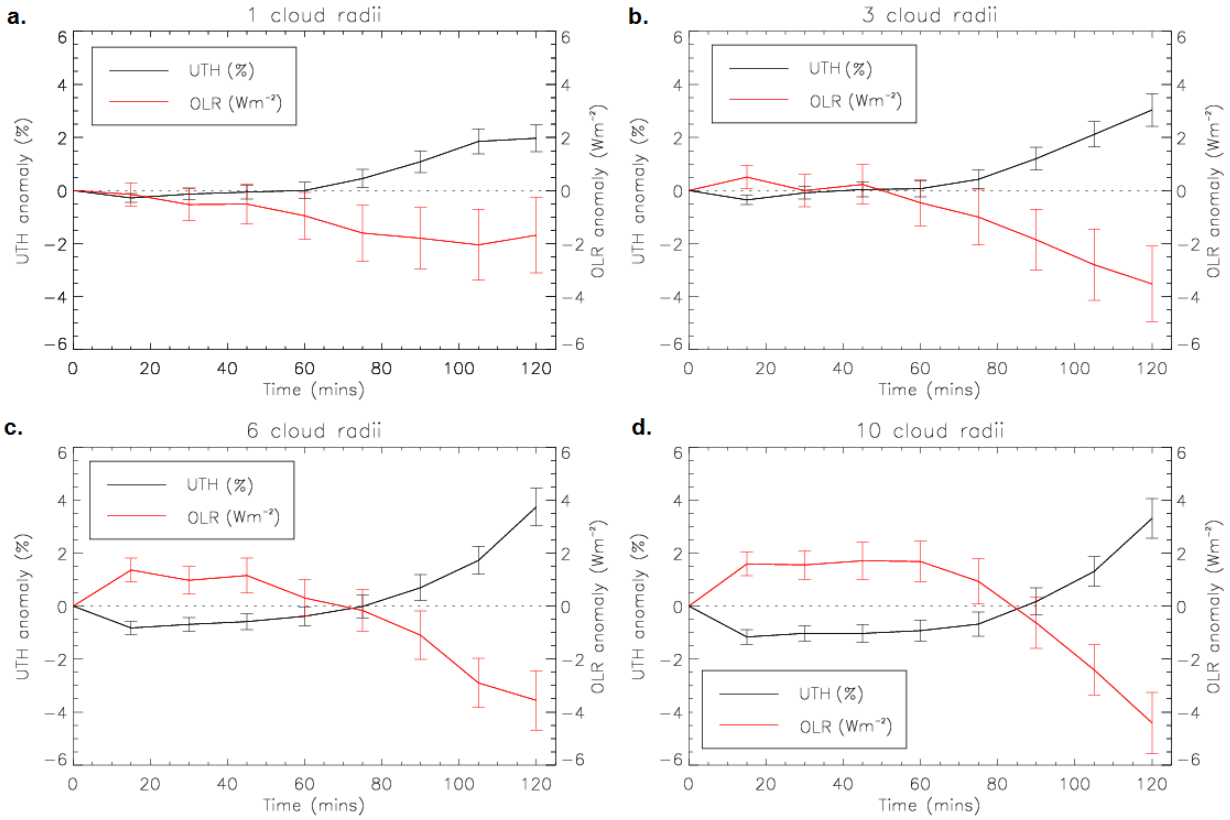

Figure 6.24: Clear sky UTH anomalies from the mean UTH (black) and OLR (red) at *T0* for medium sized clouds with a lifetime of 2 to 2.5 hours. The UTH anomalies are given over the life time of the cloud, in relation to distance from the cloud edge, for **a)** 1 cloud radii, **b)** 3 cloud radii, **c)** 6 cloud radii and **d)** 10 cloud radii. The standard error is also given.

UTH anomalies are also presented for clouds with a lifetime of 3.5 to 4 hours in June 2010 (figure 6.25). As seen for the clouds with a shorter lifetime presented above, it is found that a significant increase in UTH above that at *T0* is seen towards the end of the clouds lifetime for all radii bins. Again, the UTH anomaly becomes larger with greater distances from the cloud edge. The maximum anomaly at 1 cloud radii is 6.1% above the mean UTH at *T0* (figure 6.25a), whilst at 10 cloud radii we see a maximum anomaly of 14.3% (figure 6.25d).

The OLR again shows an almost inverse relationship to UTH suggesting no time lag exists between UTH and OLR perturbations. Maximum OLR perturbations are found towards the end of the clouds lifetime and in larger analysis domains, for example -16 Wm^{-2} at 6 cloud radii, corresponding to a 13% UTH anomaly, much larger than anomalies found for clouds with shorter lifetimes.

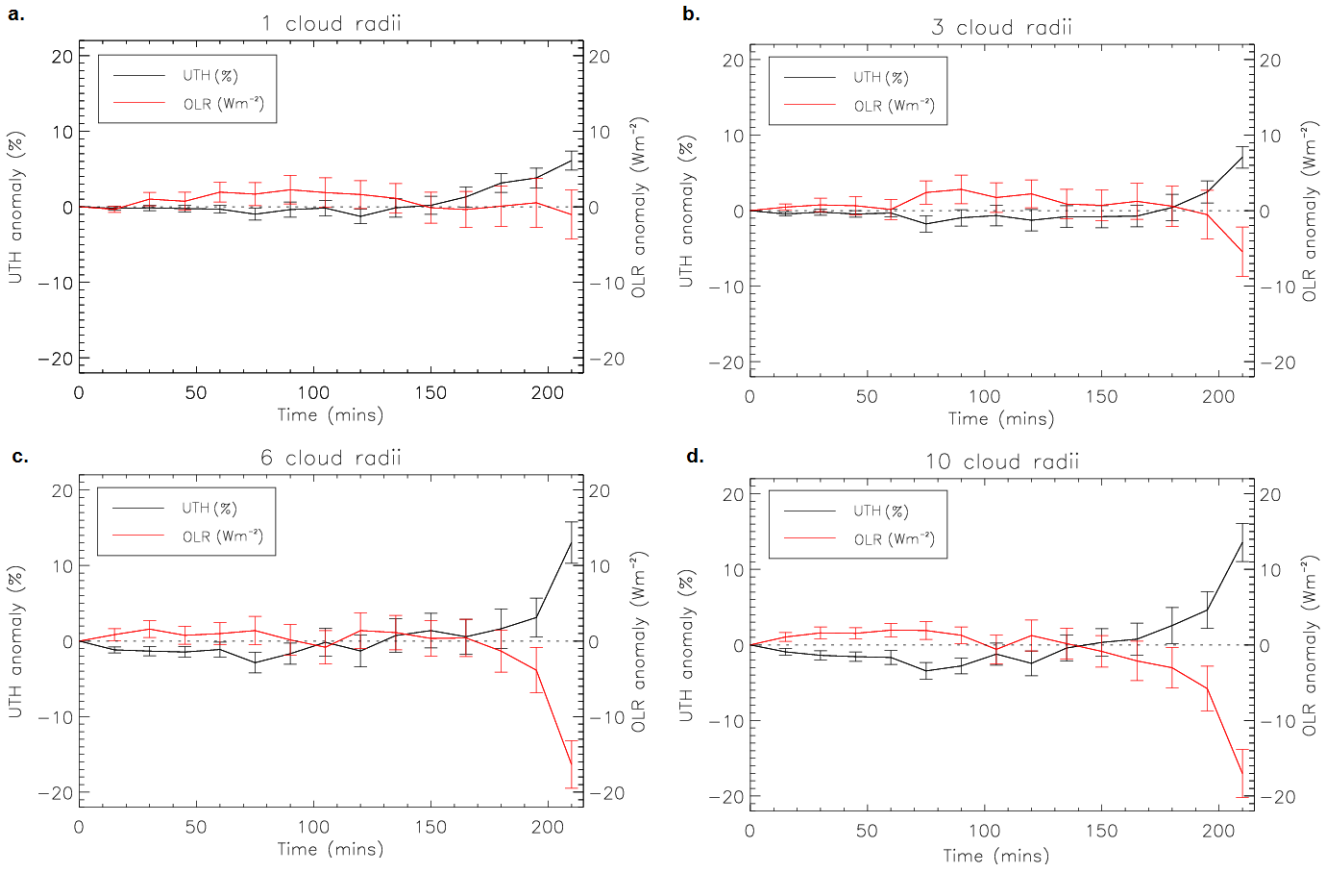

Figure 6.25: Clear sky UTH anomalies from the mean UTH (black) and OLR (red) at *T0* for medium sized clouds with a lifetime of 3.5 to 4 hours. The UTH anomalies are given over the life time of the cloud, in relation to distance from the cloud edge, for **a)** 1 cloud radii, **b)** 3 cloud radii, **c)** 6 cloud radii, **d)** 10 cloud radii. The standard error is also given.

From the time series of anomalies shown above, a temporal control on the intensity of the UTH anomaly is evident, whereby a greater perturbation in UTH is found towards the end of the clouds lifetime. Larger perturbations are also found with a longer cloud lifetime. The greatest perturbations of mean UTH also appear in the larger analysis domains. The maximum anomalies for all medium sized cloud lifetime bins in June are presented in table 6.6 for each analysis domain size. Overall, it can be seen that the lifetime of the cloud exerts some control on the magnitude of the perturbation in UTH from *T0*. The largest perturbations are found to occur for clouds with a lifetime of 3.5 to 4 hours. The perturbations for clouds with a lifetime of 4-4.5 hours are smaller than that of 3.5-4 hours, though this may be a less robust representation of the UTH response due to the smaller number of clouds in this bin.

		Analysis domain size (cloud radii from cloud edge)									
		1	**2**	**3**	**4**	**5**	**6**	**7**	**8**	**9**	**10**
	2-2.5	2	2	3	3.6	3.9	3.7	3.4	3.4	3.1	2.8
Lifetime	**2.5-3**	3.2	3.2	3.6	3.7	4	4.2	4.3	4.4	4.3	4.2
bin (hours)	**3-3.5**	5.9	5.5	5.4	5	5.1	5	5	5.8	5.8	5.4
	3.5-4	6.1	5.6	7	9.8	11.9	13	13.9	14.3	13.6	11.8
	4-4.5	4.9	6.1	4.6	7.6	6.4	7.7	8.9	9.9	10.6	11.2

Table 6.6: The maximum UTH anomaly (%) with respect to UTH at *T0*, for medium sized clouds in June 2010, over all lifetime bins analysed.

A linear least-squares fit is also performed for all lifetime bins of medium sized clouds analysed in June (figure 6.26 a to e). A strong negative correlation is seen between the clear sky UTH anomalies and the corresponding clear sky OLR anomalies. The correlation coefficient ranges from -0.86 for medium sized clouds with a lifetime of 3 to 3.5 hours (figure 6.26c) to -0.93 for medium sized clouds with a lifetime of 2 to 2.5 hours (figure 6.26a). A two-tailed t-tests shows the linear fits to be statistically significant ($P = < 0.05$). Perturbations in OLR associated with a 1% perturbation in UTH range from -1.83 to -0.96 Wm^{-2}, slightly less than that found for small clouds in June 2010.

The peaks in OLR and UTH perturbations at the end of the timeseries in figures 6.24 and 6.25 are evident in each of the linear relationships in figure 6.26 as almost distinctly separate clusters towards the bottom right of the plots (figures 6.26 a to d). These clusters are generally dominated by the larger analysis domains (greater than 4 cloud radii) and are representative of the larger perturbations seen in the timeseries (figures 6.24 and 6.25) . Some outliers are also seen for clouds with a lifetime of 2.5 to 3 hours and 3 to 3.5 hours. The outliers at both time steps are within the 1 cloud radii analysis domain. These may be caused by some short lags in the OLR response to UTH. As seen for small clouds (figure 6.20), the larger cloud radii analysis domains possess more negative anomalies in UTH than smaller domains. This may be related to an initial drying from subsidence in the region surrounding the cloud. The RMSE calculated for each lifetime bin for medium sized clouds is smaller than that calculated for the smaller cloud lifetime bin, suggesting a tighter relationship between UTH and OLR for medium sized clouds. This may also be a result of the larger number of clouds in this lifetime bin creating a more robust result.

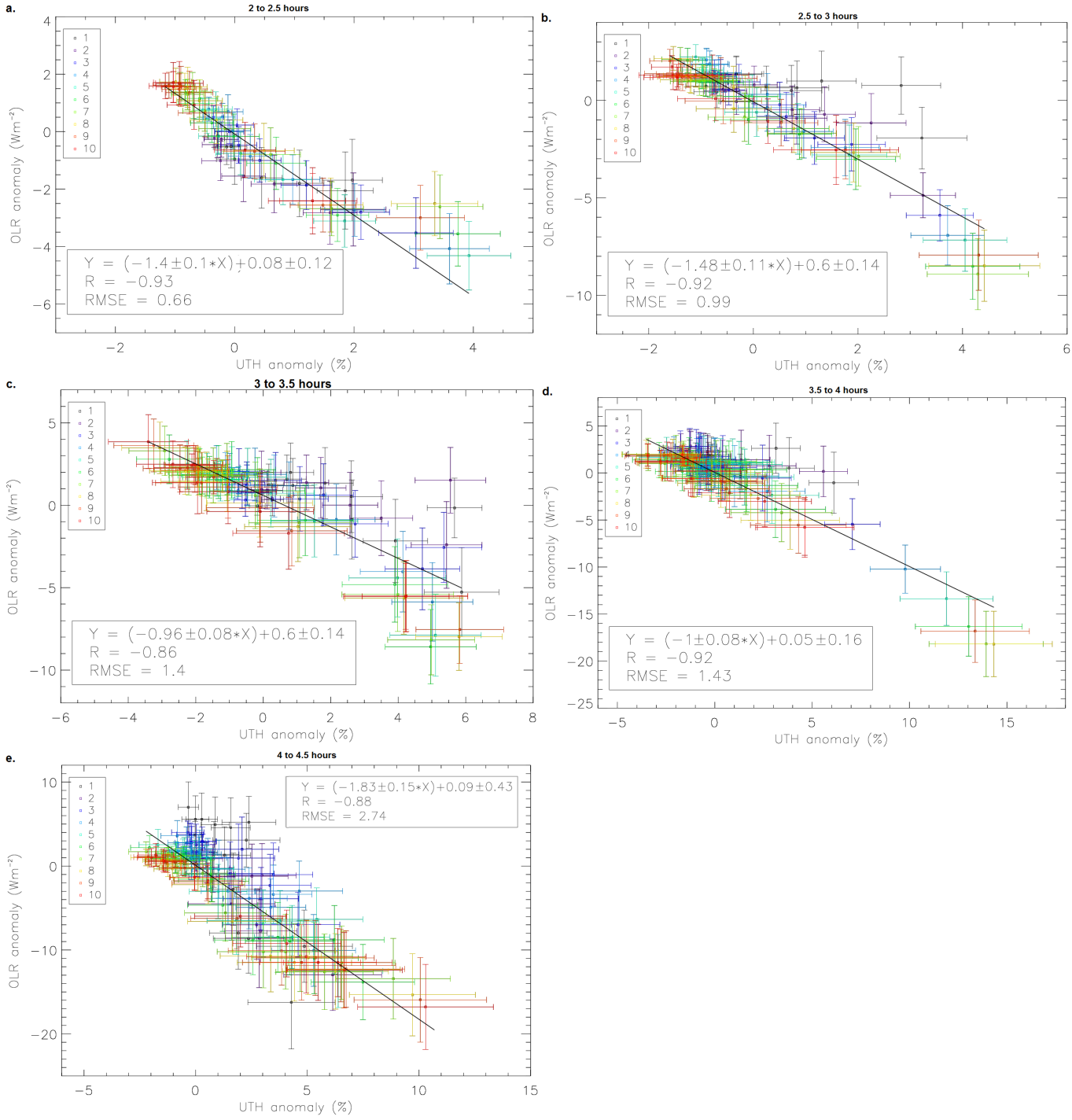

Figure 6.26: The linear least-squares relationship between UTH (%) anomalies and corresponding OLR (Wm^{-2}) anomalies for medium clouds with a lifetime of 2-2.5 hours (a) to 4-4.5 hours (e). One standard error is given for the UTH and OLR anomalies. Errors in the slope and intercept are one standard deviation. Analysis domains between 1 and 10 cloud radii are assigned a colour as shown in the legend.

6.5.3 December 2010 - medium clouds

Mean UTH anomalies with respect to UTH at *T0* are presented for clouds with lifetimes of 2-2.5 hours (figure 6.27). Although within 4 cloud radii the UTH anomalies show an initial decrease below the mean UTH at *T0,* this is not considered significant due to the standard error overlap. Within the first 4 cloud radii from the cloud edge, an increase in UTH is found as the cloud ages, with a significant perturbation in UTH seen at 105 minutes. The largest anomaly within the 1 cloud radii domain is 3% at the end of the clouds lifetime, compared to a minimum of -0.6 % within 30 minutes of the start of the cloud lifetime. Some overlap is seen between all standard errors at each timestep and the timestep proceeding it. Within distances greater than 4 cloud radii from the cloud edge the standard error implies that no perturbation to UTH occurs until 90 minutes into the cloud lifetime. This significant perturbation occurs earlier in the larger spatial domains for clouds in this lifetime bin. A seasonal difference in the size of the UTH perturbation is also seen with that of June 2010 being greater than December for the same lifetime and size bin.

A relatively large positive perturbation is seen in OLR in relation to the possible marginal drying seen in the earlier stages of the lifetime. This large perturbation is a result of the non-linear relationship between UTH and OLR, especially in drier ambient regions where any UTH perturbation result sin a larger OLR perturbation than that that would be seen in a more moist environment. Within the 1 cloud radii domain this OLR perturbation peaks at 3.1 Wm^{-2} corresponding to a mean UTH of -0.5%. In all domains, this increase in OLR with a decrease in UTH is subsequently followed by a decrease below that at *T0* when the UTH anomaly represents a significant moistening.

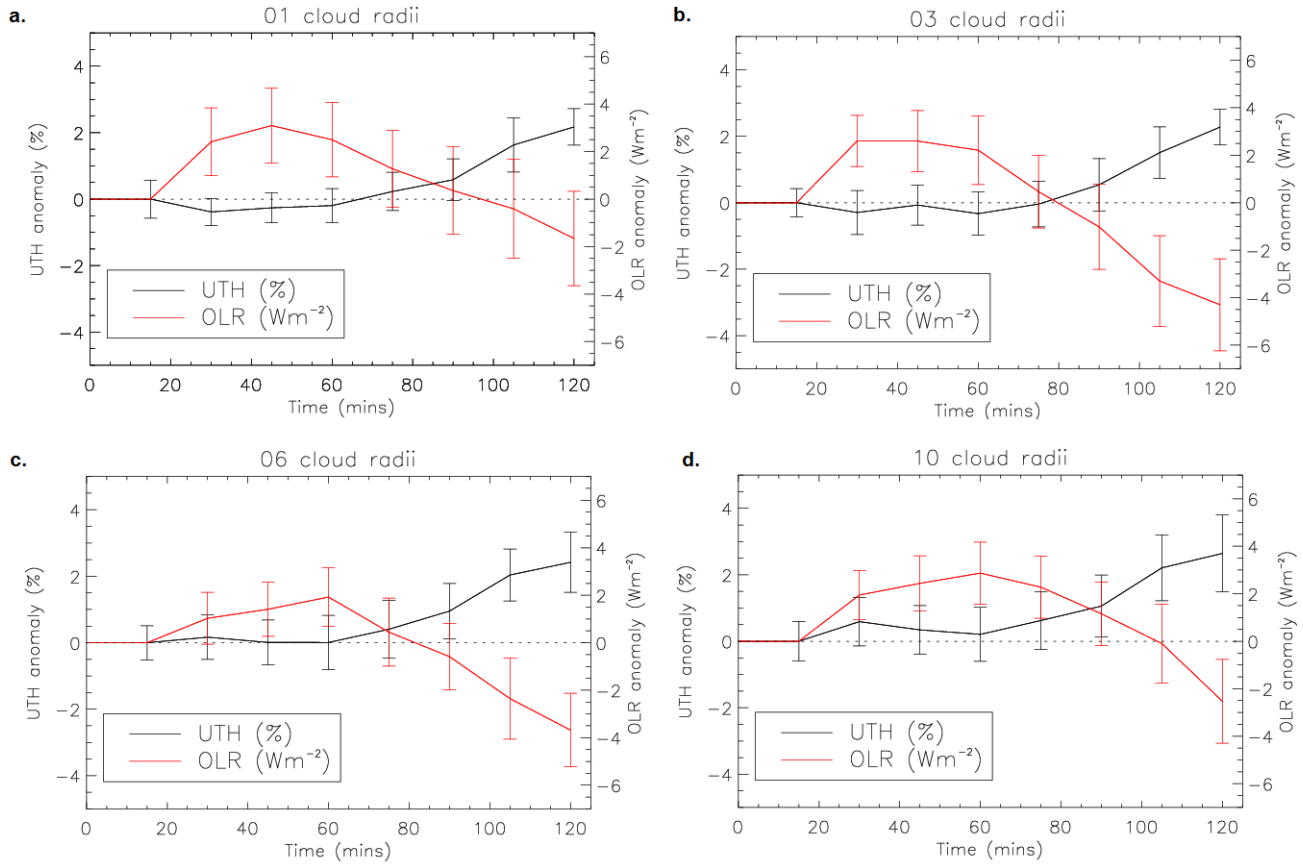

Figure 6.27: Mean UTH (%) and OLR (Wm^{-2}) anomalies from that at *T0*, for medium sized clouds with a lifetime of 2 to 2.5 hours. The anomalies are given over the life time of the cloud, in relation to distance from the cloud edge, for **a)** 1 cloud radii, **b)** 3 cloud radii, **c)** 6 cloud radii, **d)** 10 cloud radii. The standard error is also given.

For clouds with lifetimes of 3 to 3.5 hours, within the 1 cloud radii analysis domain a large significant UTH perturbation occurs at the end of the cloud lifetime. This perturbation of 8.2% corresponds to an OLR perturbation of -10.9 Wm^{-2} and follows an insignificant UTH perturbation over the first 150 minutes of the clouds lifetime. A similar pattern is seen within 3 cloud radii, though a UTH perturbation of 8.3% is found with a corresponding OLR perturbation of -2.9 Wm^{-2}. The mean UTH perturbation within 3 cloud radii is predominantly lower than that at *T0* over the first 150 minutes in the clouds lifetime. This decrease below that at *T0* continues with an increase in the size of the analysis domain, where at 6 cloud radii and larger, no significant increase above that at *T0* is seen at all. This suggests that the influence on UTH is local, which is also seen spatially in the 3D time series presented in figure 6.19 with a rapid decease in mean UTH with distance from the cloud edge.

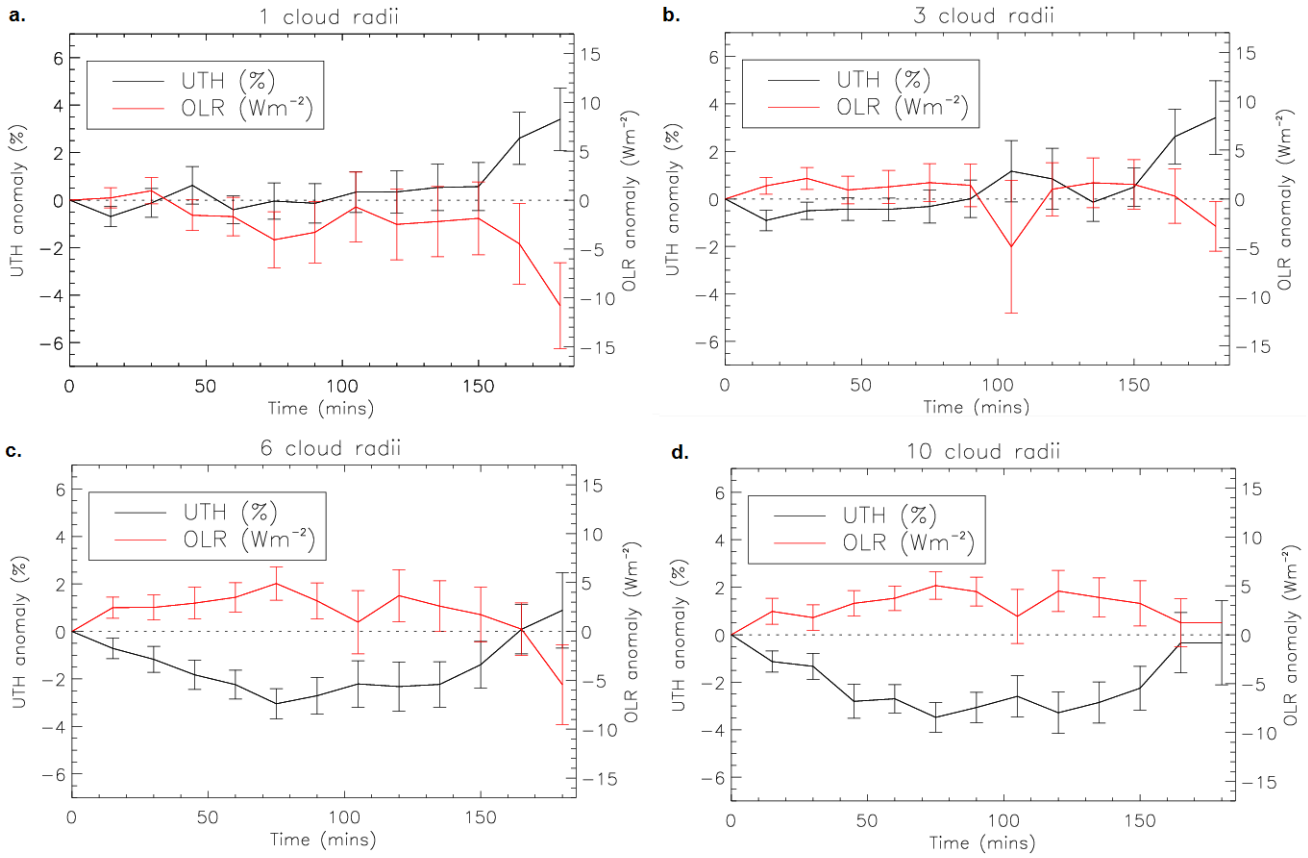

Figure 6.28: Mean UTH (%) and OLR (Wm^{-2}) anomalies from that at *T0*, for medium sized clouds with a lifetime of 3 to 3.5 hours. The anomalies are given over the life time of the cloud, in relation to distance from the cloud edge, for **a)** 1 cloud radii, **b)** 3 cloud radii, **c)** 6 cloud radii and **d)** 10 cloud radii. The standard error is also given.

The linear least-squares regression shows a strong negative correlation between UTH and OLR perturbations, ranging from -0.67 to -0.8. A two-tailed t-test shows the gradient to be significantly different from 0 ($P = <0.05$). A decrease in OLR of between -4.17 and -1.24 Wm^{-2} corresponds to an increase in UTH of 1%. This is a stronger response than that found for the same size clouds in June 2010. A similar pattern in the spatial domain is seen for December and June, with larger analysis domains possessing larger negative UTH anomalies. This corresponds to the drying seen in the early stages of the clouds lifecycle. The RMSE found in each relationship is relatively large given the range of OLR anomalies.

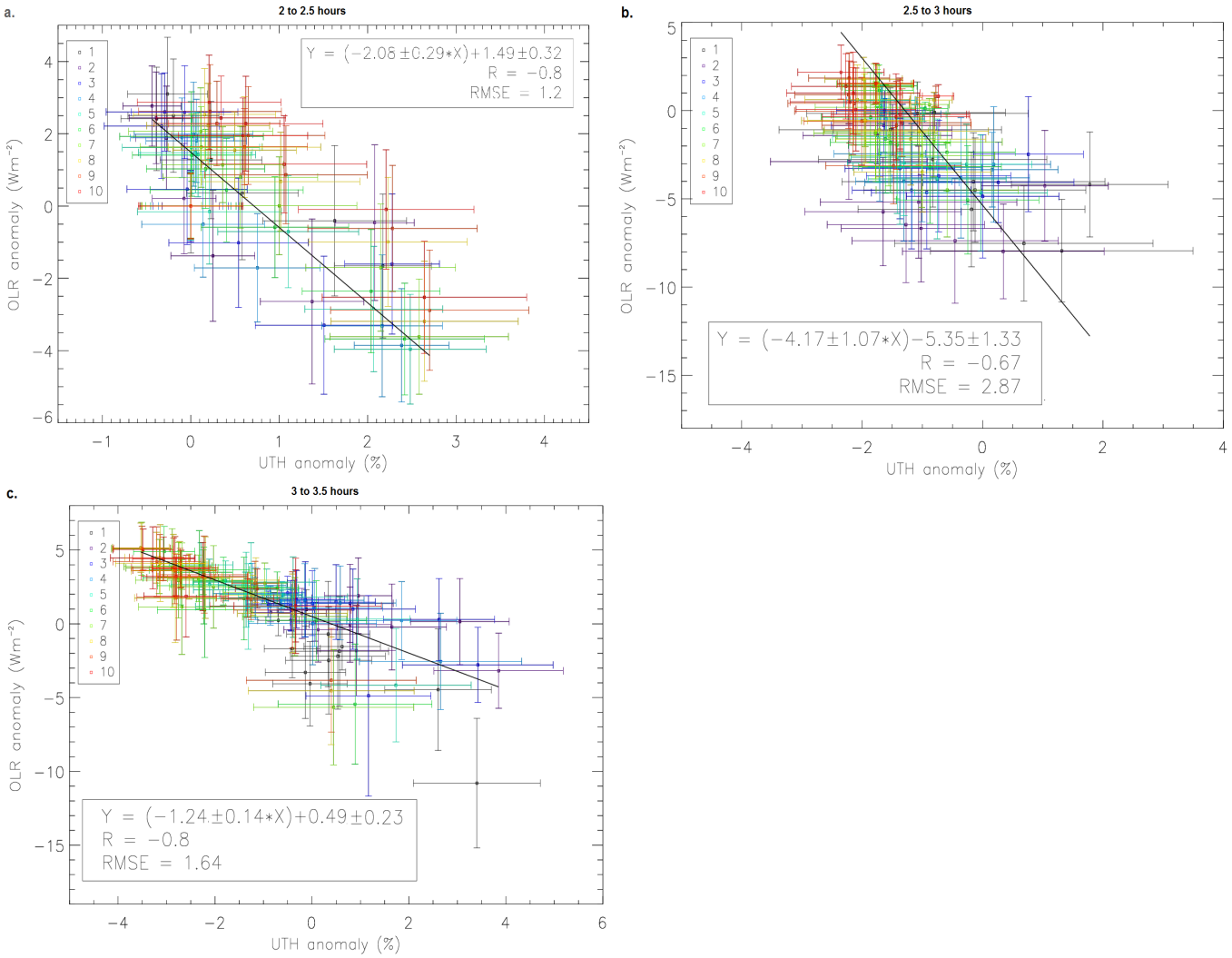

Figure 6.29: The linear least-squares relationship between UTH (%) anomalies and corresponding anomalous OLR (Wm^{-2}) anomalies for medium clouds in December 2010 with a lifetime of **a)** 2-2.5 hours, **b)** 2.5-3 hours and **c)** 3-3.5 hours. One standard error is given for the UTH and OLR anomalies. Errors in the slope and intercept are one standard deviation. Analysis domains between 1 and 10 cloud radii are assigned a colour as shown in the legend.

6.5.4 Time lags

The maximum $BTD_{6.2\text{-}7.3}$ is considered to be the point in the clouds lifetime when the convection is most intense. In relation to the maximum $BTD_{6.2\text{-}7.3}$, overall it is seen that a time lag does exist between peak convection and a significant perturbation of mean clear sky UTH above that at *T0* (tables 6.7 and 6.8).

For small clouds with a lifetime of 2-2.5 hours in June 2010, the time lags calculated between the point of maximum $BTD_{6.2\text{-}7.3}$ and a significant change in mean UTH range from 42 minutes within the 1 cloud radii analysis domain and 87 minutes within the 5-10 cloud radii domains (table 6.7). This time lag is less than that found by Soden (1996), though this may relate to the cloud size. Smaller less intense clouds may be seen to dissipate faster than those with a longer lifetime and potentially stronger updrafts, which may cause

a shorter time lag to be seen in the UTH response.

Analysis domain size (Cloud radii)											
		1	**2**	**3**	**4**	**5**	**6**	**7**	**8**	**9**	**10**
Lifetime bin (hours)	**2-2.5**	42	42	42	42	87	72	87	87	87	87

Table 6.7: The time lag (in minutes) between maximum $BTD_{6.2\text{-}7.3}$ and a significant perturbation in mean clear sky UTH above the UTH measured at *T0* for small clouds in June 2010.

The time lag for each medium cloud lifetime bin in June 2010 shows an increase with a corresponding increase in the size of the analysis domain (table 6.8). The ranges shown are within the same range as found for small clouds in June 2010. The time lags range from an average of 36 minutes to 123 minutes (not including no lag found within 1 cloud radii for clouds with a lifetime of 3-3.5 hours). The lag in the UTH response to deep convection increases with an increase in the size of the analysis domain suggesting that there is some effect of the propagation of UTH away from the cloud edge over time on the clear sky UTH. A comparison with the same time bin for small clouds shows a longer time lag in larger analysis domains for small clouds.

The length of the time lag is also found to increase with cloud lifetime. This suggests that a relationship exists between the lifetime of the cloud and the response of UTH to deep convection, whereby a longer lifetime results in a larger UTH perturbation from the ambient state. Interestingly, this pattern shows a correlation with the size of the maximum anomaly in table 6.6. Largest mean UTH anomalies are found to occur at the same point as the longer time lags.

Analysis domain size (Cloud radii)											
		1	**2**	**3**	**4**	**5**	**6**	**7**	**8**	**9**	**10**
	2-2.5	36	51	36	51	51	51	51	66	66	66
Lifetime	**2.5-3**	45	45	45	75	75	75	75	75	90	90
bin (hours)	**3-3.5**	No lag	39	55	85	85	100	100	100	100	100
	3.5-4	108	123	123	123	123	123	123	123	123	108
	4-4.5	17	47	77	92	92	92	92	92	92	92

Table 6.8: The time lag (in minutes) between maximum $BTD_{6.2\text{-}7.3}$ and a significant perturbation in mean clear sky UTH above the UTH measured at *T0* for medium clouds in June 2010.

The time lags calculated for medium sized clouds in December 2010 are shown in table 6.9. In a large number of cases, no significant increase in UTH occurred. This is especially prevalent for clouds with a lifetime of 2.5-3 hours, whereby a decrease in UTH is found in all spatial domains greater than 1 cloud radii from the cloud edge. For clouds with a lifetime of 2-2.5 hours, a longer lag is found between a significant perturbation and maximum $BTD_{6.2\text{-}7.3}$ for the smaller spatial domains.

		Analysis domain size (Cloud radii)									
		1	**2**	**3**	**4**	**5**	**6**	**7**	**8**	**9**	**10**
	2-2.5	85	85	85	75	75	75	75	75	75	75
Lifetime	**2.5-3**	90	No lag	No lag	No lag	No lag	No lag	No lag	No lag	No lag	No lag
bin (hours)	**3-3.5**	108	108	108	108	No lag	No lag	No lag	No lag	No lag	No lag

Table 6.9: The time lag (in minutes) between maximum $BTD_{6.2\text{-}7.3}$ and a significant perturbation in mean clear sky UTH above the UTH measured at *T0* for medium clouds in June 2010.

6.5.5 Discussion

A general pattern is found in the perturbation of UTH and OLR from that at *T0*. Specifically in June, based on the difference between the UTH when the cloud is first detected (the beginning of the most intense phase of the cloud lifetime) and the UTH at each subsequent time step, a spatial pattern emerges whereby larger perturbations are seen with larger analysis domains.This pattern is evident for all lifetime bins and size bins in June. This agrees with the suggestion by Udelhofen and Hartmann (1995) and McCormack *et al.,* (2000) that larger perturbations in UTH are seen in areas of lower humidity, such as larger cloud radii analysis domains which incorporate areas further from the cloud edge. These finding are also similar to that suggested by Wright *et al.,* (2009) who find that the influence of convection on moistening the upper troposphere is very much reduced when the ambient humidity is already high such as in the region surrounding the cloud, with drier areas seeing a stronger perturbation in UTH from their ambient state.

Overall, a small drying is seen within the earlier stages since the detection of the cloud. This may be attributed to the intense compensating subsidence seen around the cloud edge when updrafts are intense (see chapter 1). This is followed by an increase in the magnitude of the perturbation (positive for UTH, negative for OLR) with an increase in the cloud lifetime. A perturbation in the mean UTH tends to start later in the clouds lifetime as the distance from the cloud edge increases. This is also confirmed by the calculated time lag between the point of maximum $BTD_{6.2\text{-}7.3}$ and the point where a significant UTH perturbation is found. This may be the result of the UTH dissipating outwards over time towards areas of lower ambient UTH. The ambient UTH may be lower at distances further from the cloud edge, so in turn the ambient UTH in the larger domains may experience a greater perturbation to the UTH when a cloud is present and at a lagged time when compared to smaller domains. This is in disagreement with Comer *et al.,* (2006) who suggest that there is no lag between convection and a perturbation in UTH due to the water vapour being transported to the upper troposphere with the vertical ascent associated with convection. The ambient UTH in close proximity to the cloud edge is likely to always be higher than that at distances further from the cloud edge due to the presence of the cloud. The mean UTH in the analysis domain close to the cloud edge may therefore experience less of a perturbation from its ambient state as the cloud decays. The strong perturbation at the end of the clouds lifecycle in the 1 cloud radii domain may be due to the evaporating detrained cloud enhancing the UTH further from its already higher state.

This general pattern seen in June in the UTH perturbation of a larger UTH perturbation towards the end of the lifetime and in larger analysis domains may relate to the amount of time over which cirrus has propagated and dissipated. As the cloud ages and hydrometeors dissipate away from the core, a larger perturbation in UTH may occur towards the end of the lifetime and in the drier areas to which the hydrometeors have dispersed to. A similar temporal relation is found between the cloud lifetime and the UTH by Chung

et al., (2007). They found that the number of cloud hydrometeors detrained from the cloud top increase with the lifetime of the cloud, creating a lifetime dependence on the magnitude of the UTH perturbation. It is also found that cirrus development precedes UTH perturbations in deep convective regimes, with the evaporation of cirrus acting to moisten the upper troposphere (Mace *et al.,* 2006; Chung *et al.,* 2007). The mechanical processes responsible for the development of high cloud and cirrus are found by Sherwood (1999) and Luo and Russow (2004) to be the same mechanisms responsible for moistening the upper troposphere suggesting a possible explanation of the temporal pattern in the UTH perturbation found in this study.

With a positive perturbation in UTH, a corresponding negative perturbation in OLR is also found. The UTH and OLR perturbations show a strong negative correlation, with a general spatial pattern emerging in the relationship whereby larger perturbations in OLR are seen with greater distances from the cloud edge. The negative correlation between the two variables suggest that no lag is seen in the response of OLR to a change in UTH. This is in disagreement to that found by Zelinka and Hartmann, who find that clear sky OLR is actually found to correspond to column integrated water vapour and peak 6 hours before UTH.

The range of OLR anomalies found in this study are similar to the range of OLR perturbations found by Zelinka and Hartmann (2009) who find a decrease in OLR of between ~0.69 $Wm^{-2}$and ~-2.6 Wm^{-2} with a 1% increase in UTH. The ranges in UTH and OLR anomalies found in the study performed here are also in agreement with the range found by Soden (2000) and Comer *et al.,* (2006). In contrast, the ranges in OLR anomalies are much greater than that suggested by Udelhofen and Hartmann (1995) and Jensen *et al.,* (1999), who suggest a change in RH of 10% to correspond to a 0.5-1.4 Wm^{-2} change in OLR. The perturbations in OLR found in this study are also larger than that found by Johnston *et al.*, (2013), who find a mean OLR perturbation of ~-4 Wm^{-2} with a corresponding UTH perturbation of 1%. They also show a lag between maximum UTH and OLR, with OLR preceding the maximum UTH perturbation by ~12 hours which is also not seen here.

In December the UTH and OLR perturbation does not show as strong a signature as June with regards to the emergence of a distinct spatial pattern. For medium sized clouds clouds with a lifetime of 2-2.5 hours a similar maximum perturbation is seen at all distances from the cloud edge. Close to the cloud edge a small initial drying occurs (<1%) which corresponds to a strong positive perturbation in OLR. This comes from the increasing saturation of the water vapour band with an increase in UTH causing the OLR to show less of a response to a UTH perturbation in an ambient atmosphere with a higher UTH (Allan *et al.,* 1999; Udelhofen and Hartmann, 1995). In comparison to medium sized clouds with the same lifetime in June, the perturbation at the end of the cloud lifetime is larger when closer to the cloud edge suggesting the dissipation and outflow of UTH in the spatial domain to be weaker in December than June. This may also be due to the region surrounding the cloud in June having a higher ambient UTH, as seen from the 3D timeseries, whereby the addition of a cloud to an already moist UT may have less of a perturbing effect. For medium sized clouds with a lifetime of 3-3.5 hours, the largest perturbations (~9%) are found within close proximity to the cloud edge (1-4 cloud radii), whilst a substantial drying is seen within the early stages of the lifecycle at distances greater than 4 cloud radii. This is not seen for the same lifetime and size bin in June 2010 and suggests this is a less robust response.

6.6 Conclusion

In order to quantify the spatial and temporal response of UTH to deep convection, regression analysis following the method of Soden and Bretherton (1993) was conducted on the relationship between modelled clear sky 6.2 μm brightness temperatures and corresponding UTH from clear sky ERA-Interim profiles. 6.2 μm brightness temperatures were modelled using MODTRAN. The known random errors and instrument biases found for SEVIRI were applied to the 'measured' 6.2 μm brightness temperatures and the UTH was recalculated with the UTH regression coefficients. This showed the UTH coefficients were relatively insensitive to the added random error, and more sensitive to the added bias, though this bias represents a 'worst case' scenario and may be a manifestation of error in the modelling tools (e.g. ERA-Interim UTH) used to assess it.

The cloud detection method and tracking algorithm developed in chapters 4 and 5 respectively were implemented with the UTH coefficients applied to the SEVIRI 6.2 μm brightness temperatures over the months of June and December 2010. It was found that the tracked deep convection over tropical Africa had a qualitatively similar spatial distribution to that in ERA-Interim shown in chapter 3. Peak convection was found to correlate with areas of higher terrain. The frequency size distribution of the tracked deep convection possessed a log normal distribution. To determine whether any size effect of deep convection on UTH exists, the distribution was split into three size bins - small, medium and large - within one standard deviation from the mean. The deep convection was split further into lifetime bins to detect any UTH and OLR response to cloud lifetime.

Although the analysis is limited by the sample size, it is clear that a general spatial and temporal pattern is seen in the UTH response to deep convection. A temporal response of mean UTH to deep convection shows a weaker response over time when compared to a response over the spatial domain. This pattern was similar for all cloud lifetime and size bins, though the actual change in UTH was larger for medium sized clouds than for small clouds. For small clouds in June 2010 a change in UTH of 2% was found over the cloud lifetime for clouds with a lifetime of 2-2.5 hours. Medium sized clouds with the same lifetime show a change in UTH of approximately 4%. As the lifetime increased for medium sized clouds, the UTH change increased to 5% over the clouds lifetime.

3D plots show a larger decrease in UTH with distance from cloud edge than over the time over which the cloud is tracked. This was especially true for medium sized clouds in June, whereby a more robust pattern emerged due to the larger sample size. A change in the spatial domain between 1 and 10 cloud radii from the cloud edge showed a 20% difference in clear sky UTH, with this pattern seen for all medium sized cloud lifetime bins analysed. This compared to a change of ~4% in the temporal domain over the cloud lifetime. For small clouds in June 2010, a change of only 2% was found over the cloud lifetime compared to 6% over the spatial domain. For medium sized clouds in December the response was not as strong as the same cloud bins in June. A change in UTH over the spatial domain of ~13% was found, with an increase of ~4% in the temporal domain.

Relative to the clear sky UTH measured at the point of first detection, an interesting pattern emerged. In June, the UTH perturbation showed a stronger perturbation over time and at greater distances from the cloud edge. This corresponds well with the suggestion that deep convection will perturb UTH to a greater extent in drier ambient regions. Though this was seen in June, a comparison between months shows a weaker perturbation in December. The analysis of the UTH perturbation shows a temporal response whereby overall an initial drying is seen in the early stages of the clouds life. This is likely to be due to the updrafts in the

early stages of the lifecycle being compensated for by downdrafts, which will act to dehydrate the upper troposphere. A clear temporal signature of upper tropospheric moistening is seen in all spatial analysis domains, whereby a significant perturbation in UTH occurred towards the end of the clouds lifecycle. This may be due to the clouds dissipating and cirrus ice particles beginning to evaporate. The larger anomalies in regions of lower ambient UTH suggest the presence of consistently higher ambient UTH in the regions closer to the cloud edge. Though this was seen in all lifetime and size bins in June, this was not found in December whereby a significant perturbation was only seen close to the cloud edge. In all domains in both June and December, perturbations were found to be largest with an increase in the lifetime of the clouds, in agreement with findings of Wright *et al.,* (2009).

A time lag between peak convection, defined as maximum $BTD_{6.2\text{-}7.3}$ and a significant perturbation in mean clear sky UTH is also found in June 2010. This is found to range between 36 and 123 minutes, similar to Soden (2000) and Comer *et al.,* (2007). Interestingly, a pattern emerges whereby the greatest perturbation is found to correspond to longer time lags. This is similar to that found by Wright *et al.,* (2009). This pattern is not seen for December, whereby minimal significant increases in UTH occurs.

The corresponding OLR response shows a strong negative correlation with the UTH response and no time lag between the two variables is observed. This is in disagreement with the findings of Zelinka and Hartmann (2009). This response is found to be stronger in December than June, with a maximum decrease of -4.7 Wm^{-2} with a 1% increase in UTH in December, compared to a maximum perturbation -1.83 Wm^{-2} in June.

The standard errors found for each point in the timeseries analyses show some overlap at each timestep which is largely a result of the sample sizes available to the analysis. The $BTD_{6.2\text{-}7.3}$ classification of deep convection, due to the inherent controlling factors being the effect of the cloud top height on the weighting functions, is likely to underestimate the length of the cloud lifecycle and therefore limit the quantification of the UTH and OLR response. This may also introduce a limiting factor of the number of deep convective clouds analysed, especially with a cut off time of two hours imposed. However, the UTH and OLR responses found do show a general, consistent pattern over the lifetimes and the spatial domains under analysis. This gives confidence that the pattern that emerges is robust.

The use of a lagrangian tracking method has allowed for the novel analysis and quantification of the UTH and OLR response to deep convection over the clouds lifetime, and over a range of distances from the cloud edge. This has allowed for spatial and temporal patterns to be seen at a high temporal resolution much greater than previous studies such as Zelinka and Hartmann. The initial drying in the early stages of the cloud lifetime, especially close to the cloud edge, is not seen in previous studies. This will allow for better model parameterisation, and a better understanding of the response of OLR to UTH over the clouds lifetime. A much greater spatial resolution is also used, allowing for patterns in the response close to the cloud edge to be better quantified than in previous studies.

Chapter VII

Conclusion

7 Main findings

It is evident that there is some agreement as to the spatial and temporal response of clear sky UTH and OLR to deep convection in the tropics. Some agreement is evident with regards to the large scale domain, whereby a moistening is suggested to occur in areas of large scale ascent, whilst a drying occurs in regions of large scale descent. This large scale picture is related to the atmospheric dynamics in the tropics, including the ascending and descending branches of the Hadley cell and the ITCZ. However, There is some disagreement with regards to the more localised moistening or drying of the upper troposphere by deep convection. This area of disagreement is mainly in relation to small scale, localised responses close to the cloud. There are suggestions that a drying occurs due to downdrafts compensating for the strong updrafts associated with convection, which will act to dry the upper troposphere. There is also evidence of moistening from the evaporation of cirrus particles and also the act of moisture transport from the surface to the drier upper troposphere by the vertical ascent. Further disagreement is seen with regards to the temporal response of UTH to deep convection. This primarily stems from a combination of metrics used from which to determine lags in the response of UTH and OLR to deep convection and the temporal resolution of the UTH measurements used in these studies. Estimates of response times ranged from 0 to 9+ hours, whilst some studies suggested a drying actually occurred close to the cloud edge and therefore no lag was seen.

The region of interest in this study is over northern tropical Africa, covering 0° to 15° N and 10° to 40° E. This climate and cloud cover in this region is largely characterised by the movement of a band of ascending air known as the ITCZ. A discontinuous band of cloud cover, the ITCZ is characterised by low pressure, and a subsequent vertical ascent of moist air parcels. This in turn is associated with deep convection in this region. This ascent and subsequent descent of air in the subtropics gives rise to the Hadley cell. The movement of the ITCZ is largely seasonal, creating a distinct seasonal spatial pattern in the distribution of cloud cover over this region. The deep convection over this region is characterised using ERA-Interim Gaussian gridded vertical pressure level data. The spatial distribution of deep convection over the study region shows a greater frequency of cloud cover over the study region in June 2010 at all 6 hourly periods confirming a seasonal difference in convection between June and December. The highest frequencies of cloud cover in this region correspond to areas of high orography and the Gulf of Guinea. The areas of low frequency correspond to the Sahel, a dry region in the north of the stud region characterised by descending dry air. Low frequencies of convection were also found in the region characterised by the descending branch of the Walker circulation, a circulation of air in the zonal direction. A seasonal trend in cloud top heights is also evident, with higher mean and median cloud top heights in June. This seasonal pattern is also seen in convective frequency with 1251 deep convective profiles found in December compared to 5288 found in June. The clear sky vertical relative humidity profiles in both June and December were also compared. A drier atmosphere is found in December, attributed to the position of the ITCZ and the vertical transport of water vapour associated with the ascending deep convection.

This region was chosen to answer the three questions introduced in chapter 1 relating to the spatial and

temporal UTH and OLR response:

1. What are the temporal and spatial scales of the humidity response associated with deep convection in the upper troposphere over Tropical Africa?

2. Is there a clear signature of moisture propagation in the horizontal around the cloud, given the atmospheric dynamics discussed above?

3. What are the associated impacts on OLR and the implications for the net outgoing radiative energy balance?

In order to quantify the spatial and temporal response of clear sky UTH and the corresponding OLR to deep convection over Tropical Africa with regards to questions 1 and 2, TOA satellite radiances measured by SEVIRI, and broadband OLR measurements from GERB are employed. These provide radiance and flux measurements at a high temporal resolution, and allow for a detailed temporal analysis of the deep convection over its lifetime. The TOA radiances measured by SEVIRI are converted to brightness temperatures using the inverse of the Planck function.

In order to quantify the response of clear sky UTH and OLR to deep convection, a brightness temperature difference thresholding method of cloud detection was developed using the SEVIRI brightness temperatures. Brightness temperatures from the SEVIRI water vapour bands, 6.2μm and 7.3μm, and the window bands, 10.8μm and 12.0μm, were used to develop these brightness temperature difference thresholds to detect deep convection and cirrus cloud respectively at a high temporal resolution. The $BTD_{6.2\text{-}7.3}$ chosen to detect deep convection are largely controlled by the weighting functions of SEVIRI water vapour channel radiances and are shown by earlier studies to provide an effective method for detecting intense deep convection. To develop these thresholds, the sensitivity of brightness temperatures to a cloud layer were modelled using SBDART, with the cloud optical and vertical properties being perturbed in each model run. For deep convection, it was found that the modelled brightness temperatures were most sensitive to the cloud top height due to the large optical thickness of the cloud and the weighting functions of the water vapour bands being modelled. Little sensitivity was seen to viewing zenith angle. The modelled brightness temperature differences were similar to that found in the literature for growing, early stage convection (lower cloud top heights) and more intense, developed convection (higher cloud top heights, greater optical thickness). This modelling was also conducted for cirrus cloud due to the need to mask high clouds to determine the clear sky UTH response to deep convection. The $BTD_{12.0\text{-}10.8}$ was found to be most sensitive to cloud top height but also showed a strong dependence on the viewing zenith angle.

To determine a sensible range of $BTD_{6.2\text{-}7.3}$, co-located matchups between SEVIRI $BTD_{6.2\text{-}7.3}$ and CloudSat and CALIPSO cloud classifications were conducted. Using receiver operating characteristic curves to highlight the relationship between POD, FAR and CSI for a range of thresholds, the most suitable $BTD_{6.2\text{-}7.3}$ threshold was chosen for both day and night time convection in June and December 2010. The original matchup highlighted a discrepancy between deep convective cloud defined in SEVIRI using the brightness temperature thresholds and Altostratus/deep convection cloud classifications in the CloudSat cloud classification product. This discrepancy was manifested as a high FAR in the original matchup. Similar discrepancies were also found by / and Houze Jr. (2010). Using these probability statistics, it was found that the best agreement between $BTD_{6.2\text{-}7.3}$ thresholds and the CloudSat data were with a reclassification of contiguous Altostratus with a geometrical thickness of 5 km or less, and within 1.5 cloud radii to deep convection.

This study has shown that cloud classified as altostratus and that is contiguous to deep convection is considered to be detraining deep convective cloud in the form of an avil cloud. Based on anvil cloud thickness and distance from the cloud edge, this study confirmed limitations of the CloudSat cloud classifications as shown by Yuan and Houze jr (2010). Further to their study, this study has further classified anvil as deep convection through the comparison of the CloudSat cloud calssifications with SEVIRI $BTD_{6.2\text{-}7.3}$. This allowed for a comparison with an independent dataset, and confirmed the limitations inherent with just using a microphysical scheme to determine cloud types.

A range of $BTD_{6.2\text{-}7.3}$ was then applied to the reclassified Altostratus to calculate the POD, FAR and CSI for each threshold. A $BTD_{6.2\text{-}7.3}$ threshold of -9 K was found to be suitable for detecting deep convection during the day in June, and -3 K was suitable for night time detection. This direction of $BTD_{6.2\text{-}7.3}$ movement was the opposite in December, with a -3 K threshold found during the day and -7 K at night. This unexpected activity was prescribed to the cloud top height distribution used for the co-located matchup in December. The same method of brightness temperature difference modelling and co-located matching was conducted for cirrus cloud over the study region using the combined CloudSat-CALIPSO product. This gave 4 $BTD_{12.0\text{-}10.8}$thresholds of -3 K for June day time and -1 K for night time, and -2.5 K for December day time and 0 K for night time cirrus detection.

The temporal constraint of CloudSat and the need for $BTD_{6.2\text{-}7.3}$ thresholds to be applicable over the course of the day at 15 minutes timesteps raised the need for a sensitivity test to a step change and a sinusoidal change between the two $BTD_{6.2\text{-}7.3}$ thresholds. This sensitivity test showed similar results with regards to the frequency of detected clouds, apart from the point of the temperature change in the step change, which gave an artificial jump in the number of newly detected clouds. The sinusoidal temperature change was therefore chosen to negate this artificial increase in convective frequency with the step change. Peak convective frequency was found to be in agreement with that found by Chung *et al.,* (2007), Schröder *et al.*, (2009) and Comer *et al.,* (2007) with a peak at around 15:00 LST.

In order to effectively determine the response of clear sky UTH and OLR to the detected deep convection, a cloud tracking algorithm was developed. This was based on earlier tracking methods developed by Williams and Houze (1987), Machado *et al.,* (1998) and Ashpole and Washington (2013). Two criteria were used to track clouds. Firstly, an area overlap method was used. This is the most common method of cloud tracking and provides an effective way of tracking clouds through time. With the high temporal resolution of SEVIRI, this provides a simplistic and less ambiguous way of tracking clouds when compared with Williams and Houze (1987) who use a temporal resolution of 3 hours. Secondly, a midpoint displacement method was used. Based on earlier cloud tracking studies by Vila *et al.,* (2008), the midpoint displacement was based on the need to determine whether a cloud was the same in the next image and whether it had split or merged with another system. Implementation of this cloud tracking algorithm allowed for an effective yet simple method to track clouds through the temporal domain.

To determine the clear sky UTH response to the tracked clouds, the relationship developed by Soden and Bretherton (1993) to determine UTH using the relationship between the 6.2μm band brightness temperature and humidity between 200 and 500 hPa was modelled for June and December 2010. The coefficients of the linear relationship between the two variables were applied to SEVIRI 6.2μm band brightness temperatures over the study region and study time period. An error analysis was conducted on the modelled UTH. Estimated random errors and instrument biases found for SEVIRI were applied to the 'measured' 6.2 μm

brightness temperatures. The recalculated UTH showed the UTH coefficients were relatively insensitive to the added instrument error, and more sensitive to the added bias.

Application of the detection method, the tracking algorithm and the coefficients of the linear relationship between the logarithm of clear-sky UTH and the clear sky 6.2 μm band brightness temperatures to SEVIRI data in June and December 2010 allowed for a quantification of the spatial and temporal distribution of deep convection over the study region. A log normal distribution of cloud size was found in both June and December. This allowed for clouds to be separated into distinct size bins - small, medium and large - corresponding to a one standard deviation distribution from the mean. The detected clouds were further separated into lifetime bins of half hourly differences, between 2-2.5 hours and 6+ hours. This allowed for comparisons of both the spatio-temporal response of UTH and the corresponding OLR to deep convection over the cloud lifetime. It was found that the tracked deep convection over tropical Africa had a qualitatively similar spatial distribution to that in ERA-Interim shown in chapter 3. Peak convection was found to correlate with areas of higher terrain.

With regards to questions 1 and 2, although the analysis is limited by the sample size, it is clear that a general spatial and temporal pattern is seen in the UTH response to deep convection. For all lifetime and size bins in both June and December, a general robust pattern emerges where an increase in clear sky UTH is found over the clouds lifetime, whilst a decrease is found with distance from the cloud edge and was especially prevalent for medium sized clouds in June, whereby a more robust pattern emerged due to the larger sample size. The temporal response of mean UTH to deep convection shows a weaker response over time when compared to a response over the spatial domain.

The actual change in UTH was larger for medium sized clouds than for small clouds. For small clouds in June 2010 a change in UTH of 2% was found over the cloud lifetime for clouds with a lifetime of 2-2.5 hours. Medium sized clouds with the same lifetime show a change in UTH of approximately 4-5%. A change in the spatial domain between 1 and 10 cloud radii from the cloud edge showed a 20% difference in clear sky UTH, with this pattern seen for all medium sized cloud lifetime bins analysed. This compared to a change of ~4% in the temporal domain over the cloud lifetime. For small clouds in June 2010, a change of only 2% was found over the cloud lifetime compared to 6% over the spatial domain. A seasonal pattern also emerged, whereby the response was stronger in June than December. A change in UTH over the spatial domain of ~13% was found, with an increase of ~4% in the temporal domain for medium sized clouds in December.

It is suggested by Udelhofen and Hartmann (1995) and Russo *et al.*, (2011) that the perturbation of UTH to deep convection may be principally governed by the ambient temperature and RH of the region surrounding the deep convective cloud. On a large spatial scale, areas of low ambient UTH were found by Udelhofen and Hartmann (1995) and Russo *et al.*, (2011) to experience a greater perturbation by deep convection than those with a high ambient UTH. On a smaller, localised scale Wright *et al.,* (2009) suggest that the act of convection may pull the UTH towards saturation, with moistening or drying occurring dependent on the ambient RH. If ambient UTH is below saturation, deep convection may moisten the upper troposphere, whilst if UTH is already above saturation, the water vapour transported to the upper troposphere by the deep convection may precipitate out, drying the UT. The UTH anomalies were calculated for the clouds detected in this study. UTH anomalies from that measured at the point of first detection showed an interesting pattern. Temporally, in June the UTH perturbation showed a stronger perturbation over time. The analysis of the UTH perturbation shows a temporal response whereby overall an initial drying is seen in the early stages of

the clouds life. This is likely to be due to the updrafts in the early stages of the lifecycle being compensated for by downdrafts, which will act to dehydrate the upper troposphere. A clear temporal signature of upper tropospheric moistening is seen in all spatial analysis domains, whereby a significant perturbation in UTH occurred towards the end of the clouds lifecycle. This may be due to the clouds dissipating and cirrus ice particles beginning to evaporate. The larger anomalies in regions of lower ambient UTH suggest the presence of consistently higher ambient UTH in the regions closer to the cloud edge. Though this was seen in all lifetime and size bins in June, this was not found in December whereby a significant perturbation was only seen close to the cloud edge. In all domains in both June and December, perturbations were found to be largest with an increase in the lifetime of the clouds, in agreement with findings of Wright *et al.,* (2009). Spatially, larger perturbations were found at greater distances from the cloud edge. Though this was seen in June, a comparison between months shows a weaker perturbation in December.

The time lag defined as difference between the point in the clouds lifetime when a significant perturbation in mean clear sky UTH occurs and the point of maximum $BTD_{6.2\text{-}7.3}$ is also found in June 2010. This ranged between 36 and 123 minutes. This was not found in December 2010 due to minimal significant increases in UTH occurring. Interestingly, a pattern emerges whereby the greatest perturbation is found to correspond to longer time lags. This is similar to that found by Wright *et al.,* (2009).

To quantify the answer to question 3, the corresponding clear sky OLR was also analysed. The OLR anomalies were calculated for the same lifetime and size bins as the UTH anomalies. The OLR response shows a strong negative correlation with the UTH. No time lag between the two variables is observed. This response is found to be stronger in December than June, with a maximum decrease of -4.7 Wm^{-2} with a 1% increase in UTH in December, compared to a maximum perturbation -1.83 Wm^{-2} in June. The response of clear sky UTH and OLR found in this study are in agreement with several studies in the literature. A weaker temporal response emerged, with an initial drying followed by a significant moistening of the upper troposphere towards the end of the clouds lifetime. This was expected and may be due to the physical mechanisms discussed in chapter 1 as being a possible source of moistening. An analysis of UTH anomalies and corresponding OLR anomalies show an strong negative correlation. This also shows a seasonal pattern, with a strengthening of this relationship in December. This is attributed to the saturation of the water vapour band as discussed by Allan *et al.,* (1999) in drier ambient atmospheres such as December. This therefore suggests that, with regards to the net outgoing energy balance, the effect on OLR by deep convection is to reduce the outgoing longwave, with this being stronger in December, suggesting a seasonal pattern may exist.

The analysis of the UTH and OLR response to deep convection in this study is conducted over the clouds lifetime in a lagrangian tracking framework. Though previous studies such as that of Schröder *et al.,* (2013) have tracked clouds using a similar tracking method over a similar study region using SEVIRI, previous studies have not tracked variables related to the cloud, nor has the response of these been quantified in such a way as in this study. The high temporal resolution has shown patterns in the early stages of the clouds lifetime that are not seen in studies such as Zelinka and Hartmann (2009), which analysed UTH and OLR from a Eulerian perspective but at a 3 hourly resolution. Such patterns include the initial decrease in UTH in the initial stages of the cloud lifetime. The results of this study can help to further enhance the parameterisation of the UTH response when modelling deep convection through comparison between modelled results at a high temporal resolution, with an observation based study. This study also uses a high spatial resolution, which will allow for the small spatial patterns not seen in Zelinka and Hartmann (2009),

such as the response within 1-2 cloud radii to also improve the accuracy of model parameterisations.

Further, this study differentiates clouds into size and lifetime bins to determine any size and lifetime based responses of UTH and OLR to deep convection. In comparison to previous studies discussed in chapter 1, such a distinction has not been made when analysing UTH and OLR responses to deep convection. This has shown that some differences can be seen in the magnitude of the UTH response, with this being larger for larger clouds and longer lived clouds. This also confirms that the shape of the response is similar for a clouds over all lifetimes and sizes bins.

7.1 Limitations

Though a general pattern emerges in the clear sky UTH and OLR response to deep convection over the study region, several limitations were found to be inherent in the methods used for the detection and tracking of deep convection in this study.

Firstly, the $BTD_{6.2\text{-}7.3}$ method is limited by the inherent controls on the threshold. The $BTD_{6.2\text{-}7.3}$ classification of deep convection, due to the controlling factors being the effect of the cloud top height on the weighting functions, is likely to underestimate the length of the cloud lifecycle and therefore the quantification of the UTH and OLR response. This may also introduce a limiting factor of the number of deep convective clouds analysed, especially with a cut off time of two hours imposed. The sample size is therefore limited by the intensity of convection when this threshold is set a value closer to -2 K. This threshold may not be sustainable given the clouds life cycle and the large amount of kinetic energy needed to sustain this for long periods of time. This limited the temporal element of the study, with the clouds only tracked when they were considered intense, or close to the tropopause. This in turn effects the robustness of the study, due to the limited sample size. This can be seen from the size of the standard errors for the analysed lifetime bins with limited numbers of clouds in them. The standard errors found for each point in the timeseries analyses show some overlap at each timestep. This would suggest that the results are likely to be less robust. This in turn will effect the effectiveness of the tracking algorithm. Although the cloud is considered not have ended its lifetime when the threshold has no longer been passed, the cloud itself is likely to still be in existence. This again limits the effectiveness of the tracking methodology to track cloud over large temporal domains.

The uncertainty in the UTH estimation is a further limiting factor in understanding the response of UTH to deep convection. The use of coefficients from the relationship between the modelled 6.2 μm band brightness temperatures and the associated ERA-Interim UTH introduces inaccuracies due to the ability of ERA-Interim to accurately estimate upper tropospheric humidity (chapter 2). Associated errors in UTH estimates in ERA-Interim will manifest themselves in the modelled 6.2 μm band brightness temperatures. This may increase to the spread of UTH values in the relationship, as seen in section 6.1. This is especially prevalent for the relationship developed for December 2010.

This error in the estimated UTH values limits the accuracy of the quantification of the OLR response to UTH. Further, the OLR response is also limited in its accuracy by the errors associated with GERB measurements. The errors in the longwave flux are expected to be within 10 Wm^{-2} . This value is larger than a lot of the perturbations found in the OLR response.

Further limitations of this study come from the applicability of these results to a larger climatology of the region. This results from the study only being conducted over the two months of June and December in 2010. Furthering this study by applying the same methods to the whole of 2010 or winter and summer months

in other years would allow for a stronger, more robust conclusion to be drawn as the spatial and temporal effect of deep convection on UTH and OLR. This limitation also applies to the spatial scale of the study. A larger spatial scale to incorporate all of the ITCZ region and the ascending and descending branches of the Hadley cell would give a more robust spatial and temporal pattern of UTH in response to deep convection. This would allow also allow for better comparisons with other larger scale studies.

7.2 Future work

The use of SEVIRI and GERB to detect and track the spatio-temporal response of UTH and OLR to deep convection has opened up several new lines of investigation. Firstly, a comparison of results between land based and oceanic convection would provide a further characterisation of the response and allow for more detailed comparison with other studies such as Zelinka and Hartmann (2009), who analyse the response over the Pacific warm pool. Continental convection is stronger than maritime convection with a more pronounced diurnal cycle, suggesting it reaches higher into the tropopause and UTH may have a temporal response associated with the diurnal cycle. This may also have associated impacts on the extent of the the UTH perturbation over both regions. Future work would also involve increasing the spatial domain of the study to include a larger region of tropical Africa. This would also include an extension of the temporal element of this study, so as to provide a more robust response of UTH to deep convection.

As suggested by Wright *et al.,* (2009), moistening of the upper troposphere by deep convection is found to be greatest for infrequent events. This would suggest a frequency-magnitude relationship exists between the deep convection and upper tropospheric moistening. It would therefore be interesting to see whether this is found, given the limited occurrence of intense convection in December over this study region. This would also allow for response of OLR in drier, less convectively active regions to be further quantified.

Further, a comparison with a different detection method, for example the 10.8μm method used by Fiolleau and Roca, (2013) and Konduru *et al.,* (2013). This will not only allow for a comparison of the UTH and OLR response and the effect of the detection method, but also a comparison between cloud statistics like lifetime size distributions.

Future work may also involve a change in the tracking method used in this study. Though the area overlap method is the most commonly used and can be easily implemented to track clouds, a further, more detailed method of cloud tracking was developed the course of this by Fiolleau and Roca (2013) where a 3D image processing approach is used to detect and track mesoscale convective systems in SEVIRI imagery over the systems lifetime. Fiolleau and Roca (2013) find this method to be much more effective than other tracking methods, with the 3D method allowing the cloud to be tracked for a much longer period, and for the delineation of convective cores and associated stratocumulus from the mesoscale system in which they are embedded. Application of this method, rather than using a simplistic area overlap method may allow for a more detailed quantification of the UTH response to deep convection. The use of Fiolleau and Roca's (2013) method may also negate the need for reclassification of contiguous altostratus to deep convection in the CloudSat-2BCLDCLASS product.

This study also has future implications for climate modelling with regards to understanding the temporal responses at shorter timescales and at a high temporal resolution. With cloud processes and feedback being the greatest uncertainty in understanding the Earth's energy budget in climate models (Tsushima, *et al.,* 2015), this study and a further expansion of these methods to larger spatial domains and longer timescales

will allow for such cloud processes to be more robustly and better constrained in climate models. Using the methods in this study, alongside modelling tools such as the CFMIP Observation Simulator Package (COSP) may allow for biases in modelling the energy budget to be reduced and our understanding and constraint on cloud processes and response of UTH and OLR to clouds to be better defined. Similarly, this study also has implications for analysing important processes in climate modelling studies. For example, the method in this study with regards to cloud detection and the reclassification of altostratus to anvil may allow for an understanding of the relationship between convective core size and the spatial extent of anvil fractions. In some models the anvil fraction is underestimated, whilst the cloud fraction with regards to deep convection is overestimated (Ringer and Allan, 2004). The methods used in this study could help to further constrain and parameterise convective processes.

Chapter VIII

References

Allan, R. P., Shine, K.P., Slingo, A. and Pamment, J.A. (1999), The dependence of clear-sky outgoing longwave radiation on surface temperature and relative humidity. *Quarterly Journal of the Royal Meteorological Society,* 125, 2103-2126.

Allan, R.P., Slingo, A., Milton, S.F., Brooks, M.E. (2007) Evaluation of the Met Office global forecast model using Geostationary Earth Radiation Budget (GERB) data. *Quarterly Journal of the Royal Meteorological Society.* 133, 1993–2010.

Andrews, D. G. (2010) *An Introduction to Atmospheric Physics.* Cambridge, Cambridge University Press.

Arnaud, Y., Desbois, M., and Maizi, J. (1992) Automatic Tracking and Characterization of African Convective Systems on Meteosat Pictures. *Journal of Applied Meteorology.* 31, 443-453.

Ashpole, I. and Washington, R. (2013) A new high-resolution central and western Saharan summer time dust source map from automated satellite dust plume tracking. *Journal of Geophysical Research: Atmospheres,* 118(13): 6981-6995.

Aspliden, C. I., Tourre, Y. and Sabine, J. B. (1976) Some climatological aspects of West African disturbance lines during GATE. *Monthly Weather Review,* 104, 1029–1035.

Ba, M.B. and Nicholson, S. (1998) Analysis of convective activity and its relationship to the rainfall over the Rift Valley lakes of East Africa during 1983-90 using the Meteosat infrared channel. *Journal of Applied Meteorology.* 37(10), 1250-1264.

Bantges, R.J. (2000) *Cirrus Cloud Radiative Properties in the Thermal Infrared.* Thesis: Imperial College London.

Baran, A.J. and Francis, P.N. (2004) On the radiative properties of cirrus cloud at solar and thermal wavelengths: A test of model consistency using high-resolution airborne radiance measurements. *Quarterly Journal of the Royal Meteorological Society Part A.* 130(598), 763–778.

Barbosa, H. A., da Silva Junior, I. W., Ertük, A. G., & Prieto, J. (2011). The cloud-top SEVIRI data for monitoring convective storms. Anais XV Simpósio Brasileiro de Sensoriamento Remoto—SBSR, Curitiba, PR, Brasil, 30, 2179.

Barry, R.G. and Chorley, R.J. (2003) *Atmopshere, weather and climate.* London: Routledge.

Bates, J.J. and Jackson, D.L. (2001). Trends in upper-tropospheric humidity. *Geophysical Research Letters.* 28(9), 1695-1698.

Bechtold, P. (2009) *Atmpospheric Moist Convection.* [Lecture] ECMWF Training - Meterological training course lecture series.

Berens, C. (2013) *Africa natural Relief map* [Online] available at: http://www.mapland.co.za/relief [accessed 2015]

Berk, A., Bernstein, L.S., Anderson, G.P., Acharya, P.K., Robertson,D.C., Chetwynd, J.H., and Adler -Golden, S. M. (1998) MODTRAN Cloud and Multiple Scattering Upgrades with Application to AVIRIS. *Remote Sensing of the Environment.* 65, 367–375.

Besson, L. and Lemaître, Y. (2014) Mesoscale Convective Systems in Relation to African and Tropical Easterly Jets. *Monthly Weather Review,* 142, 3224–3242

Betts, A. K., (1990) Greenhouse warming and the tropical water budget. *Bulletin of the American*

Meteorological Society. 71, 1464-1465.

Bignell, K.J. (1970) The water-vapour infra-red continuum. *Quarterly Journal of the Royal Meteorological Society.* 96(409), 390–403.

Bischoff, T. and Schneider, T., (2014). Energetic Constraints on the Position of the Intertropical Convergence Zone. *Journal of Climate*, 27(13), 4937-4951.

Boehmer, S. (2012) Science debates must continue. *Energy and the Environment.* 23, 1483–1487.

Bohren, C.F. and Albrecht, B.A. (1998) *Atmospheric Thermodynamics* .USA, Oxford University Press USA.

Brindley, H.E. and Harries J.E., (1998,) The impact of far ir absorption on clear sky greenhouse forcing: Sensitivity studies at high spectral resolution. *Journal of Quantitative Spectroscopy & Radiative Transfer.* 60, 151-180.

Brindley, H., Bantges, R., Russel,l J., Murray, J., Dancel, C., Belotti, C., Harries, J., (2015) Spectral Signatures of Earth's Climate Variability over 5 Years from IASI, *Journal of Climate*, 28, 1649-1660.

Burpee, R.W. (1972) The Origin and Structure of Easterly Waves in the Lower Troposphere of North Africa. *Journal of the Atmospheric Sciences.* 29, 77–90.

CALIPSO (2013) *2B-CLDCLASS-LIDAR* [Online] available at: http://www.cloudsat.cira.colostate.edu/data-products/level-2b/2b-cldclass-lidar [accessed 2013]

Carbon Dioxide Information Analysis Center (CDIAC) (2014) *Carbon Dioxide (CO2)* [Online] available at: http://cdiac.ornl.gov/trends/co2/ [Accessed 2014]

Chaboureau, J.-P., Guichard, F., Redelsperger, J.-L., and Lafore, J.- P. (2004) The role of stability and moisture in the development of convection. *Quarterly Journal of the Royal Meteorological Society,* 130, 3105–3117.

Chae, J. H., Wu, D. L., Read, W. G., & Sherwood, S. C. (2011). The role of tropical deep convective clouds on temperature, water vapor, and dehydration in the tropical tropopause layer (TTL). *Atmospheric Chemistry and Physics*, 11(8), 3811-3821.

Chahine, M.T. (1992) The hydrological cycle and its influence on climate. *Nature.* 359, 373-380.

Chandrasekar, A. (2010) *Basics of Atmospheric Science.* California: PHI publications.

Chen, S. S., and Houze, Jr., R. A. (1997) Diurnal variation and life cycle of deep convective systems over the tropical Pacific warm pool. *Quarterly Journal of the Royal Meteorological Society.* 123, 357-388.

Chen Y-C., Christensen, M.W., Stephens, G.L., and Seinfeld, J.H. (2014) Satellite-based estimate of global aerosol–cloud radiative forcing by marine warm clouds, *Nature Geoscience* 7, 643–646.

Chung, E.S., Sohn, B.J. and Ramanathan, V. (2004) Moistening Processes in the Upper Troposphere by Deep Convection: A Case Study over the Tropical Indian Ocean. *Journal of the Meteorological Society of Japan, Notes and Correspondence.* 82(3), 959-965.

Chung, E. S., Sohn, B.J., Schmetz, J., and Koenig, M. (2007) Diurnal variation of upper tropospheric humidityand its relations to convective activities over tropical Africa. *Atmospheric Chemistry and Physics*, 7, 2489 – 2502.

Chung, E. S., Soden, B. J., Sohn, B. J., & Schmetz, J. (2013). An assessment of the diurnal variation of upper tropospheric humidity in reanalysis data sets. *Journal of Geophysical Research: Atmospheres,* 118(9), 3425-3430.

Chou, C. and Neelin, J.D. (1999) Cirrus detrainment-temperature feedback. *Geophysical Research Letters*,

26(9), 1295-1298.

CloudSat (2010) *CloudSat Quicklooks Documentation.* [Online] available at: http://www.cloudsat.cira.colostate.edu/quicklooks/quicklooks-documentation [accessed 2013]

Clough, S.A., Kneizys, F.X. and Davies, R.W. (1989) Line shape and the water vapor continuum, *Atmospheric Research,* 23, 229-241.

Clough, S.A., Iacono, M.J. and Moncet, J-L. (1992) Line-by-line calculations of atmospheric fluxes and cooling rates: Application to water vapor. *Journal of Geophysical Research.* 97(D14), 15761 -15785.

Comer, R. E., Slingo, A. and Allan, R. P. (2006) The diurnal cycle observed by Meteosat-8 and simulated by a climate model. In: *EUMETSAT Meteorological Satellites Conference.* Finnish Meteorological Institute, Helsinki, 12 – 16 Jun.

Comer, R.E., Slingo, A. and Allan, R.P. (2007) Observations of the diurnal cycle of outgoing longwave radiation from the Geostationary Earth Radiation Budget instrument. *Geophysical Research Letters.* 34, L02823.

Comstock, J. M., Ackerman, T. P., & Mace, G. G. (2002). Ground based lidar and radar remote sensing of tropical cirrus clouds at Nauru Island: Cloud statistics and radiative impacts. *Journal of Geophysical Research: Atmospheres (1984–2012)*, 107(D23).

Cook, K. H. (1999). Generation of the African easterly jet and its role in determining West African precipitation. *Journal of climate*, 12(5), 1165-1184.

Cooperative Institute for Meteorological Satellite Studies (CIMSS) (2010) *IREMIS Global Infrared Land Surface Emissivity: UW-Madison Baseline Fit Emissivity Database* [Online] available at https://cimss.ssec.wisc.edu/iremis/ [accessed 2013]

Corti, T. and Peter, T. (2009) A simple model for cloud radiative forcing. *Atmospheric Chemistry and Physics.* 9, 5751–8 .

Dee, D.P. and Uppala, S. (2009) Variational bias correction of satellite radiance data in the ERA-Interim reanalysis. *Quarterly Journal of the Royal Meteorological Society.* 135, 1830–1841.

Dee, D. P., Uppala, S. M., Simmons, A. J., Berrisford, P., Poli, P., Kobayashi, S., Andrae, U., Balmaseda, M. A., Balsamo, G., Bauer, P., Bechtold, P., Beljaars, A. C. M., van de Berg, L., Bidlot, J., Bormann, N., Delsol, C., Dragani, R., Fuentes, M., Geer, A. J., Haimberger, L., Healy, S. B., Hersbach, H., Hólm, E. V., Isaksen, L., Kållberg, P., Köhler, M., Matricardi, M., McNally, A. P., Monge-Sanz, B. M., Morcrette, J.-J., Park, B.-K., Peubey, C., de Rosnay, P., Tavolato, C., Thépaut, J.-N. and Vitart, F. (2011) The ERA-Interim reanalysis: configuration and performance of the data assimilation system. *Quarterly Journal of the Royal Meteorological Society,* 137, 553–597.

Desbois, M., Kayiranga, T. and Gnamien, B. (1989) Diurnal cycle of convective cloudiness over tropical Africa observed from Meteosat: Geographic characterization and interannual variations. *Annales Geophysicae.* 7,395-404.

Dessler, A.E. and Minschwaner, K. (2007) An analysis of the regulation of tropical tropospheric water vapor. *Journal of Geophysical Research,* 112.

Diongue, A., Lafore, J.P. Redelsperger, J.L. and Roca, R. (2002), Numerical study of a Sahelian synoptic weather system: Initiation and mature stages of convection and its interactions with the large-scale

dynamics. *Quarterly Journal of the Royal Meteorological Society.* 128, 1899-1927.

Duvel, J.P (1989) Convection over tropical Africa and Atlantic Ocean during Northern summer. Part I: Interannual and diurnal variations. *Monthly Weather Review.* 117, 2782-2799.

Emanuel, K.E. (2005) *Divine Wind: The History And Science Of Hurricanes.* USA, Oxford University Press USA.

European Centre for Medium-Range Weather Forecasts (2009) *European Centre for Medium-Range Weather Forecasts (ECMWF) Re-Analysis Interim (ERA-Interim) model data.* NCAS British Atmospheric Data Centre, 2012. http://catalogue.ceda.ac.uk/uuid/00f58d1d7b6c8f38993e77c79e72da92

EUMETSAT (2014) *METEOSAT design - METEOSAT SECOND GENERATION SPACECRAFT* [Online] available at: http://www.eumetsat.int/website/home/Satellites/CurrentSatellites/Meteosat/MeteosatDesign/index.html#sev [accessed 2013].

Ewald, F., Bugliaro, L., Mannstein, H., and Mayer, B. (2013) An improved cirrus detection algorithm MeCiDA2 for SEVIRI and its evaluation with MODIS. *Atmospheric Measurement Techniques.* 6, 309-322.

Feng, Z., Dong, X., Xi, B., McFarlane, S. A., Kennedy, A., Lin, B., and Minnis, P. (2012), Life cycle of midlatitude deep convective systems in a Lagrangian framework. *Journal of Geophysical Research.* 117, D23201.

Fiolleau, T., & Roca, R. (2013). Composite life cycle of tropical mesoscale convective systems from geostationary and low Earth orbit satellite observations: method and sampling considerations. *Quarterly Journal of the Royal Meteorological Society,* 139(673), 941-953.

Fischer, J., Schüller, L., Preusker, R. (2000) *Algorithm Theoretical Basis Document ATBD 2.1, 2.2 Cloud Albedo and Cloud Optical thickness.* MERIS-ESL. Doc. No: PO-TN-MEL-GS-0005

Flato, G., J. Marotzke, B. Abiodun, P. Braconnot, S.C. Chou, W. Collins, P. Cox, F. Driouech, S. Emori, V. Eyring, C. Forest, P. Gleckler, E. Guilyardi, C. Jakob, V. Kattsov, C. Reason and M. Rummukainen, (2013) Evaluation of Climate Models. *In:* Climate Change 2013: The Physical Science Basis. Contribution of Working Group I to the Fifth Assessment Report of the Intergovernmental Panel on Climate Change [Stocker, T.F., D. Qin, G.-K. Plattner, M. Tignor, S.K. Allen, J. Boschung, A. Nauels, Y. Xia, V. Bex and P.M. Midgley (eds.)]. Cambridge University Press, Cambridge, United Kingdom and New York, NY, USA

Flentje, H., Dornbrack, A., Fix, A., Ehret, G., Holm, E. (2007) Evaluation of ¨ ECMWF water vapour fields by airborne differential absorption lidar measurements: a case study between Brazil and Europe. *Atmospheric Chemistry and Physics.* 7, 5033–5042.

Fu, R., Del Genio, A.D., and Rossow, W.B., (1990) Behavior of deep convective clouds in the tropical Pacific deduced from ISCCP radiances. *Journal of Climate*, 3, 1129-1152.

Futyan, J., and Del Genio, A. (2007) Deep convective system evolution over Africa and the tropical Atlantic. *Journal of Climate.* 20, 5041-5060.

Garrett, T. J., Dean-Day, J., Liu, C., Barnett, B., Mace, G., Baumgardner, D., Webste, C., Bui, T., Read, W. and Minnis, P. (2006). Convective formation of pileus cloud near the tropopause. *Atmospheric Chemistry and Physics.* 6(5), 1185-1200.

Geer A.J., Harries J.E., Brindley H.E. (1999) Spatial patterns of climate variability in upper-tropospheric water vapor radiances from satellite data and climate model simulations. *Journal of Climate.* 12,

1940-1955.

Gettelman, A., Salby, M.L. and Sassi, F. (2002) The distribution and influence of convection in the tropical tropopause region, J*ournal of Geophysical Research*, 107.

Gettelman, A., Collins, W.D., Fetzer, E.J., Eldering, A., Irion, F.W., Duffy, P.B. and Bala, G., (2006) Climatology of Upper Tropospheric Relative Humidity from the Atmospheric Infrared Sounder and Implications for Climate, *Journal of Climate*, 19(23), 6104-6121.

Hagos, S., Feng, Z., McFarlane, S., and Leung, L. R. (2013) Environment and the lifetime of tropical deep convection in a high resolution regional model simulation. *Journal of Atmospheric Science.* 70(8), 2409–2425.

Hall, T.J. and Vonder Haar, T.H. (1999) The Diurnal Cycle of West Pacific Deep Convection and Its Relation to the Spatial and Temporal Variation of Tropical MCSs. *Journal of the Atmospheric Sciences.* 56, 3401-3415.

Harries, J.E., Russel,l J.E, Hanafin, J.A, Brindley, H., Futyan, J., Rufus, J., Kellock, S., Matthews, G., Wrigley, R., Last, A., Mueller, J., Mossavati, R., Ashmall, J., Sawyer, E., Parker, D., Caldwell, M., Allan, P.M., Smith, A., Bates, M.J., Coan, B., Stewart, B.C., Lepine, D.R., Cornwall, L.A., Corney, D.R., Ricketts, M.J., Drummond, D., Smart, D., Cutler, R., Dewitte, S., Clerbaux, N., Gonzalez, L., Ipe, A., Bertrand, C., Joukoff, A., Crommelynck, D., Nelms, N., Llewellyn-Jones, D.T., Butcher, G., Smith, G.L., Szewczyk, Z.P., Mlynczak, P.E., Slingo, A., Allan, R.P., Ringer, M.A., (2005), The geostationary Earth Radiation Budget Project, *Bulletin of the American Meteorological Society,* 86, 945-945–960.

Henderson, D., L'Ecuyer, T. S., Stephens, G., Partain, P. and Sekiguchi, M. (2012) A Multi-sensor Perspective on the Radiative Impacts of Clouds and Aerosols. *Journal of Applied Meteorology Climatology.* 52, 853–871.

Henken, C. K.C., Schmeits, M.J., Wolters, E.L.A. and Roebeling, R.A. (2009) *Detection of Cb and TCu clouds using MSG SEVIRI cloud physical properties and weather radar observations.* Thesis. KNMI WR.

Henken, C. C., Schmeits, M. J., Deneke, H., & Roebeling, R. A. (2011). Using MSG-SEVIRI cloud physical properties and weather radar observations for the detection of Cb/TCu clouds. *Journal of Applied Meteorology and Climatology*, 50(7), 1587-1600.

Holloway, C. and Neelein, J. (2009) Moisture vertical structure, column water vapor, and tropical deep convection. *Journal of Atmsopheric Science.* 66, 1665-1683.

Holton, J.R., Wallace, J.M., Young, J.A. (1971) On boundary layer dynamics and the ITCZ. *Journal of the Atmospheric Sciences.* 28, 275–280.

Houghton, J. (2002) *The Physics of Atmospheres.* 3rd Ed. Cambridge, Cambridge University Press.

Houshangpour, A. John, V. O. and Buehle, S.A. (2005) Retrieval of upper tropospheric water vapor and upper tropospheric humidity from AMSU radiances. *Atmospheric Chemistry and Physics.* 5, 2019–2028.

Houze, R.A. (1993) *Cloud Dynamics.* London: Academic Press.

Hurst, D. F., Hall, E. G., Jordan, A. F., Miloshevich, L. M., Whiteman, D. N., Leblanc, T., Oltmans, S. J. (2011). Comparisons of temperature, pressure and humidity measurements by balloon -borne radiosondes and frost point hygrometers during MOHAVE-2009. *Atmospheric*

Measurement Techniques, 4(12), 2777-2793.

Inoue, T. (1987) A cloud type classification with NOAA 7 split-window measurements. *Journal of Geophysical Research: Atmospheres* (1984–2012). 92(D4), 3991–4000.

Inoue, T., Vila, D., Rajendran, K., Hamada, A., Wu, X., & Machado, L. A. (2009) Life cycle of deep convective systems over the eastern tropical Pacific observed by TRMM and GOES-W. J*ournal of the Meteorological Society of Japan. Ser. II. Special Issue: Precipitation Measurements from Space* 87, 381-391.

International Satellite Cloud Climatology Project (2014) *ISCCP DEFINITION OF CLOUD TYPES - Cloud Parameter Definitions And Measurement Methods.* [Online] available at: http://isccp.giss.nasa.gov/cloudtypes.html [accessed 2014].

Janicot, S., Caniaux, G., Chauvin, F., de Coëtlogon, G., Fontaine, B., Hall, N., Kiladis, G., Lafore, J.-P., Lavaysse, C., Lavender, S. L., Leroux, S., Marteau, R., Mounier, F., Philippon, N., Roehrig, R., Sultan, B. and Taylor, C. M. (2011), Intraseasonal variability of the West African monsoon. *Atmospheric Science Letters.* 12, 58–66.

Jedlovec, G. J., Lerner, J. A. and Atkinson, R. J. (2000) A satellite-derived upper-tropospheric water vapor transport index for climate studies. J*ournal of Applied Meteorology.* 39, 15-41.

Jensen, E. J., Toon, O. B., Selkirk, H. B., Spinhirne, J. D., & Schoeberl, M. R. (1996). On the formation and persistence of subvisible cirrus clouds near the tropical tropopause. *Journal of Geophysical Research: Atmospheres (1984–2012)*, 101(D16), 21361-21375.

Jensen, E.J., Read, W.G., Mergenthaler, J., Sandor, B.J., Pfister, L. and Tabazadeh, A. (1999) High humidities and subvisible cirrus near the tropical tropopause. *Geophysical Research Letters.* 26(15), 2347-2350.

Jensen, M.P., and Del Genio, A.D. (2003) Radiative and microphysical characteristics of deep convective systems in the tropical Western Pacific. *Journal of Applied Meteorology,* 42, 1234-1254.

Johnston, M.S., Eliasson, S.,Eriksson, P., Forbes, R.M., Wyser, K. and Zelinka, M.D. (2013) Diagnosing the average spatio-temporal impact of convective systems – Part 1: A methodology for evaluating climate models. *Atmospheric Chemistry and Physics,* 13, 12043-12058.

Johnston, M.S., Eliasson, S., Eriksson, P., Forbes, R.M., Gettelman, A., Räisänen, P., and Zelinka, M.D. (2014) Diagnosing the average spatio-temporal impact of convective systems – Part 2: A model intercomparison using satellite data, *Atmospheric Chemistry and Physics,* 14, 8701-8721.

Kanamitsu, M. and Krishnamurti, T. N. (1978) Northern Summer Tropical Circulations During Drought and Normal Rainfall Months. *Monthly Weather Review*, 106, 331–347.

Kayiranga, T. (1991) Observation of convective activity from satellite data over Lake Victoria region in April 1985. *Veille Climatique Satellitaire.* 37, 44-55.

Kneizys, F.X., Shettle, E.P., Abreu, L.W., Chetwynd, J,H., Anderson, G.P., Gallery, W.O., Selby, J.E.A. and Clough, S.A. (1988). *Users' Guide to LOWTRAN7*, Report No. AFGL-TR-88-0177, Air Force Geophys. Lab., Hanscom AFB, MA, 138 pp.

Konduru, R.T., Kishtawal, C.M. and Shah, S. (2013) A new perspective on the infrared brightness temperature distribution of the deep convective clouds. *Journal of Earth System Science.* 122(5), 1195–1206.

Krauss, T., Sinkevich, A., Veremey, N., Dovgalyuk, Y., and Stepanenko, V. (2007). Study of the development

of an extremely high cumulonimbus cloud (Andhra Pradesh, India, September 28, 2004). *Russian Meteorology and Hydrology*, 32(1), 19–27.

Krebs, W., Mannstein, H., Bugliaro, L., and Mayer, B. (2007) Technical note: A new day and nighttime METEOSAT second Generation Cirrus Detection Algorithm MeCiDA, *Atmospheric Chemistry Physics*, 7, 6145–6159.

Kumar, V.V., Protat, A., Jakob, C. and May, P.T. (2014) On the atmospheric regulation of the growth of moderate to deep cumulonimbus in a tropical environment. *Journal of the atmospheric sciences.* 71, 1105-1120.

Kunz, A., Spelten, N., Konopka, P., Müller, R., Forbes, R. M. and Wernli, H. (2014) Comparison of Fast In situ Stratospheric Hygrometer (FISH) measurements of water vapor in the upper troposphere and lower stratosphere (UTLS) with ECMWF (re)analysis data. *Atmospheric Chemistry and Physics,* 14, 10803–10822.

Laing, A. G. and Fritsch, J.M. (1993) Mesoscale convective complexes in Africa. *Monthly Weather Review.* 121, 2254-2263.

Laing, A.G., Carbone, R., Levizzanib, V. and Tuttle, J. (2008) The propagation and diurnal cycles of deep convection in northern tropical Africa. *Quarterly Journal of the Royal Meteorological Society.* 134, 93–109.

Lindzen, R.S. (1990) Some coolness concerning global warming. *Bulletin of the American Meteorological Society,* 71, 288-299.

Lensky, I.M. and Rosenfeld, D. (2008) Clouds-Aerosols-Precipitation Satellite Analysis Tool (CAPSAT). *Atmospheric Chemistry and Physics.* 8, 6739–6753

Ludlam, F. (1980) *Clouds and Storms.* Pennsylvania, Pennsylvania State University Press.

Luo, Z. and Russow, W.B. (2004) Characterizing tropical cirrus life cycle, evolution and interaction with the upper-tropospheric water vapour using Lagrangian trajectory analysis of satellite observations. *Journal of Climate.* 17, 4541-4563.

Lynch, D. K., Sassen, K., Star, D. and Stephens, G. L. (Editors) (2002) *Cirrus.* Oxford, UK: Oxford University Press.

Mace, G. G., Deng, M., Soden, B. and Zipser, E. (2006) Association of tropical cirrus in the 10 – 15-km layer with deep convective sources: An observational study combining millimeter radar data and satellite-derived trajectories. *Journal of Atmospheric Science.* 63, 480 – 503.

Machado, L.A.T., Rossow, W.B., Guedes, R.L. and Walker, A.W. (1998) Life cycle variations of mesoscale convective systems over the Americas. *Monthly Weather Review.* 126, 1630-1654.

Machado, L. A. T., and H. Laurent (2004), The convective system area expansion over Amazonia and its relationships with convective system life duration and high-level wind divergence. *Monthly Weather Review.* 132, 714 – 725.

Maddox, R. A., (1980) Mesoscale convective complexes. *Bulletin of the American Meteorological Society.* 61, 1374–1387.

Martin, D.W. and Schreiner, A.J. (1981) Characteristics of West African and East Atlantic cloud clusters: A survey from GATE. *Monthly Weather Review.* 109, 1671-1688.

Massie, S. T., Gille, J., Craig, C., Khosravi, R., Barnett, J., Read, W., and Winker, D. (2010), HIRDLS and CALIPSO observations of tropical cirrus. *Journal of Geophysical Research*, 115, D00H11.

Mathon, V., and Laurent, H. (2001), Life cycle of the Sahelian mesoscale convective cloud systems, Quarterly Journal of the Royal Meteorological Society, 127, 377 – 406.

McCormack, J. P., Fu, R. and Read, W. G. (2000) The influence of convective outflow on water vapor mixing ratios in the tropical upper troposphere: An analysis based on UARS MLS measurements. *Geophysical Research Letters.* 27(4), 525 – 528

McIlveen, R., (1998) *Fundamentals of Weather and Climate.* 1 ed. Surrey, Stanley Thorns Ltd.

Mecikalski, J. R., Mackenzie, W. M., Koenig, M. and Muller, S. (2010) Use of Meteosat Second Generation infrared data in 0-1 hour convective initiation nowcasting. Part 1. Infrared fields. *Journal of Applied Meteorology and Climate.* 49, 521-534.

MetOffice (2013a) *Cloud types for observers - Reading the sky* [Online] available at: http://www.metoffice.gov.uk/media/pdf/r/i/Cloud_types_for_observers.pdf [accessed 2013].

MetOffice (2013b) *Deep convective cloud – cumulonimbus – reaches the tropopause and spreads out.* [Online] available from: http://www.metoffice.gov.uk/research/modelling-systems/large-eddy-model [accessed 2013].

MetOffice (2014) *Altocumulus Castellanus* [Online] available at: http://www.metoffice.gov.uk/learning/learn-about-the-weather/clouds/altocumulus-castellanus [accessed 2014].

Moisselin, J.M. and Autonès, F. (2013) RDT-CW: toward a multidimensional description of convection. *In:* Understanding the past, observing the present and protecting the future. 2013 EUMETSAT meteorological satellite conference. 16-20 September 2013. Vienna, Austria.

Mohr, K.I. and Thorncroft, C.D. (2006) Intense convective systems in West Africa and their relationship to the African easterly jet. *Quarterly Journal of the Royal Meteorological Society.* 132, 163-176.

Mosher, F. (2002) Detection of deep convection around the globe. *In:* Preprints, 10th Conferene on Aviation, Range, and Aerospace Meteorology, Portland, OR, American Meteorological Society, 289–292.

NASA (2012) *NASA - The Cloud Profiling Radar* [Online] available at: http://www.nasa.gov/mission_pages/cloudsat/spacecraft/index.html#.VZqLMPlVgyE. [accessed on 2013]

Nicholson, S.E. (2009) A revised picture of the structure of the "monsoon" and land ITCZ over West Africa. *Climate Dynamics.* 32(7-8), 1155-1171.

Park, J.-H., Ha, J.-Y., Park, S.-M., and Lee, K.-M. (2007) Validation of upper tropospheric humidity inferred for the water vapour channel of geostationary satellites for the summer season in the east-Asian region. *Journal of the Korean meteorological society.* 43(3), 223-237.

Perry, K.D. and Hobbs, P.V. (1996) Influences of Isolated Cumulus Clouds on the Humidity of Their Surroundings. *Journal of the Atmospheric Sciences.* 53(1), 159-174.

Petty, G. W. (2006) *A First Course in Atmospheric Radiation.* 2nd Ed. Wisconsin: Sundog Publishing.

Pili, P. (2000) Calibration of SEVIRI. In: *Proceedings of the 2000 EUMETSAT Meteorological Satellite Data User's Conference.* 29 May – 2 June 2000, Bologna, Italy .pp33 - 39.

Raval, A. and Ramanathan, V. (1989) Observational Determination of the Greenhouse Effect. *Nature*, 342, 758-761.

Ricchiazzi, P., Yang, H., Gautier, C., and Sowle, D. (1998) SBDART: A Research and Teaching Software Tool for Plane-Parallel Radiative Transfer in the Earth's Atmosphere. *Bulletin of the American Meteorological Society.* 79(10), 2101-2114.

Riehl, H. (1979) *Climate and weather in the tropics.* London, Academic Press.

Rind, D., Chiou, E.-W., Chu, W., Larsen, J. Oltmans, S., Lerner, J., McCormkk, M.P. and McMaster, L. (1991) Positive water vapour feedback in climate models confirmed by satellite data. *Nature.* 349, 500-503.

Ringer, M. A., & Allan, R. P. (2004). Evaluating climate model simulations of tropical cloud. *Tellus A*, 56(4), 308-327.

Roach, W.T. and Goody, R.M. (1958) Absorption and emission in the atmospheric window from 770 to 1,250 cm^{-1} . *Quarterly Journal of the Royal Meteorological Society.* 84(362), 319–333.

Roca, R. and Ramanathan, V. (2000) Scale Dependant properties of Monsoonal Clouds Sytems over the Indian Ocean. *Journal of Climate.* 13, 1286-1298.

Roca, R., Viollier, M., Picon, L., & Desbois, M. (2002). A multisatellite analysis of deep convection and its moist environment over the Indian Ocean during the winter monsoon. *Journal of Geophysical Research: Atmospheres* (1984–2012), 107(D19).

Roebber, P.J. (2009) Visualizing Multiple Measures of Forecast Quality. *Weather and Forecasting: Notes and Correspondence.* 24, 601-608.

Rogers, R.R. and Yau, M.K. (1989) *A short course in cloud physics.* 3rd ed., Oxford, Pergamon Press.

Russell, J.E. (2011) *QUALITY SUMMARY: GERB L2 ARG: 3 scan average Edition 1 product.* Technical Report.

Russo, M.R., Marecal , Marecal, V., Hoyle, C.R., Arteta, J., Chemel, C., Chipperfield, M.P., Dessens, O., Feng, W., Hosking, J.S., Telford, P.J., Wild, O., Yang, X., and Pyle, J.A. (2011) Representation of tropical deep convection in atmospheric models – Part 1: Meteorology and comparison with satellite observations. *Atmospheric Chemistry and Physics.* 11, 2765-2786.

Salby, M.L. (1996) *Fundamentals of Atmospheric Physics.* London, Academic Press Inc.

Sandford, M.C.W., Allan, P.M., Caldwell, M.E., Delderfield, J., Oliver, M.B., Sawyer, E., Harries, J.E., Ashmall, J., Brindley, H., Kellock, S., 2003. The geostationary earth radiation budget (GERB) instrument on EUMETSAT's MSG satellite. *Acta Astronautica.* 53 (11), 909–915.

Santurette, C. and Georgiev, P. (2005) *Weather Analysis and Forecasting: Applying Satellite Water Vapor Imagery and Potential Vorticity Analysis.* London, Academic Press Inc.

Sassen, K. and Wang, Z. (2008) Early Results from CloudSat: Applying the Cloud Type Algorithm around the Globe, *Geophysical Research Letters.* 35, L04805.

Sassen, K. and Wang, Z. (2008) Classifying clouds around the globe with the CloudSat radar: 1-year of results. *Geophysical research letters.* 35(4).

Sassen, K., Wang, Z. and Liu, D. (2008) Global distribution of cirrus clouds from CloudSat/Cloud-Aerosol Lidar and Infrared Pathfinder Satellite Observations (CALIPSO) measurements. *Journal Geophysical Research.* 113, D00A12.

Sassi, F., Salby, M. and Read, W.G. (2001) Relationship between upper tropospheric humidity and deep convection. *Journal of Geophysical Research,* 106.

Savtchenko, A. (2009) Deep convection and upper-tropospheric humidity: A look from the A-Train. *Geophysical Research Letters.* 36(6).

Schmetz, J., Pili P., Tjemkes, S., Just, D., Kerkmann, J., Rota, S., and Ratier, A., (2002) An introduction toMeteosat Second Generation (MSG). *Bulletin of the American Meteorological Society*,

83(7), pp. 977-992.

Schmetz, J., K¨onig, M., Pili, P., Rota, S., Ratier, A.and Tjemkes, S. (2003) Meteosat Second Generation (MSG): status after launch. *In:* 12th Conference on Satellite Meteorology and Oceanography, Long Beach, California, February 10-13.

Schneider, T. and Bischoff, T., and Haug G. (2014). Migrations and Dynamics of the Intertropical Convergence Zone. *Nature,* 513, 45-53.

Schröder, M., König, M., and Schmetz, J., (2009) Deep convection observed by the Spinning Enhanced Visible and Infrared Imager on board Meteosat 8: Spatial distribution and temporal evolution over Africa in summer and winter 2006, *Journal of Geophysical Research,* 114.

Scribano, Y. and Leforestier, C. (2007) Contribution of water dimer absorption to the millimeter and far infrared atmospheric water continuum. *Journal of Chemical Physics.* 126, 234301.

Seidel, D.J., Ross, R.J., Angell, J.K. and Reid, G.C. (2001) Climatological characteristics of the tropical tropopause as revealed by radiosondes. *Journal of Geophysical Research: Atmospheres (1984–2012).* 106(D8), 7857–7878.

Shenk, W.E., Holub, R.J. and Neff, R.A. (1976) A multispectral cloudtype identification method developed for tropical ocean areas with Nimbus-3 MRIR measurements. *Monthly Weather Review.* 104, 284–291.

Sherwood, (1996) Maintenance of the free-tropospheric tropical water vapor distribution, Part I: Clear regime budget. *Journal of Climate*, 9(11), 2903-2918.

Sherwood, S.C. (1999) On moistening of the tropical troposphere by cirrus clouds. *Journal of Geophysical Research*, 104(D10), 11949-11960.

Sherwood, S. C., Minnis, P. and McGill, M. (2004) Deep convective cloud top heights and their thermodynamic control during CRYSTAL-FACE. *Journal of Geophysical Research.* 109(20).

Sherwood, S. C., Roca, R., Weckworth, T.M. and Andronova, N.G. (2010) Tropospheric water vapor, convection, and climate. *Reviews of Geophysics.* 48(2).

Shine, K.P. and Sinha, A. (1991) Sensitivity of the Earth's climate to height-dependent changes in the water vapour mixing ratio. *Nature.* 354, 382-384.

Sinha, A. and Allen, M.R. (1994) Climate sensitivity and tropical moisture distribution. *Journal of Geophysical Research.* 99(D2), 3707-3716.

Soden, B. J., (1998) Tracking upper tropospheric water vapor radiances: A satellite perspective. *Journal of Geophysical Research.* 103(D14), 17,069-17,081.

Soden, B.J. (2000) The diurnal cycle of convection, clouds, and water vapor in the tropical upper troposphere. *Geophysical Research Letters*, 27(15), 2173-2176.

Soden, B.J. (2004) The impact of tropical convection and cirrus on upper tropospheric humidity: A Lagrangian analysis of satellite measurements. *Geophysical Research Letters.* 31(20).

Soden, B.J. and Bretherton, F.P. (1993) Upper tropospheric relative humidity from the GOES 6.7 μm channel: Method and climatology for July 1987. *Journal of Geophysical Research: Atmospheres.* 98(D9), 16669-16688.

Soden, B. J., Ackerman, S. A., Starr, D. O'C., Melfi, S. H. and Ferrare, R. A. (1994) Comparison of upper tropospheric water vapor from GOES, Raman lidar, and CLASS measurements. *Journal of Geophysical Research.* 99(D10), 21,005-21,016.

Soden, B.J. and Fu, R. (1995) A satellite analysis of deep convection, upper tropospheric humidity, and the greenhouse effect. *Journal of Climate.* 8, 2333-2351.

Soden, B. J., and Lanzante, J. R. (1996). An assessment of satellite and radiosonde climatologies of upper-tropospheric water vapor. *Journal of Climate.* 9(6), 1235-1250.

Soden, B.J., Jackson, D.L., Ramaswamy, V., Schwarzkopf, M.D., and Huang, X. (2005) The Radiative Signature of Upper Tropospheric Moistening. *Science.* 310(57), 841-844.

Sohn, B.-J. and Schmetz, J. (2004) Water vapour-induced OLR variations asscoaited with high cloud changes over the Tropics: A study from *Meteosta-5* observations. *Journal of Climate.* 17, 1987 -1996.

Stamnes, K., Tsay, S.C., Wiscombe, W., Laszlo, I. (2000) *'DISORT, a general-purpose Fortran program for discrete-ordinate-method radiative transfer in scattering and emitting layered media: Documentation of methodology'.* DISORT Report v1.1. Department of Physics and Engineering Physics, Stevens Institute of Technology: Hoboken, NJ.

Stein, T. H., Parker, D. J., Hogan, R. J., Birch, C. E., Holloway, C. E., Lister, G., Marsham, J.H. and Woolnough, S.J. (2015) The representation of the West African monsoon vertical cloud structure in the Met Office Unified Model: an evaluation with CloudSat. *Quarterly Journal of the Royal Meteorological Society.*

Sun, D.Z. and Lindzen, R.S. (1993) Distribution of tropical tropospheric water vapour. *Journal of the Atmospheric Sciences.* 50(12), 1643-1660.

Suzuki, S., Seto, S. and Oki, T. (2011) Relationship between cloud droplet effective radius and cloud top height for deep convective clouds in CloudSat data product. *In:* Conference: 2011 IEEE International Geoscience and Remote Sensing Symposium, IGARSS 2011, Vancouver, BC, Canada, July 24-29, 2011.

Szyndel, M.D.E., Kelly, G., Thepaut, J-N. (2005) Evaluation of potential ´ benefit of assimilation of SEVIRI water vapour radiance data from Meteosat-8 into global numerical weather prediction analyses. *Atmospheric Science Letters.* 6, 105–111.

Tian, B., Soden, B. J., & Wu, X. (2004). Diurnal cycle of convection, clouds, and water vapor in the tropical upper troposphere: Satellites versus a general circulation model. *Journal of Geophysical Research: Atmospheres* (1984–2012), 109(D10).

Tjemkes, S. (2012) *The Conversion from Effective Radiances to Equivalent Brightness Temperatures.* EUMETSAT. Version 1.

Tompkins, A. M., Gierens, K., and Rädel, G. (2007) Ice supersaturation in the ECMWF integrated forecast system, *Quarterly Journal of Remote Meteorological Society.* 133, 53–63.

Tourville, N., Stephens, G., DeMaria, M. and Vane, D. (2015) Remote Sensing of Tropical Cyclones: Observations from CloudSat and A-Train Profilers. *Bulletin of the American Meteorological Society.* 96, 609–622.

Trier, S.B., (2003) Convective storms: Convective initiation. In: Holton, J.R., Curry, J.A., and Pyle, J.A. (eds.) *Encyclopedia of Atmospheric Sciences,* London: Academic Press, pages 560-570.

Tsushima, Y., Ringer, M. A., Koshiro, T., Kawai, H., Roehrig, R., Cole, J., ... & Webb, M. J. (2015). Robustness, uncertainties, and emergent constraints in the radiative responses of stratocumulus cloud regimes to future warming. *Climate Dynamics*, 1-15.

Udelhofen, P.M. and Hartmann, D.L. (1995) Influence of tropical cloud systems on the relative humidity in the upper troposphere. *Journal of Geophysical Research,* 100.

UNEP (2015) *Map of aridity* [Online] available at: http://na.unep.net/atlas/africaWater/images/maps/pngs/aridity_zones.png [accessed 2015]

University of Paris (2008) *The imaging Radiometer SEVIRI.* [Online] available at: http://e-cours.univ-paris1.fr/modules/uved/envcal/html/msg/2-performancesmsg/seviri.html [accessed 2013]

Velasco, I. and Fritsch, J.M. (1987) Mesoscale convective complexes in the Americas. *Journal of Geophysical Research: Atmospheres (1984–2012).* 92(D8), 9591-9613.

Vila, D. A., Machado, L. A. T., Laurent, H., & Velasco, I. (2008). Forecast and Tracking the Evolution of Cloud Clusters (ForTraCC) using satellite infrared imagery: *Methodology and validation. Weather and Forecasting,* 23(2), 233-245.

Virts, K.S. and Wallace, J.M. (2014) Observations of temperature, wind, cirrus, and trace gases in the tropical tropopause transition layer during the MJO. *Journal of the Atmospheric Sciences.* 71, 1143-1157.

Waliser, D.E and Gautier, C. (1993) A Satellite-derived Climatology of the ITCZ. *Journal of Climate*, 6, 2162–2174.

Wallace, J.M. and Hobbs, P.V. (2006) *Atmospheric Science: An Introductory Survey.* 2nd ed. London, Academic Press Inc.

Wang, J. and Curry, J.A. (1998) Relative humidity variations in the tropical western Pacific and relations with deep convection clouds. In: *Proceedings of the Eight Atmospheric Radiation Measurement (ARM) Science Team Meeting*, Tucson, AZ, ARM, pp. 787-790.

Wielicki, B.A., Barkstrom, B.R., Harrison, E.F., Lee III, R.B., Smith, G.L., and Cooper, J.E. (1996) Clouds and the Earth's Radiant Energy System (CERES): An Earth Observing System Experiment. *Bulletin of the American Meteorological Society,* 77, 853–868.

Williams, M., and Houze Jr, R. A. (1987). Satellite-observed characteristics of winter monsoon cloud clusters. *Monthly Weather Review.* 115(2), 505-519.

Woodley, W., Griffith, C.G., Griffin, J.S., and Stromatt, S.C. (1980) The influence of GATE convective rainfall from SMS-1 imagery. *Journal of Applied Meteorology.* 19, 388-408.

Wright, J.S. (2006) *Influences of Tropical Deep Convection on Upper Tropospheric Humidity.* PhD Thesis. Georgia Institute of Technology.

Wright, J. S., Fu,, R., and Heymsfield, A. J. (2009) A statistical analysis of the influence of deep convection on water vapor variability in the tropical upper troposphere, *Atmospheric Chemistry and Physics,* 9, 5847–5864.

Wu, D. L., Ackerman, S. A., Davies, R., Diner, D. J., Garay, M. J., Kahn, B. H., Maddux, B. C., Moroney, C. M., Stephens, G. L., Veefkind, J. P. and Vaughan, M. A. (2009) Vertical distributions and relationships of cloud occurrence frequency as observed by MISR, AIRS, MODIS, OMI, CALIPSO, and CloudSat. *Geophysical Research Letters*, 36, L09821.

Wylie, D., Jackson, D. J., Menzel, W. P., and Bates, J. J. (2005) Trends in high and low clouds from the analysis of 20 years of HIRS and ISCCP data. *Journal of Climate,* 18, 3021–3031.

Yang, G-Y. and Slingo, J. (2001) The diurnal cycle in the tropics. *Monthly Weather Review.* 129, 784-801.

Young, A.H., Bates, J.J. and Curry, J.A. (2013) Application of cloud vertical structure from CloudSat to

investigate MODIS-derived cloud properties of cirriform, anvil, and deep convective clouds. *Journal of Geophysical Research: Atmospheres.* 118(10), 4689–4699.

Yuan, J., and Houze, Jr., R. A. (2010) Global variability of mesoscale convective system anvil structure from A-train satellite data. *Journal of Climate*, 23, 5864-5888.

Zelinka, M.D. and Hartmann, D.L. (2009) Response of Humidity and Clouds to Tropical Deep Convection. *Journal of Climate.* 22, 2389-2404.

Zinner, T., Mannstein, H., and Tafferner, A. (2008) Cb-tram: Tracking and Monitoring Severe Convection from Onset over Rapid Development to Mature Phase using Multi-channel Meteosat-8 Seviri Data. *Meteorology and Atmospheric Physics* 101 (3–4): 191–210.

Zisper, E.J., Cecil, D.J., Liu, C., Nesbitt, S.W., and Yorty, D.P. (2006) Where are the most intense thunderstorms on Earth? *Bulletin of the American Meteorological Society,* 87, 1057-1071.